UNIVERSITY OF SOUTHAMPTON

FACULTY OF MEDICINE

Clinical and Experimental Sciences

Design and development of a novel artificial Bruch's membrane for ocular-based therapies

by

Gareth Ward

Thesis for the degree of Doctor of Philosophy

May 2016

UNIVERSITY OF SOUTHAMPTON

ABSTRACT

FACULTY OF MEDICINE

DOCTOR OF PHILOSOPHY

DESIGN AND DEVELOPMENT OF A NOVEL ARTIFICIAL BRUCH'S MEMBRANE FOR OCULAR-BASED THERAPIES

By Gareth Steven Ward

Age-related macular degeneration is a complex disorder causing irreversible loss of central vision in nearly 50 million individuals globally. The underlying pathology of this degenerative disorder is poorly understood, but impairment of the retinal pigment epithelium (RPE) layer and its supportive structure, the Bruch's membrane (BrM), are considered to be of critical importance to disease onset and progression.

Although the less common form of this disease (neovascular or wet AMD) can be managed in most patients, the prevalent geographic or dry form of AMD has no treatment. Consequently, several therapeutic strategies are being persued to develop a long-lasting and effective treatment. Replacement of the damaged RPE and BrM offers the simplest form of therapy that has the potential to bring about the most rapid patient benefits. Studies along these lines have sought to directly inject RPE cell suspensions into rodent disease models. However, this has resulted in reflux of cells from the site of injection or misformed grafts.

Such issues may be circumvented by creating a biocompatible prosthetic BrM, onto which a monolayer of RPE cells can be grown, and then transplanted sub-retinally. Hence, methyl methacrylate and poly(ethylene glycol) methacrylate, two compounds approved for safe clinical applications, were previously used in our laboratory to create an artificial electrospun BrM scaffold.

In this project, the biophysical properties of this first generation BrM scaffold have been refined, such that its thickness, tensile strength, diffusional characteristics and surface properties were more akin to native BrM. Its suitability has been tested by culturing primary mouse RPE cells for long periods. These findings indicated that RPE grown on this novel synthetic BrM scaffold formed stable monolayers and expressed cell-specific markers, adopting structural as well as functional specialisations observed in the native RPE.

A further modification to this scaffold using anthracene resulted in a BrM mimic that had an improved biophysical characteristic, with initial subretinal transplantation experiments carried out by clinical colleagues indicating that this artificial scaffold can potentially act as a promising BrM replacement for AMD patients, as well as those suffering from rare conditions such as retinitis pigmentosa.

Table of Contents

List of Tables

List of Figures

DECLARATION OF AUTHORSHIP

I, ...

declare that this thesis and the work presented in it are my own and has been generated by me as the result of my own original research.

....

....

I confirm that:

1. This work was done wholly or mainly while in candidature for a research degree at this University;
2. Where any part of this thesis has previously been submitted for a degree or any other qualification at this University or any other institution, this has been clearly stated;
3. Where I have consulted the published work of others, this is always clearly attributed;
4. Where I have quoted from the work of others, the source is always given. With the exception of such quotations, this thesis is entirely my own work;
5. I have acknowledged all main sources of help;
6. Where the thesis is based on work done by myself jointly with others, I have made clear exactly what was done by others and what I have contributed myself;
7. None of this work has been published before submission.

Signed: ....

Date:...

Acknowledgements

I would firstly like to express my deepest appreciation and gratitude to my supervisors, Dr. J Arjuna Ratnayaka, Ms. Angela Cree, Dr. Martin Grossel and Prof. Andrew Lotery for their invaluable academic support and guidance throughout my time as a PhD student.

The Vision research group (Miss. Jennifer Scott; Mrs. Helen Griffiths; Dr. Xiaoli Chen; Mr Jay Self, Miss. Savannah Lynn, Dr. Philip Alexander and Mr Ahmed Salman) have also provided excellent and continued support and advice during my PhD, without whom this project would have not been possible.

My gratitude also extends to the Grossel research group members (Dr. Nick Alderman, Dr. Darren Pitt, Dr. Adam Fisher, Dr. Dominic Wales, Dr. Bing Ja Yan, Mr. Hassan Gneid and Ms. Alya Dawood) for their vital guidance at the start of my project and their support.

I would like to extend my thanks to Mr. Andrew Wooldridge for his support and superb assistance in the processing of the electrospinning materials and techniques.

Thanks also go to Prof. Atul Bhaskar and Mr. Cuan Urquizio for their assistance in performing the mechanical testing of the artificial and native Bruch's membranes, and to Dr. Sumeet Mahajan for his investigations into RAMAN spectroscopy.

A special mention goes to Dr. David Johnston for his assistance with the confocal microscopy and for the many hours spent in the microscope room.

Thanks also go to Dr. Carolann McGuire, Mr. Ben Coles and Mrs. Maureen Gatherer for their guidance in flow cytometry and experimental techniques.

I would also like to thank my family and friends, especially my father Mr. Jon Ward for his proof-reading of this thesis, for their support and encouragement during my PhD project.

Finally, I would like to thank the Gift of Sight charity, whose financial support has made this project possible.

Definitions and Abbreviations

3D	Three dimensional
AA	Amino acid
AF	Alexa fluor
AFM	Atomic force microscopy
AIBN	Azobisiso-butyronitrile
AMD	Age-related macular degeneration
AMM	Anthrylmethyl methacrylate
ARPE-19	An immortalised human retinal pigment epithelium cell line
BrM	Bruch’s membrane
BSS	Balanced salt solution
CFH	Complement factor H
CNV	Choroidal neovascularisation
DAPI	4’,6-diamidino-2-phenylindole
DCM	Dichloromethane
DMAP	4-(*N,N’*-dimethyl amino)pyridine
DMEM	Dulbecco’s modified eagle medium
DMF	Dimethylformamide
DNA	Deoxyribonucleic acid
DSC	Di-succinimidyl carbonate
EDC	1-ethyl-3-(3-dimethylaminopropyl)-carbodiimide
EDTA	Ethylenediaminetetraacetic acid
ELISA	Enzyme-linked immunosorbent assay

FACS	Fluorescence-activated cell sorting
FAK	Focal adhesion kinase
FBS	Fetal bovine serum
FITC	Fluorescein isothiocyanate
FMA	Furfuryl methacrylate
HDI	Hexamethylene diisocyanate
HRP	Horseradish peroxidase
ICL	Inner collagenous layer
IR	Infrared spectroscopy
IRBP	Interphotoreceptor retinoid-binding protein
LDH	Lactate dehydrogenase
MMA	Methyl methacrylate
MP	Melting point
NDS	Normal donkey serum
NMP	*N*-methyl-2-pyrrolidone
NMR	Nuclear magnetic resonance
OCT	Optical coherence tomography
PAA	Poly(acrylic acid)
PBS	Phosphate-buffered saline
PEDF	Pigment epithelium-derived growth factor
PEG	Poly(ethylene glycol)
PEGM	Poly(ethylene glycol) methacrylate
PEI	Polyetherimide
PET	Polyethylene terephthalate

PETA	Pentaerythritol triacrylate
PFA	Paraformaldehyde
PIPES	1,4-piperazinediethanesulphonic acid
PMMA	Poly(methyl methacrylate)
POS	Photoreceptor outer segments
PVC	Polyvinyl choride
RBF	Round bottom flask
RNA	Ribonucleic acid
RP	Retinitis pigmentosa
RPE	Retinal pigment epithelium
RT	Room temperature
SEM	Scanning electron microscopy
TEA	Triethylamine
TEER	Trans-epithelial electrical resistance
TEM	Transmission electron microscopy
TLC	Thin layer chromatography
TMB	3,3’,5,5’-tetramethylbenzidine
THF	Tetrahydrofuran
UV	Ultraviolet
VEGF	Vascular endothelial growth factor
ZO-1	Tight junction protein

Chapter 1: Introduction

1.1 Overview

Age-related macular degeneration (AMD) is of growing concern in the developed world as the number of cases increases, reflecting the growth of an ageing population. This disease is characterised by the degeneration of light-detecting photoreceptor cells in the macula of the eye; a specialised part of the retina, leading to the loss of central vision. It is believed that possible damage to a monolayer of cells underneath the retina referred to as the retinal pigment epithelium (RPE) and associated layers is key to the onset of AMD.

Replacement of the damaged RPE monolayer has the potential to slow the progression of AMD and prevent further damage[1], however simply injecting RPE cells into the damaged site has met with limited success[2,3]. Subretinal injections of a suspension of RPE cells resulted in disorganised or misplaced grafts as well as reflux of cells from the desired location. As the underlying Bruch's membrane (BrM) is essential in providing maintenance and supporting the RPE layer, it was proposed that a RPE layer may be seeded onto an artificial BrM, with the aim of providing a localised and targeted treatment, acting as a mimic of the degenerated human BrM.

Polymer scaffolds have been synthesised previously[4], but these have not been accurate mimics of the native BrM, suffering from issues such as poor flexibility and limited mechanical strength. Further inroads into this approach would first require a substantial improvement to such synthetic BrM scaffolds so that realistic treatments can be explored.

This introduction provides a background into creating such artificial scaffolds, their application as a biomaterial, methods used for their manufacture as well as an introduction into the anatomy of the retina and the pathophysiology of AMD.

1.2 The Mammalian Eye

Eyes are our window onto the world. The eye is arguably one of the most important sensory organs in the human body and it is responsible for around 40% of the total sensory input to the human brain[5], providing us with one of our most treasured senses, sight. The eye is a delicate structure; the orbit, a bone cavity that houses the eyeball, protects the eye from physical damage.

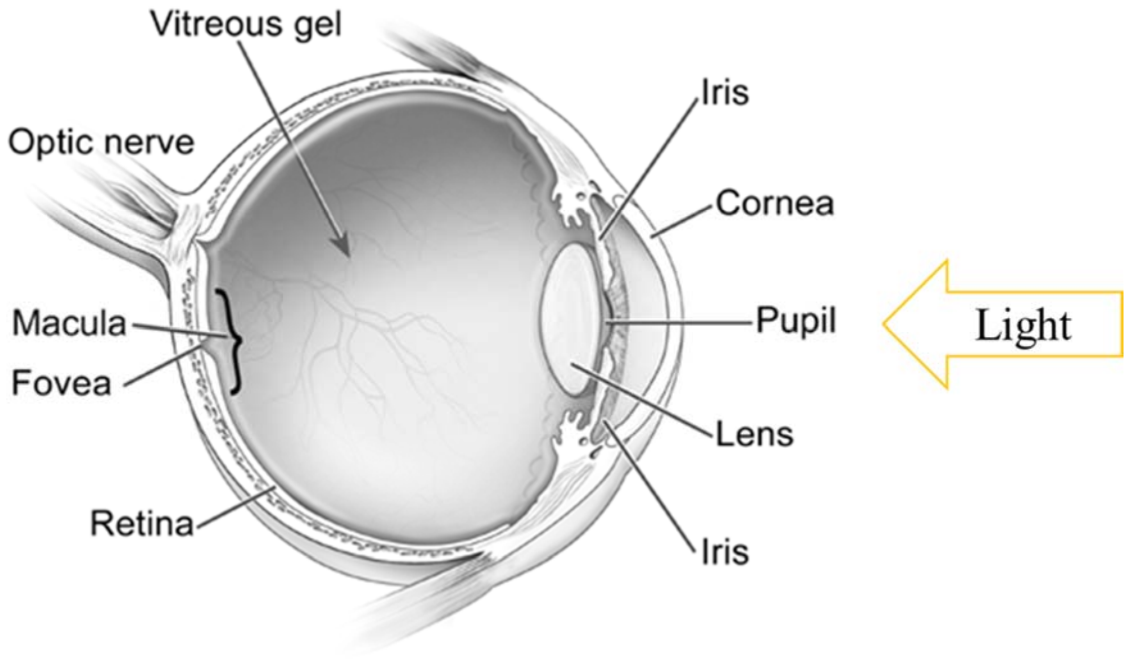

Figure 1: Schematic representation of the human eye, highlighting the key components. Light passes through the pupil, lens and vitreous humor before reaching the light-sensitive retina. From The National Eye Institute: www.nei.nih.gov.

The main body of the eye (Fig. 1) is divided into two parts by the lens, a glycoprotein-based capsule containing transparent, long lens fibres[5]. The primary function of the lens is to focus light entering the eye onto the retina, with the lens being regulated by the ciliary muscle and suspensory ligaments to achieve short or long-sight. The amount of light is controlled by the iris, a ring of muscle that relaxes or contracts to alter the size of the pupil (the circular opening of the iris). The part located in front of the lens is filled with the aqueous humour, whereas the part located behind the lens is filled with a more viscous fluid known as the vitreous humour. Light enters through the cornea and passes through the aqueous humour, the pupil, the lens and the vitreous humour, before it reaches the retina. All of these integral parts of the eye are essential in providing light to the retina, the light-sensitive layer at the back of the eye.

1.2.1 Retina and Photoreceptors

Located in the back of the eye lies the retina, a complex multi-layered light-sensitive structure which converts incident light into electrical signals that are then relayed to the brain (Fig. 2). It is composed of: (i) a ganglion cell layer, the axons which connect the retina to the optic nerve; (ii) an inner nuclear layer, which contain bipolar neurons which help transmit signals to the optic nerve; (iii) an outer nuclear layer which contains the light-sensitive cells, photoreceptors; and (iv) the retinal pigment epithelium (RPE), a monolayer of specialised cells which provides support for the photoreceptors (see section 1.2.2) and together with the underlying Bruch's membrane (BrM) forms the outer blood-retinal barrier[5].

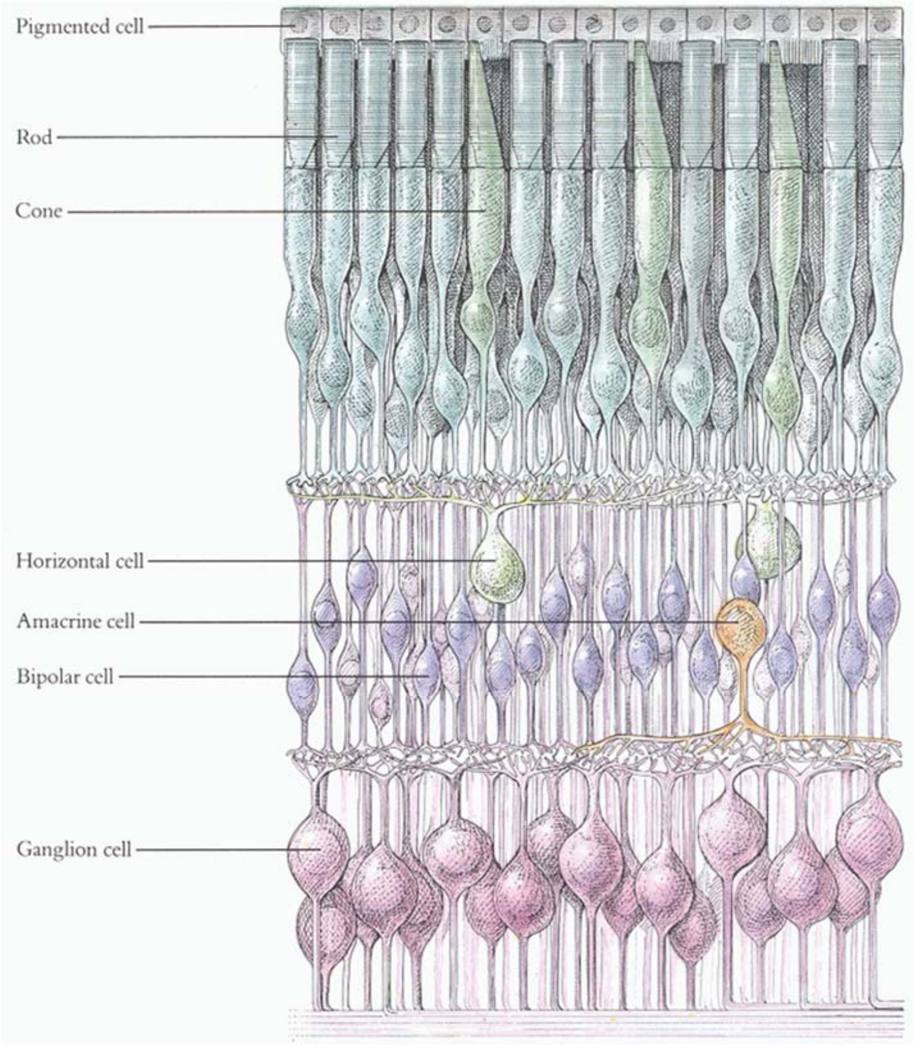

Figure 2: Cross-section of the human retina, showing: (i) the ganglion cell layer; (ii) the inner nuclear layer, consisting of bipolar, amacrine and horizontal cells; (iii) the outer nuclear layer containing the photo-sensitive columnar-like rods and cones; and (iv) the RPE layer. As taken from 'cross section of the retina' (fourier.eng.hmc.edu).

Light passes through the first two layers onto the photoreceptors, where the photosensitive molecules rhodopsin and iodopsin are bleached by the light, generating a cascade of signals which are then relayed onwards. This signal is then transmitted to second order neurons, sent through the inner nuclear and ganglion cell layers and transmitted to the optic nerve, which then conveys the information to the brain.

There are two different forms of photoreceptors, rods and cones. Rods contain a compound known as rhodopsin, a complex pigmented protein consisting of opsin and retinal (a light-sensitive molecule generated from Vitamin A, see section 1.2.2). When retinal is exposed to light it is converted into its isomeric form and detaches from opsin. This causes the opsin to change the surface membrane of the rod cell into a negative polarisation, creating an action potential and generating the nerve impulse through the attached nerve cells[6]. Cones also contain retinal, but where they differ from rods is in the composition of the attached protein, which is known as iodopsin[7,8]. A similar procedure occurs in cones, where the retinal is converted to its isomeric form and sets off a chain of events. However, cones contain a slightly different pigment, known as photopsins, and respond to different wavelengths of light, leading to the production of colour.

These photosensitive cells are pivotal in the decoding of light energy into sight, and are supported by a monolayer of pigmented epithelia, referred to as the RPE, which underlie the outer segments (Fig. 2).

1.2.2 Retinal Pigment Epithelium

Underlying the photoreceptors within the retina is a monolayer of pigmented cells known as the retinal pigment epithelium (RPE). The RPE is a cuboidal epithelium, forming a part of the blood/retina barrier[9] (Fig. 3). The apical membrane faces the photoreceptor outer segments and consists of apical microvilli, which wrap around and interdigitate with the adjacent photoreceptor outer segments establishing structural interactions. The basal membrane faces the underlying Bruch's membrane (discussed in section 1.2.3), which provides a barrier to the choriocapillaris underneath.

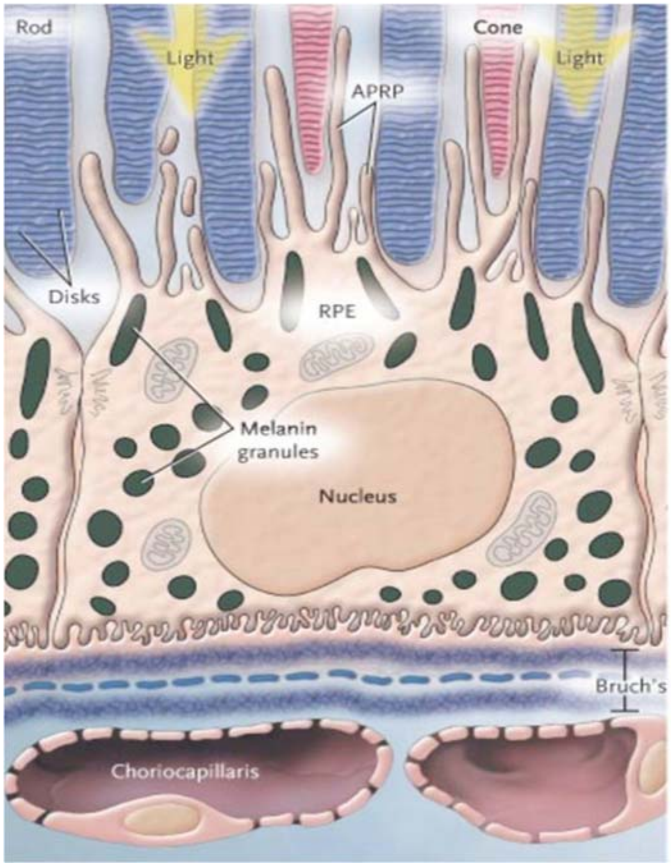

Figure 3: Diagram of a healthy RPE cell, showing: (i) the rods and cones interdigitating with the apical microvilli of the RPE cell; (ii) the melanin granules throughout the RPE cytoskeleton. These pigmented molecules absorb light that has passed the photoreceptors; (iii) the interaction between the RPE cell and the underlying Bruch's membrane. Taken from the University of Rochester pulication '"Dark Cells" of living retina imaged for the first time' (www.rochester.edu).

These cells which contain the pigment 'melanin': (i) absorb light which has passed through the retina and prevent further light scatter; (ii) transport water and ions to the choriocapillaris from the retina and removes metabolic waste from tissues in the outer retina; (iii) deliver nutrients such as glucose, retinol and fatty acids from the blood to the photoreceptors; (iv) regenerate 11-*cis*-retinal in the photoreceptors, after the production of the isomerised all-*trans*-retinal by light absorption; (v) maintain the integrity of the photoreceptors by ingesting shed outer photoreceptor segments and recycling retinal and docosahexanoic acid back to regenerate the photoreceptors; (vi) and finally the RPE is able to secrete growth factors such as vascular endothelial growth factor (VEGF) and pigment epithelium-derived growth factor (PEDF) to maintain and promote the viability and continued function of the underlying choriocapillaris and photoreceptors (Fig. 4)[10].

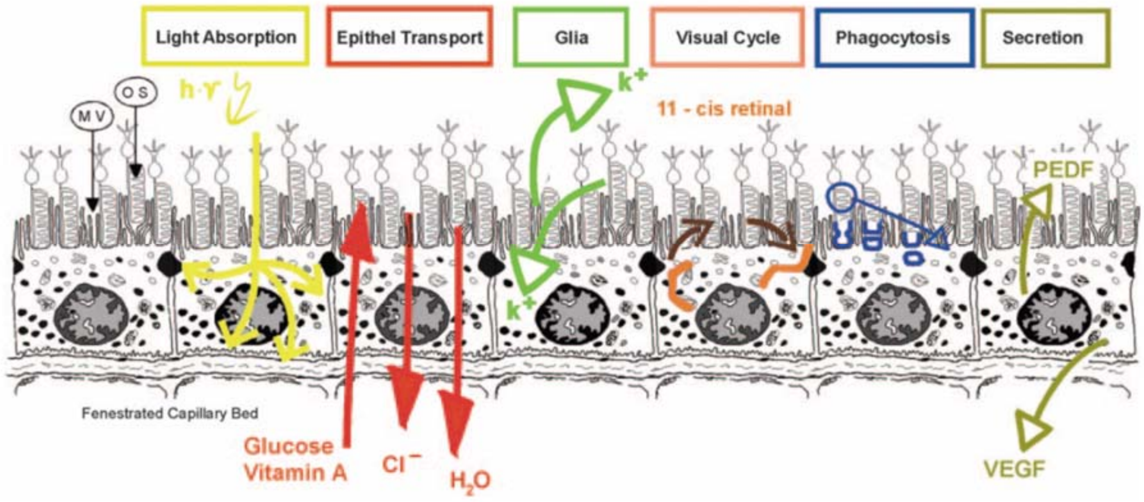

Figure 4: A representative summary of the key functions of the RPE monolayer, showing its ability in: (i) absorbing backscattered light; (ii) facilitating trans-epitethelial nutrient transport; (iii) deliver key nutrients to the retina; (iv) regenerate 11-*cis*-retinal from all-*trans*-retinol; (v) phagocytose and recycle shed outer photoreceptor segments; and (vi) secrete key growth factors. Adapted from Strauss 2005 publication on 'The Retinal Pigment Epithelium in Visual Function'[10].

The RPE forms a dark pigmented wall over the underlying choriocapillaris and Bruch's membrane, preventing the degenerative effect of unabsorbed scattered light and maintaining visual function. As discussed previously, light enters the eye *via* the pupil and is focused onto the macula by the lens. This concentrated light is directed at the retina and is absorbed by the photoreceptors *via* phototransduction. Light that isn't taken up by the photoreceptors can cause oxidative damage to proteins, DNA and lipids[11]. To prevent the formation of reactive oxygen compounds, any light that passes the photoreceptors is taken up by melanin in melanosomes found within the RPE[12]. This line of defence is crucial for the limitation of oxidative damage.

Metabolic processes within the photoreceptors create a large amount of water, leading to a significant need to remove this water from the retina. The RPE transports water from the sub-retinal space found on its apical side to the basal choriocapillaris[13]. This transport of water prevents damage caused by a build-up of water and helps maintain retina adhesion. Ions such as Na^+ and K^+ are also transported by the RPE from the sub-retinal space to the choriocapillaris and *vice versa*. The junctional properties of the RPE (presence of tight junctions) and the polarity of the membrane facilitates this, with the presence of Na^+/K^+ ATPase in the microvilli also providing the energy for transepithelial transport[14]. Nutrients such as glucose and vitamin A are also transferred from the choriocapillaris to the RPE and used for processes such as the visual cycle.

The ability to convert light into electrical signals starts with the absorption of a photon of light by ‘11-*cis*-retinal’ located in rhodopsin in the photoreceptor outer segments[15,16]. Once this has occurred, 11-*cis*-retinal converts to its isomeric form ‘all-*trans*-retinal’, which is unable to absorb a photon of light (Fig. 5). The photoreceptors are unable to reform the 11-*cis*-retinal isomer and require assistance from the underlying RPE. The RPE converts the all-*trans*-retinol back to 11-*cis*-retinal through the use of the RPE-specific protein ‘RPE65’ and 11-*cis*retinol-dehydrogenase[17]. This is then returned to the photoreceptors, completing the ‘visual cycle’.

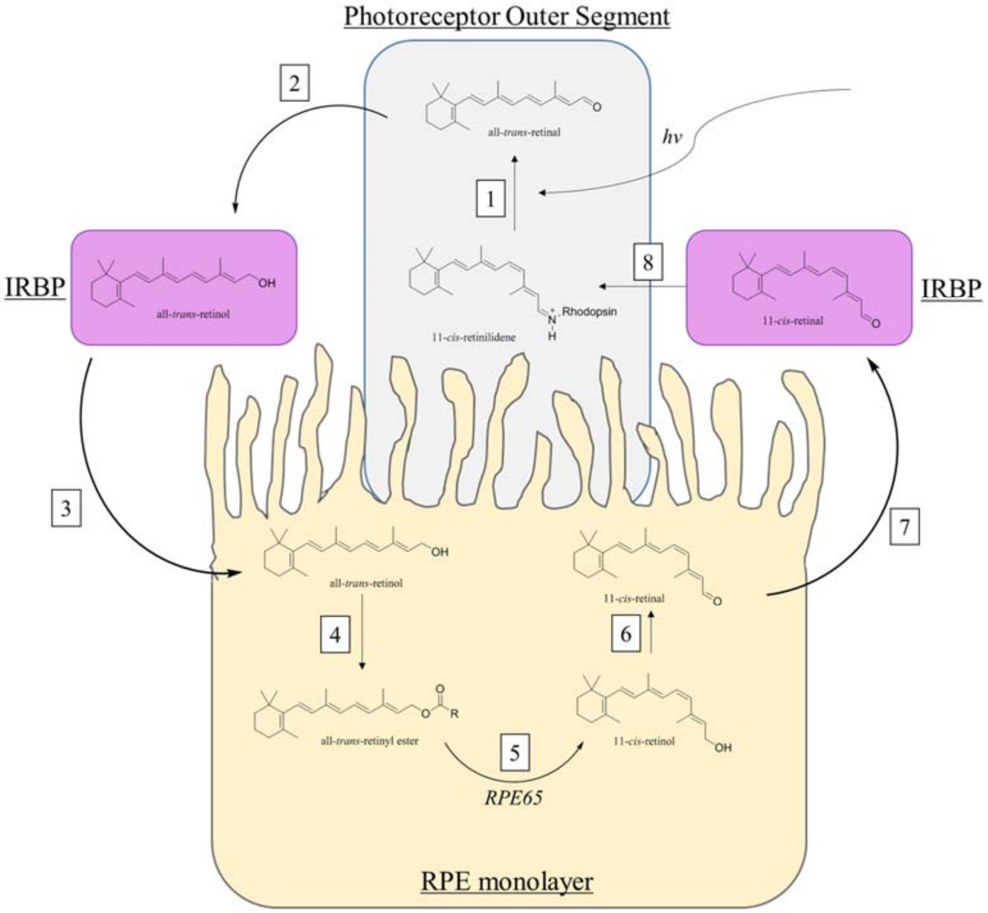

Figure 5: Schematic showing the regeneration of 11-*cis*-retinal from all-*trans*-retinol. As light is absorbed by the photo-sensitive 11-*cis*-retinilidine-rhodopsin conjugate, it is isomerised into all-*trans*-retinal (1), detaching it from rhodospin. This new aldehyde is converted to all-*trans*-retinol by retinol dehydrogenase and complexed with the interphotoreceptor retinoid-binding protein (IRBP) (2), which transfers it to the RPE monolayer underlying the photoreceptors (3). Here, it is esterified to all-*trans*-retinyl ester (4), which allows for the conversion to 11-*cis*-retinol (5) facilitated by RPE65. It is then further converted to its original aldehyde form (6), transported back to the photoreceptor (7) and complexed with rhodopsin (8).

The visual cycle is an effective way of regenerating the light-sensitive molecule retinal, however, bleaching of retinal and the associated opsin/iodopsin protein can lead to the accumulation of photo-damaged proteins and radicals[18]. This reduces the ability of the photoreceptors to convert light energy into electrical signals and therefore, in order to maintain the effectiveness of the photoreceptors, its outer segments (POS) undergo a renewal process[19]. Through the apical membrane of the RPE facing the POS, the tips of the POS containing the highest concentration of photo-damaged compounds are shed and phagocytosed by the underlying RPE, facilitated by the RPE receptors MerTK and $\alpha v\beta_5$[20]. Here, the shed POS are digested and important molecules such as retinal and docosahexanoic acid are removed and transported back to the photoreceptors. Failure of the RPE to phagocytose shed POS causes retinal degeneration and a build-up of photo-damaged molecules leading to rare diseases such as Retinitis Pigmentosa (RP)[21–23].

Alongside maintenance of the photoreceptor integrity, the RPE also secretes key growth factors, most importantly PEDF and VEGF. PEDF is secreted apically towards the retina whilst VEGF is secreted on the basolateral side to maintain choriocapillaris endothelium and maintain its fenestrations[24]. Over-expression of VEGF can induce an over-stimulation of the choriocapillaris growth, leading to complications such as choroidal neovascularisation (CNV)[25,26].

Therefore the physiological roles of the RPE are pivotal in the maintenance and integrity of the retina, and subsequent failure of any of these key processes can lead to an onset of complications such as retinal degeneration and ultimately, blindness.

1.2.3 Bruch's membrane

The function of the RPE monolayer is key in the maintenance of the retina. RPE cells are anchorage dependant through the basolateral cellular junctions to the BrM (Fig. 3), and as such the integrity of the BrM is vital to prevent cell death resulting from lack of attachment (cell anoikis)[27].

The BrM is located in-between the RPE and the choriocapillaris and acts as a semi-permeable filtration barrier, controlling the transport of nutrients and products to and from the choriocapillaris and the attached RPE monolayer (Fig. 6). Oxygen, macromolecules, vitamins and electrolytes pass from the choriocapillaries, through BrM and towards the RPE and photoreceptors. The resulting waste products and excess water from the subretinal space are transported back from the choroid towards the choriocapillaires, through BrM[28,29].

Native BrM is a penta-laminar structure[30], consisting of: (i) the basement membrane of the RPE monolayer; (ii) the inner collagenous layer; (iii) an elastin layer; (iv) the outer collagenous layer; and (v) the basement membrane of the choriocapillaris[31].

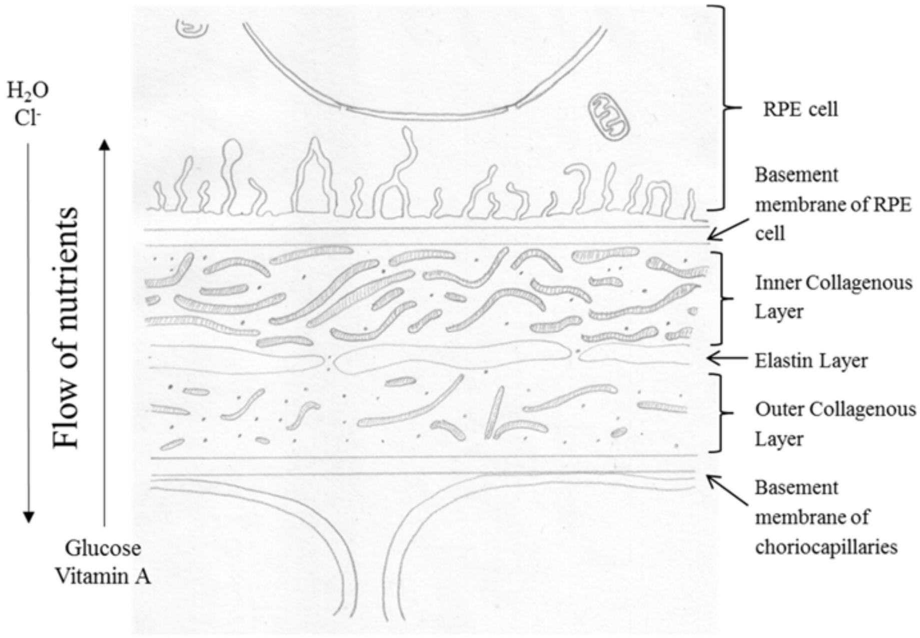

Figure 6: Representative drawing of native BrM, based on electron microscope studies[32], highlighting the penta-laminar structure and detailing the flow of nutrients from the choriocapillaris through BrM to the RPE and *visa versa*.

The RPE basal lamina (basement membrane of the RPE cell) is a nanometre thick layer composed of an interwoven mesh of Type IV collagen fine fibres[33,34]. Specialised integrins and laminins are synthesised from the RPE monolayer within this matrix to preferentially adhere BrM to the RPE[35,36].

The choriocapillaris basal lamina (basement membrane of the choriocapillaries) is also a nanometre thick layer composed of Type IV collagen fibres which, utilising the fenestrations within the adjacent choriocapillary endothelium, allow the required macromolecular permeability[37].

The inner and outer collagenous layers consist of type I, III and V collagen fibres, each providing tensile strength & elasticity[38]. The fibres are interwoven with a wide range in pore sizes, with the fibre average diameter around 1µm[39] with type I collagen providing tensile strength[38], type III providing elasticity and type V providing the anchorage to the basement membranes of the choriocapillaris and RPE, alongside the aforementioned Type

IV collagen located in the basement membrane of the choriocapillaris and the RPE[40]. The inner collagenous layer is responsible for supplying the majority of fluid movement resistance in native BrM between the RPE and the choriocapillaires, and is thus essential in providing the necessary control in the transport of solutes, water, macromolecules and oxygen[41].

The BrM covers more than half the human eye and stretches as intraocular pressure, choriocapillaris pulse and choroidal blood volume changes[42,43]. It is therefore able to retain its original shape and morphology to accommodate for these changes, thereby requiring elasticity. The central elastin layer helps BrM withstand pressure from these physiological changes, allowing it to return to its original shape and morphology[44]. The central elastin layer consists of several stacked matrices of elastin fibres, forming an interwoven fibrous sheet[32]. Interactions with the inner and outer collagenous fibres enable the elastin layer to interweave with the adjacent layers of BrM[45].

BrM is a semi-permeable layer which facilitates the transport of nutrients to the retina and the removal of waste products to the choriocapillaris. It helps control the movement of substances such as amino acids, vitamin A and fatty acids by acting as a filtration barrier. It is unknown how permeable BrM is, but studies have shown it allowing the free passage of molecules 21.2 kDa in size[46], with fluctuations in its permeability depending on the local pH surrounding the membrane[47].

BrM interactions with the RPE are essential in controlling the transport of nutrients and originate from the initial embryonic development of BrM. The initial formation of BrM begins near the RPE[48,49], which has been shown to produce significant amounts of the extracellular matrix components of BrM[50]. Bruch's membrane forms by 6-7 weeks' gestation from the basement membranes of the RPE and choriocapillaris[51]. Subsequent collagen production within the inner and outer collagenous layers is theorised to be carried out by invading fibroblasts associated with the adjacent choriocapillaris[51], with the central elastin layer developing last[52]. Fenestrations into the RPE are established (Fig. 6) and by week 13 the fenestrations into the choriocapillaris are apparent also[51,52]. The two remaining layers of the pentalaminar membrane (the basal layers from the choriocapillaris and RPE) are produced by the adjacent cell layers[49]. Subsequent development of the adjacent choriocapillaries, and the choriocapillaris basement membrane, is governed by the developed RPE monolayer and the production of vasvular endothelial growth factor (VEGF)[53]. The interactions with the neighbouring tissues stem from the gestational phases, with the resulting connections a direct result of the developmental stages.

The development of BrM from the RPE establishes a clear connection between the two fundamentally important layers of the retina, with the basement membrane of the RPE integral to the penta-laminar structure of BrM. The inner collagenous layer of BrM (Fig. 6) presents a porous, fibrous matrix to the basement membrane of the RPE and thereby allows the diffusion of key macromolecules from the RPE (facilitated *via* the connection discussed previously) to the choriocapillaris (Fig. 6).

BrM is essential as a structural support for the RPE monolayer and in the control of macromolecular diffusion from the choriocapillaries towards the retina and *vice versa*, through the use of the collagenous layers and central elastin matrix. Damage to BrM could result in the disruption in any of these processes, leading to the potential disruption in the function of the dependant RPE monolayer.

1.3 RPE-based diseases

With the RPE playing such a vital role in the maintenance of the photoreceptors and choriocapillaris, failure of this critical monolayer to carry out its required tasks has profound effects on visual acuity, leading to the development of one of the most common eye diseases in the western world.

1.3.1 Age Related Macular Degeneration

Age related macular degeneration (AMD) is the leading cause of irreversible blindness in individuals over 50 years of age in the developed world[54,55]. It is a complex, degenerative disease that affects the choriocapillaris, BrM, RPE and photoreceptors.

The disease, in its early stages, develops slowly over a number of years, making the preliminary diagnosis challenging. The condition is generally characterised by a build-up of ‘drusen’, a sub-retinal pigment epithelial deposit located in-between the BrM and RPE layer that consists predominantly of proteins, carbohydrates and lipids[56,57]. These characteristic white-yellow deposits are visible by fundus microscopy (Fig. 7), and are commonly used as an early clinical hallmark of a deteriorating BrM/RPE layer, indicative of early AMD[58].

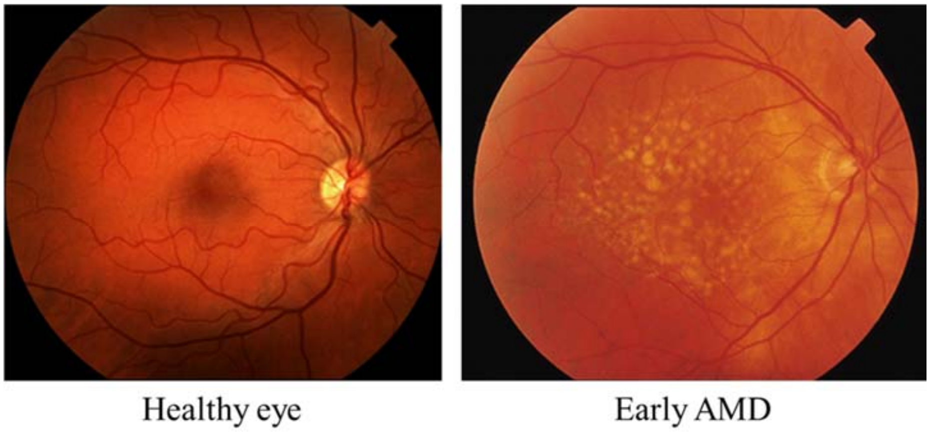

Figure 7: Fundus microscopy of (left) a healthy patient and (right) a patient with signs of AMD. Yellow-white extra-cellular deposits (drusen) are clearly visible, indicating a degenerating macula and BrM/RPE layer. Images from The National Eye Institute: www.nei.nih.gov.

There are two distinctive phenotypes of AMD, wet (exudative) and dry (atrophy).

Choroidal neovascularisation (CNV), or 'wet AMD', is a rapid degeneration of the BrM, RPE and retina caused by the development of new blood vessels penetrating from the choriocapillaris through the BrM. These new blood vessels cause retinal detachment, RPE cell apoptosis *via* disruption of the RPE-BrM complex, and leakage of blood and fluid into and under the retina (Fig. 8). This leads to the formation of a retinal scar, all of which contributes to the profound and rapid loss of central vision[59].

CNV is believed to occur as a result of an increased secretion of VEGF from the RPE layer above the choriocapillaris[60]. VEGF is crucial for the normal development of blood vessels (angiogenesis), however an increased secretion from the basal side of the RPE towards the choriocapillaris has led researchers to believe that this is the direct result for the sudden onset of CNV[25,26,61,53].

During the past 10 years, researchers have developed a number of suitable therapies to facilitate the treatment of wet AMD. Anti-vascular endothelial growth factor (VEGF) antibodies such as Bevacizumab (Avastin)[62], Aflibercept[63] and Ranibizumab (Lucentis)[64] have been developed to block angiogenesis in CNV. Treatments are applied periodically (ranging from monthly to every 2 months) *via* intravitreal injections and in the case of Lucentis have shown to improve visual acuity by 33% after 1 year[65]. However, despite treatment patients develop complications (possibly exacerbated by intra-vitreal injection) such as an RPE tear[62]. There was also little improvement from the initial change in visual acuity from year 1 to year 2 with Lucentis and Avastin[66], whilst treatment was not effective in all patients. Long-term effects of the drugs are still being monitored, with concerns that geographic atrophy may be a side effect of prolonged therapy[67].

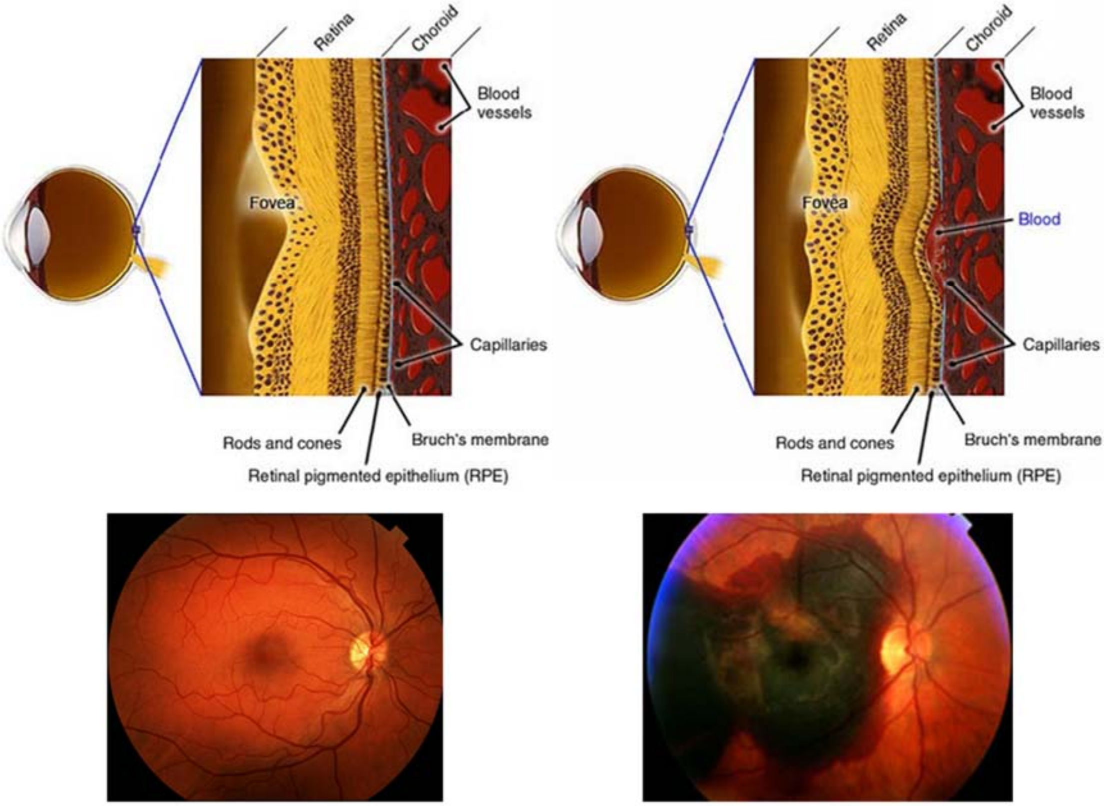

Healthy eye

Wet AMD

Figure 8: Cross-sectional diagrams and fundus micrographs showing the effect of choroidal neovascularisation. The breakthrough of the blood vessels through the BrM and distorting the retina is highlighted in the cross-section of Wet AMD (right), with the fundus micrograph showing the obvious sign of haemorrhage. Cross-sectional images and healthy eye fundus micrograph courtesy of The National Eye Institute: www.nei.nih.gov, with the wet AMD fundus micrograph courtesy of Prof A J Lotery.

Whilst these treatments are effective in improving visual acuity, they do not provide a long-term solution and require repeated injections which are invasive, require repeated hospital visits by the mainly elderly patients and methods are potentially destructive.

Geographic atrophy, or ‘dry AMD’, is a prolonged degeneration of the RPE, and subsequent photoreceptor damage, leading to the dysfunction of the macula.

It is unclear how geographic atrophy occurs; many researchers have developed theories that all link drusen, BrM and oxidative and inflammatory stress as potential causes of dry AMD (Fig. 9). Dysregulation of the immune system, in particular the complement system within the innate immune system, has been proposed by researchers as a potential cause for an inflammatory response to lipid accumulation[68]. In particular genetic mutation and therefore dysfunction of Complement Factor H (CFH), a 155kDa sialic acid that plays an integral role in the regulation of the complement innate immune system, has been theorised as a potential cause for AMD. A mutation in the complement gene could cause an unwanted inflammatory effect by allowing increased alternative complement pathway activation. Thus leading to an onset of complications and development of AMD[69,70].

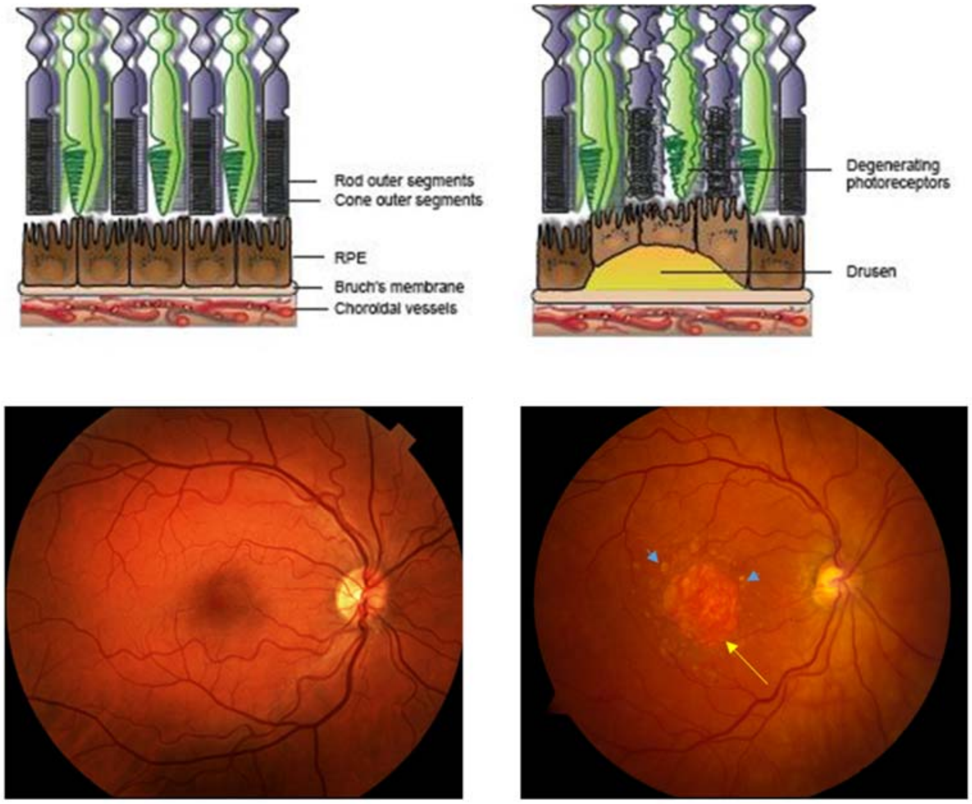

Healthy eye

Dry AMD

Figure 9: Fundus microscopy and representative schemtics showing the degradation of the macula from (left) a healthy eye to (right) the diseased retina in geographic atrophy. Blue arrows in the dry AMD fundus micrograph indicate the yellow-white deposits of drusen, with the yellow arrow highlighting atrophy of the RPE in the macula. Images courtesy of The National Eye Institute: www.nei.nih.gov.

Another indication of an inflammatory response is in the build-up of inflammatory compounds. β-Amyloid is a major pro-inflammatory component of Alzheimer's disease plaques[71], and has been located in drusen deposits of patients with AMD[72]. Work carried out by Yoshida *et al* found that mice which lack the β-amyloid-degrading enzyme demonstrated a significant increase in the deposition of β-amyloid in the sub-retinal space, whilst also displaying characteristic features of AMD[73]. This suggests that Aβ deposits in drusen may also contribute to AMD.

An alternative theory investigates the role of BrM in AMD. With age the supportive BrM thickens, with the thickness changes found predominantly in the centre of the macula[74]. This, coupled with an increase in the accumulation of lipids and less soluble collagen in the inner collagenous layer (ICL)[75], causes a reported increase in thickness of 135% in 10 decades[76]. This reduces the diffusion of nutrients and macromolecules from the choriocapillaris, across BrM to the RPE cells[77], with the hydraulic conductivity of the BrM shown to decline as demonstrated by the transport of fluid across the BrM halving every 16 years[29,78].

Alongside an increased thickness, the elasticity of BrM decreases with age[44]. Research by Ugarte *et al* found that the elastic properties of BrM decreased as a result of the potential degradation of the elastin fibres found in the centre of the penta-laminar membrane. This could contribute to a diminished choroidal blood flow and subsequent reduction in the ability of BrM to facilitate in the transfer of nutrients to the retina, leading to a potential protein and lipid build-up.

Light-induced oxidative stress has also been linked to developing geographic atrophy. The formation of carboxyethylpyrrole, an oxidised part of docosahexanoic acid[79], can cause a build-up of unwanted material in the RPE-BrM layer, forming additional drusen-like substances and lead to RPE cell anoikis. These reactive oxygen species can lead to oxidative-induced modifications, such as cross-linking, and have been shown to be associated with drusen proteins[80,81].

Currently, there is no readily available treatment for geographic atrophy. Binder *et al* suggested that an injection of RPE cells showed potential as a treatment for dry AMD, with the aim of rejuvenating the diseased macula and BrM[82,83]. However, simply injecting RPE cells into the sub-retinal space led to a lack of organisation of the injected RPE cells, resulting in the stacking of RPE cells, retinal fibrosis, proliferative vitreoretinopathy and rejection from aged BrM[84,85,39].

A recent report by Kamao *et al* investigated the implantation of a pluripotent stem cell-derived RPE sheet, which had been generated on the surface of a biodegradable collagen gel and separated from the gel after the formation of a complete confluent monolayer[86]. This had the potential of allowing the rejuvenation of the diseased macula without the lack of organisation provided by the injection of a suspension of RPE. However, there are issues with implantation, with the need for a more complicated and invasive surgical procedure to implant an intact sheet of RPE.

1.3.2 Retinitis Pigmentosa

Whilst AMD is of increasing concern in the western world, another important RPE-based disease affecting visual function is retinitis pigmentosa.

Retinitis pigmentosa (RP) is a degenerative retinal disease of the rod and cone photoreceptors and is shown in fundus microscopy as the discolouration of the retina (Fig. 10). Around 1 in 4000 have the condition, resulting in over 1 million affected individuals worldwide[21]. It is caused by the disorder or loss of the rods and cones due to genetic mutation of several genes, with subsequent degeneration of the inner nuclear layer and ganglion cell layer occurring at a later stage[22]. Current investigations have highlighted genes affecting the metabolism of vitamin A, the phototransduction cascade, the pH regulation, phagocytosis of POS and the maintenance of microvilli as all potentially contibuting towards RP[87,88].

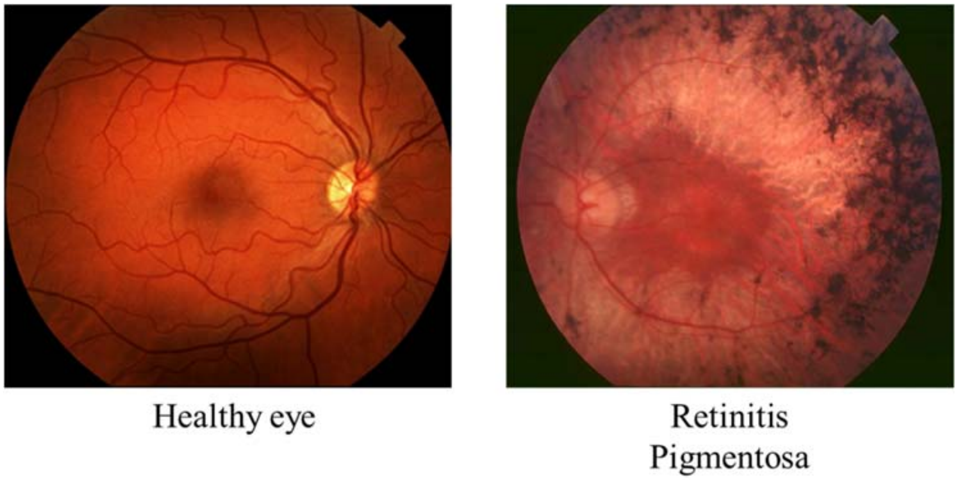

Figure 10: Fundus micrographs showing the difference between a (left) healthy eye and (right) an eye with retinitis pigmentosa (RP). Dysfunction of the photoreceptors is shown in RP as a black discolouration of the retina, highlighted in the fundus micrograph. Image of the healthy eye courtosy of The National Eye Institute: www.nei.nih.gov, with the RP fundus micrograph courtesy of Hamel *et al*[21].

Potential preventative methods include frequent Vitamin A ingestion, although this has only been shown to slow-down the decline in visual acuity[89]. Current research by Busskamp *et al* involves the investigation into gene therapy as a prospective preventative treatment for RP[90]. The recent development in the successful treatment of Leber's congenital amaurosis through the use of gene therapy[91,92] has boosted confidence in gene therapy. One example of this is in the publication by Beltran *et al*, who have found that the lengthening of the gene (gene augmentation) associated with the maintenance of the apical microvilli of the RPE cells prevents photoreceptor degeneration and preserved retinal structure and function in canine species[93]. This has the potential to prevent the development of RP in humans.

However, as in the case of AMD, there is currently no readily available treatment for the degradation of the BrM-RPE complex. These RPE-based diseases have a devastating effect on visual acuity, with current treatments ineffective in providing a suitable therapy. Therefore, alternative methods are required to afford a suitable new treatment to RPE-based diseases, with many researchers looking at the use of polymers.

1.4 Polymers

The International Union of Pure and Applied Chemistry (IUPAC) definition of a polymer states that it is 'a substance composed of molecules characterised by the multiple repetition of one or more species of atoms or groups of atoms (constitutional units) linked to each other in amounts sufficient to provide a set of properties that do not vary markedly with the addition or removal of one or a few of the constitutional units'[94]. This can be interpreted as a large molecule, or 'supramolecule', synthesised by the combination of many subunits, or 'monomers', that are easily tuneable and modified by groups of atoms (constitutional units[94]) without compromising the existing properties of the multi-monomer species. This flexibility in the modification of polymeric species leads to many varying properties, influenced by the composition of the monomers used in the synthetic process.

1.4.1 Monomers

Monomers are the backbone of the polymer species; the synthesis of polymers involves the coupling of one or many differing monomer units together to form one large molecule (Fig. 11). The only parameter for a molecule to act as a monomer is the ability to bind chemically or in a supramolecular manner to other molecules to form the required large molecule (polymer)[95]. Therefore, there are a vast number of differing monomer units available.

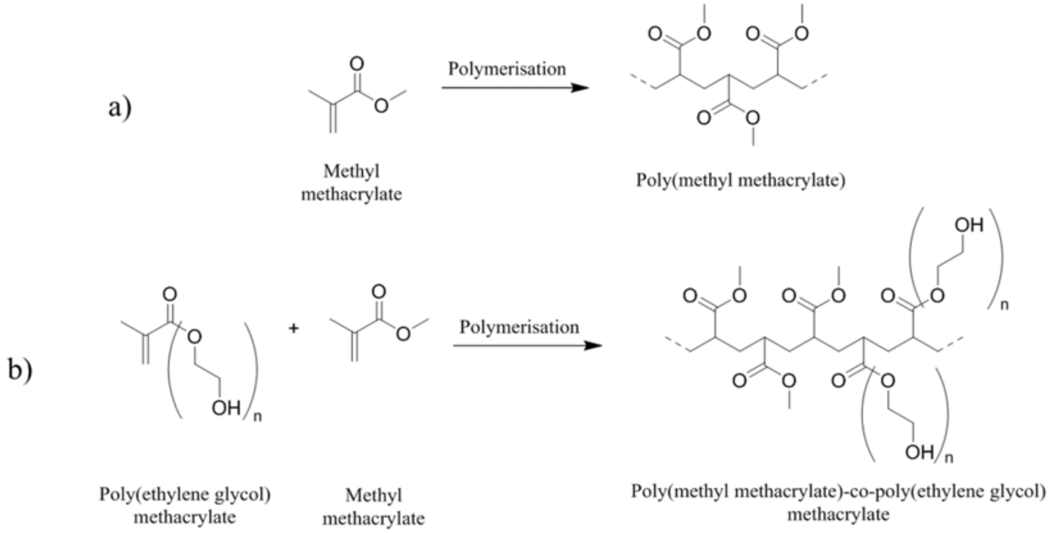

Figure 11: Schematic showing the polymerisation of: (a) one monomeric unit (methyl methacrylate) and (b) two monomeric units (poly(ethylene glycol) methacrylate and methyl methacrylate) to form a polymer species. These final polymer blends are influenced by the monomers used, affecting the properties of the products synthesised.

In nature, monomeric units such as amino acids, nucleotides and glucose are key in the formation of important macromolecules, for example cellulose, proteins and nucleic acids including deoxyribonucleic acid (DNA) and ribonucleic acid (RNA). In the case of protein synthesis, the combination of differing amino acids *via* peptide bonds provides the formation of a diverse range of proteins, allowing for the production of the most versatile macromolecules in living systems which serve crucial functions in all biological processes[96]. Similarly, nucleotides are essential in the composition of nucleic acids. Nucleotides are composed of three units: (i) a central 5-carbon sugar molecule; (ii) a nitrogenous base, essential in the hydrogen-bonded base-pairing sequences in DNA; and (iii) a phosphate group[97]. These phosphate groups link with the pendant hydroxyl groups on the sugar moieties and form a sugar-phosphate backbone, the essential polymeric strand of DNA.

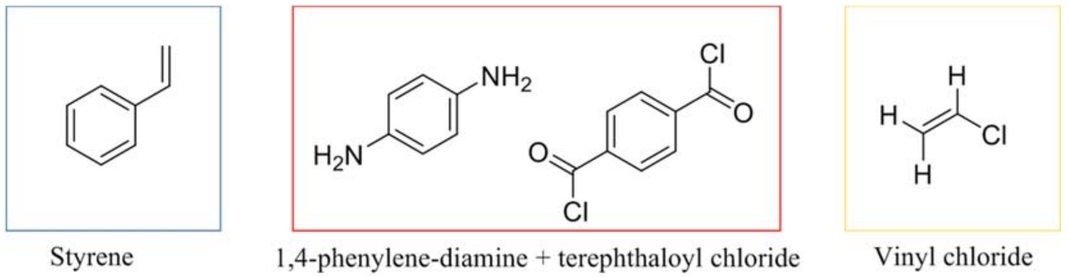

Styrene

1,4-phenylene-diamine + terephthaloyl chloride

Vinyl chloride

Figure 12: Examples of some important industrial monomers, showing the monomer(s) for: (blue) polystyrene; (red) Kevlar; and (yellow) poly(vinyl chloride) (PVC). These monomeric units are widely used within industry in the production of key polymeric species.

Within industry, the evolution and discovery of novel monomeric units has led to the formation of vital products, such as polystyrene, Kevlar and polyvinyl chloride (PVC) (Fig. 12). Through the use and manipulation of compounds such as vinyl chloride, scientists have been able to produce polymers with varied properties. Vinyl chloride was manufactured from ethene, and converted into PVC by heating in an inert solvent with benzoyl peroxide to initiate polymerisation[98]. These synthetic processes generated a polymer that could be manipulated into either a rigid or flexible form, and is the third-most widely produced synthetic polymer[99].

This flexibility and variety of monomers used in the synthesis of polymers provides a varying array of properties, which in turn are tuneable and can be modified.

1.4.2 Synthetic steps in generating polymers

The combination of monomers into a polymer can be carried out by two different methods, each with their own advantages and disadvantages. The two main routes to synthesising polymer systems are by ‘step polymerisation’ or by ‘chain polymerisation’. These polymerisation mechanisms differ in several features, including: (i) the growth of the polymer; (ii) the use of an initiator compound; and (iii) average molecular weight of the polymer formed.

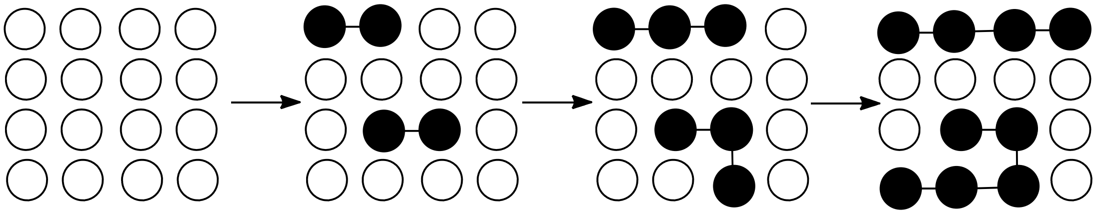

Figure 13 – A schematic showing the synthesis of a polymer chain *via* step polymerisation[100]. White dots represent monomer units, linked black dots represent the oligomer units, showing the step-by-step polymerisation process when monomer and oligomeric units combine in step polymerisation.

Step polymerisation occurs when the reactive monomer units primarily create dimer units, then form longer oligomeric units until they become long chain polymers (Fig. 13). This cascading polymer synthetic route often provides high molecular weight polymer chains, and most naturally occurring polymers are created this way (through natural condensation reactions, in which H_2O is removed from the system).

The use of step polymerisation has created many widely used polymers, such as Nylon 6 (synthesised *via* a ring opening polymerisation reaction of caprolactam)[101]; Kevlar[102,103] and polyethylene terephthalate (PET)[104]. Protein synthesis in nature is also carried out using this method, through the formation of peptide bonds between amino acids.

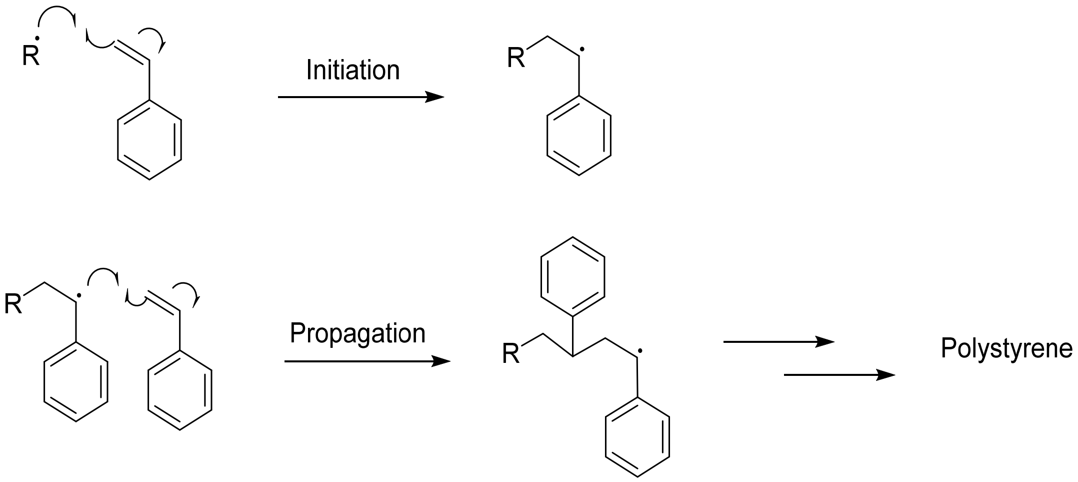

Figure 14: Schematic showing the radical initiation and subsequent propogation of polystyrene monomer units into a polystyrene polymer. The initiator (R^*) splits the double bond into a radical state (initiation), causing a rapid progression and reactions with neighbouring double bonds (propogation).

Chain polymerisation (or more commonly known as ‘living’ polymerisation) occurs by a very different mechanism. It involves a three-step process where unsaturated monomer units primarily undergo an ‘initiation’ step, when an initiator reacts with the monomer and starts the polymerisation reaction. These monomer units then ‘propagate’ to create the long-chained oligomer (Fig. 14), which is finally ‘terminated’ when either two living oligomer chains combine or when two radicals combine under intermolecular circumstances and disproportionate (Fig. 15).

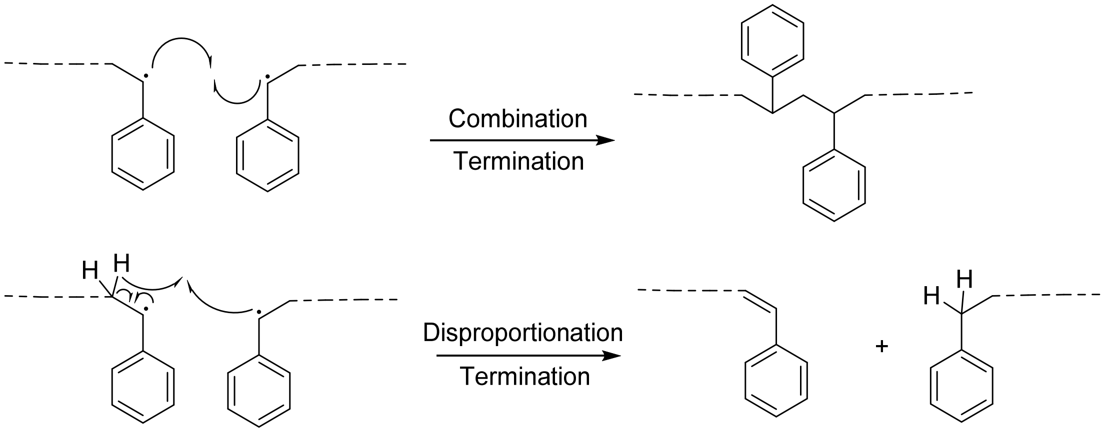

Figure 15: Two termination mechanisms showing (top) the combination method of terminating the radical polymerisation and (bottom) the disproportionation mechanism. Both are suitable in terminating the living polymerisation reactions, leading to a polystyrene polymer chain.

Living polymerisation can occur in many different ways: (i) radical polymerisation uses a radical species as the initiator, with the propagating site of reactivity being a carbon radical; (ii) cationic polymerisation uses an acid as the initiator, creating a carbocation propagating site; (iii) anionic polymerisation uses a nucleophile/Lewis base ($NaNH_2$, Bu-Li etc.) as the initiator, with a carbanion as the propagating site; and (iv) Ziegler-Natta polymerisation uses titanium chloride ($TiCl_4$) as the initiator, with polymerisation involving the empty orbital of the titanium complex[95]. These processes allow the formation of many differing polymer species, highlighting the flexibility of the living polymerisation process.

Much of the early academic and industrial research on polymerisation focused on living anionic and cationic polymerisations[105–107]. However, the drawback to these ionic techniques is the high levels of sensitivity to moisture, CO_2 and many other basic/acidic compounds. Alongside this, ionic polymerisation reactions are restricted to a limited number of monomers and as such the polymer properties were limited. Therefore, the role of radical-based living polymerisation has become increasingly important because of: (i) its ability to polymerise almost every monomer with a C=C bond; (ii) its tolerance towards side-chains and functional groups (no side-reactions occurring); (iii) and it being able to provide access to creating many differing polymer blends, allowing for a greater interest to both academic and industrial research[108–110].

1.4.3 Processing polymer materials

Once the polymer has been synthesised, it can be further manipulated into a material that can be used in many different applications. Many synthetic and naturally-occurring polymers can be moulded into required shapes and are useful as plastics for the manufacture of a wide range of articles. Techniques such as spin coating, electrospinning and injection moulding can transform a synthesised polymer into a variety of forms.

Injection moulding is one of the most commonly used processes for producing plastics and polymeric materials. It is a fast process and is used to process large numbers of items from commonly used materials such as nylon and polystyrene.

This process involves the injection, under pressure and at a high temperature, of a polymer solution into a mould[111]. The use of pressure reduces the formation of defects and air pockets, whilst the application of a high temperature ensures that the polymer solution retains its fluidity. Once the molten polymer solution has been fully injected into the mould, it is allowed to cool forming the required polymer shape. This is a very applicable way of manufacturing large quantities of polymer samples and plastics, providing smooth, reproducible polymer samples in a variety of sizes and shapes[112].

Another widely used process to produce a thin uniform film is spin coating. This uses centrifugal and vacuum forces to create a thin polymer coating on any surface, and is employed for the manufacture of coatings on colour television screens, optical devices and products in the microelectronics industry[113]. The pre-synthesised polymer is dissolved in a known amount of solvent (for example chloroform or methanol) and applied on to the desired surface. This surface is kept in place using vacuum pressure and spun at high speeds, causing the solvent in the polymer solution to evaporate leaving behind a thin film of polymer which, as a result of the centrifugal forces applied in the spin coating process is uniform.

Alternatively, in order to produce a polymer mat which has a fibrous property instead of a smooth film, the synthetic method known as electrospinning can be used. This process of utilising electrostatic forces to form synthetic fibres was first proposed over 100 years ago[114] and uses a high voltage source applied to a polymer solution. At the start of the electrospinning process, the polymer solution is loaded into a syringe with a needle attached, a high voltage is then applied to the needle and the polymer solution is pushed through at a constant flow rate. The application of a high voltage causes the polymer solution to ‘spin’ into fibres (Fig. 16), which then accelerate towards a collector of opposite polarity. These fibres then accumulate to form the required polymer mat.

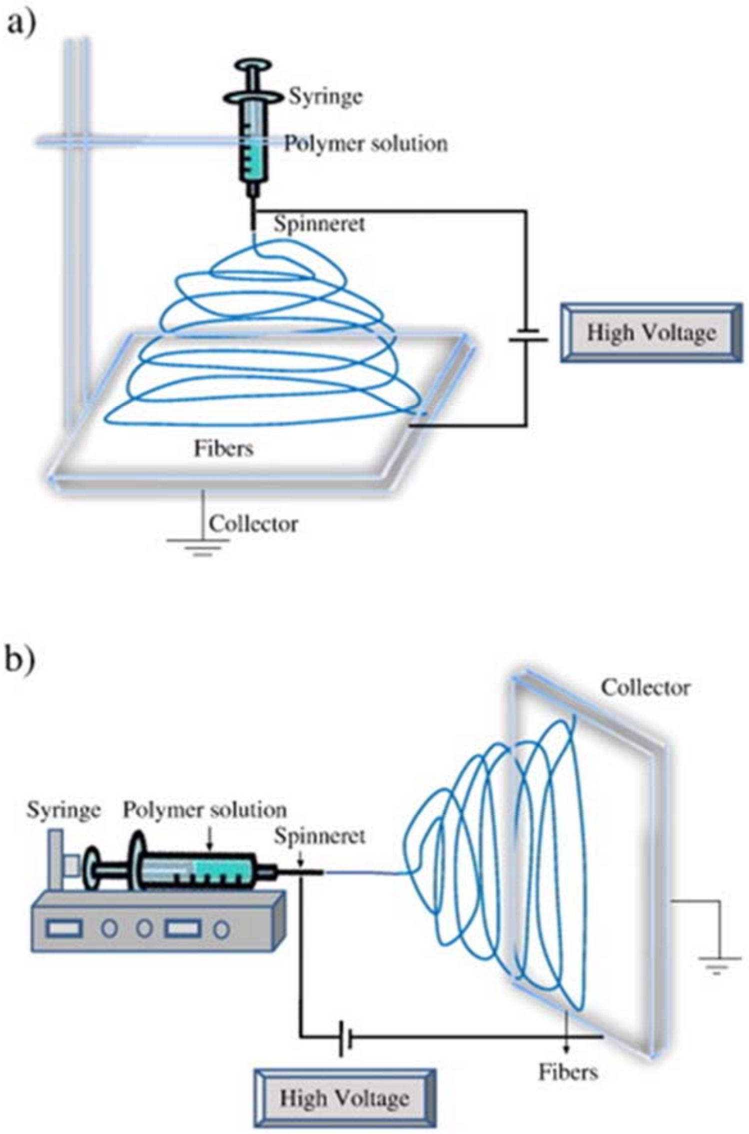

Figure 16: A typical electrospinning set-up, showing a) the vertical and b) the horizontal orientation of the electrospinning apparatus. A syringe & needle is filled with a polymer solution of known concentration, and clamped in place. A high voltage is applied across the needle, generating electrostatic repulsion and leading to the production of polymer fibre ‘spinnerets’. These fibre spinnerets are then collected on a metal plate (collector), which has the opposite polarity, generating a polymer fibre mat. Image taken from Bhardwaj *et al*[115].

Electrostatic repulsion between the charged solution and electrostatic attraction from the collector leads to the formation of a cone-like solution on the tip of the syringe needle, known as the 'Taylor cone' effect (Fig. 17)[116]. The meniscus of the solution elongates and stretches because of charge-charge repulsion to form a conical shape, and when the electric field within the solution and the collector is strong enough a fine fibre jet is ejected. This effect is responsible for the direction and production of the fibres, and modification of this directly affects the formation of the fibres.

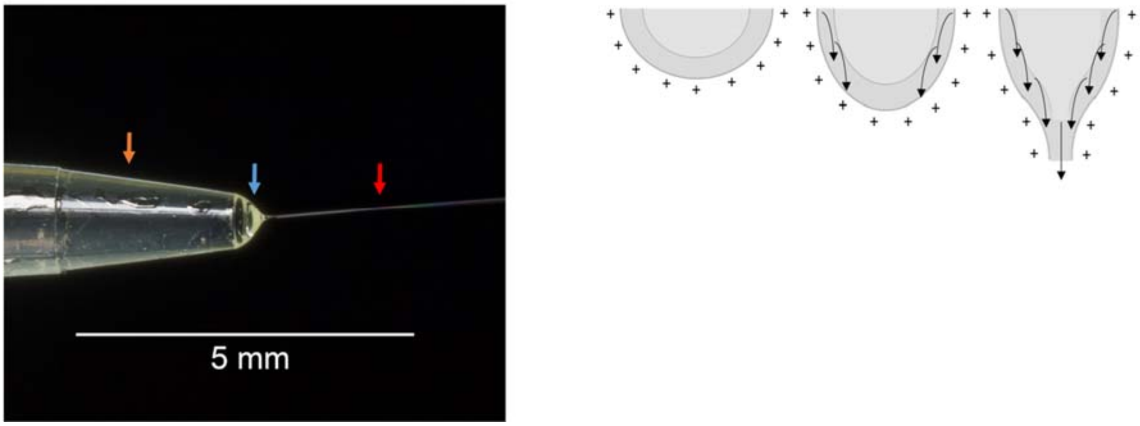

Figure 17: Images highlighting the Taylor cone effect of electrospinning, showing (left) the polymer solution jet, with the syringe (yellow arrow); the Taylor cone (blue arrow); the polymer jet (red arrow) and (right) the effect of electrostatic repulsion on the generation of the Taylor cone meniscus. As the electrostatic charge of the polymer solution increases, the repulsion (black arrows) causes a 'puckering' effect, leading to the Taylor cone. Photograph image of the Taylor cone courtesy of The New Zealand Institute for Plant and Food Research Ltd.

This process is an efficacious way of synthesising porous fibre mats by layering fibres on top of each other in an entirely random manner and has been used to create materials such as vascular graft scaffolds[117], nanowires[118] and dermal substitute scaffolds[119–121].

This method of synthesising polymeric mats is also very versatile, as it can be modified by fine tuning: (i) the voltage applied to the needle; (ii) the distance from the collector to the needle; and (iii) the flow rate of the polymer solution passing through the syringe and needle.

The choice of the collecting surface also provides added versatility; the production of aligned or random networks of fibres can be controlled by using differing oppositely charged surfaces[122]. Often, a flat metal sheet is used as the collector for the electrospun material, resulting in fibres that are random in orientation.[123–127]. However there are alternative collecting parameters that allow for differing arrangement of fibres. It has been shown that by removing a central square from the metal collection plate leaving behind a 'framed' metal collector, aligned fibres can be produced[128]. Through the use of a 'framed' metal collector, researchers have shown that the formation of aligned fibres can be achieved, increasing the potential applications of this process and thereby increasing the versatility of the technique. Use of a rotating cylinder or 'spinning manderal' can yield either an aligned or random arrangement of fibres within a polymer matrix, depending upon the speed at which the cylinder rotates[129]. If the spinning manderal is greater or equal in rotating speed to the rate of deposition of the material the fibres are aligned, whereas if the rotating speed of the cylinder is less than the deposition of material the fibres are randomly orientated. Use of a rotating cylinder also ensures that the fibres are more evenly spread across the collected surface; a flat metal sheet usually results in a mixed thickness distribution across the collected electrospun matrix. Use of a spinning manderal distributes the material more evenly, whilst also allowing for a more efficient solvent extraction from the produced electrospun matrix[122,128,129].

This, alongside the listed modifiable parameters, allows for the synthesis of polymer mats with very different properties, even if the co-polymer blend is exactly the same[130].

1.5 Biocompatible polymers for medical applications

The inherent flexibility of polymers and polymeric structures and their potential uses has led to many researchers investigating the use of polymers in many varying applications within medicine. Polymer substrates have been used as potential grafts and synthetic substrates in investigations into bone[131], dermal[120] and liver tissue engineering[132].

Work carried out by Chen *et al* utilised the polymer poly(glycerol sebacate) to generate a flexible patch for the heart[133]. By using culture moulds, the polymer was formed into a malleable patch which acted as a carrier for human embryonic stem cells and as a structural support throughout the implantation procedure. Hydrogels generated from poly(2-hydroxyethyl methacrylate)[134] and elastin[119] have been utilised in the generation of artificial skin and dermal tissue regeneration respectively.

Electrospinning has also been repeatedly used in generating biocompatible scaffolds, due to the flexibility in the polymer matrix process to produce many differing fibres on the micro or nano scale, with the aim of mimicking the native membranes. Researchers have developed electrospun poly(caprolactone)-co-gelatin scaffolds to culture nerve cells[135], with the nerve stem cells aligning parallel to the fibres within the scaffold and subsequently proliferating across the fibrous matrix.

Electrospun polydioxanone-co-elastin[136] and polycaprolactone-co-elastin[137] have been investigated as synthetic vascular grafts with controlled mechanical properties. Cellulose acetate, electrospun into a fibrous matrix, has been shown by researchers that it has the potential to act as a urinary bladder matrix implant[138]. By using electrospinning, the cellulose acetate matrix accurately mimicked the native extracellular matrix, due to the formation of a multi-layered fibrous matrix. Gu *et al* were able to replicate the nanofibrous bundles associated with skeletal muscles by producing aligned fibres of polyurethane-co-polyaniline[139]. Electrospinning allowed the synthesis of aligned polyurethane-co-polyaniline 900nm diameter fibres into artificial bundles which, due to the polymer arrangement, could respond to electrical stimuli. Poly(L-lactic) acid (PLLA) has also been used in nerve tissue engineering[140]. Porous electrospun PLLA fibres were synthesised, with the fibrous property produced by electrospinning essential in allowing the nerve stem cells to differentiate on the scaffold.

These synthesised matrices highlight the capability of electrospun scaffolds for use in medical and cell culture applications.

The application of polymeric structures for ocular-based therapies was first suggested by Sir Harold Ridley, a British ophthalmologist. After World War 2, he noticed that some Spitfire pilots returned from aerial combat with sustained injuries involving shards of plastic becoming embedded into their eyes. Not only had the plastic been incorporated, but there had been no adverse/inflammatory effect observed. The plastic was poly(methyl methacrylate) (PMMA), which formed the composition of the first intraocular lens[141]. Since this initial observation, the use of polymers like PMMA has developed significantly, with current research investigating the use of artificial corneas[142,143] and cell-delivery systems[144,145] as potential ocular-based treatments.

Corneal blindness is a major eye problem, with approximately 10 million people worldwide without vision due to this disease[146]. Current treatment of corneal blindness involves a corneal transplant (keratoplasty), however this is often costly, has a risk of infection and potential rejection of the new cornea. Therefore, to overcome these problems researchers have developed biocompatible artificial corneas. Bakhshandeh *et al* have designed a 2-part artificial cornea, consisting of a poly(ε-caprolactone) ring surrounding a polyvinyl alcohol hydrogel[146]. By using a two-part system it was reported that the artificial cornea demonstrated a central cornea with a >85% light transmittance, whilst also allowing good tissue integration through the electrospun fibrous poly(ε-caprolactone) surround. Myung *et al* have also generated a polymer as a replacement cornea, using a co-polymer blend of poly(ethylene glycol)-co-poly(acrylic acid) (PEG:PAA)[147]. This co-polymer solution was synthesised into a hydrogel, which displayed high-strength and good cell attachment, allowing for good tissue integration.

In the case of age-related macular degeneration (AMD), early research was focused on a therapeutic delivery of RPE cells to revive the diseased macula. Binder *et al* stated that an injection of RPE cells showed potential as a treatment for dry AMD, with the aim of rejuvenating the diseased macula and BrM[82,83]. However, the injection of RPE cells into the sub-retinal space led to a lack of organisation of the injected RPE cells, resulting in the stacking of RPE cells, retinal fibrosis, proliferative vitreoretinopathy and rejection from aged BrM[84,85,39]. Investigations into implanting a complete sheet of RPE led to improvements in the organisation of the RPE, however the procedure required a more invasive surgical approach for the delicate RPE sheet[86]. Therefore, it was suggested that a prosthetic BrM could transport a polarised monolayer of RPE cells into the sub-retinal space, allowing for a targeted approach in the treatment of dry AMD and facilitate the implantation of the fragile monolayer[148].

In the search for a suitable prosthetic BrM, efforts have been made by many research groups towards developing the optimal material that can facilitate the delivery of RPE cells into the sub-retinal space. An ideal prosthetic BrM should ensure: (i) the adhesion of a monolayer of RPE, whilst maintaining the phenotype and function of the cell (Fig. 18); (ii) good surgical handling; (iii) the transport of macromolecules from the choriocapillaris to the epithelium and *vice versa*; and (iv) provide no inflammatory or corrosive response in the sub-retinal space.

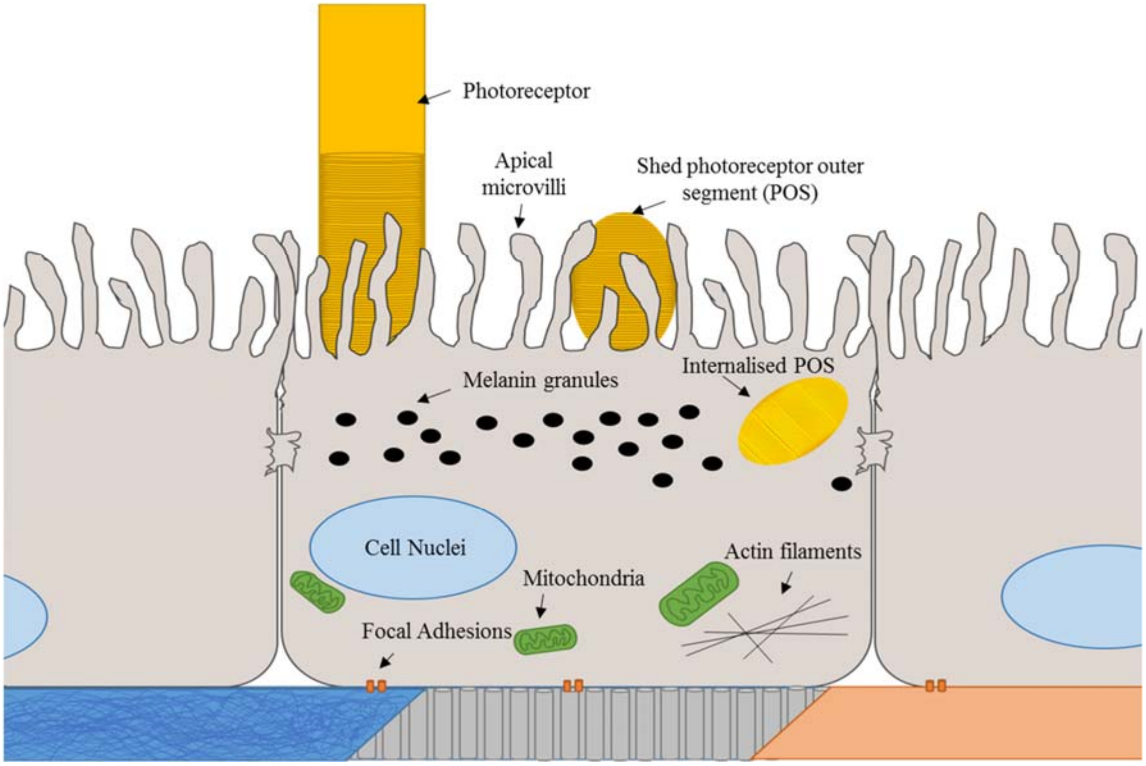

Figure 18: The ideal Bruch's membrane mimetic, showing a stable RPE monolayer on the surface of the synthetic membrane. Latest research has shown the use of three differing membranes: (i) an electrospun membrane (dark blue), which is porous and shows a fibrous morphology; (ii) a designed smooth, clean film with artificial pores (grey); and (iii) a smooth polymer film (light orange).

It has been argued that the use of a biodegradable membrane would provide the necessary properties to deliver a polarised monolayer of RPE cells to the affected site, with the aim of allowing the RPE monolayer to secrete and form a basement membrane before substrate degradation[149]. Whilst the advantages of this approach include the removal of a foreign body (the biodegradable polymer) and any long-term inflammatory consequences, issues may arise from potential unwanted side-products of the degraded substrate and whether the membrane will maintain enough integrity to allow the implanted monolayer of RPE to establish the required basement membrane.

To counter these issues, many groups have looked at designing membranes that are naturally biodegradable (collagen, gelatin, elastin, silk)[150–154]. Thumann *et al* report that an ultrathin equine collagen type I membrane shows promise as a temporary support for RPE[150]. This membrane had shown no inflammatory response, had only partial 'loosening' after 16 weeks *in vivo* and, through the use of a cell line of the RPE, showed good biocompatibility. However, the handling of the membrane was not effective, as the RPE cell line had loosened after movement from cell culture, an unwanted property of an artificial BrM. Warnke *et al* have also recently developed a collagen-based membrane, using bovine collagen type I[151]. After synthesising a designed nano-fibrous BrM mimic *via* electrospinning, the biocompatibility was quantified through the seeding of primary human RPE cells, which demonstrated good cell adhesion, RPE-specific markers and tight junction formation. One feature in particular is the production of apical microvilli - a clear sign of a well-established RPE monolayer. However, the membrane was not tested *in vivo* and future work is required to see how the membrane behaves under these conditions. Shadforth *et al* have shown that a *Bombyx mori* silk fibronin matrix can be synthesised with the following features[152]: ultrathin (≈3μm), porous and good biocompatibility (using a spontaneously arising human RPE cell line assay – ARPE-19 cells[155]). What is also interesting to note is that when the membranes are film-casted, the very nature of the material used allows a fibrous morphology. This is especially attractive as the incorporation of a fibrous nature to any prosthetic BrM will improve the overall cell adhesion & *in vivo*-like behaviour of the RPE, whilst also mimicking the nature of BrM[156–158]. However, as with Thumann *et al*, the use of a spontaneously arising human RPE cell line is not a clear indication of how native RPE cell lines will function as the ARPE-19 cell line does not display complete morphological features found in healthy RPE *in vivo*. The spontaneously immortalised RPE cells are unable to produce uniformly abundant apical microvilli[155,159] and display differences in ion transport mechanisms in diffusional studies[160–163].

Synthetic biodegradable substrates have been investigated as an alternative means to natural sources. Xiang *et al*[154] have used polycaprolactone in their recent publication as a potential synthetic biodegradable membrane, but have also infused it with regenerated wild *Antheraea pernyi* silk fibronin and gelatin (to help improve the hydrophilicity of the proposed matrix[164]). By testing varying ratios of this blend, they have shown good biocompatibility (through the use of the spontaneously arising ARPE-19 cell line, as used by Shadforth *et al*[152]) and the membrane has been successfully implanted into a rabbit eye, showing only a slight detatchment from the original implantation site after 1 month. However, as indicated previously, the use of an ARPE-19 cell line does not provide a complete understanding of the RPE monolayer, and therefore would require the use of a primary RPE cell line to fully quantify the RPE monolayer behaviour on the prosthetic BrM.

Investigations into a permanent prosthetic BrM have also been carried out, with the aim of providing long-term support to the RPE monolayer. This will remove the formation of unwanted side-products, protect the implanted RPE layer from the permanently damaged BrM and also allow the immediate incorporation of a functional RPE-BrM complex at the site of retinal damage. It is generally agreed that the ideal material for a permanent support should be an accurate mimic of native BrM; incorporating the natural properties of the existing membrane - porosity, elasticity, thin fibrous matrix - whilst maintaining a polarised monolayer of RPE on the surface.

Haneef *et al* have shown that an electrospun matrix of poly(ethylene terephthalate) displays good handling with seeded ARPE-19 cells which demonstrate desirable morphology[165]. Krishna *et al* also demonstrated good ARPE-19 cell proliferation and a settled layer of RPE cells (displaying characteristic features such as cell-cell junction formation and POS internalisation), through the use of a poly(tetrafluoroethylene) sheet plasma-treated with ammonia gas[166]. Whilst showing good biocompatibility, it is not ideal to use a harmful compound like ammonia in a sample designed for implantation into the sub-retinal space within the eye. Alongside this, further work is required to understand RPE behaviour on the surface of the polymer membranes, as any *in vivo* experiments require suitable primary or foetal RPE cell attachment to fully characterise the behaviour of the RPE monolayer on the surface of the prosthetic BrM. Research by Liu *et al* investigated the use of poly(ethylene terephthalate) combined with poly(L-lactide-co-ε-caprolactone) and electrospun into a fibrous matrix to allow good RPE cell attachment[167]. Foetal human RPE cells were seeded onto these membranes and demonstrated good attachment and differentiation. McHugh *et al* also used foetal human RPE cells, using a nano-porous poly(ε-caprolactone) membrane as a support for the epithelial layer[168]. Both research groups were able to display RPE proliferation on the surface of the membranes, however no attachment profiles were investigated and analysis of the diffusional properties of the designed membranes were also not carried out. *In vivo* studies carried out on the membrane proposed by Liu *et al* showed no inflammatory responses, however implanting the artificial BrM required an additional carrier, indicating a fragile and hard-to-handle membrane, whilst the nano-porous poly(ε-caprolactone) had not been tested *in vivo*[167].

1.6 Previous work designing a suitable BrM mimetic

In previous work undertaken within the Lotery and Grossel research groups, the design of a permanent prosthetic BrM was initiated looking at replicating the fibrous interwoven matrix of the inner and outer collagenous layers with a co-polymer blend of 60:40 Methyl methacrylate (MMA): poly(ethylene glycol) methacrylate (PEGM), functionalised with a di-succinimidyl carbonate (DSC) group (Fig. 19) being generated.

Methacrylate-based monomers were chosen for their biocompatibility with ocular tissues[169,170], with MMA chosen for its improved strength and PEGM chosen to improve the hydrophilicity of the co-polymer system (ensuring a degree of interaction with the highly hydrated environment within the eye)[127].

This co-polymer blend, combined with the DSC functional group, was found to contain the necessary cell adhesive and porosity properties for a biocompatible membrane[127].

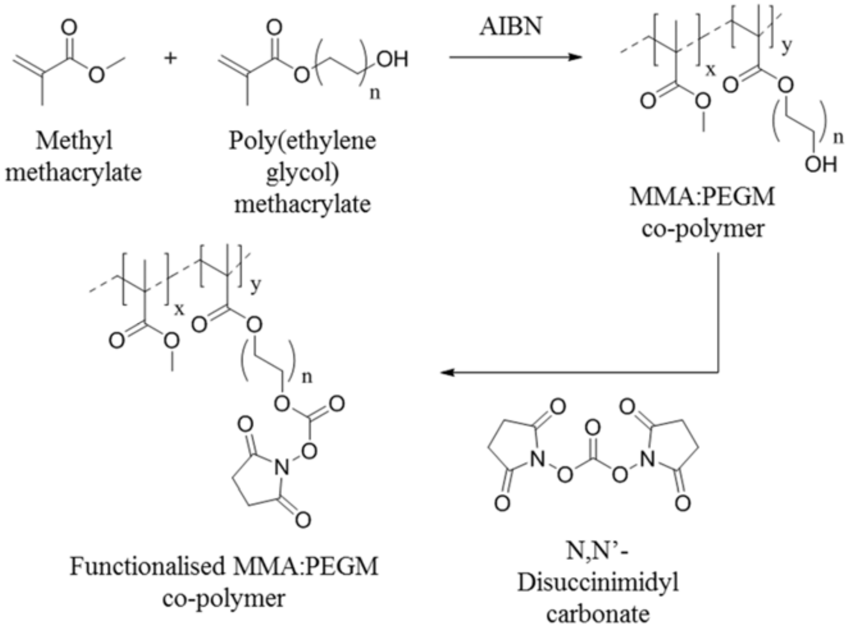

Figure 19: Reaction scheme showing the multi-step synthetic process of the functionalised MMA:PEGM co-polymer. Methyl methacrylate and poly(ethylene glycol) methacrylate undergo a radical polymerisation, using AIBN as the initiator, to form a MMA:PEGM co-polymer. This co-polymer is further functionalised with N,N'-Disuccinimidyl carbonate to form the functionalised MMA:PEGM co-polymer.

This designed co-polymer was electrospun to form a polymer mat, on which a spontaneously arising human RPE cell line (ARPE-19 cells) was grown *in vitro* for 15 days.

The process of electrospinning, as discussed in section 1.4.3, is an effective way of producing fibrous mats. It was theorised that the artificial BrM should mimic the topology of native BrM and therefore the surface presented to the RPE monolayer. The morphology of the substrate has been shown to influence cell-substrate interactions[171,172], and with the ICL of native BrM being fibrous, the artificial BrM should mimic this topology to ensure the RPE monolayer is presented with a similar morphology to that of native BrM, with researchers using electrospinning to produce such matrices[127,151,154,165] alongside the literature supporting cell growth in multiple medical applications (see section 1.5)[135,140]. This would theoretically provide a suitable surface for the RPE monolayer to be seeded onto, allowing the RPE cells to: (i) attach to the substrate; (ii) establish a polarised monolayer; and (iii) reproduce *in vivo* functionality, such as POS internalisation and VEGF production.

The designed MMA:PEGM co-polymer blend was an excellent stepping-stone in the development of a biocompatible membrane, as it provided a polymer membrane that was porous and biocompatible, with the necessary cell adhesive properties. However, this co-polymer membrane was found to be somewhat difficult to handle, as it crumbled upon touch. This was a major obstacle as it needed to be loaded into a polymer injector without distorting its shape or disturbing the RPE monolayer grown on its surface. In addition, the thickness of this early membrane could not be quantified with sufficient accuracy and the functionality of the RPE cell layer had not been quantified to observe if the layer was behaving in an *in vivo* manner.

1.7 Aims and Objectives of Research

As discussed in Section 1.6, a biocompatible permanent prosthetic BrM design was explored, with a co-polymer blend of 60:40 MMA:PEGM functionalised with a DSC group stated as being an excellent co-polymer arrangement for cell attachment. However, this co-polymer membrane was hard to handle and its thickness was not quantified. Accordingly, the understanding of the RPE cell attachment and functionality was not fully tested using a cell line which accurately represented the RPE monolayer *in vivo*.

Consequently, further work was required to understand the thickness of the co-polymer membrane and draw a realistic comparison to native BrM. In determining the thickness of the membrane, the co-polymer could then be manipulated to align it more closely to human BrM and thus produce a more feasible implantation system. For instance, an improvement in the mechanical strength of the BrM mimetic was needed to ensure the handling of the co-polymer membrane was improved, alongside a greater understanding of how the RPE monolayer behaves on this scaffold to establish that the artificial BrM can function as a suitable carrier.

Chapter 2: Materials and Methods

2.1 Polymer synthesis

2.1.1 General experimental details

All solvents used for these experiments were purchased from Fisher Scientific, Loughborough, UK with the exception of 2-butanone, which was bought from Sigma Aldrich, Dorset, UK. All starting materials and reagents were obtained from Sigma Aldrich, Dorset, UK.

All NMR spectra were collected from a Bruker AVII400 FT-NMR Spectrometer (operating at 400MHz for ^{1}H and 100MHz or 75MHz for ^{13}C NMR spectra). Samples in liquid phase using deuterated chloroform ($CDCl_3$) as solvent.

All IR spectra were collected using a Thermo Scientific Nicolet 380 FT-IR (Fisher Scientific, Loughborough, UK).

All mass spectrometry data was collected from ESI+ Blue RP UHPLC-MS (Fisher Scientific, Loughborough, UK).

All X-ray crystallography data was collected from a Rigaku FR-E+ Single Crystal X-Ray Diffractometer (Rigaku Europe, Sevenoaks, UK).

All collected spectra are located in the Appendices – Appendix B.

2.1.2 Preparation of a 60:40 (w:w) P(MMA:PEGM) co-polymer

Reaction Scheme

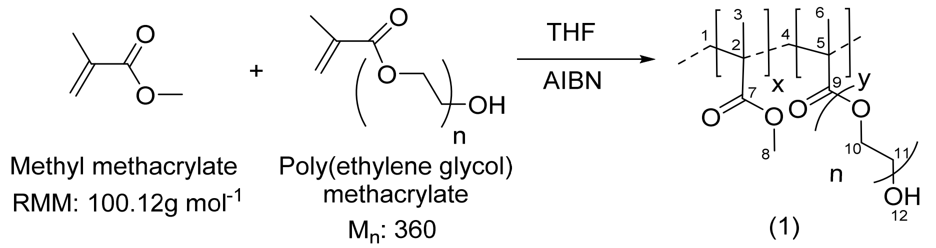

Reaction Procedure

In a round-bottom flask (RBF, 250ml), tetrahydrofuran (THF, 150ml) was added. Methyl methacrylate (MMA, 6.72 x10^{-2} mol, 6.72g, 7.18ml), poly(ethylene glycol) methacrylate (PEGM, ≈ 0.0125mol, 4.51g, 4.08ml) and azobisiso-butyronitrile (AIBN, 0.58mmol, 0.096g) were combined and the solution was degassed for 20 mins through bubbling N_2 (using a N_2 line). Solution was then refluxed for 20h under N_2 whilst stirred at 90°C. Once reflux had run for 20h, the colourless solution was cooled to room temperature and transferred to a stirring mixture of diethyl ether (200ml) in a conical flask (500ml). This produced a white powder-like solid. Subsequent solid was then collected *via* Büchner filtration, redissolved in THF (100ml) and transferred to a conical flask containing stirring diethyl ether (200ml), producing a white powder-like solid. Sample again collected *via* Büchner filtration and dissolved in dichloromethane (DCM). The desired co-polymer was then extracted from the solvent *via* rotary evaporation and dried *in vacuo* for 2h to give a yield of 7.206g (81%).

^{1}H NMR (400MHz, $CDCl_3$): δ_H 0.87 (3H, br s, H6); 1.04 (3H, br s, H3); 1.83 and 1.87 (4H, br s, H1 & H4); 3.61 (2H, m, H11); 3.67 (3H, s, H8); 4.13 (1H, s, H12).
^{13}C NMR (75MHz, $CDCl_3$): δ_C 16.58 (C6); 18.76 (C3); 44.56 (C2); 51.77 (C8); 54.10 (C1); 68.40 & 69.80 (C10 & C11); 177.20 (C9); 177.81 (C7).
FT-IR ν max (cm^{-1}): 2947 (CH), 1723 (CO).
MS: Intervals of 44 g mol^{-1} indicate the presence of a PEG chain (repeating unit of ethylene oxide)[173].

Concurrent in comparison to the literature[127].

2.1.3 Preparation of a NHS carbonate of 60:40 P(MMA:PEGM) co-polymer

Reaction Scheme

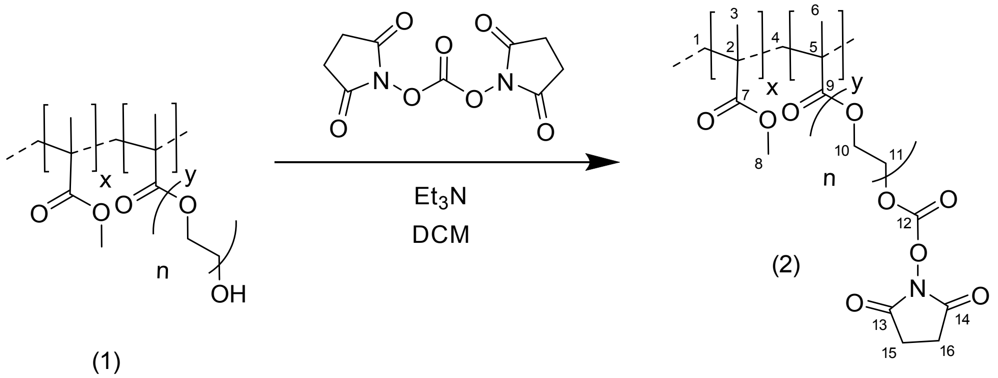

(1)

(2)

Reaction Procedure

60:40 (MMA:PEGM) co-polymer (1) (5.50g) was added to dichloromethane (DCM, 100ml) in a RBF and stirred. Disuccinimidyl carbonate (DSC, 2.31g, 8.8mmol) was added to the stirring solution alongside triethylamine (TEA, 2ml). Solution was then stirred for 18h at room temperature. The reaction mixture was then slowly added to diethyl ether (200ml) and stirred, yielding a white precipitate. Precipitate was then redissolved in DCM (100ml) and precipitated in stirring diethyl ether (200ml). The white solid was then collected *via* Büchner filtration and redissolved in chloroform ($CHCl_3$, 50ml), washed with distilled H_2O and dried over $MgSO_4$. Chloroform was then removed *via* rotary evaporation and the collected solid was then dried *in vacuo* to give a yield of 4.17g (65%).

^{1}H NMR (400MHz, $CDCl_3$): δ_H 0.86 (3H, br s, H6); 1.03 (2H, br s, H3); 1.60 (2H, s, H1); 1.82 (2H, br s, H4); 2.86 (4H, s, H15 & H16); 3.61 (3H, s, H8); 3.66 (2H, m, H11 in PEG chain); 4.11 (2H, s, H10); 4.46 (2H, s, H11, proton adjacent to carbonate group).
^{13}C NMR (75MHz, $CDCl_3$): δ_C 16.39 (C6); 18.72 (C3); 25.44 (C15 & 16); 44.58 (C5 & C2); 51.77 (C8); 54.32 (C1); 68.30 and 70.52 (C10 & C11); 177.76 (C7 & C9).
FT-IR ν max (cm^{-1}): 2947 (CH), 1790 (CO-N cyclic imide), 1723 (CO).
X-ray crystallography of side products formed:

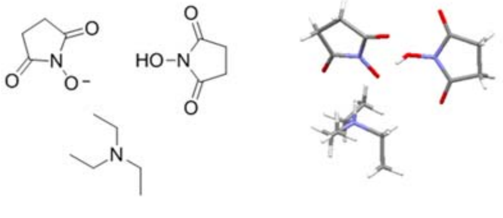

2.1.4 Preparation of a 58:40:2 (w:w) P(MMA:PEGM:FMA) co-polymer

Reaction Scheme

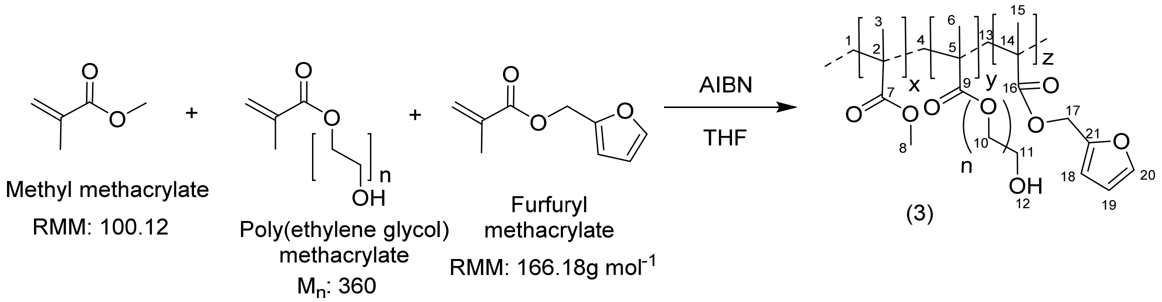

Reaction Procedure

In a RBF (250ml) a solution of THF (150ml) was added. Methyl methacrylate (MMA; 6.49 x10^{-2} mol; 6.496g; 9.911ml), poly(ethylene glycol) methacrylate (PEGM; (PEGM, ≈ 0.0125mol, 4.51g, 4.08ml), furfuryl methacrylate (FMA; 1.35mmol; 0.224g; 0.208ml) and azobisiso-butyronitrile (AIBN, 0.58mmol, 0.096g) were combined and the solution was degassed for 20 mins through bubbling N_2. Solution was then refluxed for 20h under N_2 conditions whilst being stirred at 76^{o}C. After the reflux had completed, the reaction vessel was allowed to cool to room temperature and the reaction mixture was transferred to diethyl ether (200ml, slowly) in a conical flask (500ml), resulting in the formation of a white precipitate. White precipitate was then collected & re-dissolved in THF (100ml). The reaction mixture was then again slowly transferred to diethyl ether (200ml) in a conical flask (500ml), resulting in the formation of a white precipitate. White precipitate was then collected and dried *in vacuo*, resulting in a yield of 4.74g (48%).

^{1}H NMR (400MHz, $CDCl_3$): δ_H 0.84 (3H, br s, H6); 1.01 (3H, br s, H3); 1.84 (4H, br s, H1 & H4); 1.89 (2H, m, H18 & H 19); 3.59 (2H, s, H11); 3.65 (1H, s, H8); 3.73 (2H, s, H10); 3.75 (1H, s, H20); 4.10 (1H, s, H12).
^{13}C NMR (100MHz, $CDCl_3$): δ_C 16.58 (C15); 18.68 (C3); 25.60 (C6); 44.57 (C2); 44.91 (C5); 51.79 (C8); 61.71 (C21); 67.96 & 70.56 (C10 & C11); 72.60 (C17); 177.78 (C7, C9, C16).
FT-IR ν max (cm^{-1}): 2938 (CH), 1714 (CO).

2.1.5 Functionalisation of the 58:40:2 (w:w) P(MMA:PEGM:FMA) co-polymer with DSC carbonate

Reaction Scheme

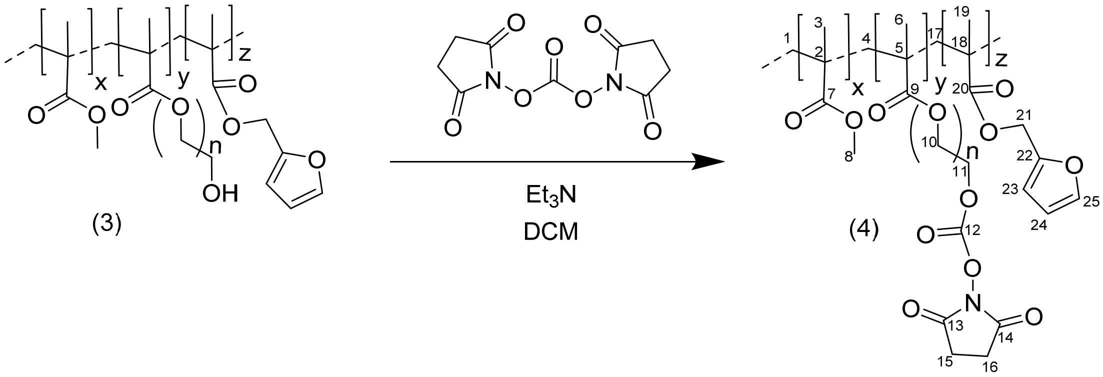

Reaction Procedure

58:40:2 (MMA:PEGM:AMM) co-polymer (3) (4.70g) was added to dichloromethane (DCM, 100ml) in a RBF and stirred. Disuccinimidyl carbonate (DSC, 1.91g, 7.5mmol) was added, alongside triethylamine (TEA, 2ml). The solution was stirred overnight at room temperature. The reaction mixture was then slowly added to diethyl ether (200ml) and stirred, resulting in a pale yellow-white precipitate. Precipitate was then redissolved in DCM (100ml) and re-precipitated by transferring to a solution of stirring diethyl ether (200ml). The collected pale yellow-white solid was then dissolved in $CHCl_3$ (50ml), washed with distilled H_2O and dried over $MgSO_4$. The solvent was removed *via* rotary evaporation and the produced solid was dried *in vacuo*, giving a yield of 2.91g (64%).

^{1}H NMR (400MHz, $CDCl_3$): δ_H 0.83 (3H, br s, H6); 1.00 (3H, br s, H3); 1.80 (s, H4 & H13); 1.84 (2H, m, H23 & H24); 2.83 (4H, m, H15 & H16); 3.58 (2H, m, H11 in the PEG chain); 3.65 (3H, s, H8); 3.79 (1H, m, H25); 4.09 (2H, m, H10); 4.45 (2H, m, H11 adjacent to the carbonyl group).

^{13}C NMR (100MHz, $CDCl_3$): δ_C 15.98 (C19); 16.48 (C3); 25.47 (C6); 44.58 (C2 & C21); 44.92 (C5); 51.78 (C8); 68.34 (C10); 70.56 (C11); 151.65 (C12); 168.61 (C13 & C14); 177.78 (C7, C9, C20).

FT-IR ν max (cm^{-1}): 2940 (CH), 1750 (CO-N cyclic imide), 1715 (CO).

2.1.6 Preparation of 9-anthrylmethyl methacrylate

Reaction Scheme

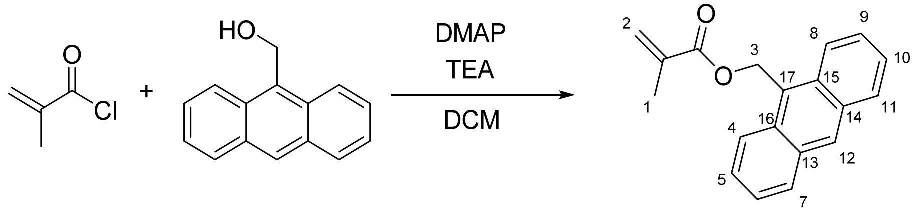

Methacryloyl chloride

RMM: 104.53 g mol^{-1}

9-hydroxymethyl-anthracene

RMM: 208.26 g mol^{-1}

(5)

RMM: 276.34 g mol^{-1}

Reaction Procedure

A 3-necked RBF (100ml) was used for this reaction, with a stopper in one side, N_2 bubbler in another and a dropping funnel in the third. 9-hydroxymethylanthracene (0.500g, 2.4mmol), 4-(*N,N'*-dimethyl amino)pyridine (DMAP, 0.0293g, 0.24mmol) and TEA (0.689ml, 4.8mmol) were combined in DCM (60ml) in the RBF. Methacryloyl chloride (0.465ml, 4.8mmol) was added to the dropping funnel alongside DCM (5ml). Methacryloyl chloride was added drop-wise at 0°C for 30mins. After the initial addition of methacryloyl chloride, solution turned from a light yellow colour to an intense yellow to colourless, then back to a pale yellow. Once all of the methacryloyl chloride had been added the reaction mixture was stirred at 0°C for 4h. After the reaction had finished, the solvent was evaporated *via* rotary evaporation at 30°C to yield a pale yellow solid. The collected solid was re-dissolved in minimum amount of $CHCl_3$ (6ml) and the desired product was isolated *via* silica gel column chromatography, using $CHCl_3$ as a solvent. The product was identified using thin-layer chromatography (TLC) throughout. The desired product was isolated and subsequently collected *via* Büchner filtration, yielding a pale yellow oil. Oil was dried in a vacuum desiccator overnight, yielding a yellow solid. Solid was then transferred to a sample vial, giving a yield of 0.602g (91%).

^{1}H NMR (400MHz, $CDCl_3$): δ_H 1.93 (s, 3H, H1); 5.52 (s, 1H, H3); 6.07 (s, 1H, H3); 6.24 (s, 2H, H2); 7.52 (t, 2H, H10 & H6); 7.60 (t, 2H, H5 & H9); 8.05 (d, 2H, H7 & H11); 8.38 (d, 2H, H4 & H8); 8.53 (s, 1H, H12). NMR concurrent with literature[174].
^{13}C NMR (75MHz, $CDCl_3$): δ_C 18.66 (C1); 124.36 (C12); 125.41 (C13, C14, C15 & C16); 126.20 (C17); 126.90 (C4, C7, C8 & C11); 129.40 (C5, C6, C9 & C10).
MS: [M + H^{+}] 277.34 g mol^{-1}.

2.1.7 Preparation of a 58:4:2 (w:w) P(MMA:PEGM:AMM) co-polymer

Reaction Scheme

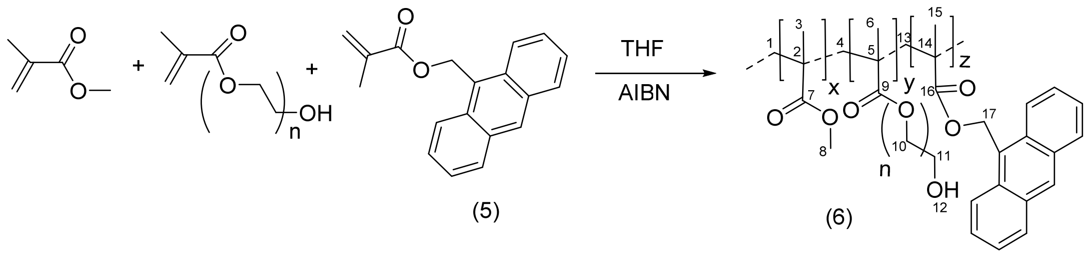

(5)

(6)

Reaction Procedure

In a round-bottom flask (RBF, 250ml), tetrahydrofuran (THF, 150ml) was added. Methyl methacrylate (MMA, 6.49x10^{-2} mol, 6.496g, 6.911ml), poly(ethylene glycol) methacrylate (PEGM, ≈ 0.0125mol, 4.51g, 4.08ml), 9-anthrylmethyl methacrylate (5, AMM, 0.224g, 8.54 x 10^{-4}mol) and azobisiso-butyronitrile (AIBN, 0.58mmol, 0.096g) were combined into the solution and subsequently degassed for 20 mins through bubbling N_2. Solution was then refluxed for 20h under N_2 whilst stirred at 90°C. Once reflux had run for 20h, the colourless solution was cooled to room temperature and transferred to a stirring mixture of diethyl ether (200ml) in a conical flask (500ml). This produced a white powder-like solid, which was collected *via* Büchner filtration, redissolved in THF (100ml) and transferred to a conical flask containing stirring diethyl ether (200ml). This produced a white powder-like solid, which was collected *via* Büchner filtration and dissolved in dichloromethane (DCM) and collected *via* rotary evaporation. The resulting solid was dried *in vacuo* for 2h and transferred to a sample vial, giving a yield of 6.11g (73%).

^{1}H NMR (400MHz, $CDCl_3$): δ_H 0.86 (3H, s, H6); 1.03 (3H, s, H3); 1.21 (3H, m, H15); 1.86 (br s, H1, H4 & H13); 3.61 (2H, m, H11); 3.67 (3H, s, H8); 4.12 (s, H11); 5.31 (2H, s, H17).

FT-IR ν max (cm^{-1}): 2945 (CH), 1710 (CO).

2.1.8 Functionalisation of the 58:40:2 (w:w) P(MMA:PEGM:AMM) co-polymer with DSC carbonate

Reaction Scheme

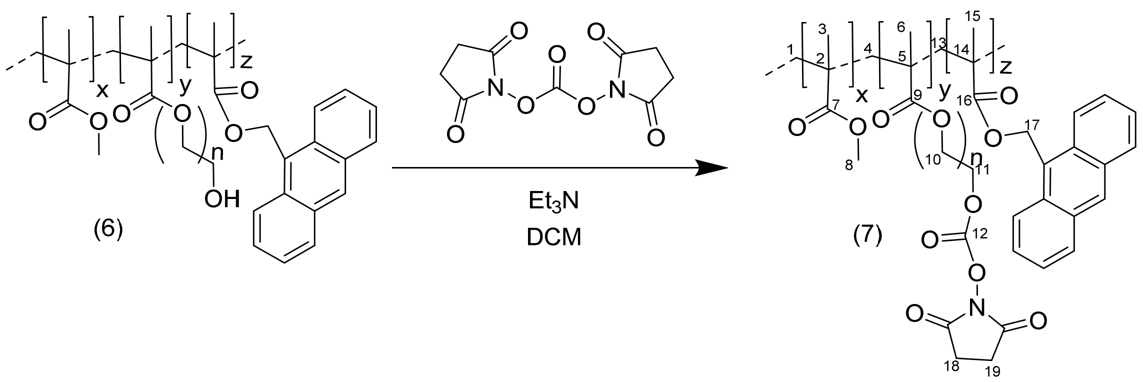

Reaction Procedure

58:40:2 (MMA:PEGM:AMM) co-polymer (6) (5.50g) was added to dichloromethane (DCM, 100ml) in a RBF and stirred. Disuccinimidyl carbonate (DSC, 2.31g, 8.8mmol) was added, alongside triethylamine (TEA, 2ml) and the solution was stirred overnight at room temperature. The reaction mixture was then slowly added to diethyl ether (200ml) and stirred, yielding a pale yellow-white precipitate. The precipitate was redissolved in DCM (100ml) and re-precipitated in stirring diethyl ether (200ml). The collected pale yellow-white solid was then dissolved in $CHCl_3$ (50ml), washed with distilled H_2O and dried over $MgSO_4$. The solvent was removed *via* rotary evaporation, yielding a pale white solid. The resulting solid was dried *in vacuo* for 2h and transferred to a sample vial, giving a yield of 4.54 (74.3%).

^1H NMR (400MHz, $CDCl_3$): δ_H 0.86 (3H, s, H3); 1.03 (3H, s, H6); 1.24 (3H, m, H15); 1.82 (6H, br s, H1, H4 & H13); 2.85 (4H, m, H18 & H19); 3.60 (2H, m, H11); 3.65 (3H, s, H8); 4.15 (s, H11); 5.32 (2H, s, H17).

FT-IR ν max (cm^{-1}): 2947 (CH), 1709 (CO).

2.1.9 Preparation of a 59:40:1 (w:w) P(MMA:PEGM:AMM) co-polymer

Reaction Scheme

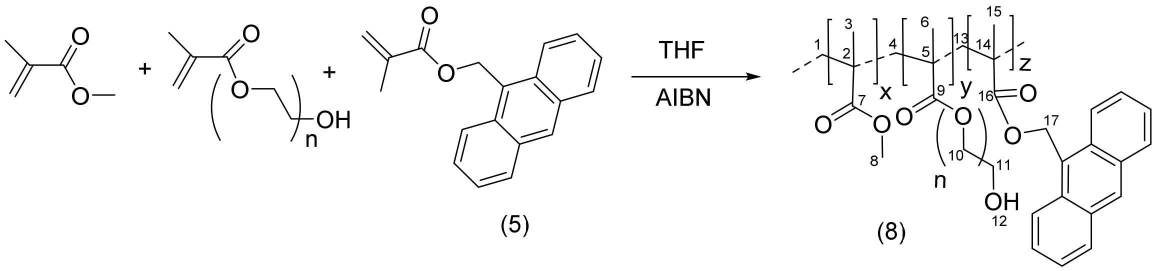

Reaction Procedure

In a round-bottom flask (RBF, 250ml), tetrahydrofuran (THF, 150ml) was added. Methyl methacrylate (MMA, 6.61 x10^{-2} mol, 6.608g, 7.045ml), poly(ethylene glycol) methacrylate (PEGM, ≈ 0.0125mol, 4.51g, 4.08ml), 9-anthrylmethyl methacrylate (AMM, 0.112g, 4.05 x 10^{-4}mol) and azobisiso-butyronitrile (AIBN, 0.58mmol, 0.096g) were combined, and the solution was degassed for 20 mins through bubbling N_2. The solution was refluxed for 20h under N_2 whilst stirred at 90°C. Once reflux had run for 20h, the colourless solution was cooled to room temperature and transferred to a stirring mixture of diethyl ether (200ml) in a conical flask (500ml). This produced a white powder-like solid, which was collected *via* Büchner filtration, redissolved in THF (100ml) and transferred to a conical flask containing stirring diethyl ether (200ml). This produced a white powder-like solid, which was collected *via* Büchner filtration and re-dissolved in dichloromethane (DCM). The resulting solid was collected *via* rotary evaporation and dried *in vacuo* for 2h, giving a yield of 7.21g (85%).

^{1}H NMR (400MHz, $CDCl_3$): δ_H 0.86 (3H, s, H3); 0.87 (3H, s, H6); 1.03 (3H, s, H15); 1.23 (2H, m, H1); 1.84 (4H, br s, H4 & H13); 3.60 (3H, m, H8); 3.66 (2H, m, H11); 4.11 (1H, m, H11); 5.58 (s, H17).

FT-IR ν max (cm^{-1}): 2905 (CH), 1714 (CO)

2.1.10 Functionalisation of the 59:40:1 (w:w) P(MMA:PEGM:AMM) co-polymer with DSC carbonate

Reaction Scheme

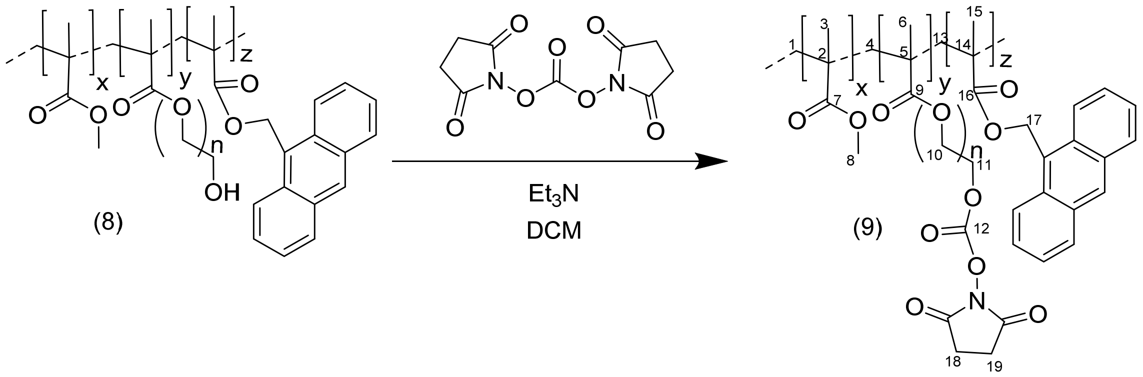

Reaction Procedure

59:40:1 (MMA:PEGM:AMM) co-polymer (8) (5.50g) was added to dichloromethane (DCM, 100ml) in a RBF and stirred. Disuccinimidyl carbonate (DSC, 2.31g, 8.8mmol) was added alongside triethylamine (TEA, 2ml) and the solution was stirred overnight at room temperature. The reaction mixture was then slowly added to diethyl ether (200ml) and stirred, yielding a pale yellow-white precipitate. This was then re-dissolved in DCM (100ml) and precipitated in stirring diethyl ether (200ml). The collected pale yellow-white solid was then dissolved in CHCl$_3$ (50ml), washed with distilled H$_2$O and dried over MgSO$_4$. The solvent was removed *via* rotary evaporation, the resulting solid was dried *in vacuo* for 2h and transferred to a sample vial, giving a yield of 5.24g (72.7%).

^{1}H NMR (400MHz, CDCl$_3$): δ_H 0.86 (3H, s, H6); 1.03 (3H, s, H3); 1.24 (3H, m, H15); 1.70 (br s, H1, H4 & H13); 2.62 (4H, m, H15 & H16); 3.61 (2H, m, H11); 3.66 (3H, s, H8); 5.65 (2H, s, H17).
FT-IR ν max (cm^{-1}): 2907 (CH), 2315 (CH), 1705 (CO)

2.1.11 Preparation of a 57:40:3 (w:w) P(MMA:PEGM:AMM) co-polymer

Reaction Scheme

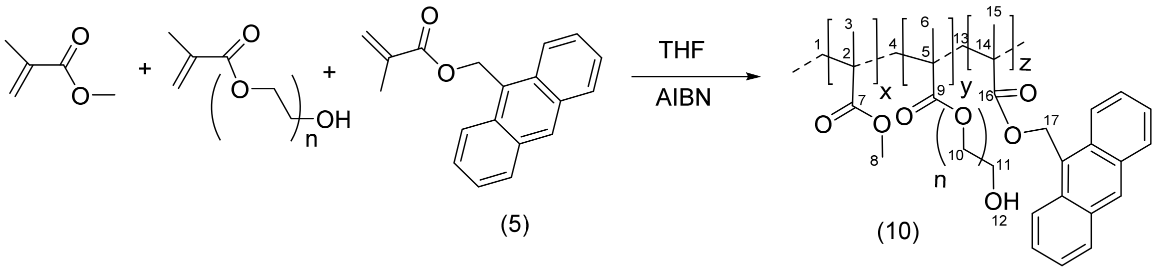

(5)

(10)

Reaction Procedure

In a round-bottom flask (RBF, 250ml), tetrahydrofuran (THF, 150ml) was added. Methyl methacrylate (MMA, 6.38 x10^{-2} mol, 6.384g, 6.886ml), poly(ethylene glycol) methacrylate (PEGM, ≈ 0.0125mol, 4.51g, 4.08ml), 9-anthrylmethyl methacrylate (AMM, 0.336g, 1.21 x 10^{-3}mol) and azobisiso-butyronitrile (AIBN, 0.58mmol, 0.096g) were combined, and the solution was degassed for 20 mins through bubbling N_2. The solution was refluxed for 20h under N_2 whilst being stirred at 90°C. Once the reflux had run for 20h, the colourless solution was cooled to room temperature and transferred to a stirring mixture of diethyl ether (200ml) in a conical flask (500ml). This produced a white powder-like solid, which was collected *via* Büchner filtration, redissolved in THF (100ml) and transferred to a conical flask containing stirring diethyl ether (200ml), producing a white powder-like solid. The solid was collected *via* Büchner filtration and dissolved in dichloromethane (DCM). The sample was collected *via* rotary evaporation and dried *in vacuo* for 2h, giving a yield of 5.34g (67%)..

^{1}H NMR (400MHz, $CDCl_3$): δ_H 0.86 (3H, s, H6); 1.03 (3H, s, H3); 1.33 (3H, m, H15); 1.82 (6H, br s, H1, H4 & H13); 3.63 (2H, m, H11); 3.65 (3H, s, H8); 3.74 (1H, s, H12); 4.11 (2H, s, H17).

FT-IR ν max (cm^{-1}): 2950 (CH), 1721 (CO)

2.1.12 Functionalisation of the 57:40:3 (w:w) P(MMA:PEGM:AMM) co-polymer with DSC carbonate

Reaction Scheme

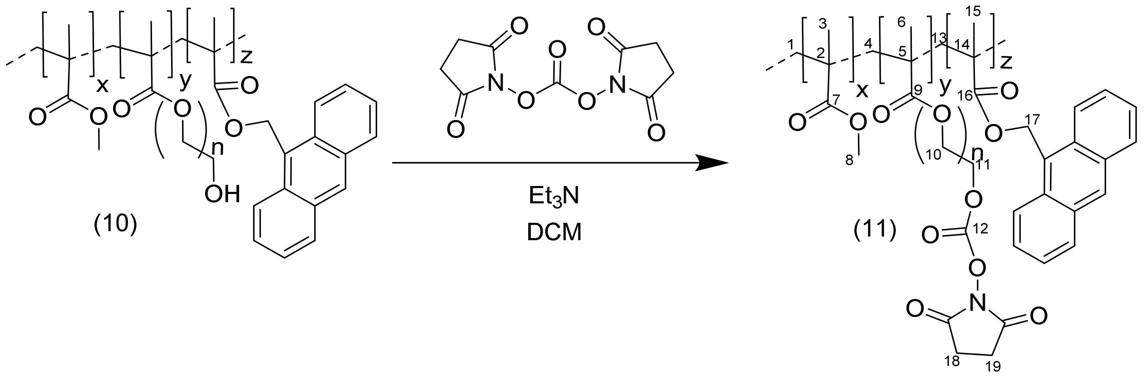

Reaction Procedure

57:40:3 (MMA:PEGM:AMM) co-polymer (10) (5.50g) was added to dichloromethane (DCM, 100ml) in a RBF and stirred. Disuccinimidyl carbonate (DSC, 2.31g, 8.8mmol) was added, alongside triethylamine (TEA, 2ml), and the solution was stirred overnight at room temperature. The reaction mixture was then slowly added to diethyl ether (200ml) and stirred, yielding a pale yellow-white precipitate. The solid was re-dissolved in DCM (100ml) and precipitated in stirring diethyl ether (200ml). The collected pale yellow-white solid was then dissolved in $CHCl_3$ (50ml), washed with distilled H_2O and dried over $MgSO_4$. The solvent was removed *via* rotary evaporation and the resulting solid was dried *in vacuo* for 2h, transferred to a sample vial, giving a yield of 3.97g (74.3%).

^{1}H NMR (400MHz, $CDCl_3$): δ_H 0.68 (3H, s, H3); 0.85 (3H, s, H6); 1.07 (3H, m, H15); 1.65 (br s, H1, H4 & H13); 2.68 (4H, m, H15 & H16); 3.43 (2H, m, H11); 3.48 (3H, s, H8); 3.94 (1H, s, H11); 4.45 (2H, s, H17).

FT-IR ν max (cm^{-1}): 2948 (CH), 1721 (CO)

2.2 Generation of electrospun co-polymer membranes

2.2.1 Electrospinning of fibrous mats

Figure 20: Picture of the electrospinning set-up, showing: (left) the syringe pump with syringe & needle clamped in place (orange arrow); (centre) the voltage generator; and (right) the rotating collector where the electrospun membranes are generated. The needle is connected to the voltage generator and the polymer is driven through the needle (yellow arrow) and spins into a fibrous mat.

A solution (1ml) of synthesised polymer was drawn into a 1ml syringe and placed within the clamping system on the syringe pump (World Precision Instruments Inc, Sarasota, USA). A 15G gauge needle was attached to the end of the syringe containing the polymer solution. A rotating stainless steel collector was placed 15cm from the needle tip and the needle was then connected to a high voltage supply (Glassman FC-series 120 Watt regulated power supply, NJ, USA). The syringe pump was set to run at the required flow rate and the electrospun fibres were collected on the rotating collector. The electrospun membranes were then collected and dried *in vacuo* overnight.

The rotating stainless steel collector was used to allow the continued collection of an evenly distributed electrospun matrix, ensuring that the collected fibres from the electrospinning polymer matrix created a membrane with a greater uniformity in thickness in comparison to a flat metal collector[128,129]. The rotation of the collector was kept at a slow rate to ensure that controlled arrays of fibres were produced, and that the individual fibres did not align and maintained their random orientation[122,129], aligning it more closely to native ICL within BrM[39].

2.2.2 Assessment of fibre diameter

Fibre diameters were quantified using SEM images (4 images per preparation or adjustment in electrospinning parameter). To analyse the fibre diameter of a given sample, 20 fibre areas per image were measured and pooled into GraphPad Prism 6 software for calculation of the range of fibre diameter per sample.

2.3 Thickness characterisation of designed membranes & BrM

2.3.1 Thickness measurements of co-polymer membranes

Electrospun polymer membranes were dried *in vacuo* overnight and a 2 x 2cm sample was cut. Samples were then transferred to a glass slide and analysed on a ZeMetrics ZeScope three-dimensional optical profilometer, under Cleanroom Class 1000 conditions using ZeMetrics ZeMaps software (versions 1.07.15 and 1.07.17). The data which had been collected was analysed using SPIP (version 5.1.3).

2.3.2 Thickness measurements of native BrM

Human donor eyes, with consent granted for research, (10 eyes, age range, 71–99 years) were obtained from the Bristol Eye Bank (United Kingdom). The donor eyes were managed in compliance with the Declaration of Helsinki for research involving human tissue. After a preliminary fundus examination with a dissecting microscope, BrM-choroid complex was isolated as described previously[175]. Samples were stored at -80°C until required.

Samples of BrM-choroid complex were placed on to glass slides in 0.1M pH 7.4 phosphate-buffered saline (PBS; Sigma-Aldrich, Poole, UK), dried for 30 minutes at 37°C (Stuart S160 Incubator, Bibby Scientific Ltd., Staffordshire, UK) and imaged on ZeMetrics ZeScope optical profilometer as discuseed in Chapter 2.3.1.

Samples of BrM-choroid complex were stained as follows: (i) Coomassie Brilliant Blue was used as per manufacturer's instructions; (ii) Oil Red O (0.5%) (Sigma-Alrich) was dissolved in 60% Triethyl phosphate (Sigma-Aldrich). BrM-Choroid samples were incubated for 20 minutes at room temperature followed by two washes with distilled water; (iii) Sundan Black B (0.1%) (Sigma- Aldrich) was dissolved in 70% ethanol. BrM-Choroid samples were incubated for 25 minutes at room temperature followed by three 10 minute washes H_2O; (iv) samples were incubated with Harris Haematoxylin (BDH) for 10 minutes followed by three 5 minute washes with H_2O. Samples were then transferred to glass slides and dried for 30 minutes at 37°C and then analysed by the non-contact Zemetrics ZeScope three-dimensional optical profiler, as detailed in Chapter 2.3.1.

Gold-sputtering of BrM-choroid samples was carried out as follows: samples of 2x2 cm BrM-choroid complex were mounted onto carbon stubs prior to sputter-coating with gold

(Anatech Hummer 6.2 Sputter Coater, Anatech USA) twice for two minutes under manual conditions. Gold sputtered BrM-choroid complex samples were measured on a Zemetrics ZeScope three-dimensional optical profiler as detailed in Chapter 2.3.1.

2.4 ARPE-19 cell lines

2.4.1 ARPE-19 cell culture

ARPE-19 cells[155] were purchased from the American Tissue Culture Collection (Manassas, VA, USA) (ATCC). ARPE-19 cells were maintained at 37°C in a humidified atmosphere with 5% CO_2 in ARPE-19 culture medium (see Chapter 2.4.2).

2.4.2 ARPE-19 cell tissue media preparation

Chemicals/Equipment Required:

- DMEM, High Glucose, Pyruvate (196ml)
- Fetal Bovine Serum (FBS, 2ml)
- Antibiotic (Antimycotic solution A5955, 2ml)
- Millipore Stericup/filter flask (250ml)

Procedure:

DMEM (196ml), FBS (2ml) and Antibiotic (2ml) were combined in the Millipore filter flask and filtered through to the Stericup under vacuum. Filter section removed and lid carefully added to the Stericup.

2.4.3 ARPE-19 cell splitting and seeding onto 60:40 MMA:PEGM co-polymer membranes

2cm^2 samples of 60:40 MMA:PEGM co-polymer fibre were cut and placed in individual wells in a 12 well plate. PBS (sterile, 1ml) was added to each well, covered and left overnight under UV irradiation.

Once left overnight, the fibres were transferred to a fresh 12 well plate alongside PBS (600µl per well). Samples were washed carefully and PBS was removed. ARPE-19 cell tissue media (see 2.4.3, 600µl) was added to each well and incubated at 37°C.

During the polymer incubation period, the T75 flask containing ARPE-19 cells was removed from the incubator. The media was removed from the T75 flask and washed carefully with Hanks BSS (3x, 6ml). Trypsin-EDTA (0.25%, 6ml) was added and the cells were incubated for 6 mins. After incubation, the flask was disturbed repeatedly until all RPE cells had detached from the base of the flask. ARPE-19 cell tissue media (8ml) was added the flask was washed repeatedly. The Trypsin-EDTA/ARPE-19 cells/ARPE-19 cell media solution (14ml) was transferred to a centrifuge tube, counterweight assigned and spun at 1000rpm for 5mins (during centrifugation the T75 flask was re-immersed in ARPE-19 cell media and incubated). After completion of the centrifugation, the supernatant was removed and the pelleted ARPE-19 cells were immersed in ARPE-19 cell media (3ml). ARPE-19 cells were counted using a haemocytometer with Tyrpan Blue (100µl for 100µl cell solution):

$$\frac{Cells\ in\ quadrant\ 1\ (Q1) + Q2 + Q3 + Q4}{4} = No.of\ cells\ per\ square$$

$$Dilution\ factor\ (DF) = Ratio\ of\ Trypan\ Blue\ to\ cell\ solution$$

$$\frac{(No.of\ cells\ per\ square\ x\ DF)}{100} = x\ million\ cells\ per\ ml$$

With this calculation, ARPE-19 cell tissue media was combined with ARPE-19 cells in an eppendorf (1ml) and distributed to 9 out of the 12 polymer-containing wells (100µl ea.). ARPE-19 cell tissue media (100µl) was added to 3 of the 12 polymer-containing wells and the samples were incubated for 2h at 37^{o}C. Additional ARPE-19 cell tissue media (300µl) was added to each well after 2h and samples incubated overnight.

The ARPE-19:co-polymer samples were maintained by repeated feeding of fresh ARPE-19 cell tissue media. The 12 well plate containing ARPE-19 cell seeded co-polymer fibres was removed from the incubator and placed in a sterile fume flow. Media within the wells was removed *via* pipette and transferred to a waste glass beaker. Fresh ARPE-19 cell tissue media was carefully administered to each well and the 12 well plate was placed back into the incubator.

2.4.4 LDH Assay of ARPE-19 cell tissue media

ARPE-19 cell tissue media was collected from ARPE-19 seeded co-polymer membranes and aliquoted into eppendorf vials. The ARPE-19 media was transferred (100µl) to a 96 well plate in triplicate (-ve controls (tissue media & LDH), samples and +ve control (media alongside Triton X-100 solution)). In a centrifuge tube (15ml), catalyst (0.25ml) was added alongside the dye solution (11.25ml) and the solution was immediately transferred to each media sample (100µl). The 96 well plate was incubated in the dark for 30 mins at RT. After incubation time had passed, 96 well plate was analysed and the absorbance change caused by the colourimetric change was measured on a colourimetric plate reader (FLUOstar Optima microplate reader (BMG Labtech, Offenburg, Germany))..

2.4.5 DAPI staining of ARPE-19 cell seeded co-polymer membranes

A 12 well plate containing ARPE-19 cell seeded fibre mats was taken out of the incubator and transferred to a sterile fume flow. Samples were removed from the 12 well plate and placed in a fresh 12 well plate containing PFA (1ml per well). Samples were then incubated for 30 mins at 4°C. After incubation, the PFA solution was removed and the samples were washed with PBS (3x, 1ml). The samples were then washed with ddH$_2$O (1x, 1ml). DAPI solution was then added to each well (500µl) and incubated in the dark at RT for 6 mins. DAPI was then removed and samples were washed with ddH$_2$O (3x, 1ml). The fibre mats were carefully transferred to a coverslip containing a small amount of Mowiol fixative. Samples were then complexed with a second coverslip and dried overnight in the dark at RT. Samples imaged *via* epifluorescent microscope and images collected randomly.

2.4.6 Phalloidin staining of ARPE-19 cell seeded co-polymer membranes

A 12 well plate containing ARPE-19 cell seeded fibre mats was taken out of the incubator and transferred to a sterile fume flow. The samples were removed from 12 well plate and placed in a fresh 12 well plate containing PFA (1ml per well). Samples were then incubated for 30 mins at 4°C. After incubation, the PFA solution was removed and samples were washed with PBS (3x, 1ml). Samples were then immersed in Phalloidin 488 solution (250µl), incubated for 1h at RT and then subsequently washed with PBS (3x, 1ml). Samples were then washed with ddH$_2$O (1x, 1ml) to prepare for DAPI staining. DAPI solution was then added to each well (500µl) and the samples were incubated in the dark at RT for 6 mins. DAPI solution was then removed and the samples were washed with ddH$_2$O

(3x, 1ml). The fibre mats were carefully transferred to a coverslip containing a small amount of Mowiol fixative, complexed with a second coverslip and dried overnight in the dark at RT. Samples were then imaged *via* epi-fluorescent microscope and images collected randomly.

2.5 Primary murine RPE cell lines

2.5.1 Primary murine RPE extraction

C57BL/6 P8-10 black mice were culled, eyes removed and transferred to a small petri dish containing Hanks BSS (2ml). Using a light microscope, peripheral tissue was removed and a small incision was made just below the iris. Using the forceps and surgical scissors the incision was carried forward to a clean cut, until the iris, lens and cornea had been removed. The remaining ‘cup’ was transferred to a fresh small petri dish containing Hanks BSS (2ml). Using a light microscope, the vitreous and retina were carefully removed and the black RPE layer underneath was peeled off. The RPE was carefully transferred to an eppendorf containing PBS (1ml), pelleted for 10s and the sterile PBS was removed. Trypsin-EDTA (1ml) was added and the solution was incubated for 10mins at 37^{o}C. The RPE pellet was agitated until fully complexed by the Trypsin-EDTA. The sample was spun down for 1min and the pellet was isolated. Primary murine RPE media (see 2.5.2, 1ml) was added and the solution was transferred to a 6 well plate and incubated at 37^{o}C.

2.5.2 Primary murine RPE cell tissue media (5% FBS)

Chemicals/Equipment Used:

- Centrifuge tube
- Pipette and pipette tips
- MEM – α modification
- NI supplement
- Glutamine – penicillin – streptomycin solution
- Non-essential amino acid (AA) solution
- THT supplement
- FBS solution

Procedure:

Into a 50ml centrifuge tube, the following was added:

MEM – α modification	45.9ml
NI supplement	500µl
GPS solution	500µl
Non-essential AA solution	500µl
THT supplement	100µl
FBS solution	2.5ml

Media kept at 4°C for up to 1 month.

2.5.3 Primary RPE cell seeding onto co-polymer membranes

1cm^2 samples of co-polymer fibrous membrane were cut and placed in a 24 well plate alongside PBS (1ml). Samples were incubated overnight under UV irradiation. The PBS was removed and 5% primary RPE cell media (500µl) was added and incubated at 37°C. Primary RPE cell cultures were then removed from incubation and the media was removed. Primary RPE cells were then washed with PBS (2x, 2ml), trypsin-EDTA (2ml) was added and the cultures were incubated at 37°C for 6 mins. After incubation, the cultures were disturbed until the complete RPE cell detachment was achieved from the well plate. 5% FBS primary RPE cell media (4ml) was added and the solution was transferred to a centrifuge tube, counterweight assigned and RPE cells pelleted at 1000rpm for 5 mins. The RPE pellet was then isolated and immersed in primary RPE cell media (12ml). The RPE cell-RPE media solution was distributed to each polymer fibre-containing well (500µl per sample) and incubated at 37°C.

2.5.4 Immunofluorescence studies of primary RPE cell seeded monolayers on the co-polymer membranes

Primary RPE cell seeded co-polymer membranes were transferred to a 24 well plate containing PBS, washed (3x, 1ml) and incubated in PFA (1ml) for 30 mins at 4°C. The samples were then washed with PBS (3x, 1ml) and incubated in NDS (500µl) for 1h at 4°C. Excess liquid in the samples were allowed to drain away and the samples were then transferred to a fresh well plate containing the primary antibody, where they were incubated for 16h at 4°C. Samples were then washed with PBS (3x, 1ml) and immersed in 2° antibody (500µl) for 1h at rt in the dark. Samples washed with PBS (3x, 1ml) and incubated in Phalloidin 488 (500µl) for 1h at RT in the dark. Samples were then washed with PBS (3x, 1ml) and ddH_2O (1x, 1ml), and then incubated in DAPI (500µl) for 6 mins at RT in the dark. The samples were washed with ddH_2O (3x, 1ml), dried and transferred to a glass slide alongside Mowiol fixative and covered. The samples were then dried at RT in the dark for 2h and incubated at 4°C. Slides were kept at 4°C in the dark for long-term storage. Confocal images generated on Leica SP5 Laser Scanning Confocal microscope (Leica Microsystems, Milton Keynes, UK) with assistance from David Johnston.

2.5.5 Primary antibody table

Primary Antibody	Product code	Solution concentration	Secondary Antibody	Solution concentration
Vinculin	Ab18058	1:100	Anti-mouse Alexa Flour (AF)	1:100
RPE 65	Ab78036	1:100	Anti-mouse AF	1:100
ZO-1	Ab59720	1:100	Anti-rabbit AF	1:100
Focal Adhesion Kinase (FAK)	AHO0502	1:100	Anti-rabbit AF	1:100
Na^+/K^+ ATPase	Ab7671	1:100	Anti-rabbit AF	1:100
Rhodopsin	Ab3267	1:100	Anti-mouse AF	1:100
αVβ5 receptor	Ab24694	1:100	Anti-mouse AF	1:100
Mert-K	Ab95925	1:100	Anti-rabbit AF	1:100

Table 1: Primary antibody table showing the primary antibodies used throughout this project. Product codes of the antibodies used, the concentrations at which they were used and the required secondary antibodies (with concentrations) used.

2.5.6 Western Blotting

Mature primary RPE monolayers seeded on scaffolds were removed from the incubator (37°C, 5% CO_2) and immersed in Trypsin-EDTA (0.25%, 1ml / well) for incubation: 6 mins at 37°C. Following this, the cell lysates were pooled in a 12ml centrifuge tube. A further wash using primary RPE cell culture medium (4ml) was used to wash the wells and added into the lysate centrifuge tube. The sample was centrifuged for 4 mins at 18000rpm at 4°C. The collected pellet was isolated from the Trypsin-EDTA solution and resuspended in primary RPE medium (4ml).

Into an eppendorf tube, RPE- primary RPE medium solution (100µl) and Trypan Blue (100µl) were combined. The produced solution was carefully loaded onto a haemocytometer and the cells were counted.

The cells in primary RPE cell medium were pelleted (4 mins, 1800rpm, 4°C) and washed with PBS (2x, 3mins, 1800rpm, 4°C).

A BCA protein assay (Pierce BCA Assay Kit, Thermo Scientific # 23225) was used to quantify the samples. RIPA buffer, protease inhibitor and the isolated RPE pellet were kept on ice throughout the procedure. A 'working reagent' and protein standards were generated as per manufacturer's instructions. RIPA buffer (250µl) and protease inhibitor (35µl) were added to an eppendorf containing the RPE lysate. Into a 96 well plate, 25µl of the sample and protein standards were added as outlined in a predefinied layout. Working reagent was added to each well (200µl) and the 96 well plate was mixed by orbital shaker for 30s. The samples were covered and incubated for 30 mins at 37°C. They were then allowed to cool and any change in colour was measured on absorbance at 562nm on a colorimetric plate reader (FLUOstar Optima microplate reader (BMG Labtech, Offenburg, Germany)). Samples (lysates) were kept at -20°C.

Gel electrophoresis of the samples was then carried out as follows: lysates stored at -20°C were allowed to thaw into a 1.5ml eppendorf tube containing: lysate (10µl) and sample buffer (10µl, formed of: glycerol (2ml); β-mercaptoethanol (1.5ml); 20% SDS; 1M Tris-HCL pH 6.8 (1.875ml); 1% Bromophenol blue (125µl)). Once combined, the solutions were heated to 95°C for 4 mins using a digital heating block. Samples were then returned to RT. Pre-cast gels (12% Mini-PROTEAN TGX Gel, 12 well, 20µl, #456-1045) were used with the western blot tank apparatus (Bio Rad Mini-PROTEAN Tetra Cell #1658029) alongside 1X Running Buffer (10X stock: Tris-base (30.2g); Glycine (144g); SDS (10g); ddH_2O (1000ml)). 8µl ladder (Prescision Plus protein dual colour standards ladder #161-0374) was loaded alongside 20µl of cell lysate into the wells. Voltage setting was adjusted to 150V and the electrophoresis was allowed to continue for 45 mins. Following this, the gel was isolated and transferred to 1X Transfer buffer (10X Running buffer (100ml); Methanol (200ml); ddH_2O (700ml)).

The transfer of proteins and subsequent staining was then carried out. The isolated gel was placed on top of a filter paper/sponge arrangement and overlaid with a nicrocellulose membrane. Further filter paper and mesh were applied and encased in a transfer apparatus. This was transferred to the Western blot tank and 1X Transfer buffer was loaded. A stirrer bar and an ice pack were added and voltage generator attached and the transfer of proteins was run for 1h at 100V. After completion of the transfer, the nitrocellulose membrane was isolated and washed with ddH_2O. The membrane was incubated in a TBS-t/BSA solution (3% BSA in TBS-t (0.1%) solution) for 30 mins at 4°C whilst gently rocking on an orbital shaker. The suitable primary anitbodies were then applied to the nitrocellulose membrane in TBS-t/BSA solution (5µl in 3ml) and then incubated at 4°C on an orbital shaker for 16h. Membranes were then washed with TBS-t (0.1%, 3x, 5mins) and subsequently incubated in the suitable 2° antibody (1µl in 3ml TBS-t/BSA) for 1h at 4°C. The membranes were washed with TBS-t. Western blot image acquisition was carried out using an ECL substrate (Clarity Western ECL Substrate #170-5060), Versadoc Imaging System (Bio-Rad Laboratories, Hertfordshire, UK) and Bio Rad Quantity One 1-D Analysis Software.

2.5.7 VEGF ELISA

An Abcam VEGF ELISA (murine) kit (ab100751) was used for all VEGF ELISA analysis. Assay diluent, wash, standards, Biotinylated VEGF detection antibody and HRP-Streptavidin solutions were all used following the manufacturer's instructions. Cell culture medium was isolated from samples and diluted 65x. Using the well strips provided, standards and samples (100µl) were applied to each well, covered and incubated for 2.5h at RT on the orbital shaker. Solution was discarded and washed with 1X wash solution (4x). 1X Biotinylated VEGF detection antibody was added to each well (100µl) and incubated for 1h at RT on the orbital shaker. The solution was once again discarded and washed with 1X wash solution (4x). HRP-Streptavidin solution (100µl) was added to each well, covered and incubated for 45 mins at RT on the orbital shaker. This solution was also discarded and the wells were washed with 1X wash solution (4x). TMB One-stop substrate reagent (100µl) was added to each well, covered and incubated for 30 mins at RT in the dark on the orbital shaker. The stop solution (50µl) was subsequently added to each well and the subsequent colour change was read at 450nm on a colorimetric plate reader (FLUOstar Optima microplate reader (BMG Labtech, Offenburg, Germany)). Concentration values were calculated from the standard curve.

2.5.8 FACS cell cycle analysis

Primary RPE cells growing on scaffolds were gently trypsinised (Trypsin-EDTA (0.25%, 1ml per well) and transferred to a FACS tube (BD Falcon PRB tubes #352052) *via* a cell strainer (Fisherbrand Sterile Cell strainer, 40µm, #22-363-547). The cells were centrifuged for 5 mins at 2000rpm and the resulting pellet was washed with PBS (2ml, 2000rpm for 3 mins, 2x) and immersed in ethanol (70%). Fixation was performed for 30 mins at 4°C and the RPE cells were pelleted (2000rpm, 5 mins, 2x) and washed with PBS (2x, 2000rpm, 3 mins). The pellet was then resuspended in PI/RNAse solution (300µl, Cell Signaling # 4087) and incubated for 15 mins in the dark at RT. Cell sorting according to granularity/size criteria was carried out on a FACS Calibur (BD Biosciences, Oxford UK).

2.5.9 Scanning Electron Microscopy

Primary RPE-artifcial BrM samples were isolated from the cell culture incubator and immersed in fixative (3% glutaraldehyde; 4% formaldehyde; 0.1M PIPES), for 1h at 4°C. Samples were then dried on a paper towel and freeze-dried at -20°C for 20 mins. The samples were then mounted onto carbon stubs prior to sputter-coating with gold (Anatech Hummer 6.2 Sputter Coater, Anatech USA) twice for two minutes. Images were aquired using FEI Quanta 200 Scanning electron microscope (FEI materials science, OR, USA).

2.5.10 Photoreceptor outer segment isolation and labelling with FITC

Retinae were isolated from adult porcine eyes 3 hours after death as described[176]. Isolated photoreceptor outer segments (POS) were resuspended in WASH 3 solution (sucrose (10%); phosphate buffer pH 7.2 (20mM); Taurine (5mM))[177], and FITC stock solution (1.5ml, consisting of: FITC (10mg); 0.1M Na-carbonate buffer pH 9.5 (4.5ml)) was added. Solution incubated at RT in the dark for 1h on the orbital shaker. After incubation, POS-FITC solution was then transferred to eppendorf tubes (1.5ml) and POS-FITC was pelleted (Eppendorf Centrifuge 5417R, 300g, 5 mins, 20°C). The POS-FITC pellet was resuspended in WASH 3 solution and pelleted (300g, 5 mins, 20°C, 2x). POS-FITC pellet was then resuspended in DMEM (2.5% sucrose) and the pellets were stored at -80°C[178].

2.5.11 Photoreceptor outer segment internalisation

The POS-FITC was thawed from -80°C and were subsequently pelleted at 2400g for 5 mins at 20°C. The isolated pellet was resuspended in 5% FBS primary RPE medium (1ml).

The primary RPE-artificial BrM samples were immersed in the collected POS-FITC solution (950µl) over multiple time-frames (0, 30, 60, 90, 120 and 180 minutes in incubatin). After desired timepoint, the POS phagocytosis was terminated by washing with PBS-CM (3x, 1 min, 1ml, solution contained: PBS; 1mM $MgCl_2$; 0.2mM $CaCl_2$)[177]. Sample were then fixed with PFA (4°C, 20 mins), the PFA was removed and the sample was quenched with PBS-CM/NH_4Cl solution (1ml, 20 mins, RT, dark, solution contained: PBS-CM; 50mM NH_4Cl). The sample was blocked with 1% BSA in PBS-CM at RT for 10 mins in the dark and then incubated with primary antibody (1ml, Rhodopsin (see antibody chart), 25mins, RT, dark, PBS-CM). The samples were then washed with PBS-CM and 1% BSA in PBS-CM, incubated in the suitable 2° antibody (1ml, 30 mins, RT, dark) and washed with PBS-CM. The samples were then incubated in Phalloidin 647 (1ml, 30 mins, RT, dark), washed with PBS-CM and incubated in DAPI (500µl, 6 mins, dark , RT). After washing with PBS-CM, the samples were transferred to a coverslip containing Mowiol fixative. Confocal microscopy analysis was carried out by a Leica SP5 Laser Scanning Confocal microscope with assistance from David Johnston.

2.5.12 Transmission Electron Microscopy (TEM) of RPE-POS internalisation

The POS-FITC was thawed from -80°C and the sample was pelleted at 2400g for 5 mins at 20°C. The isolated pellet was then resuspended in 5% FBS primary RPE medium (1ml). Primary RPE-artificial BrM samples were immersed in POS-FITC solution (950µl) for 2h. The internalisation process was terminated with 3x PBS-CM washes (1 min each, 1ml), the RPE was trypsinised (0.05%, 5 mins, 37°C) and a RPE-POS was pellet produced. The sample was then fixed in a 4% PFA, 3% glutaraldehyde and 0.1M PIPES solution and embedded in algenate. The samples was then processed for TEM imaging, with images generated using FEI Technai12 Transmission Electron Microscope (FEI materials science, OR, USA).

2.5.13 Trans-epithelial electrical resistance (TEER)

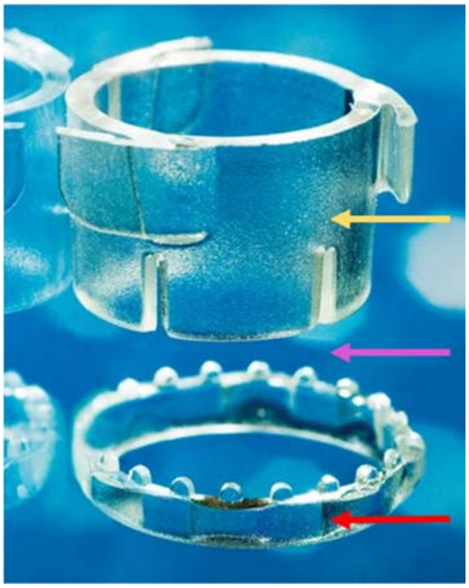

Figure 21: A Cell Crown^{TM} system, showing: (yellow) the main insert for the well plate; (pink) the location of the polymer membrane; and (red) the plastic ring that pins the polymer in place and forms the desired polymer-transwell.

Primary RPE-artificial BrM samples in a Cell Crown^{TM} arrangement (Fig. 21) were removed from the incubator. TEER equipment (World Precision Instruments, Sarasota, FL, USA) was set up and the Ohms setting was activated. The TEER probe was cleaned through a series of solutions: IMS; ddH_2O; primary RPE medium. The baseline taken from the primary RPE medium and the probe was then inserted into the wells. Repeated readings were taken per well (every 7 days from initial seeding, 4 samples, readings taken 5x per well).

2.5.14 Diffusional studies

Primary RPE-artificial BrM samples were obtained from tissue culture and immersed in PBS. Transferred to a petri dish and loaded onto the central cassette of the Ussings chamber (a kind gift to Prof A. Lotery by Prof A. Hussain). The central cassette was clamped in place into the Ussings chamber between two liquid reservoirs. One reservoir was filled with FITC-labelled dextran (1.2ml) and PBS (1.2ml). Both reservoirs were stirred magnetically. 100µl samples from both reservoirs were collected and loaded into a 96 well plate every timepoint. Colormetric analysis of the well plate (FLUOstar Optima microplate reader (BMG Labtech, Offenburg, Germany)), alongside a standard curve, gave the absorbance values and subsequently the required diffusional properties of the membranes.

2.6 Mechanical Testing

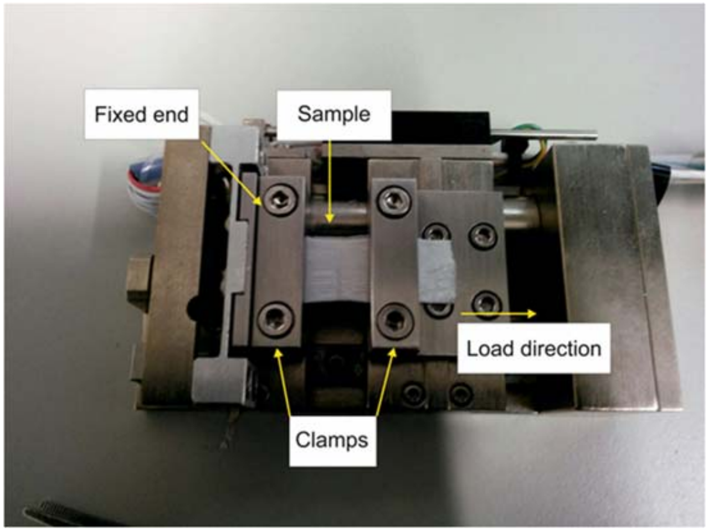

Figure 22: Picture of the DEBEN microtest tensile tester, showing the mechanical testing of the artificial BrM. The sample is loaded onto the clamps and fixed in place. As the testing begins, the load direction of the movable clamp stretches the prosthetic BrM to analyse its tensile strength.

The equipment employed for the mechanical tests was a DEBEN microtest tensile tester 300N. This work was done in collaboration with the Bhaskar research group at the University of Southampton. The device was connected to a tensile tester controller (MT10239) which was connected directly to a PC (DELL latitude D610). The device consisted of two jaws, one fixed and one movable (Fig. 22). The device was actuated with a motor and threaded loadscrew that moved one of the jaws linearly. The minimum distance between the jaws was 1 cm, and the maximum stroke was also 1 cm. The device had a loadcell of 300N, to sense the force being applied, and a linear potentionmeter to obtain the extension of the sample during testing. On the PC, the software (DEBEN microtest V5.5.29) was used to control the experiment by starting/stopping the motor and to set up the testing parameters such as: motorspeed, sampletime and zero setup. It also provided a visual live monitoring of the force being applied and the extension, both graphical and numerical.

Samples were mounted horizontally, and the device set on displacement control, moving the free jaw at a strain speed of 0.1 mm/min (motorspeed). From the software the data for the force and elongation was obtained and further processed to obtain the required tensile strength, stress at failure, toughness and elongation at break values, using the samples dimensions and thickness (software used: Matlab 2014). The samples tested were longer than 1 cm, to remove error caused by issues clamping the samples into the jaws, alongside ensuring that the sample was long enough to test. Samples were folded twice to deliberately increase the thickness. This was because the artificial BrM samples were too thin, and to avoid background noise and to ensure reliable data the membranes were folded.

2.7 Statistical analysis

Statistical methods:

All results are presented as mean ± SEM (standard error of the mean), unless otherwise stated; n, represents the number of replicates. For normally distributed data, statistical comparisons were made using an unpaired t-test, with a significance threshold of $p < 0.05$. For comparison of more than two groups a one way analysis of variance (ANOVA) was used with a Bonferroni multiple comparisons test, with a significance threshold of $p < 0.05$. GraphPad Prism Software (GraphPad San Diego, USA) was used for statistical analysis and graph production.

Chapter 3: Refinement of the first generation of artificial BrM scaffolds

3.1 General Introduction

As described in Chapter 1, the generation of co-polymer membranes developed within the research group had provided the platform to further refine the design of a novel and more effective mimic of native BrM[127]. By electrospinning this novel co-polymer, a porous, fibrous membrane had been produced, which mimicked a key feature of human BrM, in particular its inner collagenous layer (ICL) (Fig. 23). Methods such as injection moulding and spin coating would not provide this fibrous nature, hence the use of electrospinning.

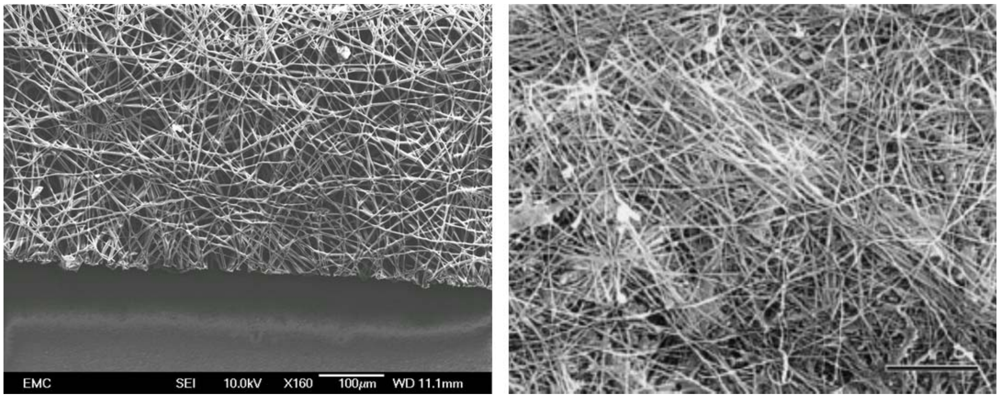

Figure 23: Representative SEM images showing (left) the synthesised electrospun co-polymer membrane and (right) the inner collagenous layer (ICL) of native human BrM (scale bar - 20µm)[39]. These images show the striking topographical resemblance of the electrospun P(MMA:PEGM) co-polymer membrane to native BrM, mimicking its interwoven fibrous nature and random alignment of fibres.

This chapter describes the steps taken to quantify the thickness of the first generation of artificial BrM scaffolds, how that compares with native BrM and the refinement of the proposed existing membrane into a new generation of suitable and accurate mimics of native BrM through the tailoring of its thickness.

3.2 Characterising the thickness of the polymer membrane

The proposed electrospun MMA:PEGM (60:40) co-polymer membrane had provided a fibrous matrix that was porous, biocompatible and easy to handle. It was able to: i) host ARPE-19 cells (a spontaneously immortalized cell line of human retinal pigment epithelium[155]), with good proliferative capacity; ii) act as a reasonably good barrier to the fluorescent dye ‘Dextran’ in diffusional studies; and iii) be easily handled for surgical applications. This provided an excellent stepping stone for subsequent work outlined here.

However to allow a full comparison to native BrM, and to fully understand the properties of the synthesised membrane, its thickness needs to be quantified. Membrane thickness is one of the crucial properties for an electrospun membrane. It significantly influences the permeability of the substrate[179–181], affecting the potential of the artificial BrM to provide the necessary control for the diffusion of macromolecules from the choriocapillaris to the RPE and *vice versa*, and the maximal stress the synthesised membrane can withstand alongside its tensile strength. In order to characterise the tensile strength of the artificial BrM, accurate thickness measurements were required to allow for the analysis of the material properties (Fig. 24).

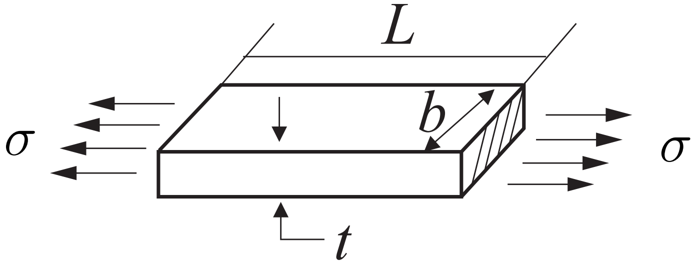

Figure 24: Schematic of the mechanical testing of a co-polymer sample, analysing its tensile strength and subsequent mechanical properties. In order for the tensile strength to be calculated, the following values are required: the length (L) of the sample; the width of the sample (b); the thickness of the sample (t); and the load direction (σ).

Measuring the thickness of an ultrathin membrane has been attempted *via* many differing routes. Scanning electron microscopy can be used to quantify the thickness of a given membrane[180]. However due to the high range of error associated with the measurements (arising from the need to orientate the material to face the scanning beam, creating the potential for the membrane to fold upon itself) alongside the error associated with measuring the thickness *via* the scale bar; and the need to capture a single image at a time (which introduces random error due to membrane positioning) it is a less than ideal approach for quantifying micron-scale thickness measurements[182]. Raman spectroscopy (including ‘total internal reflection’[183] and ‘scanning angle microscopy’[184]) has also been utilised for thickness measurements of thin polymeric samples. This has provided nanometre thickness data by measuring the incident angle of the excitation light released from the surface of the membrane. Whilst the error associated with the measurement of the angle is minimal, the use of a calibration plot and a fitting equation derived from the measurements allows a greater room for error and is largely theoretical[185]. Atomic force microscopy (AFM) provides an invasive approach for thickness measurements, determining the absolute thickness of samples by ‘scratching’ the surface of the sample and generating a 3D image, whilst also providing a high vertical resolution of less than 0.1nm[186,187]. Unfortunately AFM is not applicable for multi-layered polymer samples, because of the requirement of a substrate to be stiff, and would therefore be unsuitable for the thickness measurements of an interwoven fibrous matrix[188]. Whilst improvements to the technique’s suitability have been made by artificially creating ‘steps’ in the polymer sample[189], this invariably compromises the desired result by altering the sample and is less desirable in providing accurate thickness measurements.

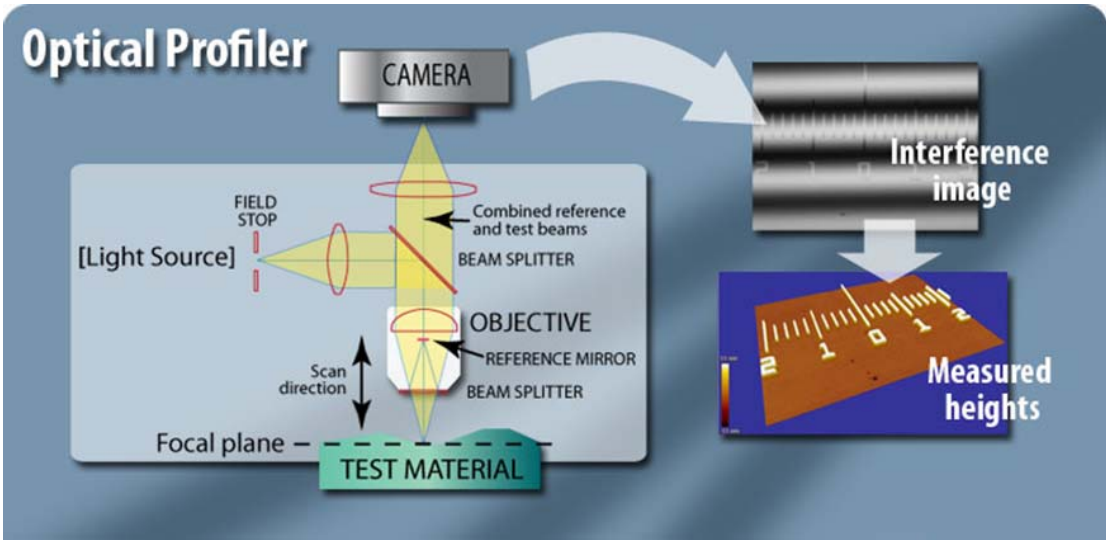

Figure 25: Operational schematic of the optical profilometer, detailing the splitting of the light beam from the sample (test material) towards the reference mirror and generating the required interferogram ‘Intereference image’, allowing the formation of a 3-dimensional map.

A minimally invasive method for thickness measurements that allows for a multi-layered substrate was proposed through the use of an optical profilometer, which measures the height variations on surfaces with precision. It uses the wave properties of light to compare the optical path difference between a test surface and a reference surface, with Angstrom-level resolution that can be further analysed according to the specific requirements of each application (Fig. 25). One class of optical profilometer is an interference microscope inside which a light beam is split. Half the beam is reflected from a sample and is passed through the focal plane of a microscope objective, whilst the other half is reflected from a reference mirror. When the distance from the beam splitter to the reference mirror is the same as that of the beam splitter is from the sample, interference occurs, creating an ‘interferogram’, which maps the interference areas and allows the optical profilometer to quantify the difference. This difference represents one-half of a wavelength, from which height differences across a surface can be measured, in fractions of a wave. From these height differences, a 3-dimensional map can be generated.

Use of an optical profilometer has been previously reported to show accurate measurements of the topology of the measured surface and its roughness[190–193]. A given sample could be analysed through the use of the wave properties of light to generate an accurate 3-dimensional map of the topography. This could then be further analysed through computer software to profile the fluctuations in the height of the sample. By using this accuracy in testing defects, it is theorised that the optical profilometer would be able to measure the thickness of a sample by defining the distance between the top of the sample to its base. This would provide sub-nanometre accurate thickness measurements of the polymer sample, without compromising its structural integrity.

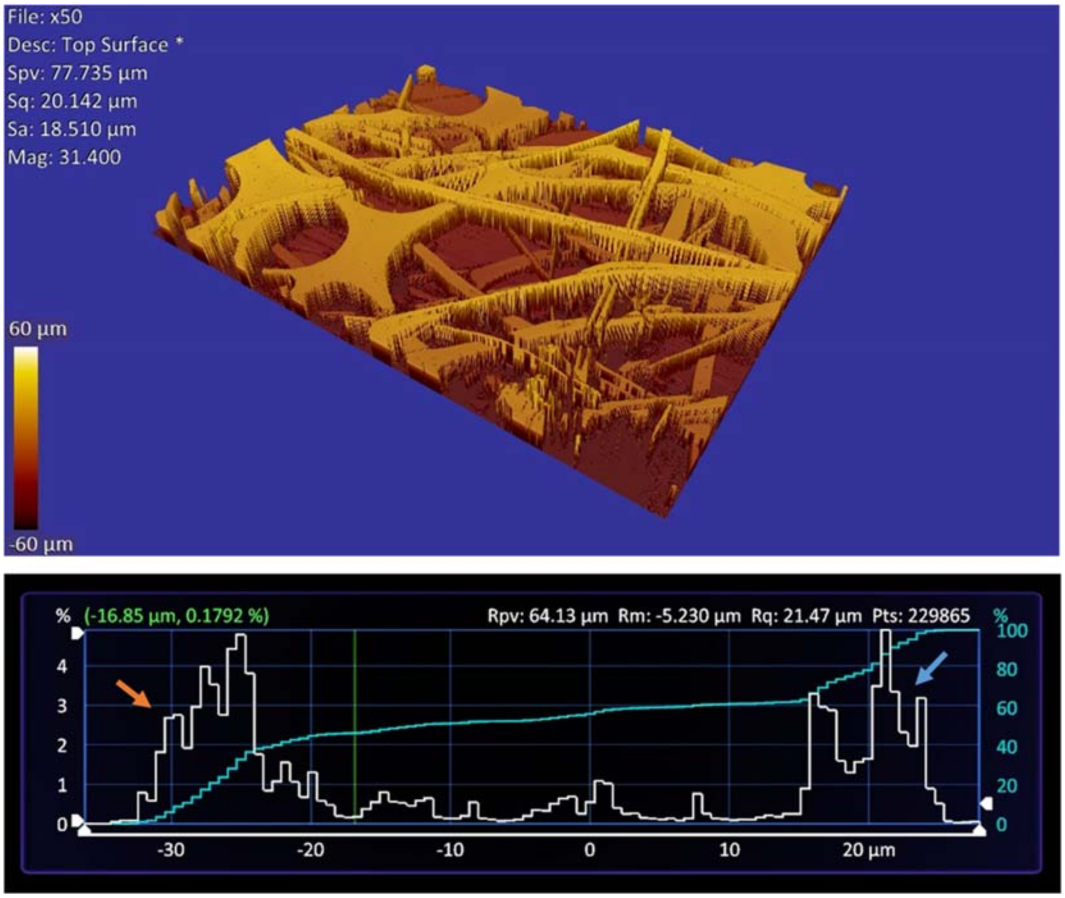

Figure 26: 3D optical profile spectra of the generated (MMA:PEGM) co-polymer substrate, showing (top) the topography and 3-dimensional structure of the membrane and (bottom) a histogram of the average thickness across the entire membrane, with two arrows showing (orange) the base and (blue) the top of the membrane.

Therefore, the generated (MMA:PEGM) co-polymer membrane, designed previously, was introduced to the optical profilometer and the thickness of the substrate was quantified (Fig. 26).

From the generated 3D optical profile, it was possible to visualise the interwoven fibres, noting the porous nature of the membrane. With the aid of analytical software (SPIP 5.0.1), the co-polymer mat fibre thickness was quantified through the use of a profile plot at a chosen point on the membrane and a histogram of the entire membrane thickness. From the generated histogram of the average thickness measurements across the entire co-polymer membrane, it was observed that the thickness range across the entire membrane is 51 ± 3µm. Thickness measurements at given points were taken and added to the generated optical profile (see Fig. 26), showing the 'step' from the base of the membrane to its top and giving a thickness of 51µm, with a range of 48-54µm.

3.3 Thickness measurements of native BrM

With the co-polymer membrane thickness characterised, a comparison could now be made to native BrM. The synthetic (MMA:PEGM) membrane is designed to be an accurate mimic of the native tissue, therefore it was important to quantify the thickness of BrM and to carry out a comparison of the two differing membranes.

Human BrM thickness has been characterised previously *via* many differing approaches. Optical coherence tomography (OCT) has been widely used as a way of measuring native BrM thickness[194–197]. OCT provides non-invasive, high-resolution, cross-sectional images of the macula that can penetrate deeply into tissue through the use of near-infrared wavelengths, and has enabled visualisation of the microscopic anatomy of retinal structures involved in the pathogenesis of AMD[198–200]. Karampelas *et al* have quantified the thickness of the RPE-BrM complex in a study directed at understanding the change in thickness in patients with early and intermediate dry AMD[194]. Through the use of a spectral domain OCT (SD-OCT) 50 patients were analysed for their RPE-BrM thickness. Karempelas *et al* were able to measure the thickness to a micrometre scale without disturbing the macula. However, they were unable to distinguish between BrM and the RPE layer, because the basement membrane of the RPE was integral to BrM, with sub-micrometre measurements also being difficult.

Transmission electron microscopy (TEM) has also been utilised as a method for characterising the thickness of BrM[46,201–204]. Using TEM, it is possible to process embedded tissue to a sub-nanometre scale. Whilst this method involves the isolation and processing of the macula from the eye, it does provide clear images on a cellular scale. Sallo *et al* used TEM to characterise the thickness of BrM, using the single-pixel resolution of TEM and taking the mean value from the scale bar associated with each image[201]. This allowed the generation of detailed and intricate TEM images and a distinction between the RPE, BrM & choroid layers. However, in order to process the tissue for TEM, it needs to be passed through a series of alcohol gradients to dehydrate the membrane prior to embedding. This will invariably affect the native architecture and thickness of the tissue, and as such would not provide a representative comparison for native BrM. Moreover, since the measurements were taken using the provided scale bar, albeit at a single-pixel resolution, a large error would be associated with these values.

Historically, BrM measurements were also made through the use of a light microscope[205–207]. Samples would be stained with a suitable agent and either through the use of a conventional or computer generated grid thickness, measurements would be taken[205,206] which would allow the samples to be visualised easily. However, as with the TEM method, the samples would need to be passed through an alcohol gradient before measurement, ensuring that the samples were dehydrated before imaging. Furthermore the use of a computer-generated grid would introduce error in these measurements.

With these limitations in mind, and with the aim of providing a comparison to native BrM tissue from our optical profile measurements of the polymer membrane discussed previously, it was decided that BrM thickness would be quantified through the use of the optical profilometer. This would allow sub-nanometre measurements of the thickness of BrM, which can be easily compared with our polymer membrane.

BrM-choroid samples were isolated from human donor eyes (it was not possible to isolate BrM only, therefore this method was carried out using BrM-choroid samples[46,29]). Samples were then dried briefly at 37^{o}C for 30 minutes to allow the PBS to evaporate whilst maintaining the level of sample hydration. Samples were then analysed on the optical profilometer (Fig. 27).

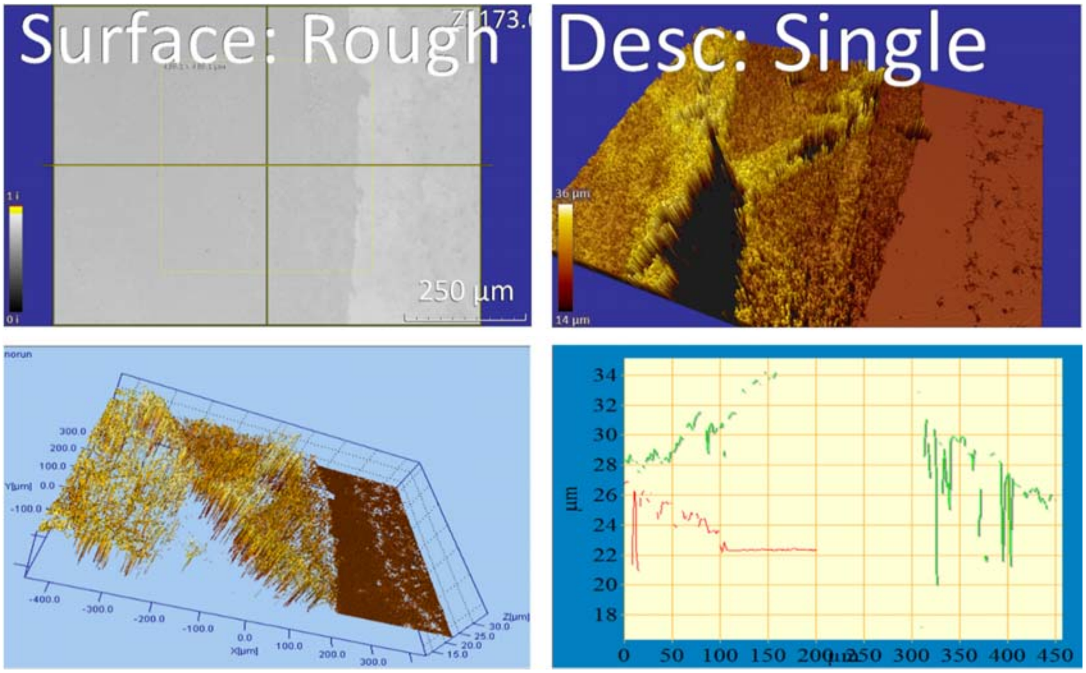

Figure 27: 3D optical profile spectra of native BrM-choroid showing (top left) a top-down view of the membrane (top right) the optical topography of BrM-choroid (bottom left) the generated 3D image of BrM-choroid and (bottom right) the resulting profile of BrM-choroid. Note – because of to the presence of 'black spots' within the optical profile, the optical profile and subsequent histogram were unable to be generated.

Whilst the optical profilometer was able to pick up the defining features of the membrane, notably the interaction between BrM-choroid and the glass slide upon which it rested, it could not generate a full optical profile because of 'black spots' in the 3D map. These were potentially the result of light emissions not reflecting back to the optical profilometer, either through absorption into the membrane or by distorting the interference bands through reduction or total removal of the sample beam, resulting in a 'gap' in the generated profile and producing an incomplete 3D map.

Therefore, in order to visualise the membrane on the optical profilometer with greater clarity, it was decided that the membrane would be stained to provide an enhanced reflection of the surface. Four different stains were applied to the BrM-choriod samples: Coomassie Brilliant Blue, which is a readily-used stain of proteins[208–211]; Haematoxylin, a stain used for treating samples for light microscopy[212–214]; Oil Red O, used by Curcio *et al* to stain membrane debris internal to the RPE basal lamina[215]; and Sudan Black, used to stain lipids[216]. These stained membranes would in theory remove distortion of the interference bands. Therefore, BrM-choroid samples were incubated for 20 minutes at room temperature, washed with H_2O and dried for 30 minutes at 37^{o}C to allow excess H_2O

to evaporate but maintain the sample hydration. Samples were then analysed on the optical profilometer (Fig. 28).

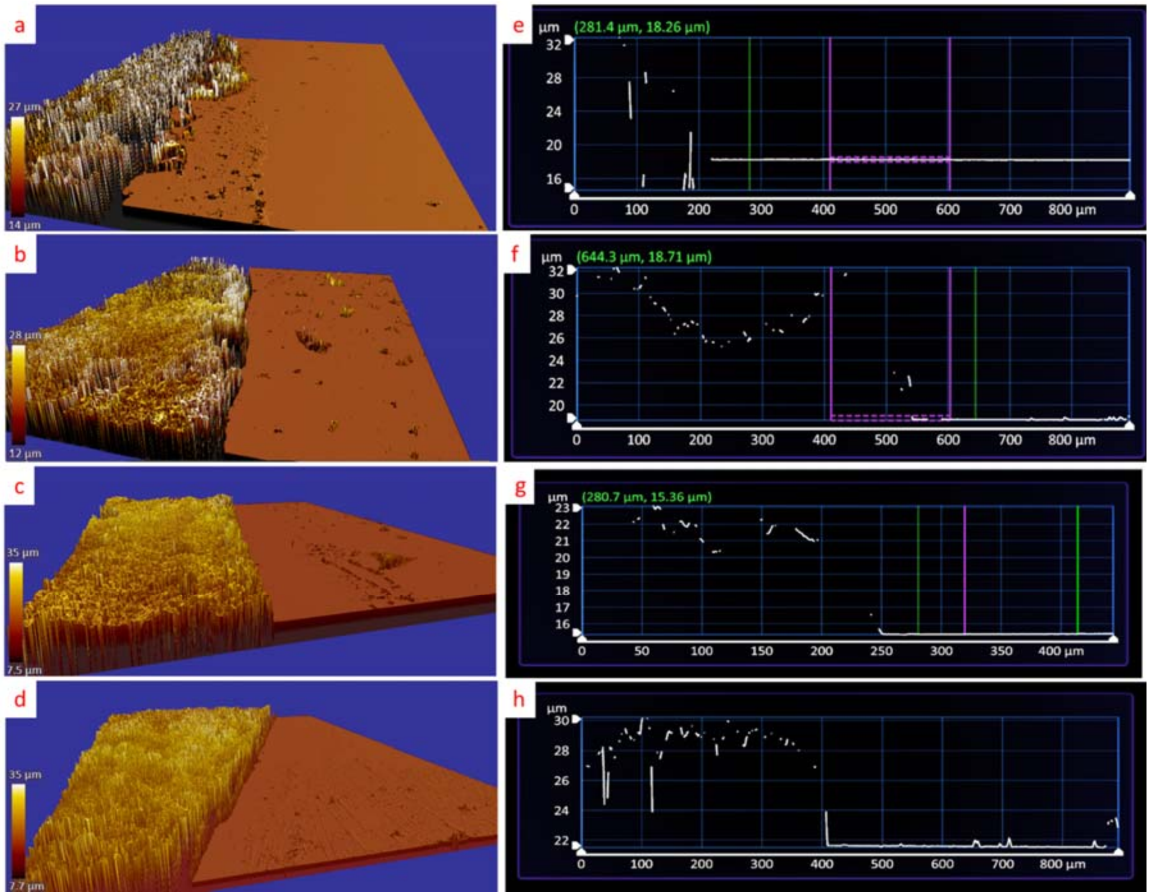

Figure 28: 3D optical profile spectra of stained native BrM-choroid, showing the topographical imagery of: (a) Coomassie Brilliant Blue-stained BrM-choroid; (b) Haematoxylin-stained BrM-choroid; (c) Oil Red O-stained BrM-choroid; (d) Sudan Black-stained BrM- choroid, with their corresponding optical profiles (e-h respectively). Note – the presence of black spots continue across all four dyed membranes, and whilst Oil Red O & Sudan Black appear to produce clean 3D spectra, their optical profiles indicate presence of incomplete spectra.

However, contrary to expectations, the results did not improve. As shown in Fig. 28 (a), Coomassie Brilliant Blue provided an inconsistent 3D spectrum which, when challenged to produce an optical profile (Fig. 28 e) showed the presence of black spots thereby preventing clean spectra. Sudan Black provided a 3D map as shown in Fig. 28 (d), and an optical profile was generated, as shown in Fig. 28 (h). However the profile plot of the stained BrM-choroid from which the thickness measurements could be taken did not provide a clear profile. Oil Red O also provided a clear 3D spectrum (Fig. 28 (c)), however the profile plot for the membrane was also sporadic and unclear (Fig. 28 (g)).

Haematoxylin provided a spectrum similar to that of Coomassie Brilliant Blue, Fig. 28 (b), and as a result a profile plot of the spectrum was inconclusive (Fig. 28 (f)).

In view of the failure of microscope-based stains to produce cleaner optical profiles *via* optical microscope-based techniques, an alternative method was sought. To improve the surface reflectivity of samples for SEM, it had been suggested in the literature that surface modification of cell and tissue by 'gold-sputtering' the surface increases the capability of this technique to image the sample[217]. In most cases with AFM, samples are gold-sputtered to allow easier analysis. Therefore, BrM-choroid samples were subjected to 2 x 2 minutes of gold sputtering, thereby applying an ultrathin layer of gold on the surface of BrM. These samples were then analysed *via* optical profilometry (Fig. 29).

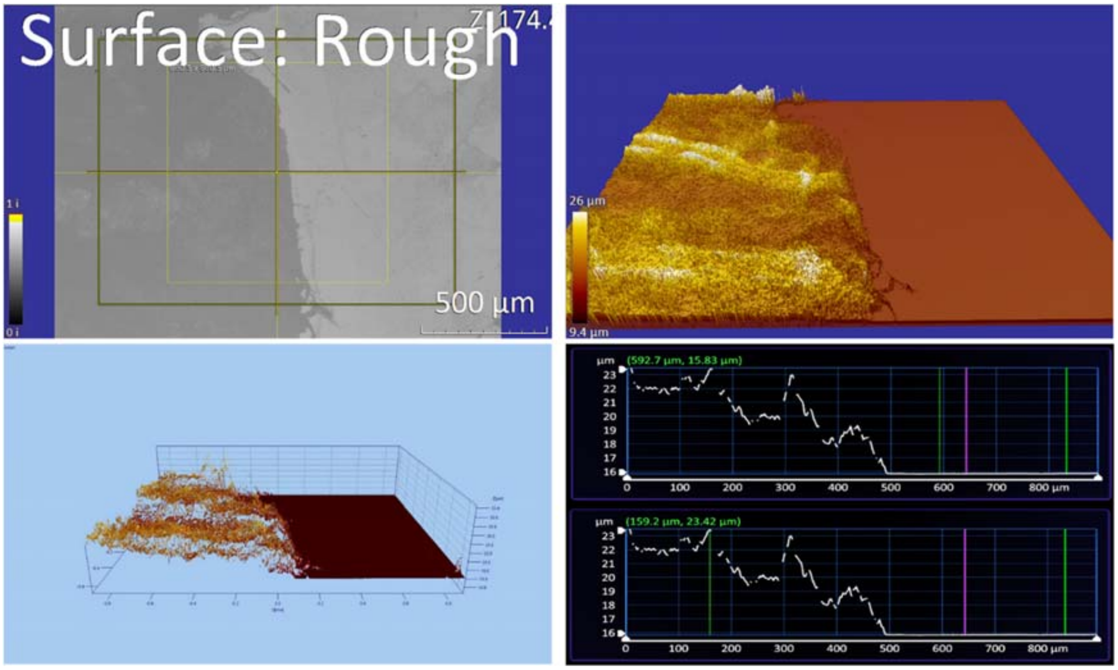

Figure 29: 3D optical profile spectra of gold-sputtered native BrM-choroid showing (top left) a top-down view of the membrane (top right) the optical topography of BrM-choroid (bottom left) the generated 3D image of BrM-choroid and (bottom right) the resulting profile of BrM-choroid. Note – due to the surface deposition of an ultrathin layer of gold, the optical profilometer was able to generate an optical profile of the membrane, allowing thickness measurements to be taken.

From the resulting data, it is clear that an ultrathin layer of gold deposited on the surface of BrM resulted in a cleaner and more accurate optical profile being generated, and allowed for a BrM-choroid thickness measurement to be taken. This produced a value for BrM-choroid thickness of 7.59 ± 0.04µm.

This measurement was taken from the central region of BrM-choroid, and therefore this process was repeated to confirm the effectiveness of the technique and to understand the thickness variability between central and peripheral regions of BrM (Table 2).

Sample Number	**Thickness Choroid-BrM Complex (µm)**			
	Central Region			**Peripheral Region**
2	10.08	16.26	17.39	16.06
3	11.48	15.73	15.45	16.79
4	11.98	12.93	15.07	16.66
5	9.54	10.95	14.99	17.32
6	8.72	12.56	12.42	13.16
7	8.14	14.18	15.55	16.29
8	10.04	15.30	17.09	17.21
9	9.66	14.12	14.68	16.05
10	10.01	14.31	13.83	16.88

Table 2: List of thickness measurements of BrM, showing the change in thickness across the membrane from the central region of BrM to its periphery.

These results indicate that the BrM-choroid complex increases in thickness as it nears the periphery of the membrane. This is expected, and correlates to the literature[218]. As the membrane goes from the macular to the periphery, the thickness increases, ranging from 8µm to 17µm.

3.4 Investigation into the reduction in thickness of the co-polymer mat

With the thickness measurement of BrM-choroid quantified, it was clear that the synthetic membrane which had been prepared was significantly thicker in comparison. In order for the co-polymer membrane to act as a suitable mimic to native BrM, its thickness needs to be as close as possible to that of the original membrane. A thicker membrane could also have profound complications *in vivo*, ranging from an increased retinal displacement during surgery, disturbance of the movement of solutes and metabolites *via* the membrane, to complications with the implantation process resulting in build-up within the surgical instrumentation. Therefore, an investigation into the reduction of the thickness of the membrane was carried out.

Reducing the thickness of the membrane without compromising the existing properties was potentially challenging. Simply reducing the amount of polymer solution applied during the electrospinning process would reduce the thickness of the membrane, but maintain the pore sizes, leading to an increase in the diffusion rate and a reduction in the membrane's ability to act as a barrier between the choriocapillaris and RPE[219]. A reduction in the concentration of the polymer solution would also cause a process known as 'electrospraying', where the surface tension forces overcome the chain entanglement and droplets form as opposed to fibres[220]. Alternatively, an increase in polymer concentration will result in an increase in fibre diameter[221]. However, the thickness of the membrane could be reduced without compromising the existing properties by reducing the individual fibre thickness. An overall reduction in the fibre diameter would decrease the membrane thickness, but would maintain the density of the fibres and theoretically maintain the existing properties. Therefore, it was decided that the amount and concentration of the polymer solution would be maintained, but the diameter of the fibres would be reduced by variation of the electrospinning parameters.

Investigations into the effect of electrospinning parameters on the diameter and the morphology of the fibres have been reported by several research groups.[130,222,223] Major factors that control the diameter of the fibres include: (i) the distance to the collector; (ii) the type of solvent used; (iii) the conductivity of the solvent; (iv) the voltage applied to the solution; and (v) the flow rate of the solution. Cramariuc *et al* carried out a comprehensive study into the effect of the electrospinning parameters on the fibre diameter using polyetherimide (PEI)[130]. They report that the average fibre diameter for PEI diminished when: (i) the flow rate of the solution was reduced; (ii) there was an increase in the voltage applied to the solution; and (iii) the distance to the collector from the needle is reduced. This is further described by Fridrikh *et al*, who generated an analytical model that is based on the differences between surface tension of the solution and the electrostatic charge repulsion in the jet[223] (Equation 1).

$$D = \left(\gamma c \frac{Q^2}{I^2} \frac{2}{\pi(2 \ln \left(\frac{l}{d} - 3 \right))} \right)^{\frac{1}{3}}$$

Equation 1: Analytical model of the effect of electrospinning parameters on the fibre thickness. D = diameter of fibre; γ = surface tension of the solution; Q = flow rate of the solution; I = current across needle; L = initial jet length; d = diameter of the nozzle[223].

This equation determines the diameter of the fibres, and takes into account the flow rate, the current, the diameter of the nozzle and the surface tension of the solution. It states that by increasing the current and by decreasing the flow rate, the fibre diameter will be reduced. There are some flaws in this model, notably the volatility of the solvents and the effect of changing the co-polymer cocktail. However, this model is in agreement with the work carried out by Cramariuc *et al*, and therefore the defining parameters listed in this model (flow rate; voltage across needle) were investigated as a potential method for reducing the thickness of the synthesised P(MMA:PEGM) co-polymer membrane.

The standard flow rate and voltage used to prepare the current generation of electrospun synthetic membranes were 9.5ml/h & 15kV respectively. This combination provided an electrospun membrane with an individual fibre diameter of ≈ 9-10µm (Fig. 30). Whilst producing a desired membrane with good macromolecular diffusion control & biocompatibility, this is ultimately too thick since the thickness of native BrM is thinner than the individual fibres present in this membrane.

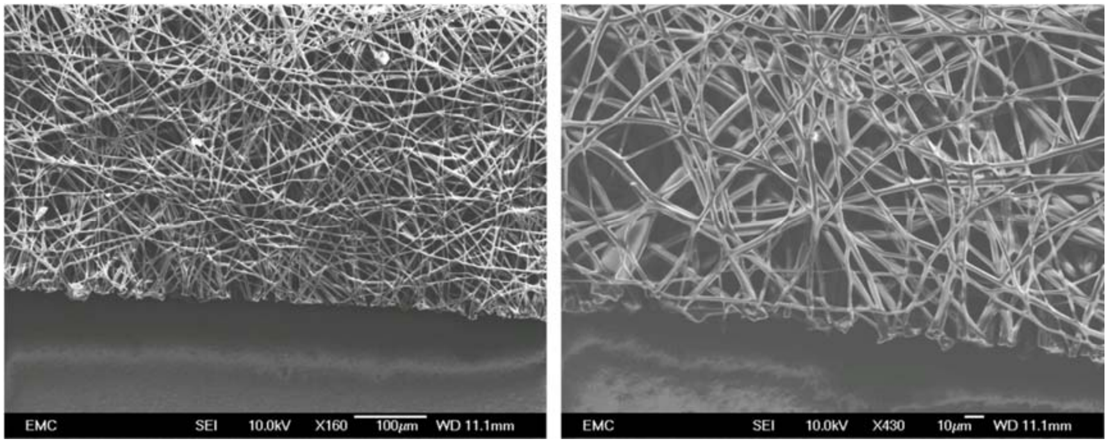

Figure 30: SEM images of the first generation of polymer substrates, showing the topography of the membrane at (left) x160 and (right) x430 magnification. Note – the thickness of the individual fibres shown clearly on the SEM image at x430 magnification is around 9-10µm.

Therefore, our experiments started by monitoring the effect of the flow rate on the thickness on the fibres (Table 3). Observations to note included that an increase in the flow rate of (MMA:PEGM) not only increased the thickness of the fibres (as a result of an increase in the amount of solution available for electrospinning) but it also increased the chance of polymeric beads forming throughout the membrane (Fig. 31).

Polymer mat sample	Voltage (kV)	Flow Rate (ml/hr)	Distance to the collector (cm)	Average fibre thickness (µm)	Presence of polymeric beads	Obvious signs of fibre mat breakages
1	15	0.05	15	0.5-2	Yes	Yes
2	15	0.1	15	1.5-3	Yes	No
3	15	0.2	15	1.5-3	Yes	No
4	15	0.5	15	1.5-3	Yes	No
5	15	1	15	3-5	Yes	Yes

Table 3: Results of the initial investigation into the effect of the flow rate on the individual fibre thickness. Whilst the voltage was initially quite low, the influence of the flow rate on the fibre thickness is clear, showing that a reduced flow rate reduces the average fibre thickness.

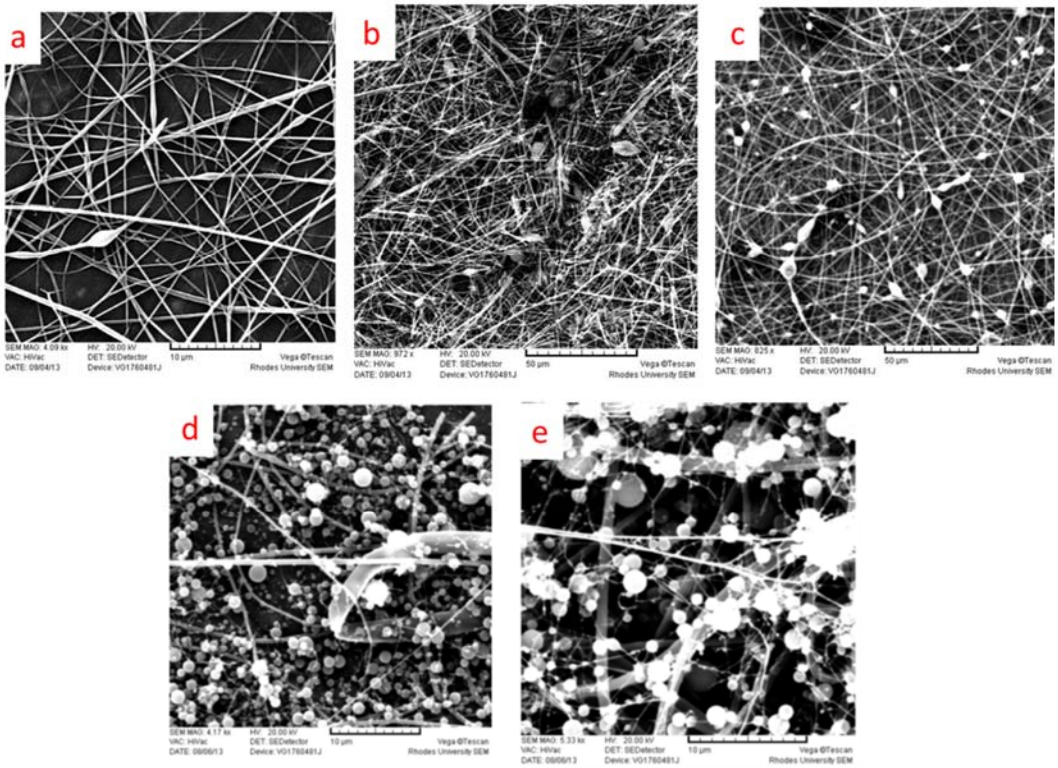

Figure 31: SEM images of electrospun polymer membranes showing the fluctuation in fibre thickness when the flow rate is at (a) 0.05ml/h (b) 0.1ml/h (c) 0.2ml/h (d) 0.5ml/h and (e) 1ml/h. What is also interesting to note is the apparent increase in the number of polymeric beads when the flow rate is increased as shown through comparison of a-e.

Polymeric beads are the result of a build-up on polymer solution that hasn't formed a spinneret. This is a result of a greater volume of solution that is 'drawn away' from the needle. There are many factors that influence the formation of these beads, including voltage & flow rate, with the polymeric cocktail also influencing the effect of bead formation (because of the relative viscosity of the solution)[224,225]. These beads are undesirable as they will have an effect on the primary properties of the membrane (porosity; strength; thickness), and it is critical to produce fibres of near uniformity so that the process is reproducible.

With this result, the effect on the voltage applied to the solution was then investigated, whilst also determining the effect of an increased flow rate & increased voltage on the fibres produced (Table 4).

Polymer mat sample	Voltage (kV)	Flow Rate (ml/hr)	Distance to the collector (cm)	Average fibre thickness (µm)	Presence of polymeric beads	Signs of fibre mat breakages
6	15	0.05	15	0.5-2	Yes	No
7	20	0.05	15	0.1-1.5	Yes	No
8	25	0.05	15	0.1-1	No	No
9	30	0.05	15	0.1-1	No	Yes
10	35	0.05	15	0.1-0.8	No	No
11	15	0.1	15	1.5-3	No	Yes
12	20	0.1	15	4-2.5	Yes	No
13	25	0.1	15	0.1-2	Yes	No
14	30	0.1	15	0.1-1.5	Yes	No
15	35	0.1	15	0.1-1.5	Yes	No
16	15	0.2	15	0.5-3	Yes	No
17	20	0.2	15	1-3	Yes	No
18	25	0.2	15	0.3-2.5	Yes	No
19	30	0.2	15	0.1-1.5	Yes	No
20	35	0.2	15	0.1-1	Yes	No
21	15	0.5	15	0.5-3	Yes	No
22	20	0.5	15	0.5-2	Yes	No
23	25	0.5	15	0.1-1.5	Yes	No
24	30	0.5	15	0.1-1.5	Yes	No
25	35	0.5	15	0.1-0.5	Yes	No

Table 4: Summary of the investigations into the effect of an increase in voltage and an increase in flow rate on the thickness of the electrospun polymer fibres, with the highlighted row (purple) showing the ideal conditions to produce sub-micron fibre thickness.

This investigation allowed a better understanding into the voltage effects on the fibre thickness, and how it may influence the presence of forming polymeric beads. As indicated in Table 4, it is clear that at a low flow rate and a high voltage, it is possible to produce a membrane that is free from polymeric beads, with an average fibre thickness of 0.1-0.8µm. The voltage supplied to the tip of the needle and the resultant electric field have an influence in the stretching of the jet produced, resulting in a greater stretching of the solution as a result of the stronger electric field. This will therefore ensure the reduction of the diameter of the fibres[226–228].

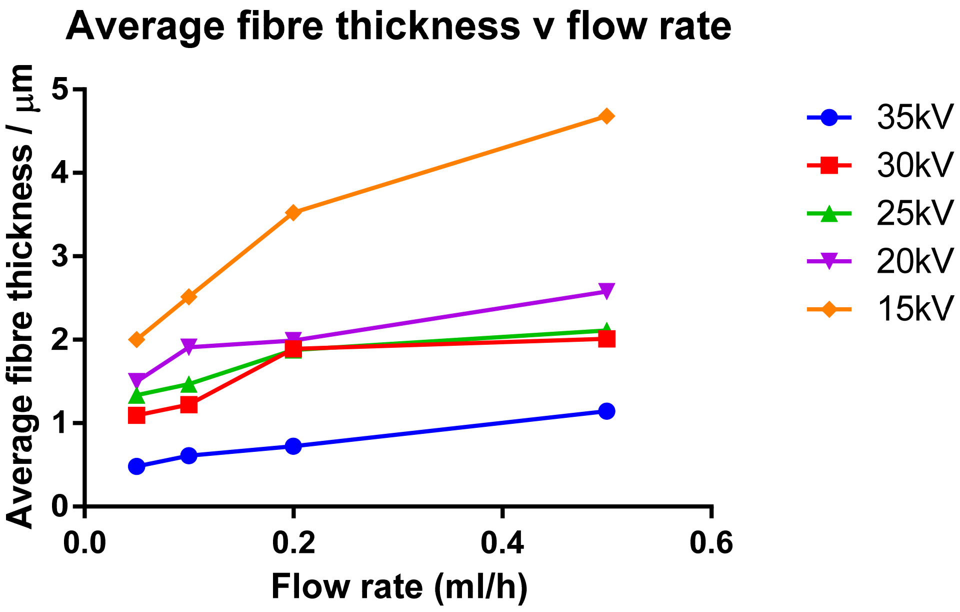

Figure 32: Graph showing the effect of flow rate on the thickness of the individual fibres. By increasing the voltage and decreasing the flow rate, the average fibre thickness has been reduced significantly.

With this result, the thickness of the overall fibre mat was then analysed by optical profilometer to quantify the effect of the reduction of the polymer fibre diameter on the entire polymer mat thickness (Fig. 33).

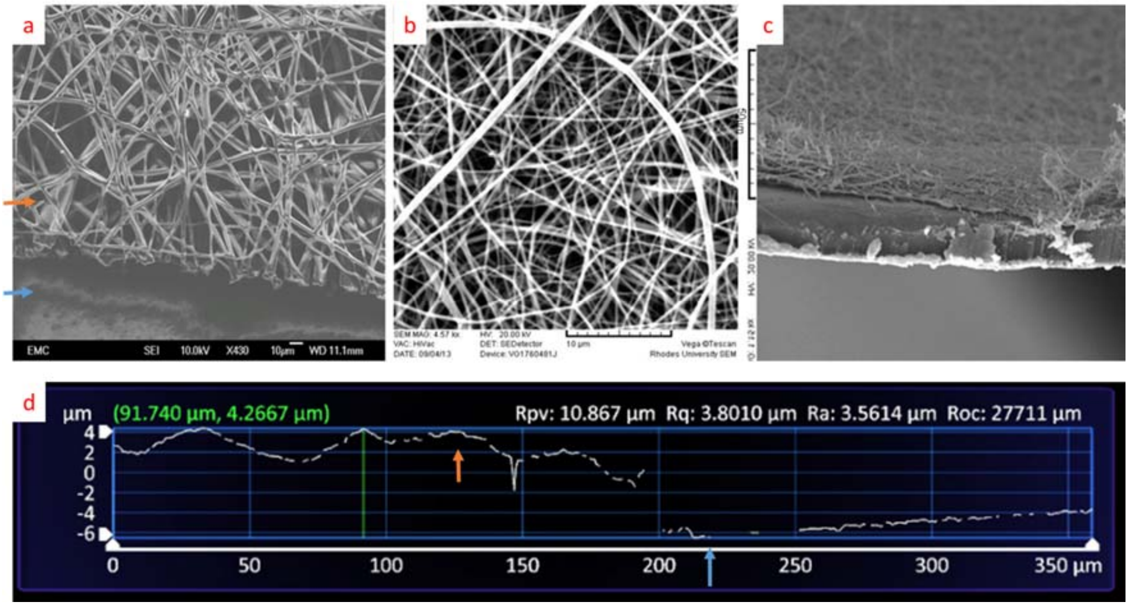

Figure 33: The result of the thinning of the fibres, showing: (a) a representative topographical SEM image of the first generation of polymer fibres with an average fibre thickness of 9-10μm; (b) a representative topographical SEM image of the second generation of polymer fibres (Sample 10) with an average fibre thickness of 0.1-0.8μm; (c) a side-on SEM image of the second generation of polymer fibres, with the membrane resting on a sheet of foil; and (d) the optical profile of Sample 10, showing a membrane thickness of 12.2667μm (orange arrow indicates the membrane and blue arrow indicates the base of the sample).

Through the thinning of the individual fibres whilst maintaining the interwoven nature of the membrane we successfully reduced the thickness of the membrane from 51 ± 3μm to 12μm.

3.5 Characterising additional biophysical properties of the new generation of membranes

By reducing the flow rate and increasing the voltage of the electrospinning process, the thickness of the individual polymer fibres and ultimately the thickness of the membrane was reduced. This allowed for a more accurate mimic of BrM, whilst maintaining the desired interwoven fibrous matrix produced *via* electrospinning.

These new generation of membranes were then tested for their biocompatibility, tensile strength & diffusional capabilities to quantify and understand any changes in the biophysical properties of the membrane created by the thinning of the matrix.

In order to assess the tensile strength of the matrix, the mechanical strength and maximal strain properties of the membrane were investigated. Native human BrM is composed of predominately Type IV collagen & elastin[31,32,229], which combined with the interwoven fibrous nature of the membrane gives a strong & flexible matrix. This allows for full RPE attachment and provides structural resistance to the choriocapillaris pulse & changes in blood volume[43,51]. Therefore, in order for the synthetic variant of BrM to withstand the choriocapillaris pulse and the surgical implantation procedure, the membrane is required to be similar, if not greater, in strength to native BrM. To quantify this, comparative stress-strain assays on both native BrM and the synthesised membranes were required.

Through the use of a DEBEN microtest tensile tester 300N, the two artificial BrM samples (1st generation – 51 ± 3μm; 2nd generation - 12μm) and native human BrM-choroid samples were mounted horizontally and stretched (Fig. 34). The quantification of the prosthetic BrM thickness allowed an understanding into the tensile strength, looking at: (i) the Young's modulus (the individual fibre strength); (ii) the stress at failure (the maximum amount of stress that can be applied to the membrane before failure); (iii) the yield strength (the amount of resistance the membrane provides to the stress); and (iv) the overall calculated toughness of the material (the strength of the fibrous material).

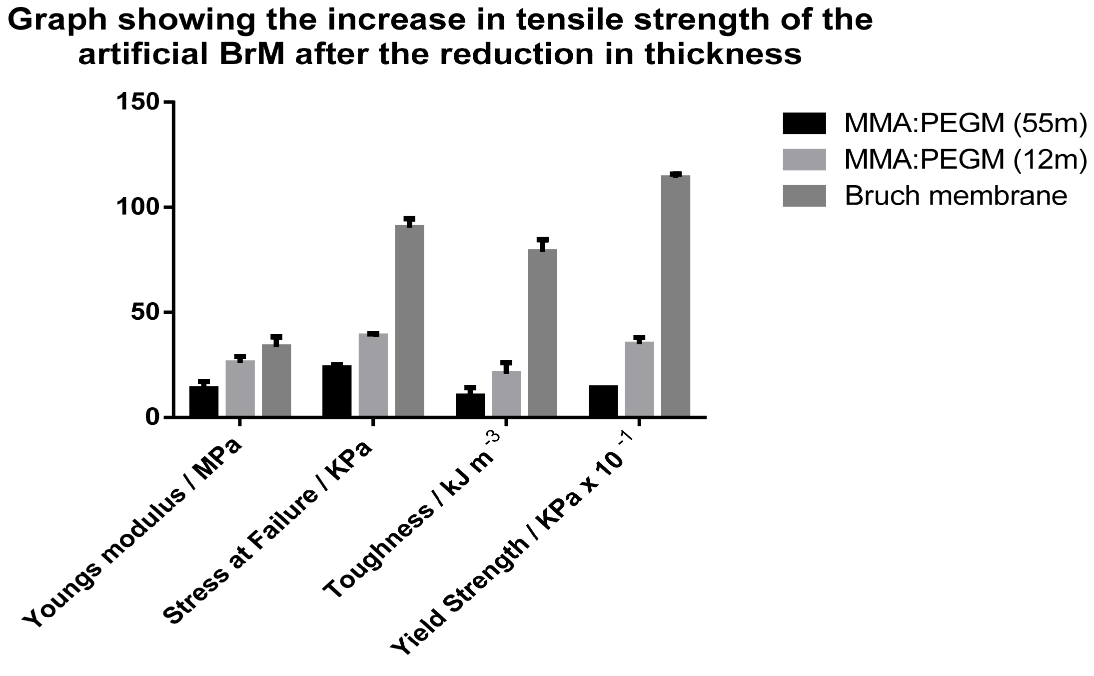

Figure 34: Graph showing the increase in all four tensile strength parameters as a result of the thinning of the artificial BrM thickness. Young's modulus increased from 13.6 ± 3.65 MPa (1st generation of membranes – 51 ± 3μm) to 26.0 ± 3.14 MPa (2nd generation of membranes - 12μm). The stress at failure increased from 22.0 ± 3.00 KPa to 38.7 ± 1.20 KPa, a significant increase of p = 0.0088. The calculated toughness of the material increased from 10.2 ± 3.98 kJ m^{-3} to 20.9 ± 5.24 kJ m^{-3}. The yield strength of the artificial BrM also increased, from 1.4 ± 0.01 MPa to 3.48 ± 0.32 MPa, a significant increase of p=0.0125.

The application of stress and strain upon the membrane has allowed a comparison to be made between the differing generations of synthetic membranes and native BrM. What was observed was an increase in all four tensile strength parameters after the reduction in fibre thickness and subsequent membrane thickness, aligning it more closely to native human BrM.

With the mechanical strength quantified and analysed, it was important to test the diffusion of the artificial membrane. As BrM is primarily a diffusion barrier between the photoreceptors, RPE and the choriocapillaris[230], it is fundamentally important to ensure that the new thinner membranes provided a macromolecular barrier. Work on testing the diffusional properties of native BrM have been reported by Hussain *et al*[46]. It was found that diffusion across BrM decreases with age, using a modified Ussings chamber with two reservoirs (Fig. 35). One reservoir was filled with a solution of fluorescein isothiocyanate labelled dextran and the other with PBS.

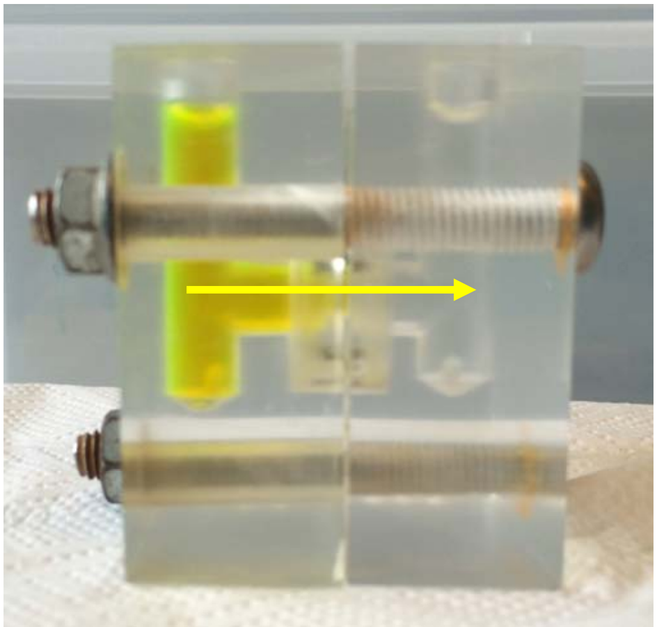

Figure 35: Picture of the modified Ussings chamber, with Dextran (yellow) in the left chamber, PBS (grey) in the right chamber and the polymer membrane inside the membrane casing (centre). Flow of dextran shown by arrow (yellow), with the rate measured by colorimeter.

Samples were taken routinely from both chambers and the change in fluorescence (casued by the diffusion of Dextran from the left chamber to the right chamber *via* the membrane) was analysed by a colorimeter.

The effect of the thinning of the membrane on the diffusional properties was analysed *via* this method and the results of this are shown in Fig. 36.

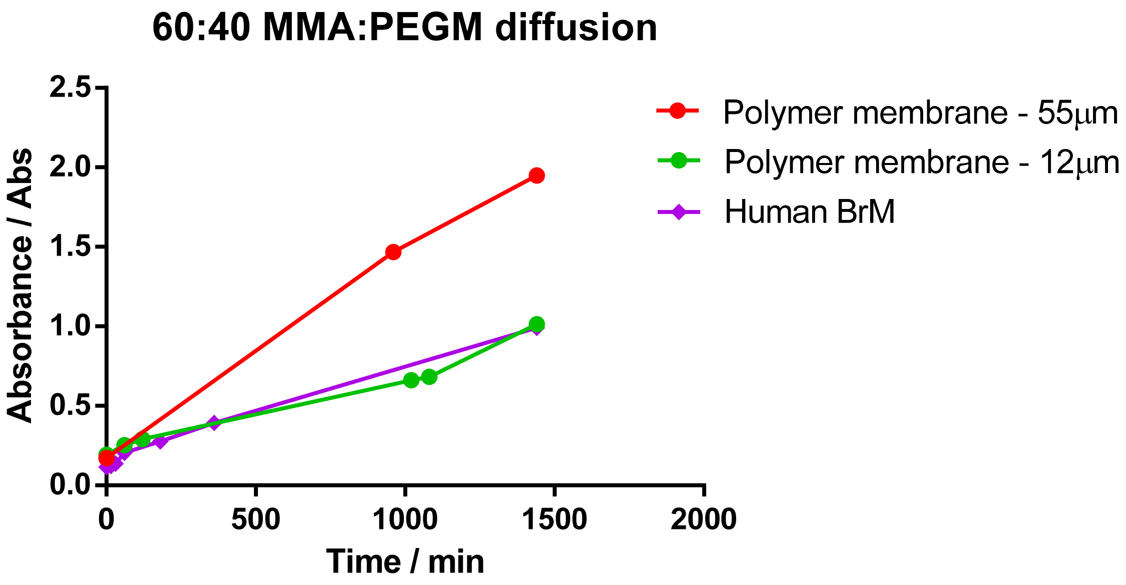

Figure 36: Graph showing the increase in presence of Dextran over a period of 24 hours. The thicker version of the membrane (red) is shown to provide a poorer barrier to Dextran when compared to the thinner variety of co-polymer membrane (green), aligning it with native BrM (purple).

From these experiments, it was clear that the reduction of the fibre diameter of the membrane had a profound effect on its porosity. The membrane had reduced the flow of Dextran through its pores, and as a result had closely aligned with the diffusional data from native BrM. This was potentially the result of the reduction of the pore sizes, arriving from the tighter weave of the new membrane and the maintaining of the interwoven nature of the membrane whilst reducing the fibre diameter. This allowed for a more compact and tightly interwoven matrix.

In order to assess the response of RPE to the new thinner membranes, an immortalised human RPE cell line (ARPE-19) was seeded onto the fibrous mats. Samples were seeded in triplicate, with membranes with no ARPE-19 cells as a negative control and ARPE-19 cells in a 12 well tissue culture plate as a positive control to measure cell proliferation. Samples were maintained under cell culture conditions for a period of 4 weeks, with control and seeded samples being maintained in the same culture environment.

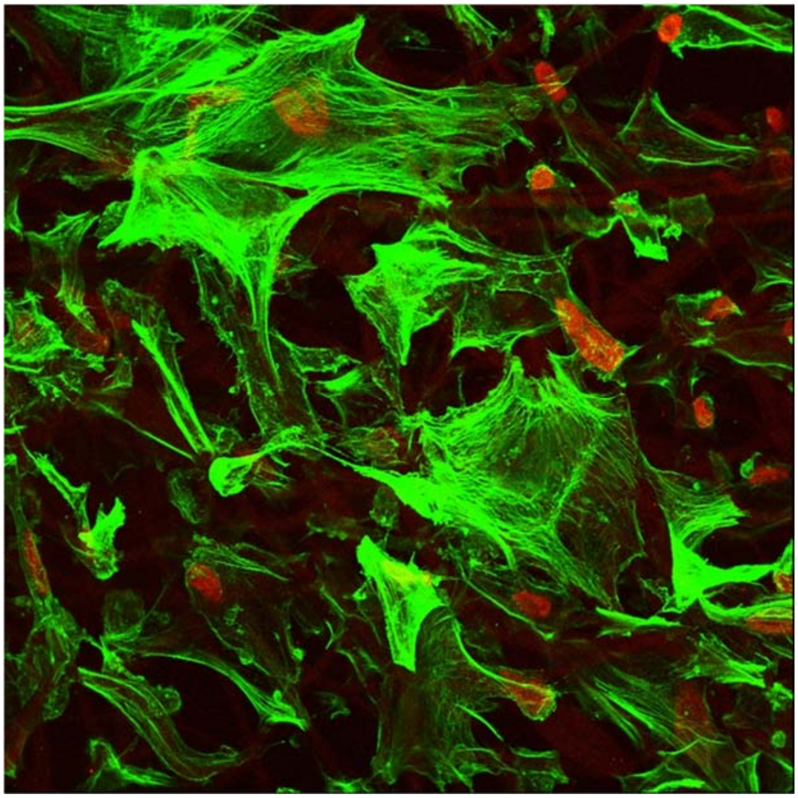

Figure 37: Representative sample image showing immunofluorescence of ARPE-19 cells on the surface of the thinner membrane, highlighting the extent of the ARPE-19 proliferation. Actin filaments (green) and cell nuclei (red) are stained with Phalloidin and DAPI respectively.

Immunofluorescence was carried out to confirm that the ARPE-19 cells were successfully seeded onto the polymer membranes. After 2 weeks in cell culture, the first triplicate of samples were fixed and probed for 4’,6-diamino-2-phenylindole (DAPI) and Phalloidin (specific markers for cell nuclei and actin filaments respectively) to investigate whether the ARPE-19 cell line had successfully proliferated on the surface of the membrane (Fig. 37).

Once it had been established that the ARPE-19 cell line had been seeded successfully and had proliferated on the artificial BrM, it was essential to investigate the cell viability of the samples *via* a lactate dehydrogenase (LDH) assay. The presence of LDH in the test medium is a sign of a compromised plasma membrane, and is therefore indicative of cell stability and plasma membrane integrity[231] (Fig. 38).

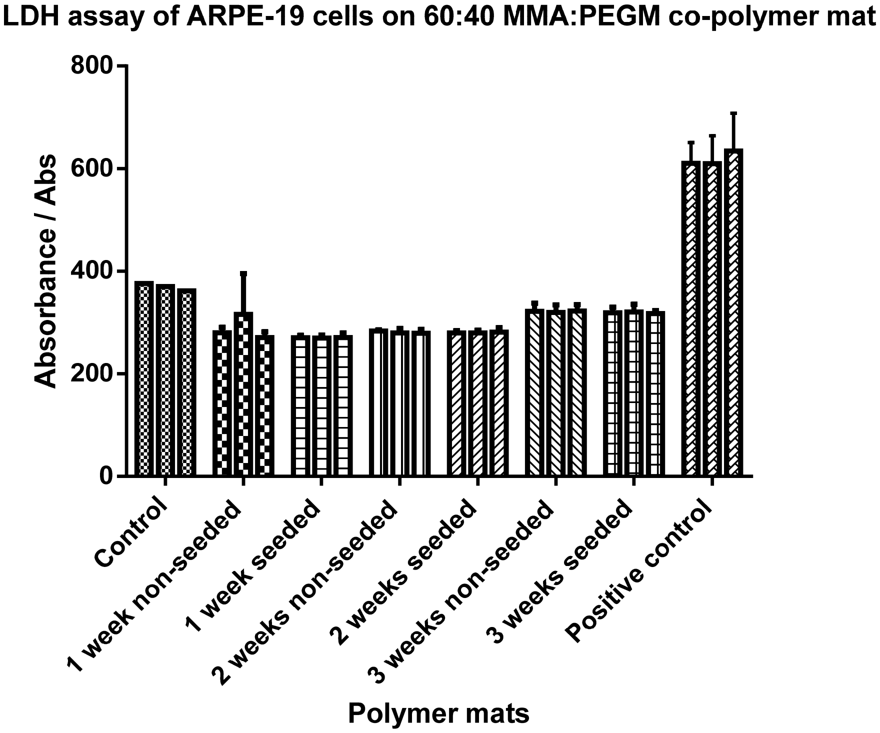

Figure 38: LDH assay of ARPE-19 cells on the co-polymer membrane, showing the low levels of LDH in the culture medium of ARPE-19 cell seeded membranes, membranes without ARPE-19 cells and a positive control.

The results of this assay indicated that the ARPE-19 cells retained their viability once established on the co-polymer membrane.

The result of reducing the fibre diameter had led to a co-polymer membrane that was thinner, biocompatible, mechanically stronger and less diffuse, allowing for a more comparable mimic to native BrM.

Chapter 4: Quantification of RPE functionality on the artificial BrM

4.1 General introduction

This chapter describes the work carried out to assess the suitability of the improved BrM scaffold (the second generation membrane) outlined in the previous chapter. To briefly summarise, the biophysical charcteristics of this BrM scaffold is similar in many ways to native BrM. Consequently, our ex-*vivo* modelling studies should be highly informative; providing an accurate assessment of its suitability for potential downstream clinical applications.

We opted to test its suitability by using primary adult mouse RPE cells, which have been shown to be superior in many respects to the widely used ARPE-19 cell. The latter is an immortalised cell-line that has important genotypic and phenotypic differences which may unfavourably impact on our assessment of this BrM scaffold.

Whilst the use of an ARPE-19 cell line is generally acceptable as a biocompatibility assay; indeed ARPE-19 cells arose spontaneously from a primary RPE cell culture and as such display common RPE morphological features (hexagonal cobblestone layer & polarisation)[232], it remains to be seen how ARPE-19 cells are comparable in terms of the overall functional properties[233]. An ARPE-19 cell line does not provide the full range of morphological features found in healthy RPE *in vivo*, with the spontaneously immortalised RPE cells unable to produce uniformly abundant apical microvilli[155,159]. Alongside this, ARPE-19 cells have been shown to display differences in both ion transport mechanisms in diffusional studies[160–163] and in α5 integrin expression[234], thereby differentiating it futher from native RPE.

Primary human RPE cells would have been a more suitable choice over primary murine RPE, however the limited availability of human donor eyes made the primary human RPE difficult to obtain and the apparent finite lifespan of the RPE cells would not allow long-term cultures to be established[235,236].

Therefore, to achieve a greater understanding of the co-polymer matrix's ability to host a RPE monolayer on its surface, primary murine RPE cells were used, investigating the BrM mimetic's capability in promoting RPE proliferation, attachment to the matrix, and key physiological roles (polarity, secretion of growth factors, photoreceptor outer segment phagocytosis and barrier formation).

4.2 Culture and seeding of a primary murine RPE layer on co-polymer fibres

Cell culture models of RPE play an important role in gaining knowledge about native tissue and its behaviour. Much of our current understanding about RPE function has arisen from *in vitro* studies using different RPE cell lines. Key RPE physiological properties, such as work done by Joseph *et al* on the apical and basal membrane ion transport mechanisms, were characterised by primary bovine RPE cultures[237]. Stamer *et al* found that RPE transepithelial water movement was facilitated by the expression of an Aquaporin-1 integral membrane protein, characterised by a primary human RPE culture[238]. Studies into the role of vascular endothelial growth factor (VEGF) on the survival and maintenance of RPE integrity was assisted by the use of APRE-19 cultures[53]. These studies have allowed the manipulation and improvement to potential extracellular matrices to enhance RPE attachment and proliferation.

The majority of these studies were carried out through the use of a primary RPE cell line. Primary RPE cell lines are cultures of RPE cells isolated directly from the desired species, either from the initial material (i.e. eyes from culled mice) or from certain research laboratories or 'eye banks', and are then maintained in cell culture laboratories. Primary cultures of RPE cells from various species have been shown to retain normal physiological functions, including polarisation[239], transport of retinoids and phagocytosis of photoreceptor outer segments (POS)[177]. These cultured RPE cells closely mimic cells in native tissue and can provide a clear understanding of the precise behaviour of RPE on synthetic membranes.

With this in mind, it was reasoned that to provide a clearer understanding of the RPE cell behaviour on the artificial BrM scaffold, a primary RPE model would be preferable to using cell-lines. Murine RPE cells were used for this model as established murine RPE cultures display characteristics which accurately represent the *in vivo* behaviour of the RPE, such as a polarised membrane, typical cobble-stone like morphology and apical microvilli[240–243]. Alongside this, mice have been widely used for generating models that simulate human AMD features for investigating the pathogenesis, treatment and prevention of the disease. Since 1924, when the first inherited form of retinal degeneration was identified, the mouse has been the main model organism for the study of diseases involving retinal degeneration[244,245].

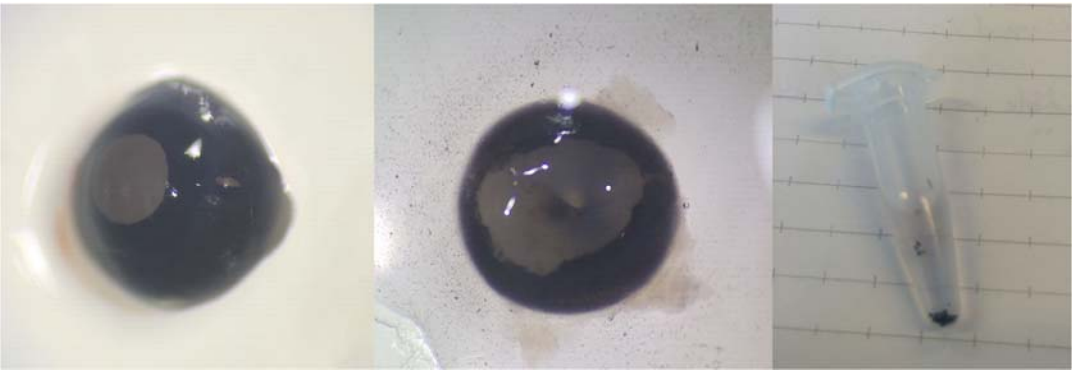

Figure 39: Photographic images showing (left) a mouse eye with an insicion made in line with the ciliary body (orange arrow), (middle) a mouse eye with the anterior segment removed and (right) the isolated retinal pigment epithelium cells in PBS.

Primary murine RPE cells were harvested from C57 BL/6 mice between P8-10 and cultured as previously described (see Chapter 2.5.1). In brief, after removing the anterior segment of the eye and retina, the eyecups were transferred to a petri dish and the RPE carefully peeled away (Fig. 39). After RPE incubation in trypsin-EDTA, the cell suspension was seeded into culture dishes with primary RPE culture medium. RPE layer was then allowed to establish (2-3 weeks) before transferring to polymer matrix samples in the culture medium. It was essential that multiple passages of murine RPE cells were avoided, as differentiated RPE cells from multiple passages loose their specialised properties (such as RPE-specific markers)[246].

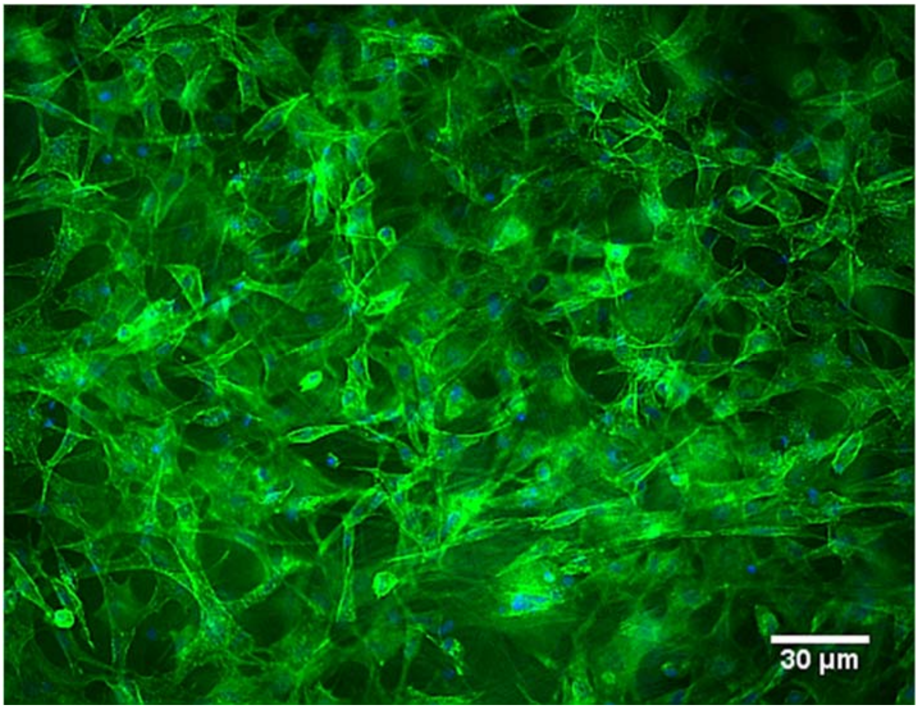

Figure 40: Representative fluorescent image of primary murine RPE cells (after 2 weeks post-seeding) on the surface of the co-polymer membrane, highlighting the extent of RPE cell proliferation. Cell nuclei labelled with DAPI (blue) and actin filaments tagged with phalloidin (green).

After a period of 2 weeks, the RPE-polymer matrix was analysed for RPE cell proliferation on the membrane. Immunofluorescent tagging for cell nuclei and actin filaments using DAPI and phalloidin respectively was carried out on 2 week samples, with fluorescent microscopy used to image the RPE-polymer matrix (Fig. 40).

The extent of the RPE cell proliferation was shown by the spread of actin filaments across the surface of the co-polymer membrane. Long term cultures (2 and 5 month cultures) were also analysed *via* the same method to understand the extent of long-term RPE cell proliferation (Fig. 41).

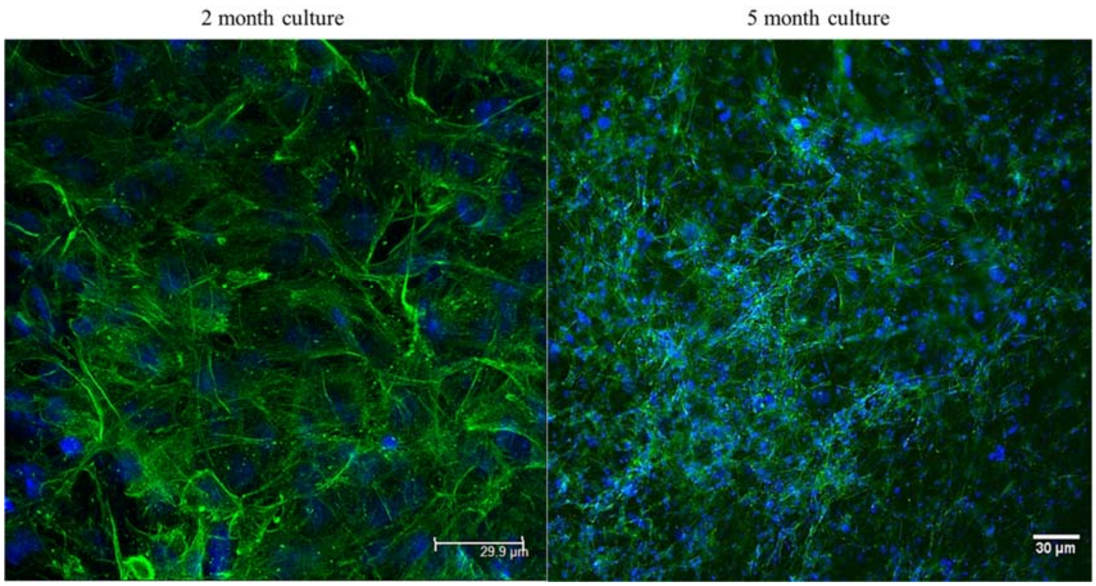

Figure 41: Representative confocal immunofluorescence images showing a 2 month primary murine retinal pigment epithelium (RPE) culture (left) and a 5 month RPE culture (right), showing proliferation of the epithelia on the surface of the polymer matrix. RPE cell nuclei (blue, DAPI) and actin filaments (green, phalloidin).

After 4 weeks, the RPE-polymer matrix was further analysed for RPE cell proliferation on the co-polymer membrane through immunofluorescent staining, with orthogonal sections taken to understand the distribution on the surface of the polymer matrix (Fig. 42).

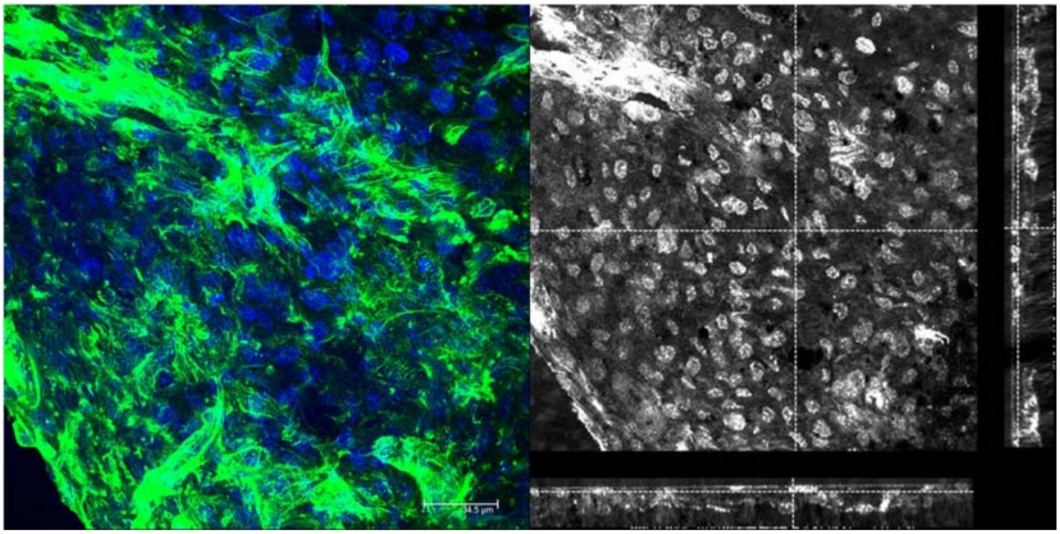

Figure 42: Representative confocal immunofluorescence images showing a 4 week primary murine retinal pigment epithelium (RPE) culture showing (left, scale bar 34.5μm) the extent of proliferation on the surface of the polymer matrix and (right) an orthogonal section highlighting the predominantly apical arrangement of the RPE layer. RPE cell nuclei (Blue, DAPI) and actin filaments (Green, phalloidin).

Whilst the RPE proliferation did not appear to diminish, it was also interesting to note the predominantly apical distribution seen on the RPE-polymer matrix. A longer term culture (8 weeks) was also analysed *via* immunofluorescence to monitor any changes in the distribution and RPE behaviour on the co-polymer membrane (Fig. 43), with similar observations made in the apical distribution of the RPE layer.

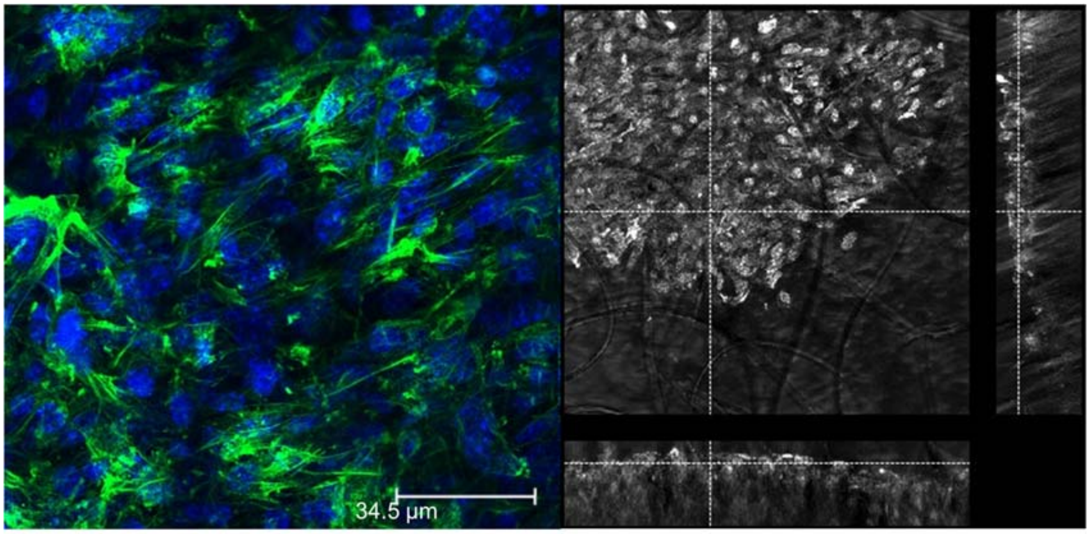

Figure 43: Representative confocal immunofluorescence images showing an 8 week primary murine retinal pigment epithelium (RPE) culture highlighting (left) the extent of the epithelial proliferation on the surface of the polymer matrix and (right) an orthogonal section highlighting the predominantly apical arrangement of the RPE layer. RPE cell nuclei (Blue, DAPI) and actin filaments (Green, phalloidin).

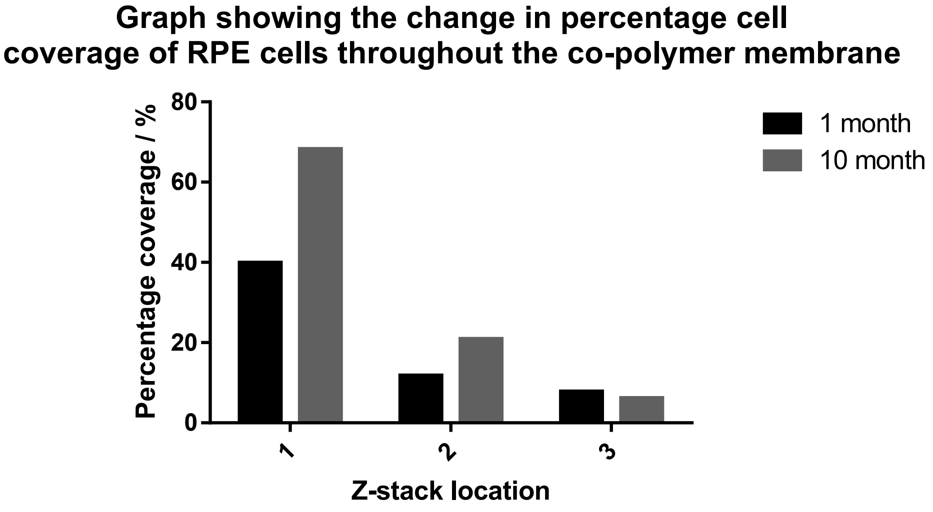

Figure 44: Graph showing the change in RPE cell distribution on the co-polymer membrane from Z-stack layer 1 (within the cell layer) to Z-stack layer 3 (within the co-polymer matrix). This analysis shows that the distribution of RPE cells becomes more apical and a reduced population within the porous co-polymer matrix.

Investigations into the apical distribution of the RPE layer were then carried out over a period of 10 months, to assess how the monolayer developed over time. Confocal microscopy was used to analyse the distribution of RPE cell nuclei (stained with DAPI) and actin filaments (stained with Phalloidin) across the surface of the artificial BrM. Images were taken at three points on the Z-stack of the RPE-polymer matrix orthogonal sections and through the use of Image J to select and measure areas based on colour (highlighting the cell nuclei and actin filaments and forming an understanding into the cell cytoskeletal network and artificial BrM surface coverage), the presence of RPE cell nuclei and actin filaments was quantified as a percentage coverage across the entire image over 5 differing time points at three locations on the co-polymer matrix (Z-stack sections 1,2 and 3), allowing a comparison to be made based upon the presence of RPE cell nuclei & actin filaments in the Z-stack location between 1 month and 10 month cultures (Fig. 44). The investigation showed an increase in the percentage of RPE cell nuclei and actin filament arrangement on the surface of the membrane (Z-stack sections 1 & 2) and a decrease in the percentage of RPE cells delving into the porous membrane (Z-stack section 3) over a period of 10 months (Fig. 45).

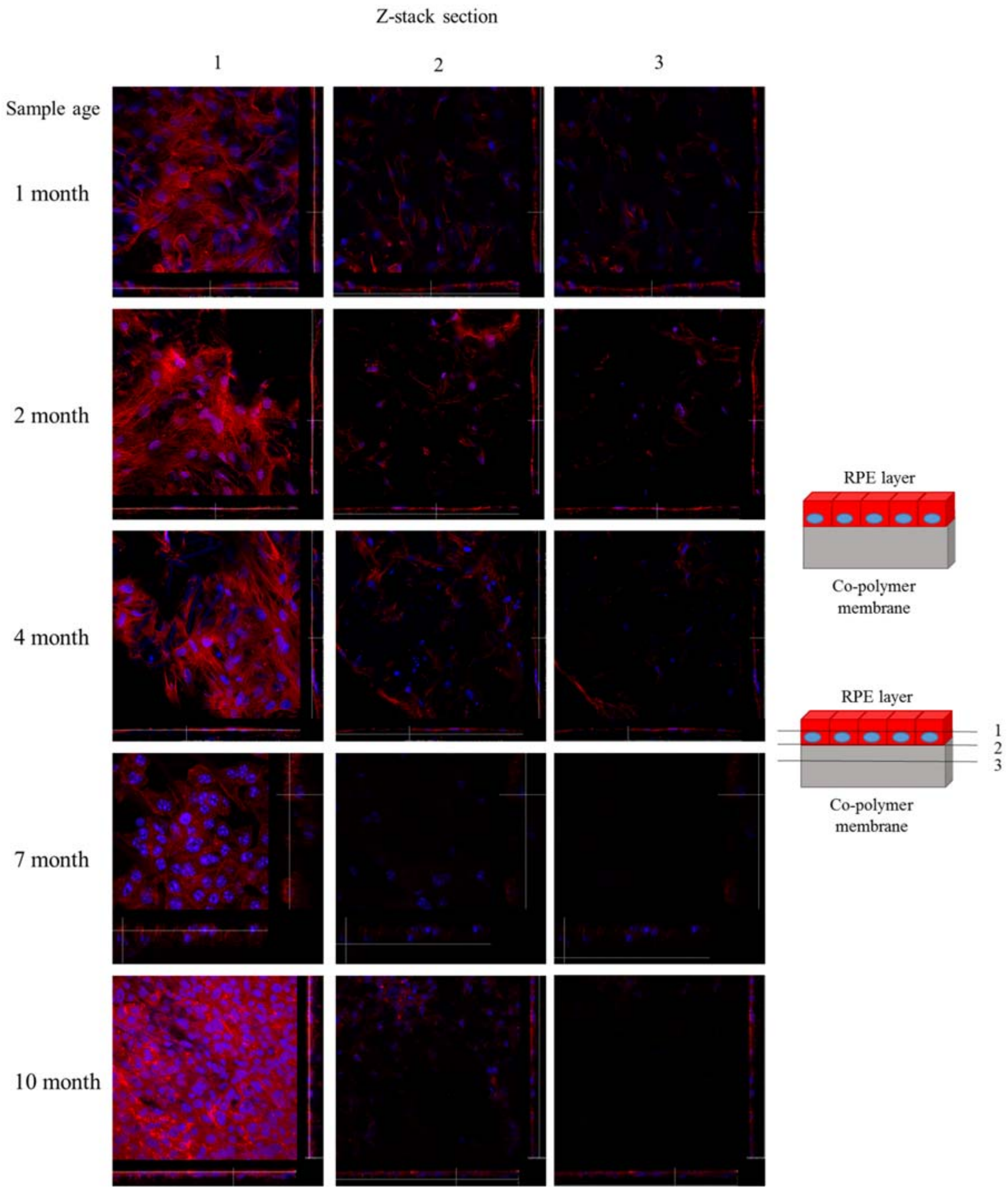

Figure 45: Representative images of the immunofluorescent assay of RPE-polymer matrix samples, showing serial z-stack confocal sections taken at three points in the RPE-polymer matrix, highlighted in the schematic. Over 10 months, the distribution of the RPE layer on the surface of the co-polymer membrane becomes increasingly apical, with the cell nuclei (DAPI, blue) and the actin filaments (Phalloidin, red) highlighted in these images, showing a decrease in the percentage of RPE in deeper parts of the co-polymer matrix.

4.3 RPE cell attachment complexes

With the proliferation of the RPE cells highlighted by immunofluorescent analysis and the use of orthogonal sections to show apical distribution of the RPE layer, it was then imperative to understand how well RPE cells for attachments on the underlying fibre matrix.

As discussed in Chapter 1, RPE cells are anchorage-dependant, hence the integrity of the substrate can influence factors such as cell adhesion and proliferation[27]. It is therefore imperative that the seeded RPE layer forms attachment complexes with the polymeric support to avoid cell anoikis and for the co-polymer membrane to act as a suitable BrM mimetic. Typical cell-to-substratum complexes comprise certain specific proteins and kinases, for example focal adhesion kinase (FAK) and vinculin. These proteins play important roles in the formation of focal adhesions.

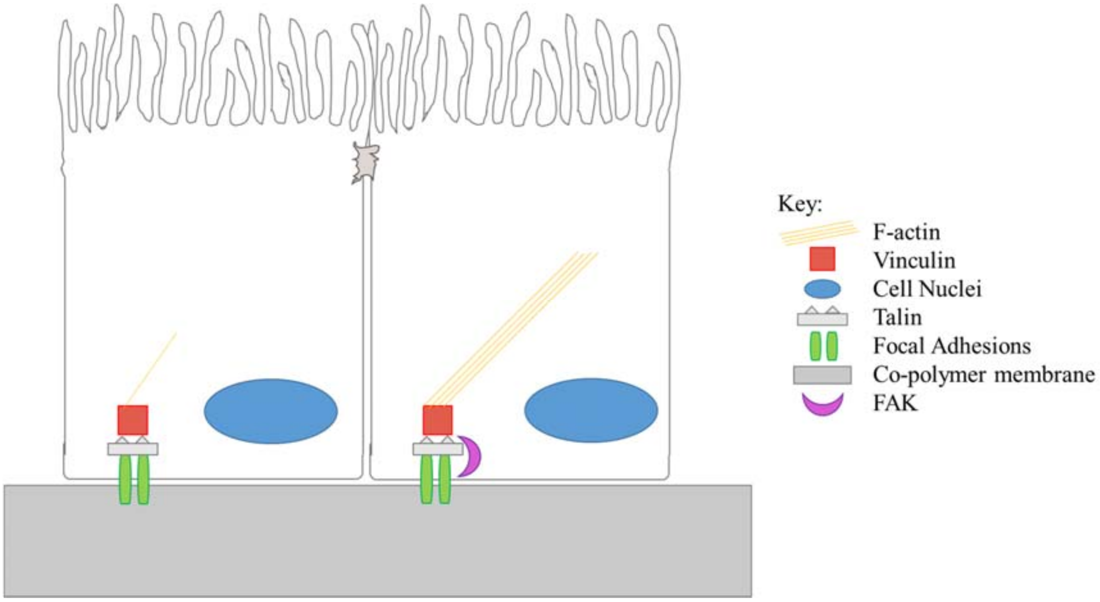

Figure 46: A representative schematic highlighting the cell-substratum contacts and the key components that allow the formation of the required attachment complexes. Initial binding of the RPE cell to the extracellular membrane (co-polymer membrane) is carried out by integrin bundles forming focal adhesions. These adhesions then bind to the cytoskeletal network (f-actin) *via* vinculin. Further binding of FAK promotes integrin clustering and greater association with the cytoskeleton.

Cells adhere to extracellular membranes by binding ligands in the extracellular matrix, mediated by integrins. Upon binding to an extracellular membrane, these integrins localise at the sites of contact and form 'focal adhesions' (Fig. 46). These focal adhesions cause the re-organisation of the cytoskeletal structure of the cell; a process facilitated by vinculin.

Vinculin, a 130,000 Mw protein[247], is involved in linking the ends of actin filaments to the cell membrane in the cell-substratum focal adhesions, resulting in the formation of surface-associated patches of vinculin and is localised almost exclusively at these sites[248–250] (Fig. 46). By binding the actin filaments to the plasma membrane when in contact with a substrate, vinculin helps maintain the integrity of the cell.

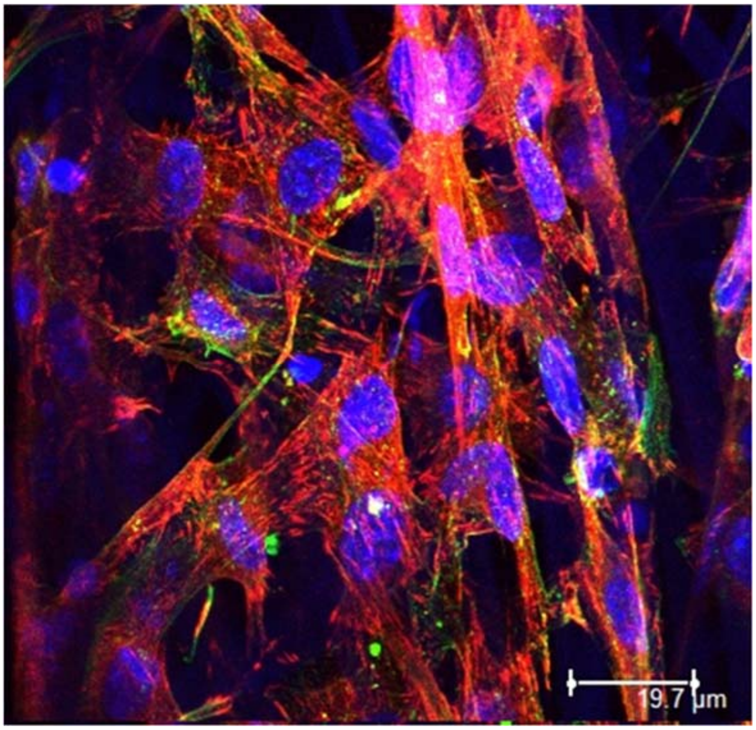

Figure 47: Representative confocal immunofluorescent image of vinculin expression of the RPE-polymer complex, showing (red) the distribution of vinculin throughout the cytoskeleton of the RPE layer. Sample counterstained with phalloidin (green) and DAPI (blue).

Expression of this protein in the RPE cell layer is indicative of an established RPE layer with cell-substrate contacts. Immunofluorescent tagging of vinculin through the use of an anti-vinculin antibody, counterstained with DAPI, highlighted the cell-substrate complexes formed within the RPE-polymer matrix (Fig. 47).

As shown in Fig. 47, the expression of vinculin (red) is shown throughout the cytoskeletal network of the RPE layer, indicating that RPE cells form firm attachments with underlying fibres.

Alongside vinculin, focal adhesion kinase (FAK) is also key to the formation of focal adhesion points. It is a cytoplasmic tyrosine kinase that resides at sites of integrin bundles at focal adhesion contacts[20], and is vital as a regulator of cell apoptosis. It binds to the integrins either directly[251] or *via* talin and subsequent binding of FAK causes cell growth

(Fig. 46). It is therefore a key component of the maintenance of the cell after adhesion to the extracellular matrix, with its presence indicative of RPE cells attached to the underlying fibres.

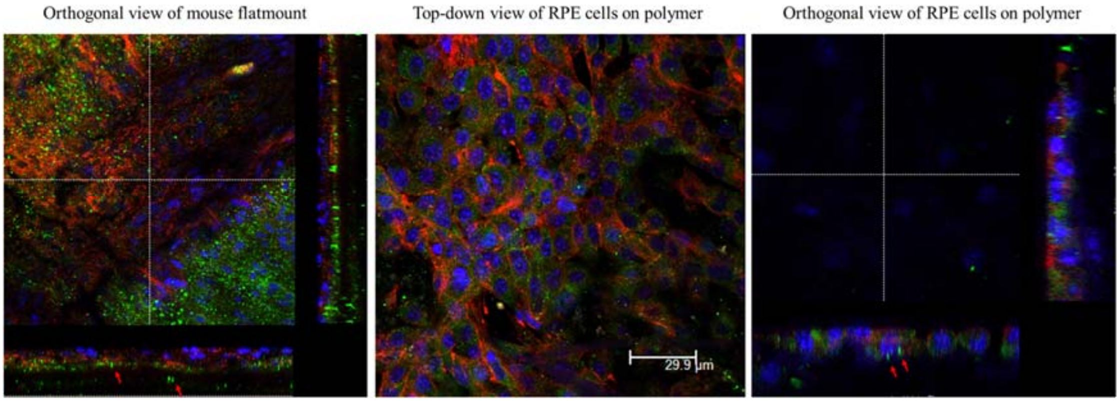

Figure 48: Representative confocal immunofluorescence images of FAK distribution (green) within a positive control (mouse eye flatmount, left) and on 3 month samples of a RPE layer on the co-polymer membrane (centre and right). Orthogonal views of the RPE cells on the co-polymer membrane show the punctate focal adhesions formed with the extracellular matrix, showing the association of FAK, in comparison to the mouse flatmount, which displays the same punctate focal adhesions to native BrM. Samples counterstained with phalloidin (red) and DAPI (blue).

Immunofluorescent tagging of FAK through the use of an anti-FAK antibody, counterstained with DAPI and phalloidin, showed the presence of punctate focal adhesion points linking the RPE to the co-polymer matrix (Fig. 48). Orthogonal sections show clear points of basal RPE focal adhesion to the co-polymer membrane, similar to the positive control (flat-mount of mouse eye with RPE exposed) where the points of adhesion are also basal and in contact with BrM.

Whilst displaying a RPE layer with attachment proteins, in order to assess how well cells form attachments with underlying fibres, the proliferative activity of the RPE cells was measured by fluorescence activated cell sorting (FACS). A non-proliferative cell is indicative of a ‘settled’ RPE layer, whereas a proliferative state is indicative of migrating and/or dividing cell. Analysis of this can be achieved through the study of the RPE cell cycle, monitoring the cells’ replication state by fluorescence labelling the cell nuclei and subsequently analysing the fluorescence properties of each cell in the population. Cells in the $G_{0/1}$ phase of the cell cycle (non-dividing) will have one copy of DNA and will therefore have a single fluorescence intensity, cells in the S phase (initial division of cell) are producing DNA and will therefore have between a single and a double fluorescence intensity and cells in the G_2/M phase (subsequent dividing cell) of the cell cycle will have two copies of DNA and will therefore have a double fluorescence intensity.

Proliferative RPE isolated from cell culture

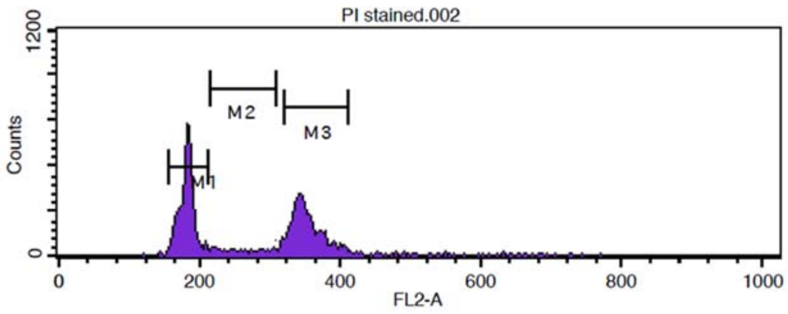

RPE on co-polymer membrane

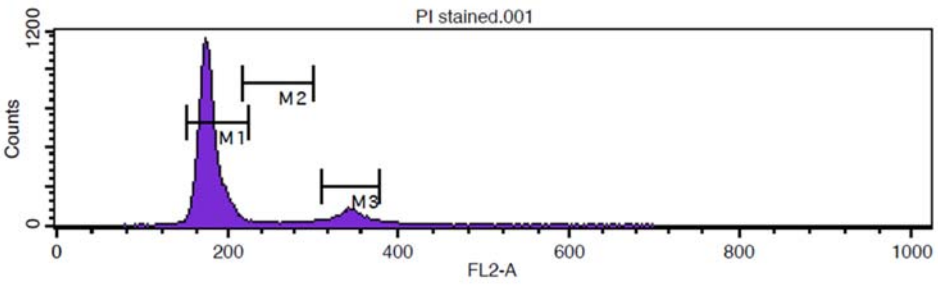

Figure 49: FACS cell cycle analysis of the proliferative activity of the RPE layer on the surface of the co-polymer membrane (bottom, 2 month post-RPE seeding samples), with a comparison to a proliferative RPE in cell culture. The RPE layer on the co-polymer membrane displays a predominantly $G_{0/1}$ phase, compared to a proliferative RPE layer which displays both $G_{0/1}$ and G_2/M phase.

Quantification of the 2 month RPE layer seeded on the co-polymer surface *via* this method showed a predominantly $G_{0/1}$ phase (Fig. 49), compared with a RPE cell culture with proliferative activity (Table 5). Alongside the presence of key attachment proteins (vinculin, FAK) *via* immunofluorescence, this displayed an established RPE layer with key cell-substrate attachment complexes.

Sample	$G_{0/1}$-phase / %	S-phase / %	G_2/M-phase / %
Proliferative RPE isolated from cell culture	47.2	5.87	43.4
RPE on co-polymer membrane	81.1	4.80	11.5

Table 5: Summary of the results of the FACS cell cycle analysis, displaying the predominant $G_{0/1}$ phase of the RPE layer on the co-polymer membrane compared to the $G_{0/1}$ and G_2/M phase dominance of the proliferative RPE layer in cell culture.

4.4 Tagging for RPE specific markers

In order to ensure that the cells on the surface of the co-polymer membrane had retained their phenotype and maintained their epithelial-like structure (i.e. not developed into fibroblastic-like arrangements), an investigation into RPE-specific markers was required to confirm that the seeded cells were in fact RPE cells.

RPE65 is a retinyl ester binding protein that is pivotal in the conversion of trans-retinol to 11-cis retinal in the visual cycle (see Chapter 1.2.2), essential in the regeneration of photoreceptors, and is specific to the RPE monolayer[17,252]. This specificity can be used to determine whether the cultured RPE cells have retained their phenotype on the surface of the co-polymer membrane.

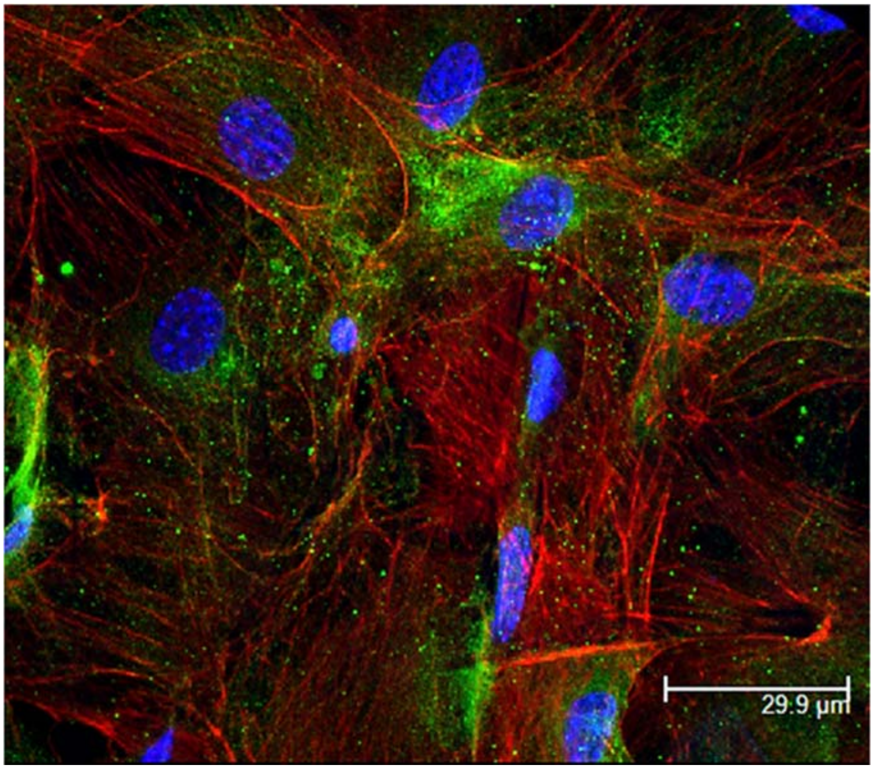

Figure 50: Representative confocal immunofluorescent image showing the presence of RPE65 (green) in 4 month primary RPE cultures, highlighting the extent of protein production within the RPE layer on the artifical BrM. Sample counterstained with phalloidin (red) and DAPI (blue).

An immunofluorescent assay was conducted on RPE cells on co-polymer membranes, tagging for RPE65 using an anti-RPE65 antibody and counterstaining with DAPI & phalloidin (Fig. 50). The expression of RPE65 (green) in the cytoskeletal network of the RPE layer of a 4 month primary RPE culture on the surface of the co-polymer matrix is profound, showing a clear indication of the RPE layer maintaining its phenotype.

4.5 Formation of apical microvilli

A key component of the RPE layer is its ability to interdigitate with the photoreceptors through its apical microvilli. Alongside this, the presence of apical microvilli is a clear sign that the RPE layer has matured and become specialised on the co-polymer membrane, allowing it to establish the required polarised membrane and develop an apical microvilli surface.

To analyse the production of apical microvilli by the seeded primary RPE layer on the co-polymer membrane, transmission electron microscopy (TEM) was used. TEM is a technique which uses a beam of electrons to transmit through a sample, generating an image from the interaction between the sample and the beam of electrons. By using electrons, samples are able to be imaged at a significantly higher resolution (compared to SEM) at a micron-scale. This has allowed the analysis of cells at its ultrastructure. Using this spectroscopic technique, a 12 month sample of primary RPE cells were removed from the co-polymer membranes, fixed (using a PFA : Glutaraldehyde : PIPES fixative) and embedded in algenate (Fig. 51).

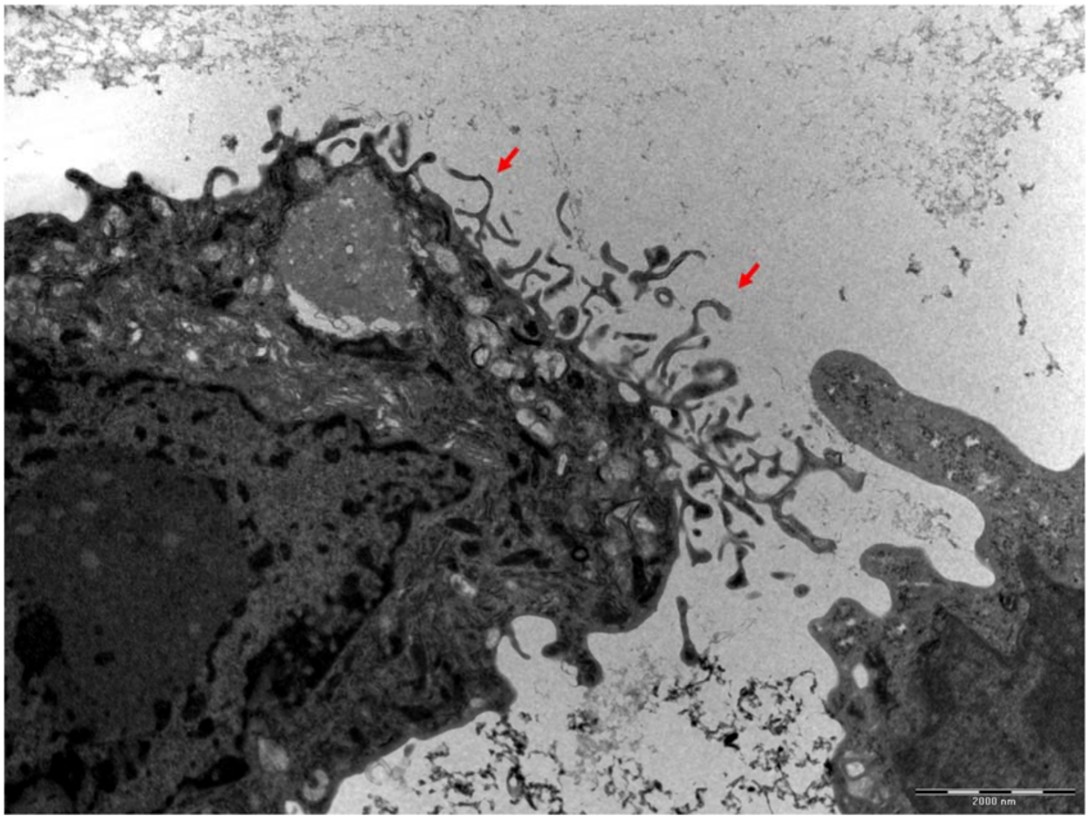

Figure 51: Transmission electron microscopy of a RPE cell isolated from a 12 month culture on the surface of the co-polymer membrane, displaying microvilli across its apical surface (red arrows). Scale bar – 2000nm.

The findings from TEM analysis indicated that the RPE cell had successfully produced apical microvilli. Further experiments using immunofluorescence (Fig. 52) confirmed the presence and apical distribution of the Na^+/K^+ ATPase pumps, essential in the maintenance of Na^+ and K^+ electrochemical gradients across the plasma membrane and, in contrast to other epithelial layers, located in the apical side of the RPE monolayer[253].

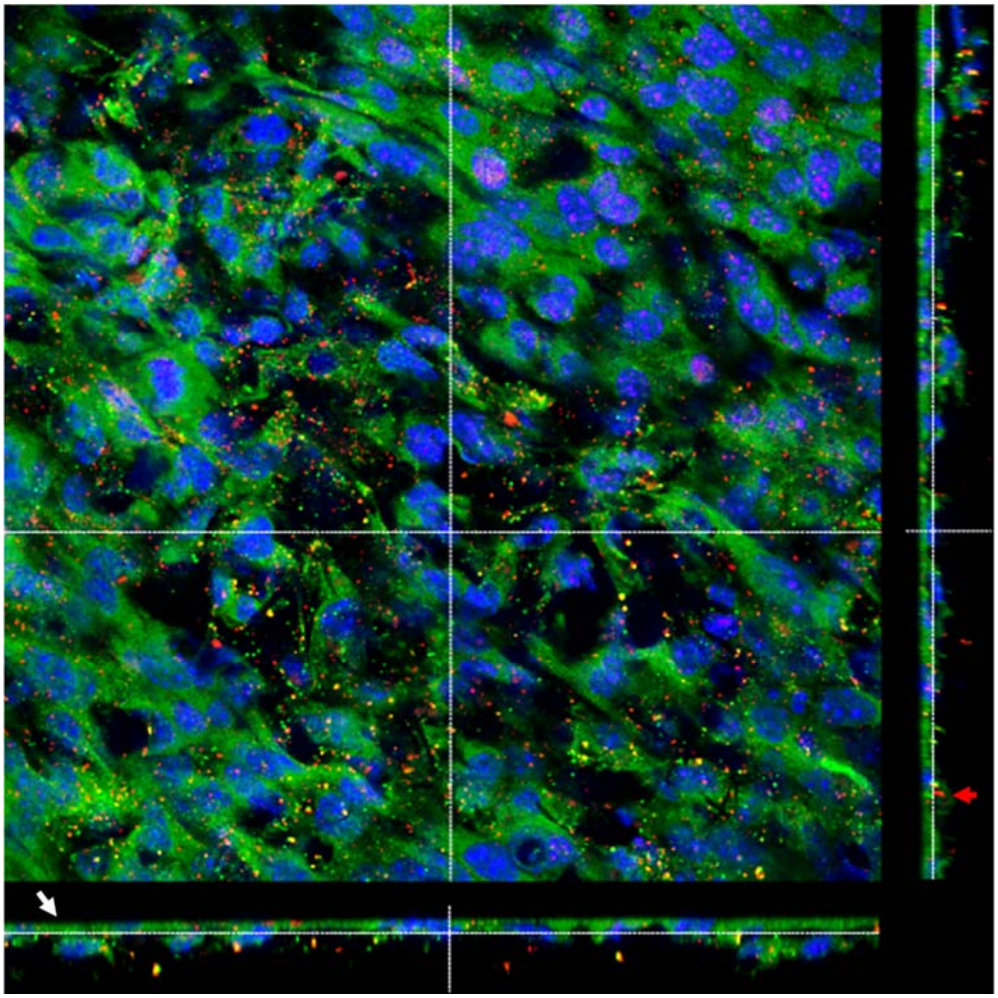

Figure 52: Immunofluorescent orthogonal assay of Na^+/K^+ ATPase (green), showing the apical distribution of Na^+/K^+ ATPase across the surface of the RPE layer on artificial BrM (white arrow). Counterstained with FAK (red, highlighted with the red arrow) and DAPI (blue).

4.6 Secretion of growth factors in RPE-PM complexes

Another vital role is the production and secretion of vascular endothelial growth factor (VEGF). The choriocapillaris underlying the RPE-BrM is dependent on the basal secretion of VEGF from the RPE, through the BrM to facilitate the production of new choriocapillaries[53]. Therefore, a RPE-BrM mimetic complex must allow the production of VEGF if it is to be a suitable replacement for the degenerated BrM associated with AMD.

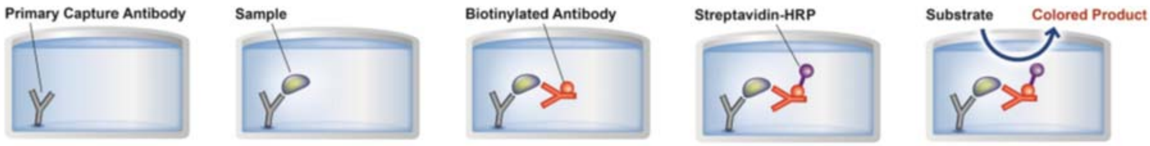

Figure 53: A representative schematic showing the ELISA process. A sample is bound to the 'primary capture antibody', from which a biotinylated antibody and streptavidin-HRP is added. Addition of a substrate (TMB) creates a colour change when in contact with HRP, generating a colour which is analysed on a colorimeter.

In order to analyse the BrM mimetic's capability to allow an attached RPE layer to secrete VEGF, a VEGF enzyme-linked immunosorbent assay (ELISA) was carried out. The ELISA employs an antibody specific for murine VEGF coated on a 96-well plate (Fig. 53). Samples are pipetted into the wells, alongside standards, and any VEGF present in the sample is bound to the wells by the immobilised antibody. The wells are washed and a biotinylated anti-murine VEGF antibody is added to fix the VEGF in place. Horseradish peroxidase (HRP)-conjugated streptavidin is pipetted into the wells, followed by a 3,3',5,5'-tetramethylbenzidine (TMB) substrate solution (TMB is a chromogen that yields a blue colour when oxidised, i.e. when hydrolysed by HRP). The addition of TMB develops a colour which is directly proportional to the amount of VEGF in solution. A 'stop' solution is added (changing the colour from blue to yellow) and the plate is read in a colorimeter at 450nm. Over a period of 9 months, cell culture supernatant from primary murine RPE cultures on co-polymer scaffolds was collected at time points – 1 month, 5 months and 9 months, and frozen at -20^{o}C. VEGF ELISA results appear in Figure 54.

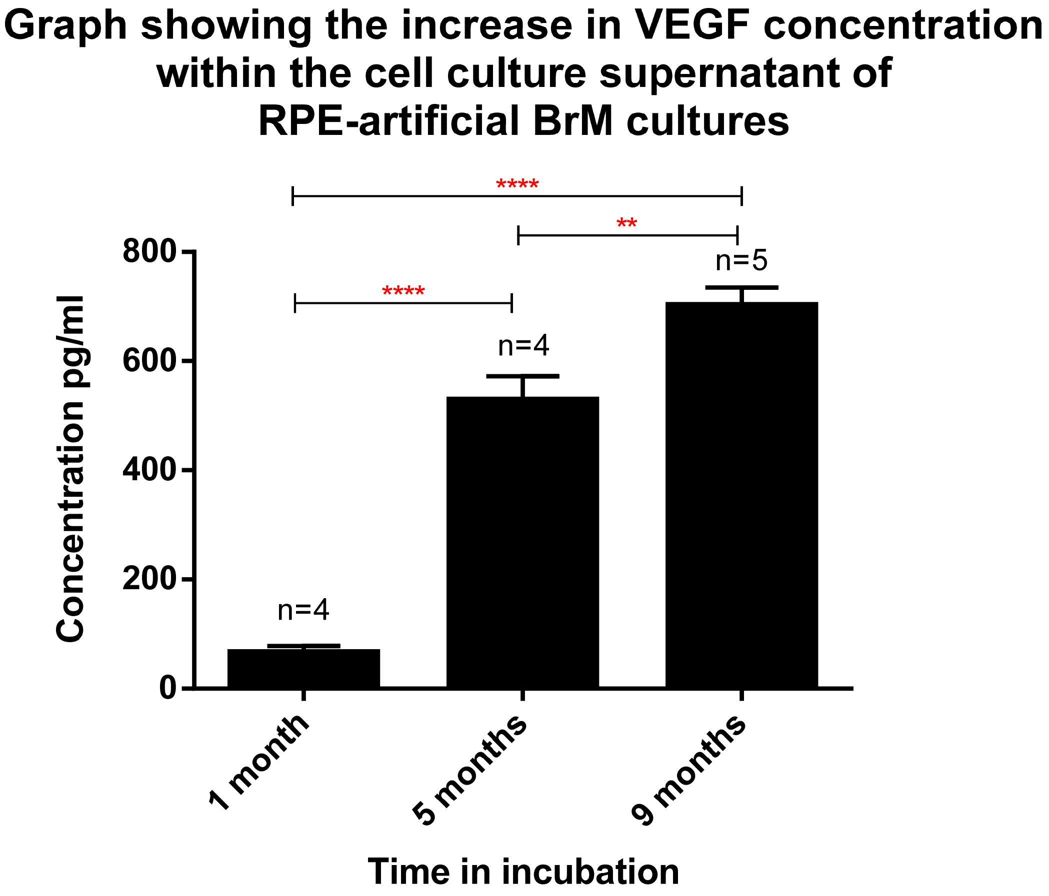

Figure 54: Graph showing the concentration of VEGF secretion over a period of 9 months. Concentration of VEGF secreted by RPE cells seeded on the artificial BrM after 1 month was 66.5 ± 11.7 pg ml^{-1}. After 5 months in incubation, the concentration of VEGF secreted by the RPE layer was 528.8 ± 28.2 pg ml^{-1} and after 9 months the concentration of VEGF secreted was 702.4 ± 27.3 pg ml^{-1}.

After a period of 5 months, the concentration of VEGF present was 528.8 ± 28.2 pg ml^{-1}, compared to 1 month cultures (66.5 ± 11.7 pg ml^{-1}), a significance of $p < 0.0001$. This significant increase in VEGF secretion showed that after 5 months, the RPE layer was established to the point that VEGF production had significantly increased. Nine month samples displayed a VEGF concentration of 702.4 ± 27.3 pg ml^{-1}, a significant increase from the 5 month samples ($p = 0.0032$) and from the 1 month samples ($p < 0.0001$). The 9 month VEGF concentration of 702.4 ± 27.3 pg ml^{-1} was close to the reported concentration of human RPE VEGF secretion levels (1000 pg ml^{-1})[254].

In order to establish whether the secretion of VEGF was secreted from the RPE basolateral membrane, highlighting a polarised RPE layer on the surface of the co-polymer membrane, a Cell Crown^{TM} system was employed (see Chapter 2.5.13). The Cell Crown^{TM} inserts allowed the co-polymer membrane to act as a transwell in cell culture plates. This therefore separated the basal cell culture compartment from the apical compartment, allowing the measurement of proteins secreted in a polarised manner.

Scaffolds were fixed in Cell Crown^{TM} inserts, placed in 24 well sized plates and seeded with primary murine RPE. These were then cultured for 2 months. Media was routinely changed as previously described in Chapter 2.5.7. Two months after RPE cells were seeded, conditioned media was collected and VEGF levels determined by ELISA quantification (Fig. 55).

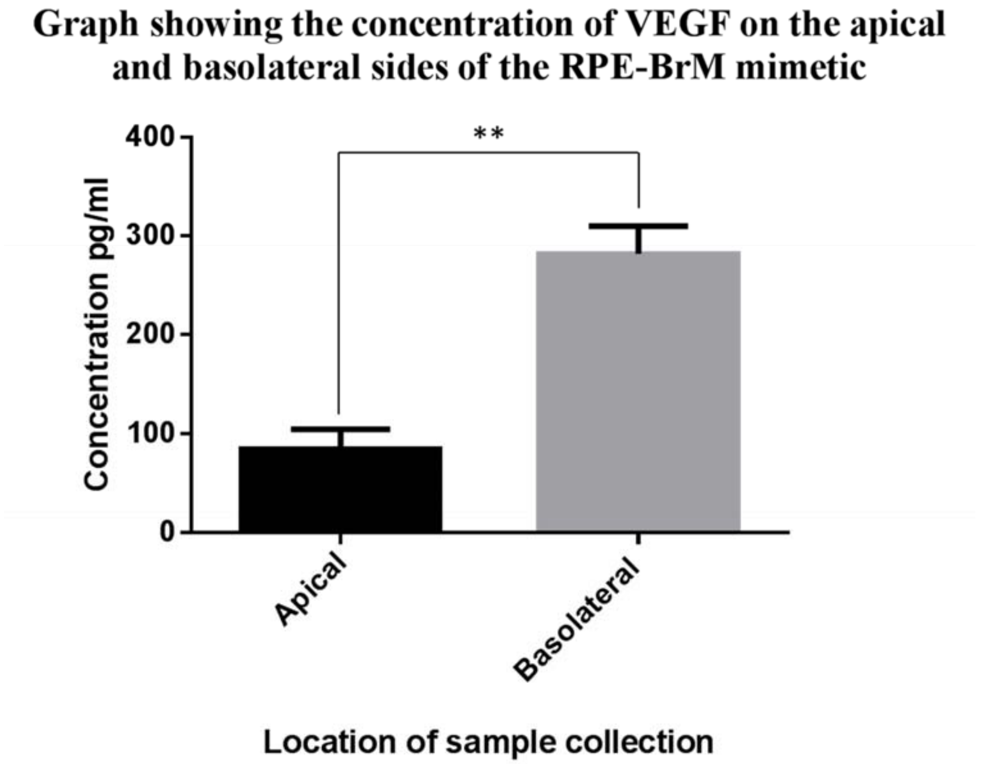

Figure 55: Graph showing the difference in basolateral and apical VEGF secretion. VEGF was produced on the RPE apical compartment at a concentration of 84.8 ± 20.2 pg ml^{-1}, whereas on its basolateral side the concentration of VEGF was found to be 281.8 ± 28.04 pg ml^{-1}, a significance of $p = 0.0013$. This significant secretion of VEGF from its basolateral side indicates a functional RPE layer on the surface of the artificial BrM. For both samples, n=4.

4.7 Formation of tight junctions and barrier properties

The RPE-BrM layer forms a barrier between the retina and the choroid, monitoring and controlling the flow of macromolecules from the choriocapillaris to the retina and *vice versa*. This barrier is key in the maintenance of the retina, and is one of the many important properties of the RPE layer.

An artificial BrM with a layer of primary RPE cells was required to mimic this property, and investigations into the formation of a barrier towards macromolecular diffusion and epithelial resistance were carried out.

We used a set-up involving an Ussings chamber to analyse the diffusional properties of the primary RPE layer on the surface of the co-polymer membrane. As detailed in Chapter 2.3.14, the Ussings chamber creates a closed environment from which the diffusion of Dextran, a fluorescein isothiocyanate labelled compound, which when measured on a colorimeter can identify the porosity of a membrane. The ability of the RPE layer to form a layer would be analysed by this method, as any decrease in permeability would indicate the presence of a barrier.

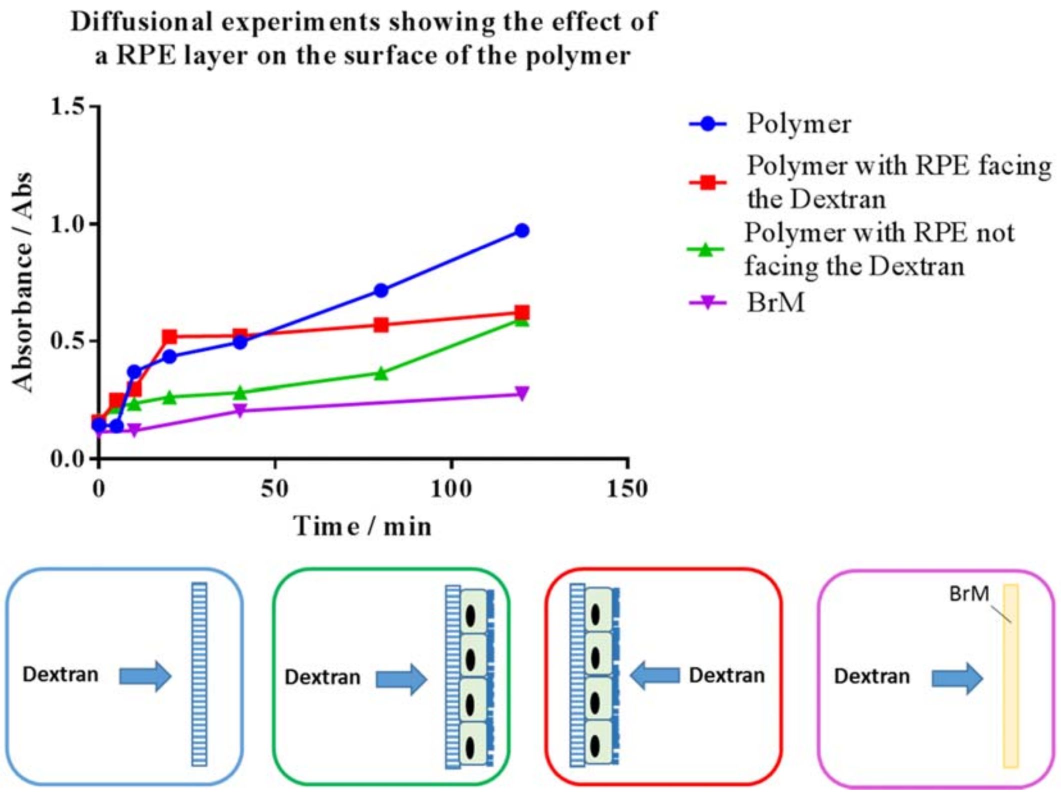

Figure 56: Graph displaying the result of the diffusional experiments, showing the decreased diffusion of dextran through the RPE-artificial BrM compared to the artificial BrM without RPE, indicating the formation of a barrier.

BrM-choroid, artificial BrM and 1 month cultures of primary RPE on synthetic scaffolds were placed in the Ussings chamber and the diffusion of dextran was measured (Fig. 56). Samples were either placed with the RPE layer facing the fluorescent dextran or facing towards the PBS reservoir.

From these diffusional experiments the effect of a layer of primary RPE cells on the surface of the co-polymer membrane was clear. The reduction in the diffusion of dextran due to the seeding of a layer of RPE cells indicated the formation of a barrier, showing an increase in the control of macromolecular diffusion.

To understand the formation of the barrier over time, an investigation into the transepithelial electrical resistance (TEER) of the membrane was carried out. TEER is able to measure the epithelial integrity and its subsequent viability as a barrier to macromolecular diffusion by measuring the difference in the epithelial resistance between its apical and basolateral sides[178,255].

Using this technique, an experiment to measure the change in epithelial resistance over time was carried out. Over a period of 6 weeks, TEER measurements were taken of primary RPE cell cultures on the surface of a Cell Crown™ co-polymer system, to understand the development of a barrier across the artificial BrM as the RPE layer established the formation of its tight junctions and provided resistance to the transfer of solutes across the polymer membrane (Fig. 57).

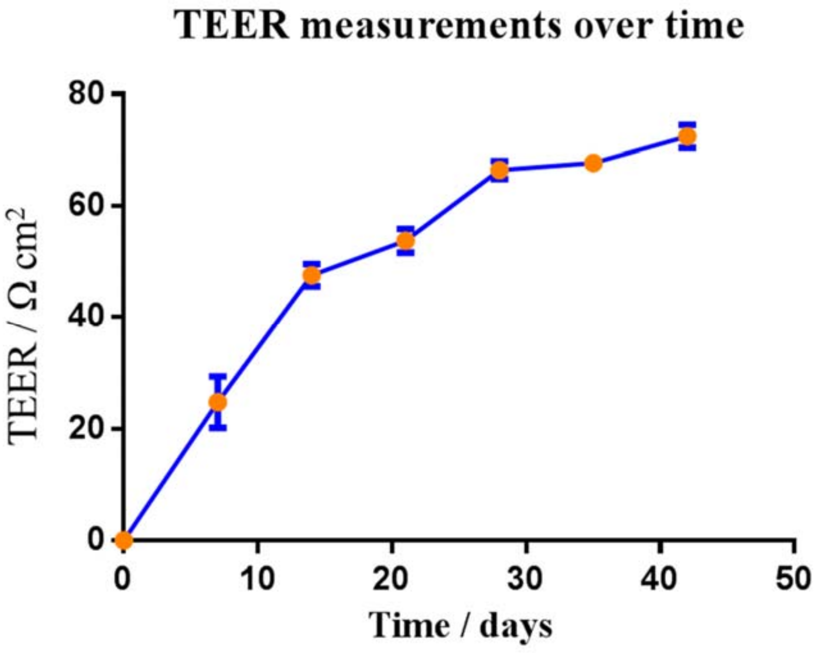

Figure 57: Graph showing the increase in epithelial resistance of the RPE layer on the artificial BrM over a period of 42 days.

From these measurements, it was clear that the epithelial layer had formed a barrier across the co-polymer membrane surface, with a gradual increase in electrical resistance finishing with the RPE monolayer displaying a plateau after 28 days. TEER measurements of the established layer after 28 days showed similarity to human RPE-choroid resistance (79 ± 48 Ω cm^2)[255].

The formation of the RPE barrier across the co-polymer membrane requires the layer of epithelial cells to form close contact points with each other. Tight junctions in-between cells regulate the diffusion through the intracellular space, preventing any gaps in the barrier[256]. In order to analyse whether the RPE layer was producing the necessary tight junctions, experiments were carried out to locate the production of ZO-1. ZO-1 is a protein that co-localises with the contact points in tight junctions and subsequently can be detected by confocal immunofluorescence and western blotting[254,256].

Therefore, to initially confirm the presence of ZO-1 within the RPE cell culture on the surface of the co-polymer membrane, a western blotting assay was carried out (Fig. 58).

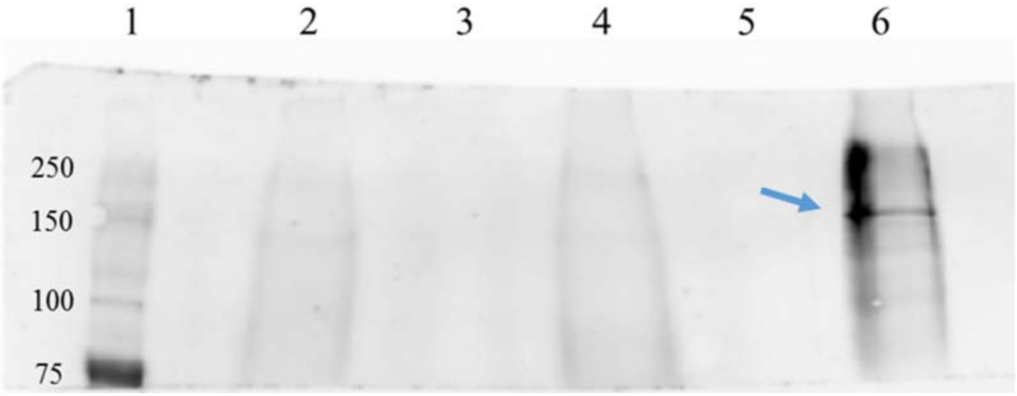

Figure 58: Western blotting assay, showing the presence of ZO-1 in the primary RPE culture on the artificial BrM. ZO-1 (blue arrow) was found at 195kDa (lane 6), with a protein ladder in lane 1 and no protein present in lanes 2-5.

ZO-1 expression was highlighted by the presence of a clear band at 195kDa (concurrent with the manufacturers expected value for ZO-1 and with the reported values in the literature using the same antibody[257]) and gave an initial insight into the RPE cell monolayer forming tight junctions on the surface of the co-polymer matrix.

After the confirmation of the expression of ZO-1, an immunofluorescent assay was conducted to detect the formation of the tight junctions (Fig. 59).

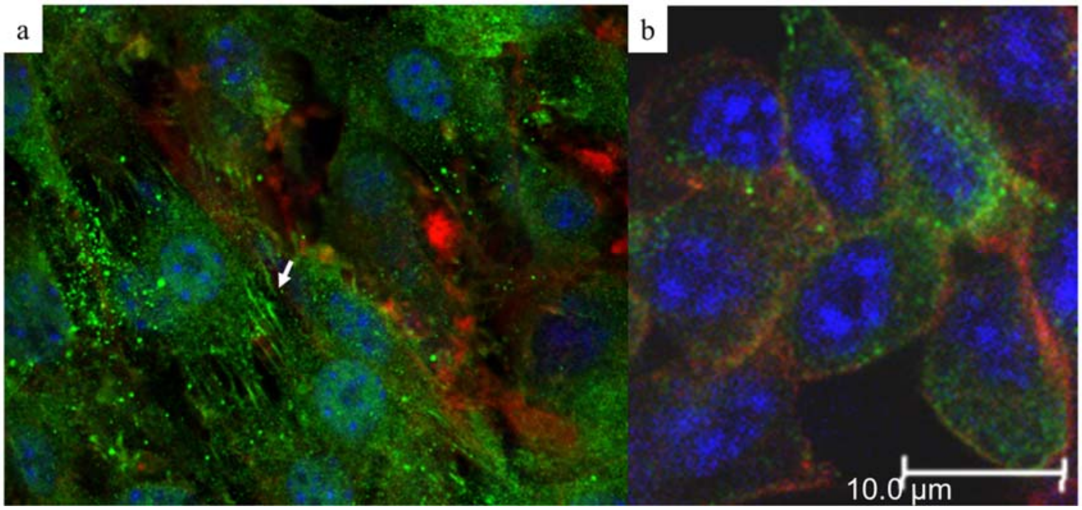

Figure 59: Representative immunofluorescent images highlighting ZO-1 expression, showing (a) the initial contacts of tight junction formation (white arrow), and (b) the formed tight junctions, showing an RPE cluster displaying a tight barrier.

Confocal immunofluorescence confirmed the presence of ZO-1 expression detected by immunoblotting.

4.8 Internalisation of photoreceptor outer segments by RPE

Following on from the RPE barrier formation, an investigation was carried out into another key RPE function, photoreceptor outer segment phagocytosis.

As discussed in Chapter 1.2.1, photoreceptors contain high amounts of photosensitive molecules. These molecules are exposed to high levels of light, leading to degeneration into photo-damaged proteins and lipids. Therefore, to ensure the continued function of the photoreceptors, the photoreceptor outer segments (POS) are routinely renewed. This is achieved through selective POS phagocytosis into the RPE layer underlying the photosensitive layer, where POS is digested and key molecules such as docosahexanoic acid and retinal are retained and recycled.

In order to ensure that the RPE layer on the surface of the co-polymer membrane is behaving in an *in vivo* manner, an investigation into the ability of the RPE-BrM mimetic to phagocytose POS was carried out.

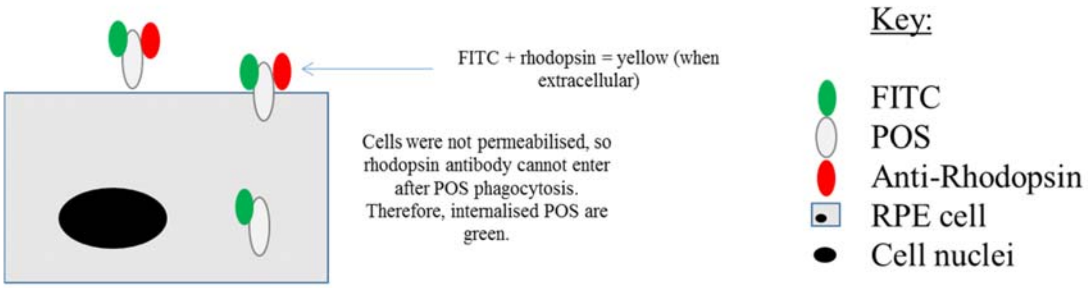

Figure 60: A representative drawing of the immunofluorescent assay set-up, showing the internalisation of FITC-labelled POS. Extracellular POS was tagged with an anti-rhodopsin antibody after fixing, whilst intracellular POS remained untagged.

Porcine photoreceptor outer segments were isolated in a procedure detailed in the literature[176], and were subsequently labelled with FITC using a FITC isomer 1 solution in a 0.1M Na-carbonate buffer (pH 9.5)[177]. Using this method, FITC conjugates to the POS, with subsequent washing removing untagged FITC and thereby isolating FITC-POS. This ensured that the POS was specifically tagged with an individual marker – FITC. Sequential feeding of FITC labelled-porcine POS to 4 month primary RPE cultures on co-polymer membranes was carried out over defined time points – 0, 30, 60, 90, 120 & 180 mins. After completion, the samples were immersed in an anti-rhodopsin antibody, however the RPE cells were not permeabilised to ensure that the rhodopsin antibody could not enter the RPE cell after POS phagocytosis and thereby exclusively tag extracellular POS, therefore allowing a comparison to be made between POS that has undergone phagocytosis and extracellular POS (Fig. 60).

Immunofluorescent analysis was carried out on the RPE-POS samples, using topographical and orthogonal sections to quantify the proportion of internalised POS over time (Fig. 61). The process was repeated twice, measuring 3 samples of RPE-artificial BrM for each time point on each occasion.

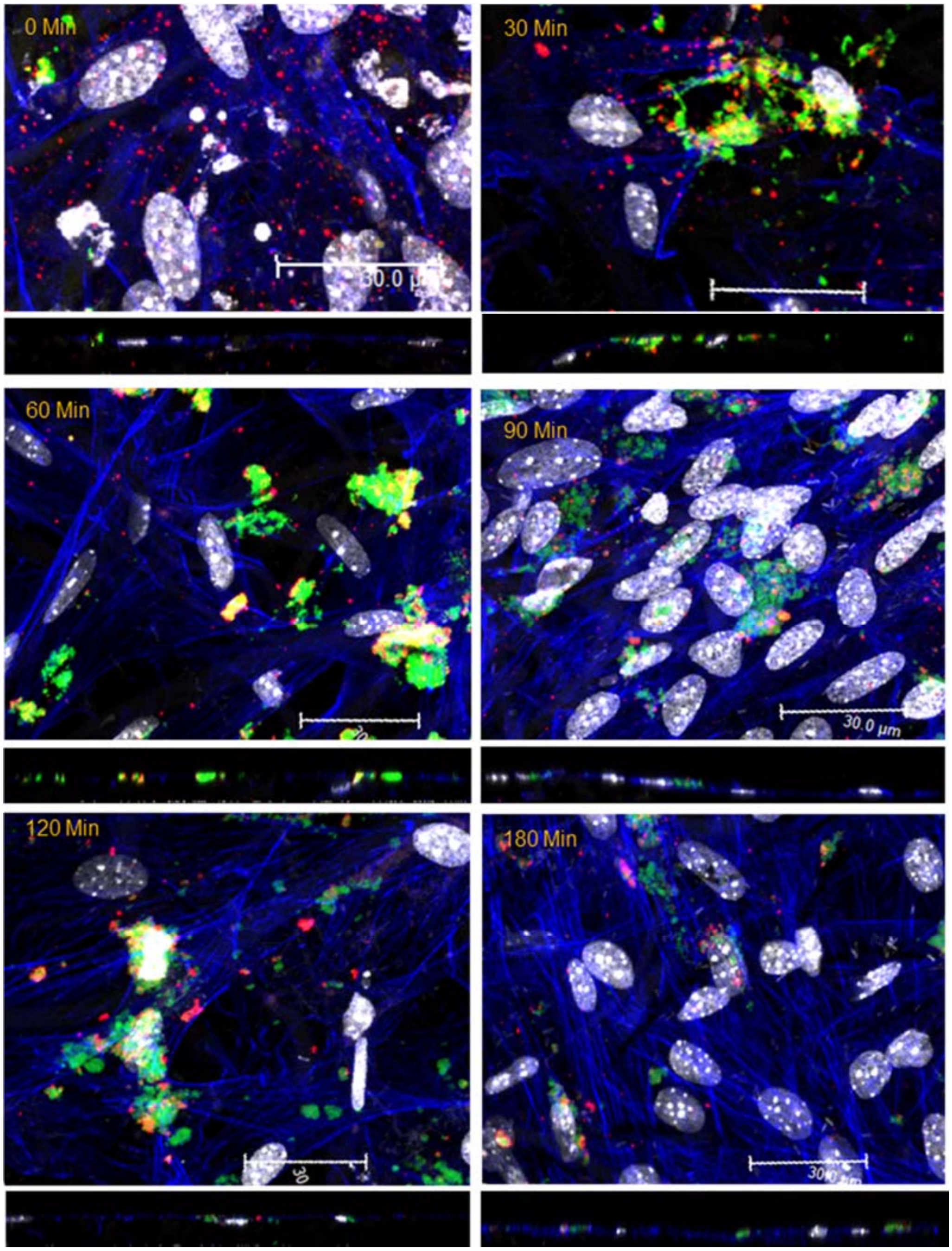

Figure 61: Immunofluorescent assay of POS internalisation, showing the progressive uptake of FITC-labelled POS (yellow for extracellular – due to anti-rhodopsin tagging (red), green for internalised POS) over a 3h period. Orthogonal sections underneath each confocal image shows the progression of POS internalisation through the RPE membrane. Samples counterstained with phalloidin (blue) and DAPI (white). Scale bars - 30µm.

From initial observations it was clear that the amount of internalised POS (green) increased over time, and through the use of Image J to select and measure areas based on colour, the increase in internalised POS and decrease in extracellular POS (yellow) could be quantified (Fig. 62).

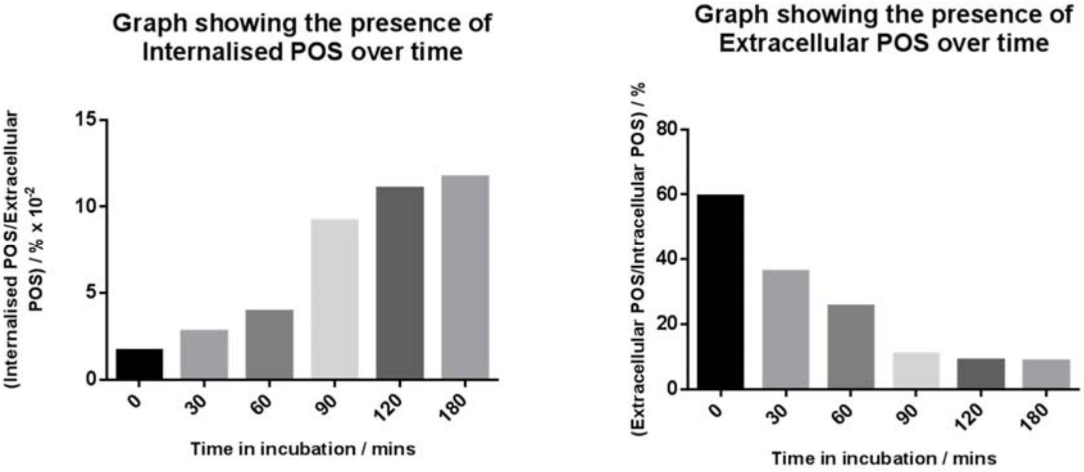

Figure 62: Graphs showing the change in internalised and extracellular POS over time. Data calculated through the use of Image J to measure areas based on colour (i.e. internalised POS – green, extracellular POS – yellow).

The produced confocal images were analysed for percentage coverage based upon the presence of extracellular POS bound with Rhodopsin (yellow) and internalised POS (green). Over the 180 minute time period of the experiment, the presence of internalised POS was shown to increase, whereas the presence of extracellular POS decreased.

TEM was also used to examine the internalisation of POS. Isolated porcine POS were fed to 12 month cultures of primary RPE-artfical BrM and left in incubation for 2h. Internalisation was then terminated by PBS-CM washing and the primary RPE cells were removed from the co-polymer membrane by Trypsin-EDTA incubation. The collected RPE-POS pellet was then embedded in algenate and processed for TEM imaging (Fig. 63).

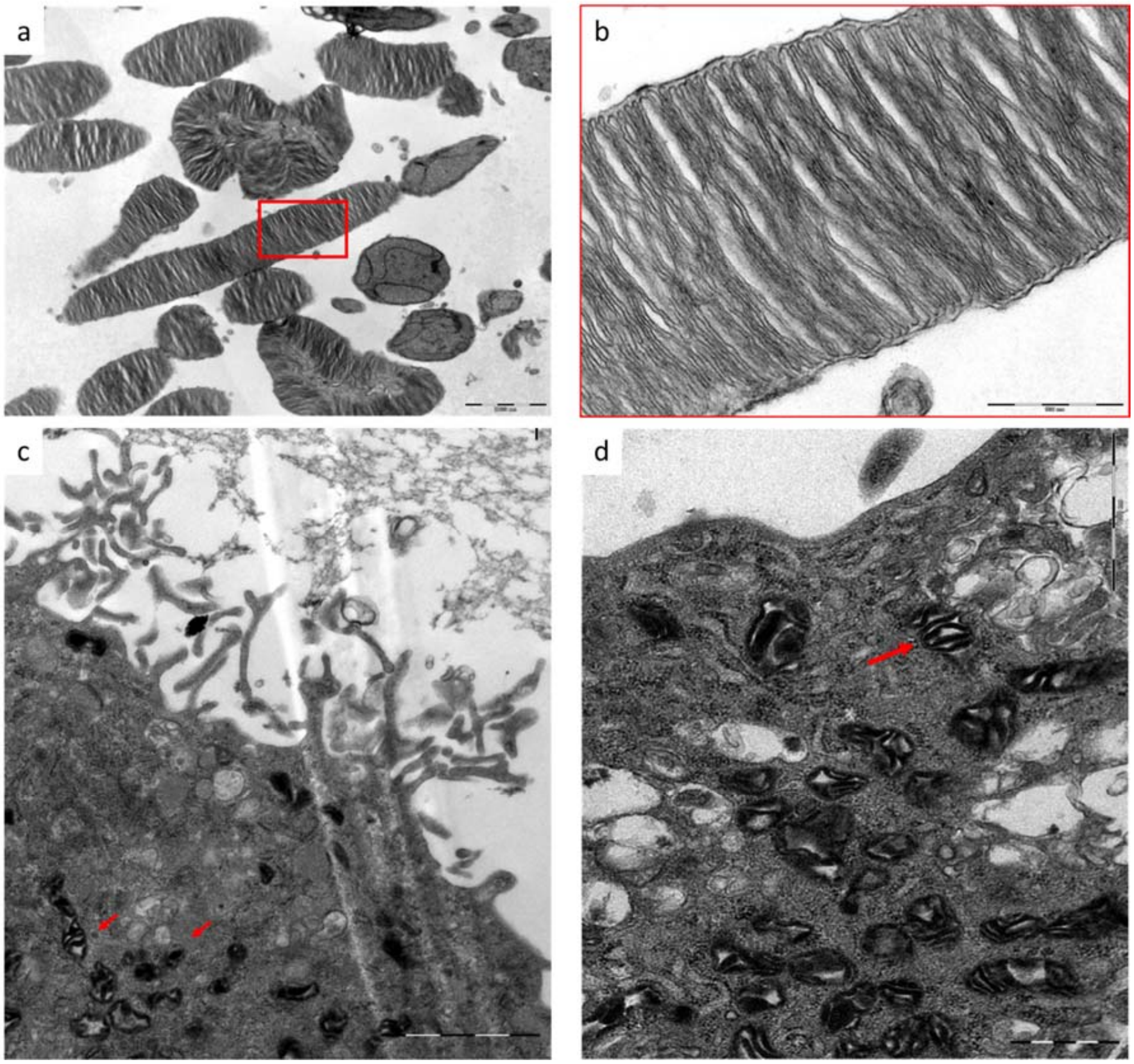

Figure 63: Transmission electron microscopy (TEM) of (a) isolated porcine POS, highlighting (b) the disk-like structure of the photoreceptors. Also, the TEM of (c) the subsequent internalisation of the porcine POS (red arrows) by the 12 month primary RPE cultures grown on the co-polymer membranes which, under a higher magnification, (d) display the internalised disk-like ultrastructure of the POS. Scale bars: (a) 2000nm; (b) 500nm; (c) 1000nm; and (d) 1000nm.

From these TEM images and in comparison to the isolated POS images, it was clear that the RPE cultures had successfully internalised the porcine POS.

Once it had been established that a primary RPE cell culture on the surface of the artificial BrM could phagocytose porcine POS, an investigation into the molecules used in selectively internalising POS (MerTK and αVβ5 receptors) was carried out.

As discussed in Chapter 1, photoreceptor outer segment phagocytosis is facilitated by the use of MerTK and αVβ5 receptors, which are involved in the regulation and binding of the POS to the RPE monolayer.

Therefore, to quantify the selective internalisation of isolated POS, an immunofluorescent analysis was carried out on the binding activity of the αVβ5 and MerTK receptors. By tagging the MerTK and αVβ5 receptors, when bound to FITC-labelled POS the fluorescence turned from blue to purple (Fig. 64).

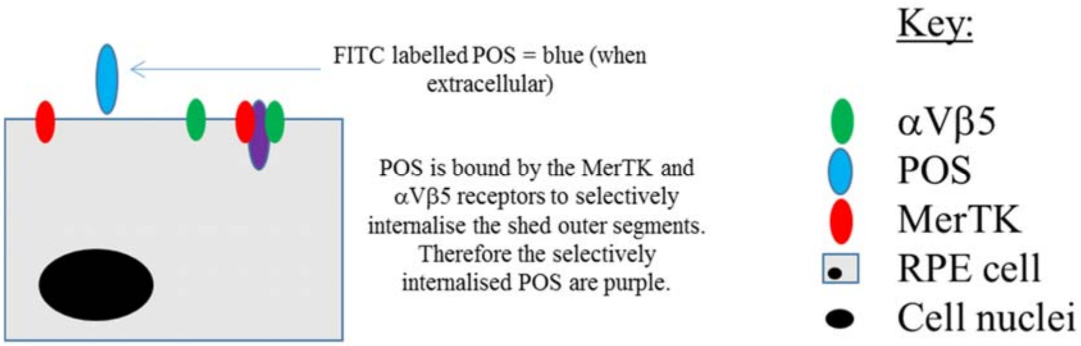

Figure 64: A representative schematic of the immunofluorescent assay set-up for MerTK and αVβ5 selective internalisation. FITC-labelled POS (blue) is bound by the MerTK and αVβ5 receptors to selectively internalise the shed POS (purple).

Immunofluorescence analysis of the time points showed an increase in bound POS complexed with the MerTK and αVβ5 receptors, indicating a selective internalisation process (Fig. 65).

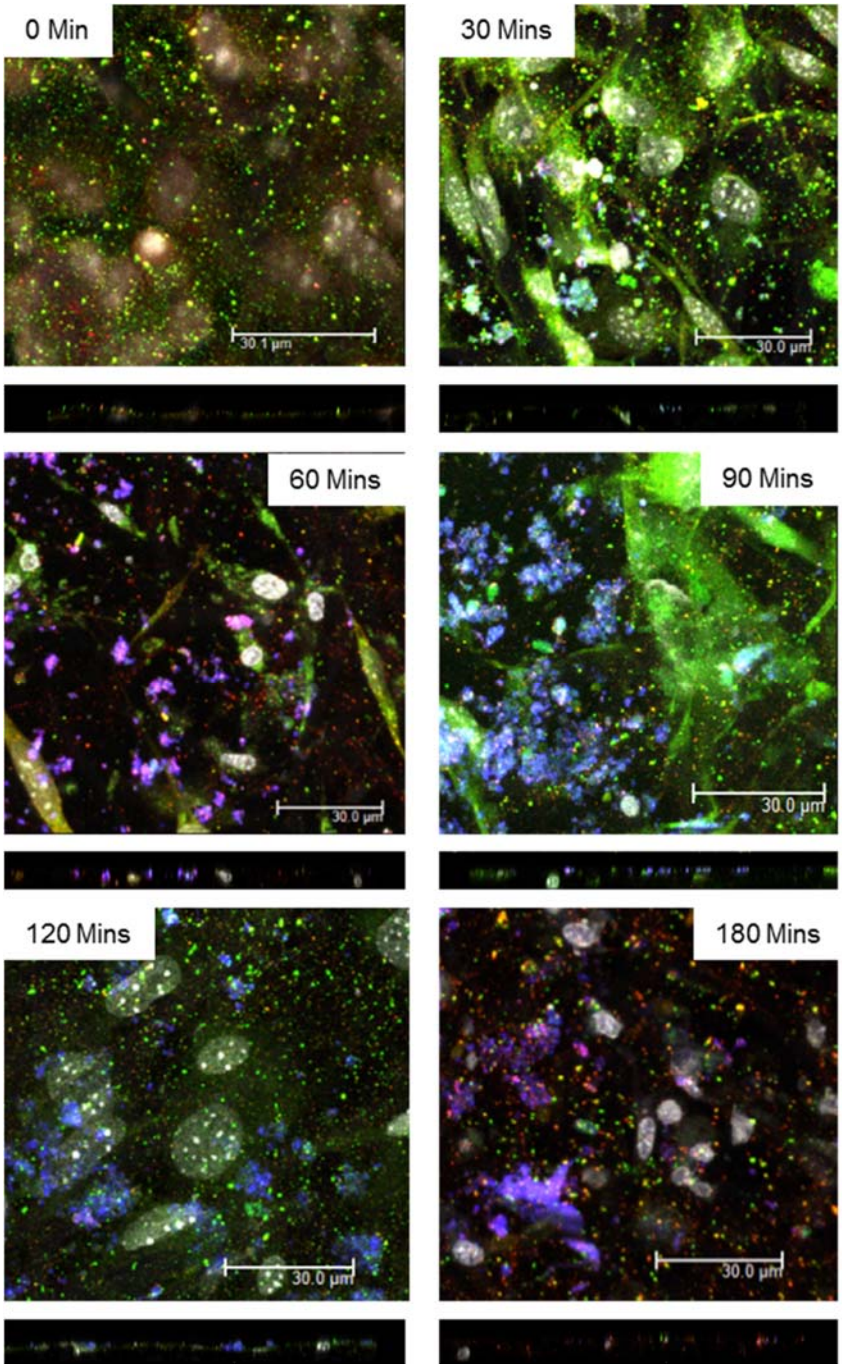

Figure 65: Immunofluorescent analysis of POS internalisation, showing the selective internalisation of POS over time. As the FITC-labelled POS (blue) is internalised, it is bound by the MerTK (green) and αVβ5 (red) receptors, forming an internalised POS (purple) signal. Sample counterstained with DAPI (white).

4.9 Pigmentation of the RPE layer

As discussed in Chapter 1.2.2, a key function of the RPE layer within the human eye is to absorb light which has passed through the retina, preventing further light transport. This is achieved through the production of melanin, contained within melanosomes within the

RPE cytoskeletal network. Melanin prevents the continued passage of light and, subsequently, the formation of reactive oxygen compounds.

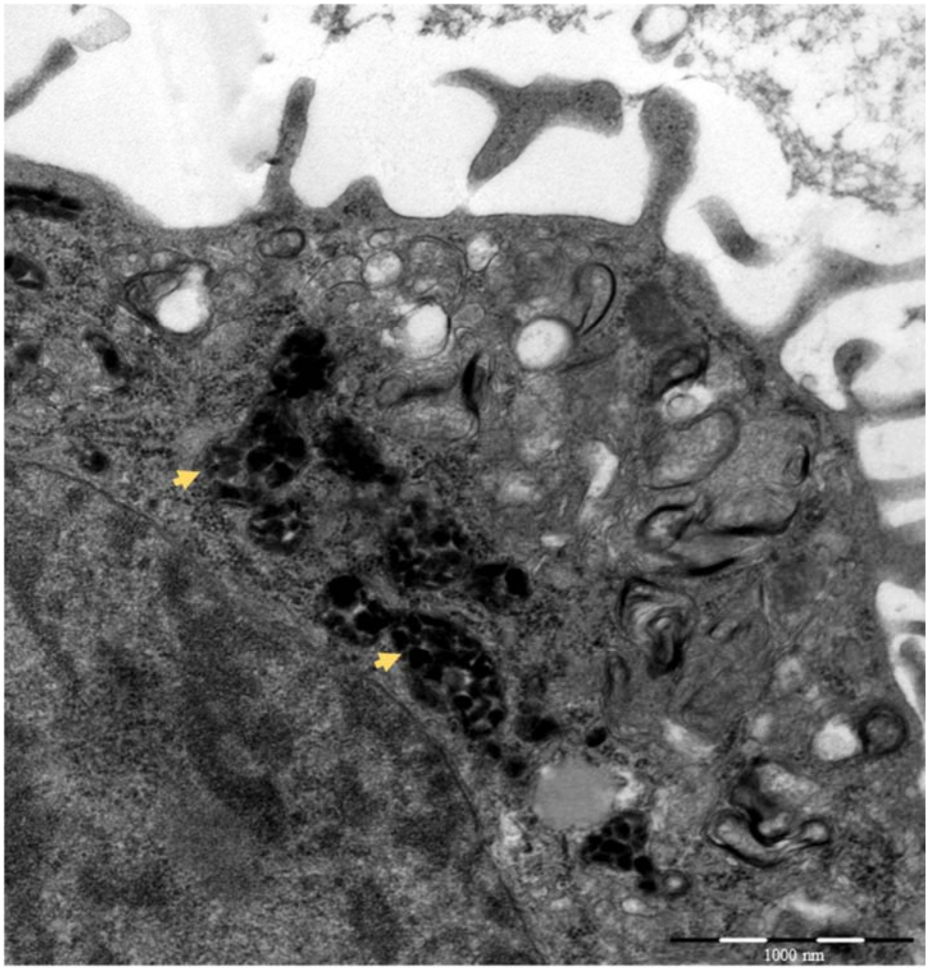

Figure 66: TEM analysis of a 12 month primary RPE cell cultured on the designed artificial BrM, showing (yellow arrows) the speckled melanin granules. Scale bar: 1000nm.

TEM analysis of 12 month primary RPE cultures on the artificial BrM showed the formation of melanin granules (Fig. 66), which displayed similar granular-like morphology to that reported in the literature[258], again indicating a RPE layer showing the formation of key physiological compounds on the surface of the prosthetic BrM.

Chapter 5: Enhancement of the artificial BrM tensile strength

5.1 General Introduction

As discussed in Chapter 3, native human BrM is composed of predominately Type IV collagen & elastin, which when combined with the interwoven fibrous nature of the membrane allows for a strong & flexible matrix. This ensures full RPE attachment and provides structural resistance to the choriocapillaris pulse & changes in blood volume. Therefore, in order for the synthetic variant of BrM to withstand the choriocapillaris pulse and the surgical implantation procedure, the membrane is required to be similar to, if not greater, in its tensile and individual fibre strength than native BrM.

Initial results found that the thinner co-polymer membrane (12µm) was mechanically stronger than the thicker co-polymer membrane (51 ± 3µm), with an increase in the tensile strength as shown by an increase in the Young’s modulus (Chapter 3.5 Fig. 34). Whilst the thinning of the membrane increased the mechanical strength, this was not comparable to that of BrM which had a much larger Young’s modulus and calculated Toughness. Alongside this result, observations were made in tissue culture where the polymer samples were ‘curling’, i.e. the membrane was folding onto itself (Fig. 67). Whilst this shows that the membrane is ‘flexible’, this property is not suitable for *in vivo* applications.

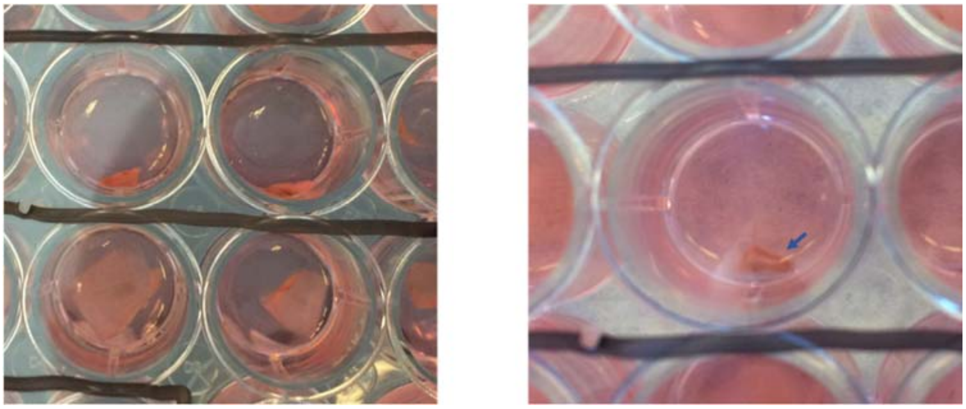

Figure 67: Colour photographs showing the curling effect of the co-polymer membrane in cell culture, showing (left) the curled co-polymer membranes seeded with ARPE-19 cells on the top row and non-seeded co-polymer membranes on the bottom row and (right) a close-up image of the curled co-polymer membrane (blue arrow).

Therefore, improving the tensile and mechanical strength of the membrane was imperative if it was to survive the implantation process and provide a long-term solution to RPE transplantation-based therapies.

Improving the mechanical strength of an electrospun fibrous matrix has been investigated by several research groups, leading to a variety of approaches. The integration of an organic or inorganic moiety to enhance the tensile strength has been explored, with silicate[259], graphite nanoplatelets[260] and carbon nanotubes[261,262] being incorporated into the polymeric structures by research groups looking to reinforce the single fibre strength. Whilst these techniques have significantly improved the individual fibre strength and associated Young's modulus, this approach is often costly, and the use of silicate or inorganic nanoparticles can lead to adverse effects if detached from the membrane *in vivo*. Welding or soldering of the fibres to enhance the junction points of the fibre mat is an alternative, effective approach in improving its strength. Yoon *et al* investigated the effect of using mixed solvents to improve the inter-fibre junction, creating 'nano-trusses'[263]. Dimethylformamide (DMF) and *N*-methyl-2-pyrrolidone (NMP) were used to weld the fibre junctional points and enhance its mechanical strength. Whilst this is an effective approach, adding highly toxic (and potentially carcinogenic) solvents to the membrane will lead to an increase in residual solvent presence in the fibrous membrane, creating adverse effects once implanted into the sub-retinal space. Recently, Huang *et al* demonstrated a less invasive post-treatment approach to enhance the strength of the junctional points of the membrane without greatly changing its morphology[264]. Through the use of DMF, the electrospun membranes were exposed to a highly volatile solvent, increasing the number of fibre-contact points throughout the membrane and improving its mechanical strength. Whilst the post-electrospinning approach is favourable in reducing the chances of morphological alterations in the strength-enhancement process of the membrane, the use of a potentially carcinogenic solvent has to be avoided if the membrane is to be used for medical applications.

Therefore, with welding/soldering processes, 'nano-truss' techniques and volatile solvent exposure not being suitable for the enhancement of the BrM mimetic, an investigation into the incorporation of an organic moiety was carried out, looking at strengthening the membrane whilst preventing the risk of adverse effects arising from membrane-detachment. Providing an additional organic substituent to the co-polymer membrane allowed for the incorporation of strength-enhancing technique known as 'cross-linking'.

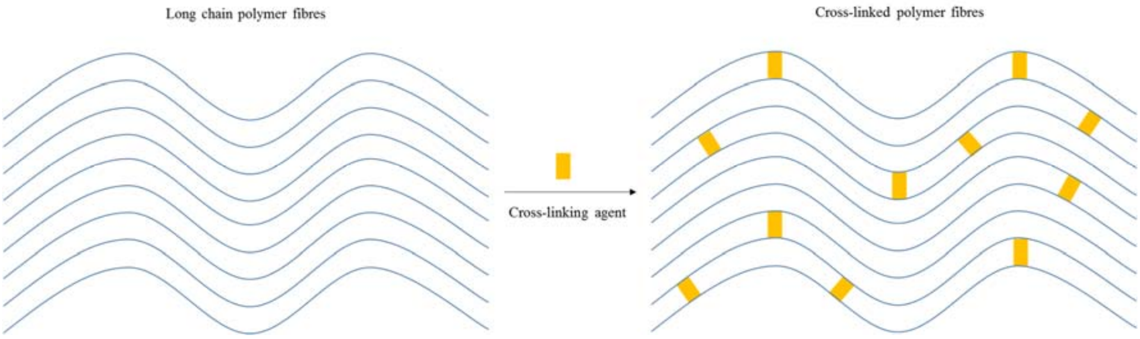

Figure 68: Representative drawing of polymer fibres (blue), showing the effect of an application of a cross-linking agent (orange) on the polymer fibres. A cross-linking agent is able to form covalent/ionic bonds to the polymer fibres, linking adjacent fibres and forming a tighter and mechanically stronger membrane.

Cross-linking can be defined as a 'reaction involving sites or groups on existing macromolecules, or an interaction between existing macromolecules, that results in the formation of a small region in a macromolecule from which at least four chains emanate'[265] (Fig. 68). Macromolecules such as a polymer chain can be inter-connected *via* permanent or reversible reactions, forming tighter fibre interactions and connections, leading to fibres that can be manipulated *via* the cross-linking mechanism to improve their thermal, mechanical and physicochemical properties. Since the fields of applications of polymer fibres are various and numerous, cross-linking reactions have been intensively studied for a long time, leading to a variety of types of cross-linking (Table 6). One example of cross-linking is the chitosan reaction with glycerol-phosphate[266,267]. The interaction between the cationic polysaccharide chitosan and the anionic glycerol-phosphate leads to an ionic cross-linking effect, allowing the polymer system to develop thermosensitivity[268]. The most stable form of cross-linking involves the covalent addition of a 'linking agent' that joins together two strands of long chain molecules. It is commonly used in biomaterials such as collagen, when glutaraldehyde[269] or hexamethylene diisocyanate (HDI)[270] is applied to provide structural stability and decrease the susceptibility towards enzymatic degradation. This method can be carried out pre- or post-membrane formation, with the rate of cross-linking controlled by the amount of the 'cross-linking agent' applied to the membrane, allowing greater flexibility with regards to strength enhancement (i.e. controlling the degree of structural stability).

In view of the flexibility and control associated with cross-linking strength enhancement, experiments were undertaken to look at improving the mechanical strength of the co-polymer membrane using this method.

Host membrane	Cross-linking agent	Type of cross-linking	Application	Comments	Reference(s)
Chitosan	Glycerol-phosphate	Ionic	Thermosensitive drug-delivery systems	Formation of a gel which has thermosensitive properties through the use of Chitosan cross-linked with glycerol-phosphate in 0.1M hydrochloric acid (HCl).	[266,267]
Collagen	Hexamethylene diisocyanate (HDI)	Covalent	Investigations into cross-linking collagen	Dermal sheep collagen were cross-linked using HDI in a phosphate buffer. Resulting mechanical studies showed an increase in tensile strength and elongation at break.	[270]
Polydioxanone & Elastin	1-ethyl-3-(dimethylaminopropyl)-carbodiimide (EDC)	Covalent	Electrospun vascular grafts	Polydioxanone - Elastin co-polymer electrospun membranes were cross-linked using EDC in a carboxylic acid – carbodiimide reaction, with significant increase in resistance to stress.	[271]
Gelatin	HDI	Covalent	Tissue engineering scaffolds	Gelatin and HDI are co-electrospun through the use of a double-barrel syringe into a polymeric mat, and cross-link *in situ* on the polymer surface.	[272]
Polybutadiene	Tri-methylol-propane 3-mercaptopropionate	Radical	Material Engineering	UV irradiation created a radical environment, which catalysed a rapid radical cross-linking effect on the host polymeric membrane.	[273]
Polystyrene	Difurfuryl adipate	Covalent	Reversible thermal materials engineering	Formation of a Diels-alder thermally reversible polystyrene, through the use of a Furfuryl and maleimidyl group.	[274]

Table 6: Table highlighting the varying types of cross-linking, detailing the polymer membrane used, the cross-linking agent, the type of cross-linking and its application.

5.2 Solution-based cross-linking

The investigation into cross-linking began with a solution-based procedure.

Solution-based cross-linking introduces the cross-linking agent either in the polymer synthetic stage[275] or post-synthesis[276]. The preparation of a desired polymer species can be carried out alongside the selected cross-linking agent, generating a ‘one-pot’ production of the required polymer and increasing efficiency.

Post-polymer synthesis cross-linking can also be carried out in solution, as demonstrated by McClure *et al*[271]. With the aim of producing an electrospun membrane which acts as a vascular graft, the research group required a membrane to show good tensile strength. The introduction of a cross-linking agent post-membrane formation in solution provided a membrane that had significant improvements in its tensile strength. The electrospun polydioxanone – elastin membrane was immersed in ethyl alcohol and 1-ethyl-3-(3-dimethylaminopropyl)-carbodiimide (EDC) was added, causing a cross-linking effect and improving the tensile strength of the electrospun matrix. Whilst this method proved effective, the use of ethyl alcohol would not be suitable for the BrM mimetic as methacrylates readily dissolve in alcohol.

Therefore, an investigation was carried out looking at suitable solution-based cross-linking methods.

5.2.1 DSC cross-linking

First investigations into the potential of a cross-linking enhancement involved the use of *N*,*N*’-Disuccinimidyl carbonate (DSC) as a covalent cross-linking agent. DSC is a highly reactive species that can facilitate the formation of carbamates and acetic anhydrides with a high reactivity towards amine and hydroxyl groups[277,278], and is used within the BrM mimetic synthetic process (Chapter 1 - the MMA:PEGM blend is functionalised with the DSC group to form a surface that allows RPE cells to attach and proliferate from). Work carried out previously by the research group had found that prolonged reaction times in the functionalisation step of the co-polymer synthesis had produced a gel-like substance. This is indicative of a cross-linking effect (Fig. 69).

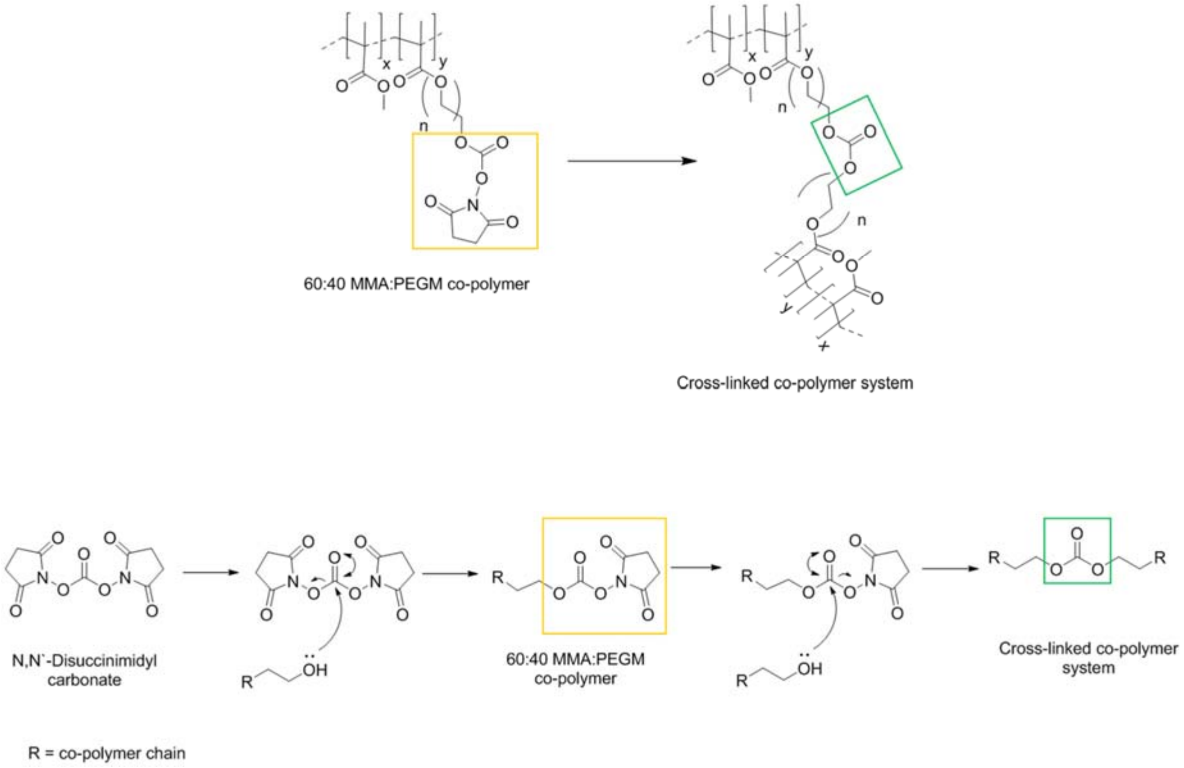

Figure 69: Reaction scheme showing the cross-linking of the succinimidyl carbonate side-chain (yellow) of the co-polymer membrane to the carbonate-based (green) cross-linked co-polymer system. This involves the repeated nucleophilic attack of the hydroxyl side-chain of poly(ethylene glycol) methacrylate from the co-polymer chain at the carbonyl group of N,N'-disuccinimidyl carbonate, leading to the carbonate cross-linked co-polymer membrane.

Triethylamine (TEA) is a catalyst for both the functionalisation of DSC to the co-polymer membrane and for the cross-linking action of an adjacent PEGM hydroxyl side chain. This method of cross-linking was not carried forward into an acceptable approach for membrane strength enhancement as the percentage of cross-linking was not controlled and the cross-linking of the RPE-binding site of the co-polymer blend would negate the ability of the co-polymer membrane to act as a RPE-binding surface.

5.2.2 Diels-Alder cross-linking

The initial investigation showed that whilst the potential for cross-linking was available, it should not be carried out by the functionalising side-chain of the co-polymer membrane and that it should be controlled. Therefore, an alternative solution-based approach was explored, which involved incorporating a third monomer into the co-polymer membrane using Diels-Alder chemistry.

Diels-Alder ‘click’ chemistry involves the coupling of an electron-rich diene (for example furan) and an electron-poor dienophile (for example - maleimide), through a 4+2 cycloaddition, to form a stable cyclohexane adduct (Fig. 70). It is one of the most common reactions used in organic chemistry, discovered by Otto Diels and Kurt Alder (for which they were awarded the Nobel Prize in 1950)[279].

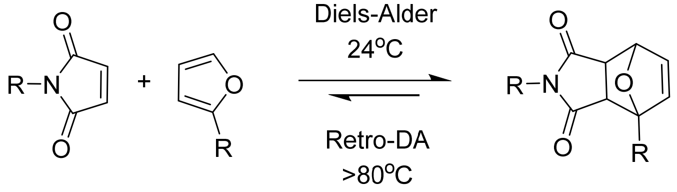

Figure 70: Reaction scheme showing the reversible thermoresponsive coupling of a maleimide and a furan (left) to form a stable cyclohexane adduct (right). This coupling occurs at 24°C, and has the ability to decouple at higher temperatures (>80°C) in a retro diels-alder reaction.

Some attractive features of Diels-Alder reactions include thermal reversibility and the ability to be controlled by temperature. The reaction can be carried out in aqueous media, which is advantageous for the cross-linking of the BrM mimetic as the membrane is fully solvated by alchohol-based solvents, and the product is insensitive to hydrolysis thereby enhancing its long-term stability.

Incorporation of this functionality to the BrM mimetic will allow for a controlled increase in tensile strength through its thermal reversibility. In order for the cross-linking to occur, the electron-rich diene was incorporated into the co-polymer membrane *via* the addition of a third monomer into the carbon-carbon backbone. A small percentage of the co-polymer blend would be involved in the cross-linking mechanism. This would theoretically avoid the formation of a gel-like substance[271], which cannot be electrospun into a fibrous mat[280]. Furfuryl methacrylate (FMA) (Fig. 71) was added to the membrane at a ratio of MMA:PEGM:FMA (58:40:2, w:w). By reducing the MMA ratio whilst maintaining the percentage of PEGM, the membrane retained its cell-binding functionality whilst allowing for an improvement in its tensile strength. Once the co-polymer membrane had been produced, it was functionalised with the DSC cell-binding side-chain and then exposed to a bis-maleimide ‘cross-linking agent’ (1,1’-(Methylenedi-4,1-phenylene)bismaleimide) to induce cross-linking.

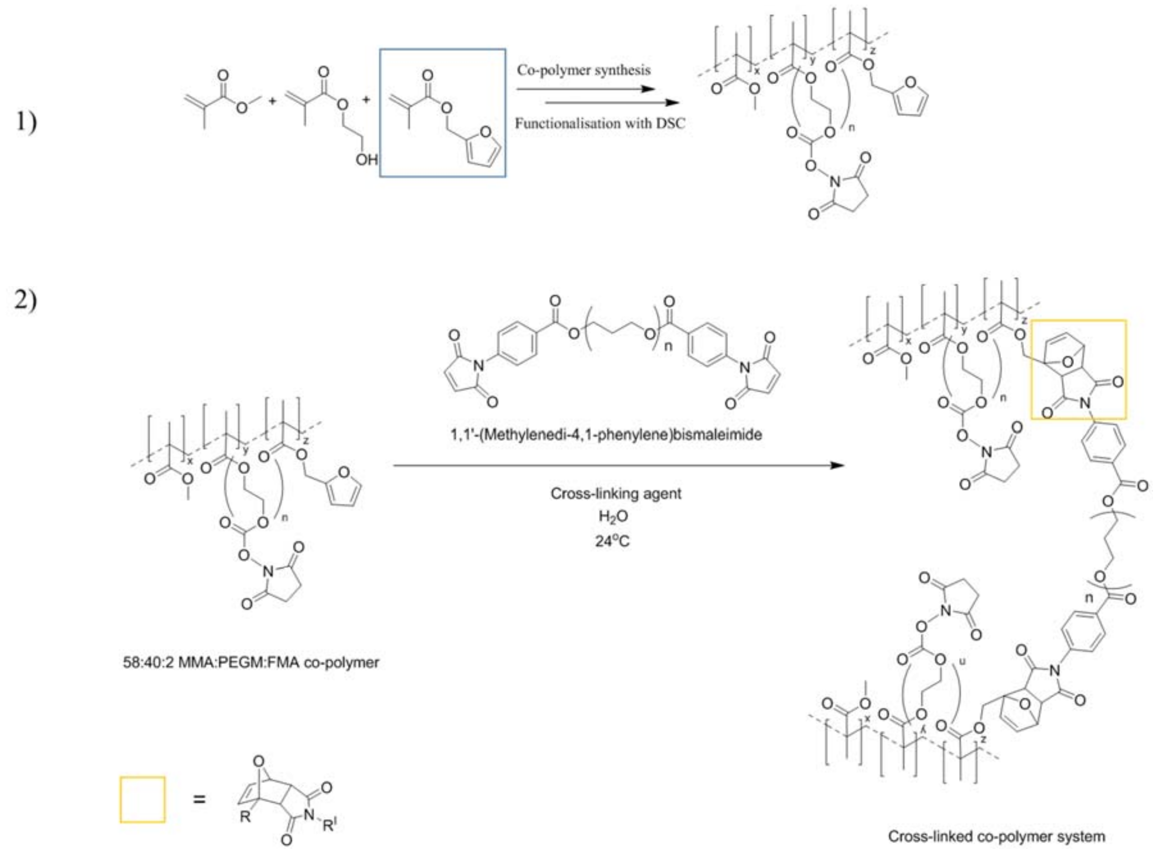

Figure 71: Reaction schemes showing 1) the formation of the furfuryl methacrylate (FMA) incorporated co-polymer system, with FMA (blue) added in a 58:40:2 (MMA:PEGM:FMA) (w:w) ratio and 2) the cross-linking mechanism showing the formation of a covalent cross-linked co-polymer system using Diels Alder (yellow) chemistry.

However, contrary to predictions, the co-polymer solution instantly formed a gel-like substance. This could therefore not be carried forward as it is not possible to electrospin a gel[280]. To understand the effect of incorporating a third monomer into the co-polymer system, the non-crosslinked membranes were electrospun into fibrous membranes, showing good surface topography and the required interwoven matrix (Fig. 72). Non-crosslinked species also showed good biocompatibility with an ARPE-19 immunofluorescent assay (Fig. 72), therefore an important observation was made in that small monomer modification did not alter the existing properties of the membrane.

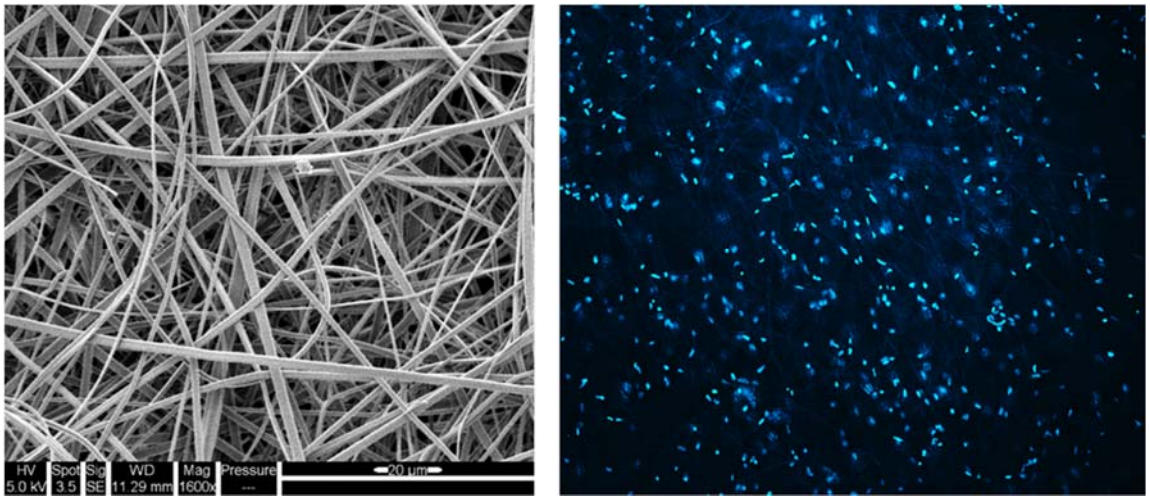

Figure 72: FMA-infused co-polymer membrane assays, highlighting (left) the topography of the membrane and (right) the proliferative activity of ARPE-19 cells on its surface. The incorporation of a third monomer into the co-polymer blend at a small percentage (2%) did not alter its surface topography, as indicated by scanning electron microscopy (left), or its biocompatibility (highlighted by the extent of ARPE-19 proliferation, right).

With this observation made, an alternative approach was investigated through the incorporation of a third monomeric unit.

5.3 Investigation into post-electrospinning crosslinking

In view of the continual formation of a gel in solution-based cross-linking approaches, an investigation was carried out into a post-electrospinning cross-linking method. The aim was to: (i) synthesise the co-polymer membrane with the cross-linking element incorporated into the structure; (ii) electrospin the fibrous mat; and (iii) provide a stimulus that would allow cross-linking to occur once the BrM mimetic had been produced. This would ensure that a fibrous matrix was synthesised, removing the complication of electrospinning a gel and the requirement for a cross-linking agent. It would allow for cross-linking strength enhancement to occur and ensure that there were no side-reactions.

Post-electrospinning crosslinking is an approach that has involved many differing methods. Ultraviolet (UV) stimulation of electrospun fibres to induce a cross-linking effect can be achieved through the use of a photoinitiator. Zhou *et al*[281] discovered that mixing a blend of pentaerythritol triacrylate (PETA) and poly(ethylene oxide) then electrospinning the required membrane, followed by UV irradiation, produced a cross-linked polymer mat. PETA forms an excited triplet state when exposed to UV irradiation, and this then combines with poly(ethylene oxide) to form a radical species, creating a series of cross-linked chains. This exposure to UV light was carried out once the electrospun membrane had been collected onto the metal collector, providing a post-electrospinning cross-linking method. Whilst this method showed a significant improvement in the mechanical studies, PETA was not incorporated into the polymeric species until after cross-linking, thereby leaving potential unwanted unreacted starting materials. Another investigation into the use of UV stimuli, led by Xu *et al*[126], employed a poly(ethyleneimine)-co-glycidyl methacrylate polymer arrangement to allow photo-cross-linking to occur. As a result of the addition of a glycidyl methacrylate side chain, stimulation through UV light would allow cross-linking across this side chain to occur, improving the tensile strength of the membrane. Unfortunately this polymer blend showed a tendency to aggregate before electrospinning had proceeded, rendering it very difficult to electrospin and highlighting the uncontrolled nature of this cross-linking approach.

Heat stimulation of electrospun fibres can also lead to a degree of cross-linking. Sullivan *et al*[282] discuss the ability of cross-linking β-Lactoglobulin through the application of heat for applications in drug delivery and tissue scaffolds. β-Lactoglobulin and poly(ethylene glycol) were co-electrospun into a fibrous mat and the stability of the fibres was improved by covalent cross-linking of β-Lactoglobulin at 70°C, when disulphide bonds between neighbouring chains were formed[283]. This method is an attractive option, though the use of β-Lactoglobulin disulphide cross-links caused the sample to become less soluble in aqueous media, which is less desirable for the BrM mimetic.

An attractive option from the researched articles in relation to the enhancement of the artificial BrM involved the use of UV light to cross-link the membrane, since UV irradiation is used to sterilise the artificial BrM prior to cell culture or sub-retinal implantation assays. This had the potential to allow a cross-linking stimulus without the requirement of inserting a cross-linking agent, providing the photoinitiator was already part of the co-polymer backbone. However, since the current methods in providing a post-electrospun treatment to the co-polymer matrix are unsuitable for the BrM mimetic, an alternative approach was required.

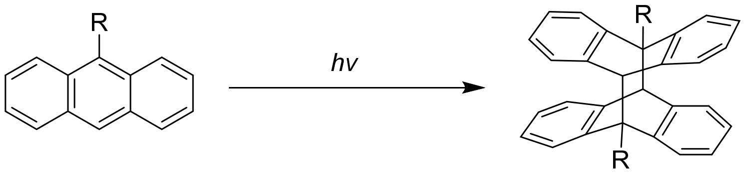

Figure 73: Reaction scheme showing the photo-dimerisation of two anthracenyl groups to form a di-anthracenyl arrangement. This coupling occurs under ultraviolet (UV) light, and has the potential to act as a cross-linking agent.

Another UV-sensitive compound, anthracene[284], is a polycyclic aromatic hydrocarbon consisting of three benzene rings fused together. It can photodimerise under the presence of UV light[285] (Fig. 73), creating two covalent carbon-carbon bonds which combine the anthracene molecules in a [4π + 4π] photo-dimerisation. It is a molecule whose detailed photochemistry has been investigated since the 1950's [286,287], highlighting its UV sensitivity and noting in particular its dimerization in a predominantly 'head-to-tail' arrangement. Significantly, initial MTT assays for cytotoxity found no significant changes in the presence of anthracene, indicating that the incorporation of this molecule into the co-polymer membrane would not lead to any cytotoxic effects[288].

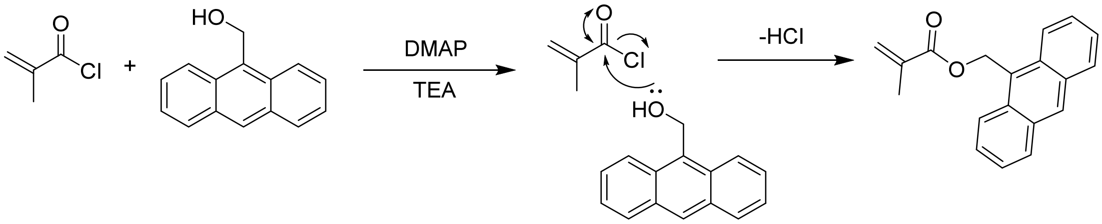

Figure 74: Reaction scheme showing the formation of 9-anthracenyl methacrylate (AMM), which can then be applied in the methacrylate-based co-polymer system used to synthesise the Bruch membrane mimetic.

In order to incorporate the anthracene molecule into the co-polymer system, and for it to provide a suitable cross-linking effect on the membrane, it needed to be integrated with the carbon-carbon backbone of the co-polymer blend by incorporating the anthracene molecule as part of the side chain. Therefore, the synthesis of an anthracenyl methacrylate was investigated to allow suitable incorporation into the methacrylate-based co-polymer system. As detailed by Sakamoto et al[174], a 9-anthrylmethyl methacrylate (AMM) was shown to be synthesised through the reaction of of 9-hydroxymethylanthracene with methacryloyl chloride (Fig. 74).

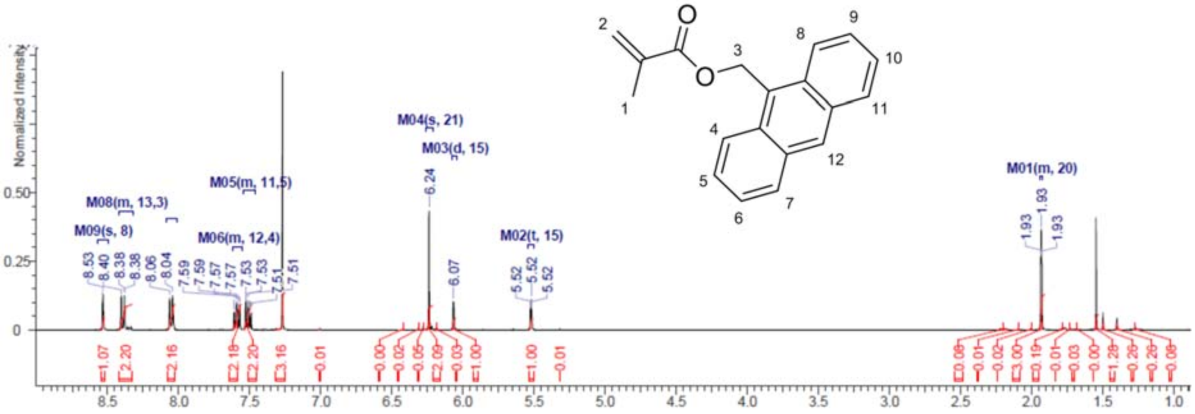

Figure 75: ^{1}H NMR spectrum of the synthesised 9-anthrylmethyl methacrylate (AMM), showing the required peaks at: 1.93 ppm (singlet (s), integral of 3 protons (3H), proton assignment 1 (H1)); 5.52 (s, 1H, H3); 6.07 (s, 1H, H3); 6.24 (s, 2H, H2); 7.52 (t, 2H, H10 & H6); 7.60 (t, 2H, H5 & H9); 8.05 (d, 2H, H7 & H11); 8.38 (d, 2H, H4 & H8); 8.53 (s, 1H, H12). This closely alligns with the reported ^{1}H NMR values in the literature[174].

Therefore, the AMM compound was produced (see Chapter 2.1.6) through the reaction of methacryloyl chloride and 9-hydroxymethylanthracene at 0°C, resulting in the desired yellow solid. NMR spectroscopy confirmed the successful production of the desired AMM compound (Fig. 75), with the produced spectra displaying all of the necessary peaks expected for this compound, further confirmed by comparison to the literature[174].

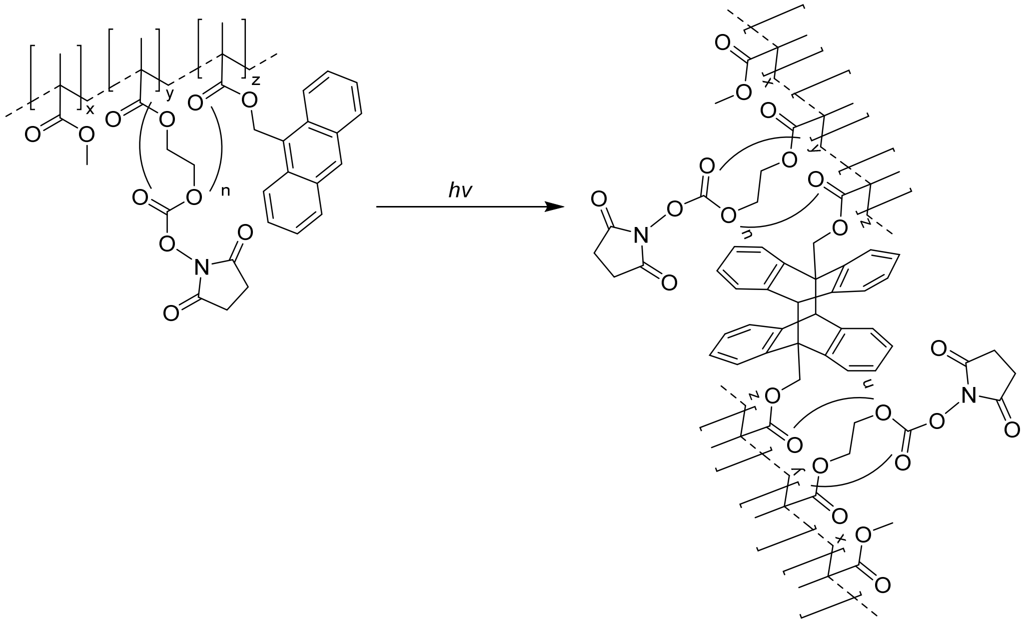

Figure 76: Reaction scheme showing the incorporation of AMM in the bruch membrane mimetic co-polymer membrane (left) and the UV-induced cross-linking mechanism (right), showing the effect of applying UV light on the co-polymer membrane.

This methacrylate-based anthracene derivative had the necessary carbon-carbon backbone which could then be incorporated into the co-polymer synthetic process to allow formation of an anthracenyl-infused co-polymer system (Fig. 76). Subsequent UV irradiation would then create a cross-linked anthracenyl-infused co-polymer.

Polymer sample number	MMA / %	PEGM / %	AMM / %
60:40	60	40	0
AMM-1	59	40	1
AMM-2	58	40	2
AMM-3	57	40	3

Table 7: Table summarising the co-polymer blends investigated, with small increments applied to the anthracenyl methacrylate (AMM) monomer whilst slightly reducing the methyl methacrylate (MMA) content. The ratio of poly(ethylene glycol) methacrylate (PEGM) remains constant.

AMM was introduced into the co-polymer synthetic process in differing percentage levels to investigate the effect of the incorporation of AMM to the co-polymer membrane (Table 7). Once the co-polymer blends had been produced, functionalisation of the PEGM side-chain with DSC was carried out and the required electrospun co-polymer mats were produced (Fig. 77).

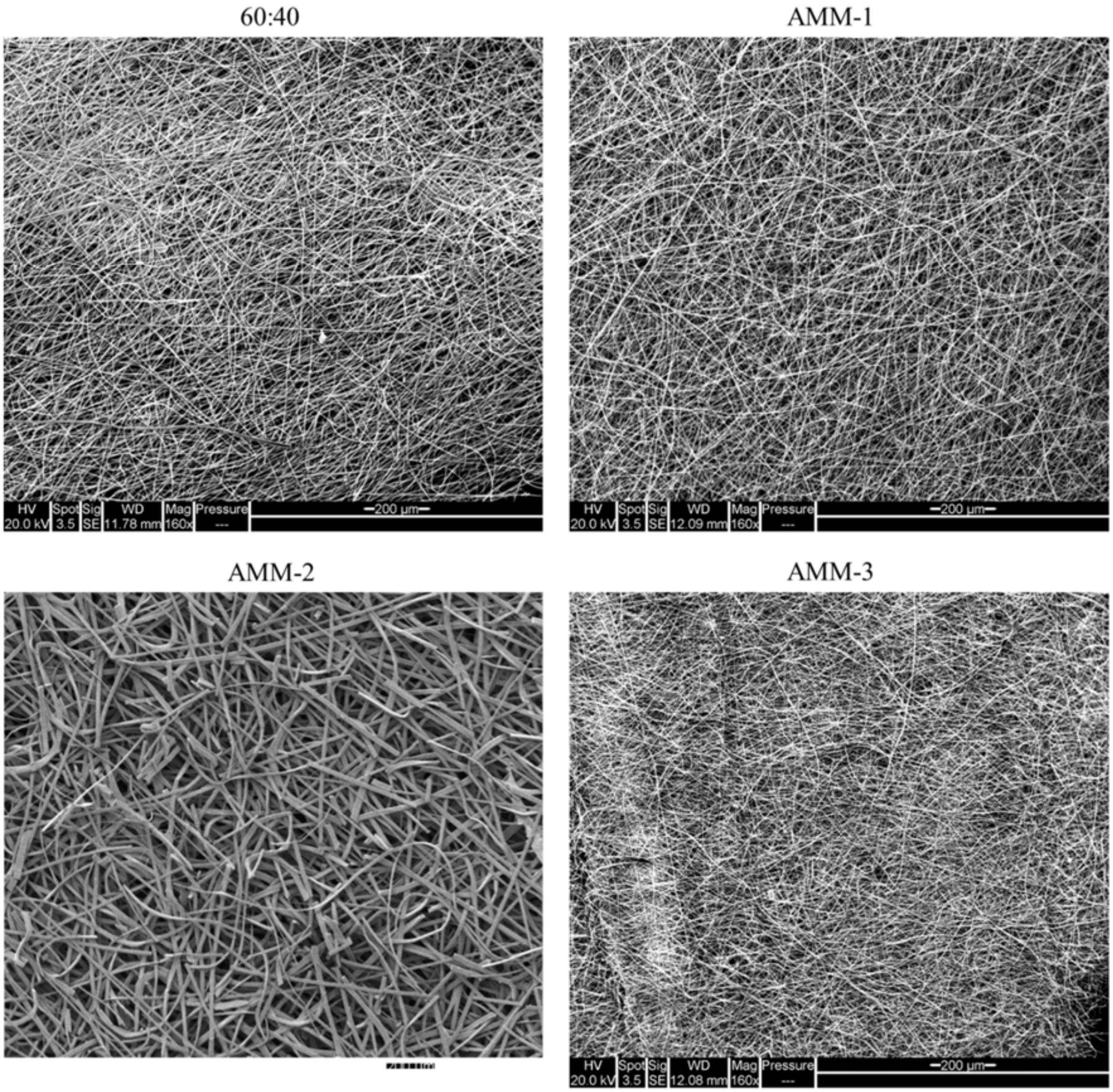
60:40

AMM-1

AMM-2

AMM-3

Figure 77: Scanning electron microscopy (SEM) of the co-polymer membranes, showing the topography of the electrospun Bruch membrane mimetics. Clockwise from top-left (60:40; AMM-1; AMM-3; AMM-2)

Samples were then cross-linked under UV irradiation for 24h. Anthracenyl co-polymer membranes appeared to ‘tighten’ after UV irradiation (Fig. 78), an indication of a cross-linking effect on the polymer fibres. SEM analysis of the irradiated co-polymer fibres showed a change in morphology of the co-polymer sample, showing a more aligned arrangement (Fig. 78). It had retained its fibrous nature, but the co-polymer fibres were in a more ordered topographical display.

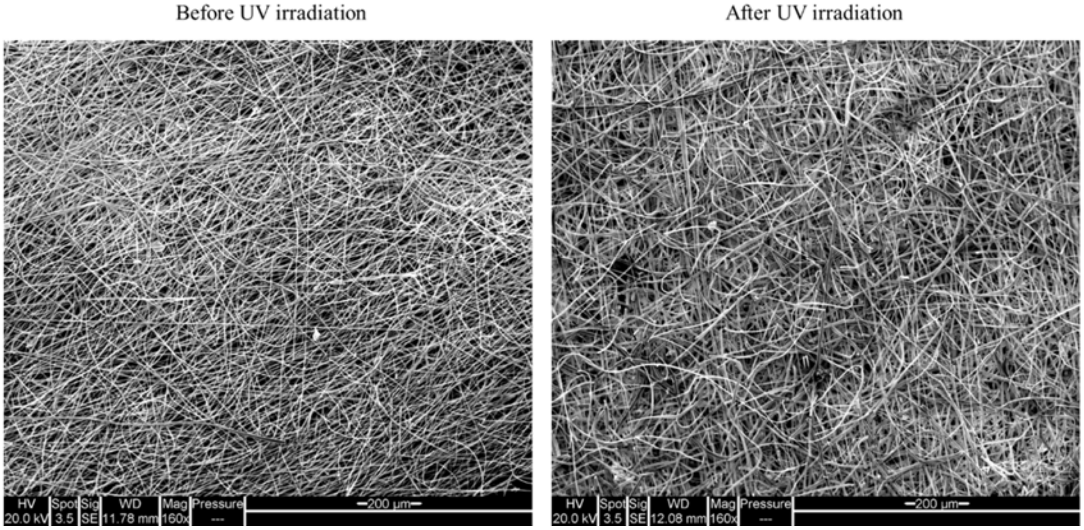

Figure 78: Scanning electron microscopy (SEM) of AMM-2, showing the topography of the membranes before (left) and after (right) UV irradiation cross-linking. Fibres appear more aligned after cross-linking.

5.4 Exploring the properties of the new generation of membranes

After the synthesis of the anthracenyl-infused co-polymer electrospun mat, a series of experimental tests were conducted to analyse the effect of AMM incorporation into the co-polymer blend, noting any changes in its mechanical strength, biocompatibility and diffusional properties.

5.4.1 Thickness measurements

In order to characterise the new generation of co-polymer membranes for its mechanical strength, its thickness needed to be quantified.

Electrospun anthracenyl-infused co-polymer membrane samples were placed on glass slides, coated with an ultrafine layer of gold *via* gold-sputtering and using the ZeMetrics ZeScope optical profilometer, thickness measurements were taken (Fig. 79).

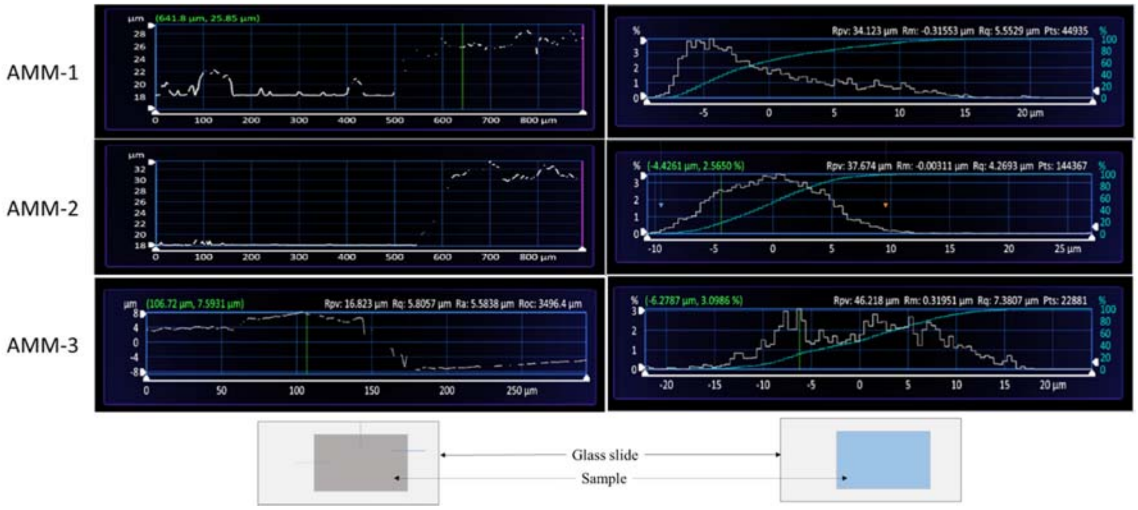

Figure 79: Thickness measurements of AMM-1, AMM-2 and AMM-3, showing both the optical profile (left) and the overall thickness of the membranes (right). Schematic underneath shows the measurement locations, with the thickness measurements taken at either cross-sections (blue, left) or over the entire membrane (blue, right).

From these measurements, it was realised that AMM-1 displayed an average thickness of 17µm, with an optical profile thickness of 11.7µm. AMM-2 showed an average thickness of 20µm, with an optical profile thickness of 12.3µm. AMM-3 displayed an average thickness of 28µm, with an optical profile thickness of 15.6µm. An apparent increase in thickness was noted as the percentage of anthracene methacrylate was raised within the co-polymer blend.

5.4.2 Characterising the tensile strength of the anthracenyl-infused membranes

The primary purpose of the cross-linking mechanism was to enhance the co-polymer membrane's mechanical strength. In order to characterise this change in tensile strength of the co-polymer membrane, a DEBEN Microtest module was used to stretch and apply stress to the membrane. As described previously for the 60:40 co-polymer variant of the designed membrane (Chapter 3.5), the anthracenyl-infused co-polymer membrane was placed on the DEBEN Microtest module, clamped into place and stretched. This allowed the characterisation of its Young's modulus (individual fibre strength), maximal stress before failure (the maximum amount of stress applied to the co-polymer membrane before membrane failure), the yield strength of the membrane and the overall calculated toughness of the membrane, whilst also providing a comparison with the 60:40 co-polymer membrane (both 51 ± 3µm and 12µm thick variants) and BrM.

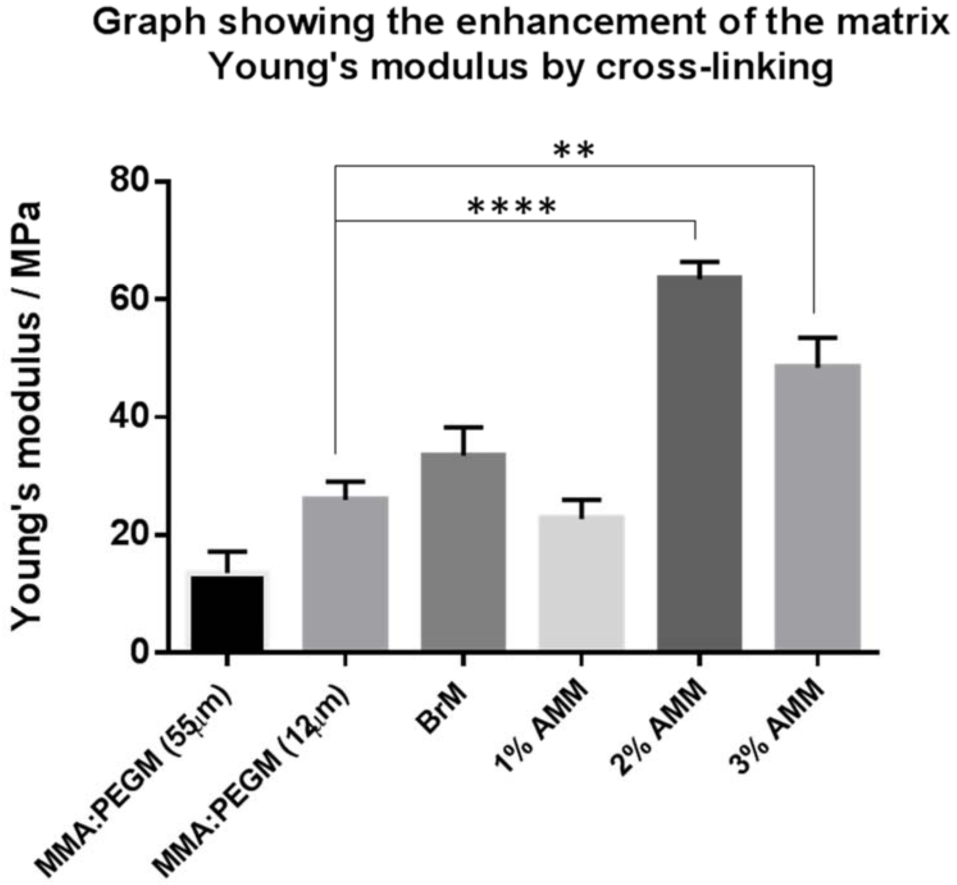

Figure 80: Graph showing the effect of cross-linking enhancement on the Young's modulus of the co-polymer membranes, comparing the previous iterations of the co-polymer matrix, native BrM and the new generation of co-polymer membranes.

The three anthracenyl-infused cross-linked co-polymer samples were tested on the DEBEN Microtest module and subsequent calculation of the Young's modulus found that for sample AMM-2, individual fibre strength was 63.4 ± 2.91 MPa (n = 6), which compared well with the non-anthracenyl based 60:40 co-polymer (25.9 ± 3.14 MPa, n = 6, significance of $p < 0.0001$). AMM-3 had a Young's modulus of 48.4 ± 5.13 MPa (n = 3, significance of $p = 0.0056$) and AMM-1 was 22.8 ± 3.29 MPa (n = 3, significance of $p = 0.6084$) (Fig. 80). Native BrM displayed a Young's modulus of 33.5 ± 4.78 MPa.

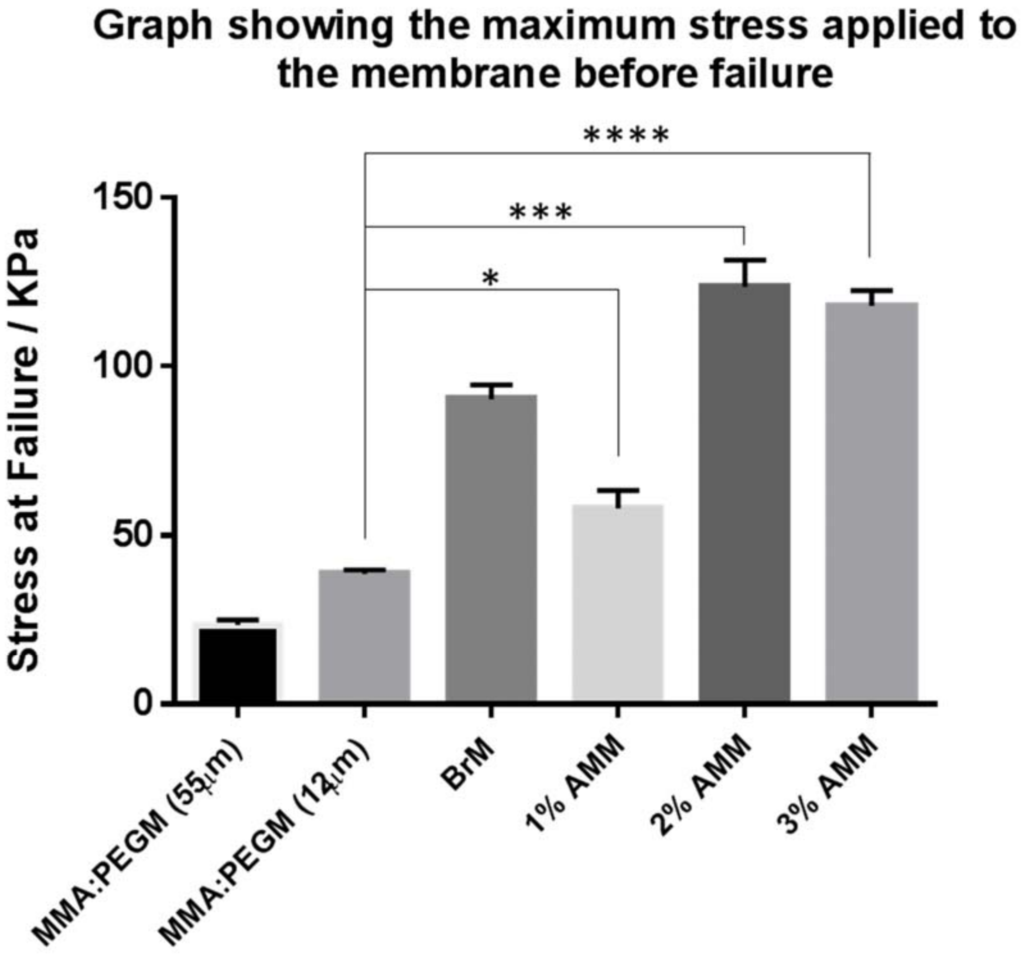

Figure 81: Graph showing the maximum amount of stress (kPa) before membrane failure, comparing the new generation of membranes with the previous generations and native BrM.

Maximal stress before failure was also tested, with AMM-2 displaying a maximal stress of 123.7 ± 7.84 KPa (n = 3) before failure, compared to the non-anthracenyl based 60:40 co-polymer, which withstood 38.7 ± 1.20 KPa (n = 3) before failure, a significance of p = 0.0004 (Fig. 81). AMM-3 showed a maximal stress before failure of 118 ± 4.58 kPa (n = 3), a significance of p < 0.0001, and AMM-1 was 58.1 ± 5.18 kPa (n = 3), a significance of p = 0.0186.

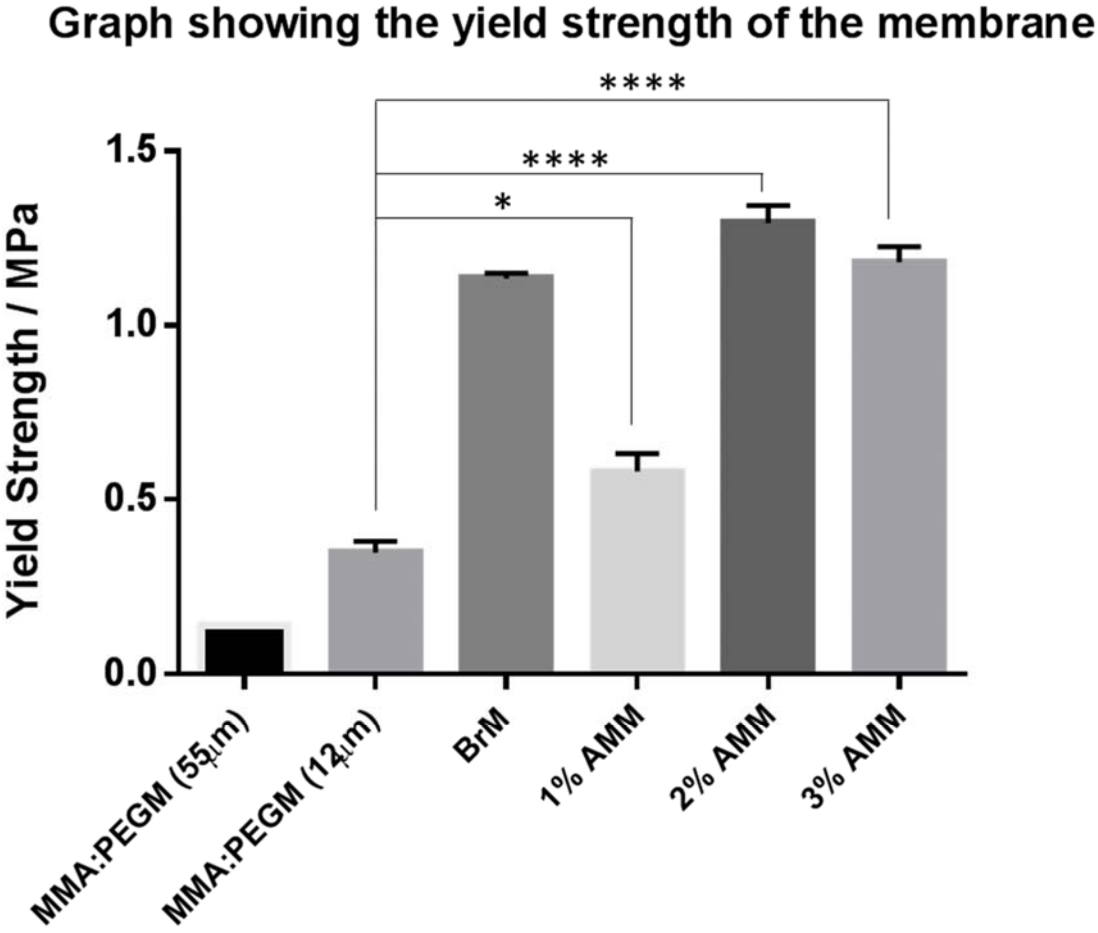

Figure 82: Graph showing the yield strength of each membrane, showing the difference in the membrane's strength when cross-linking is applied to the co-polymer.

The yield strength of the membrane was calculated; AMM-2 displayed 1.29 ± 0.05 MPa ($n = 6$), aligning the matrix closely with BrM (1.14 ± 0.015 MPa) whilst the 60:40 co-polymer membrane yield strength was 0.348 ± 0.03 MPa ($n = 6$), a significance of $p < 0.0001$ (Fig. 82). AMM-3 showed a yield strength of 1.18 ± 0.05 MPa ($n = 3$), a significance of $p < 0.0001$ when compared to the 60:40 co-polymer membrane, with AMM-1 showing a yield strength of 0.581 ± 0.05 MPa ($n = 3$), a significance of $p = 0.0109$.

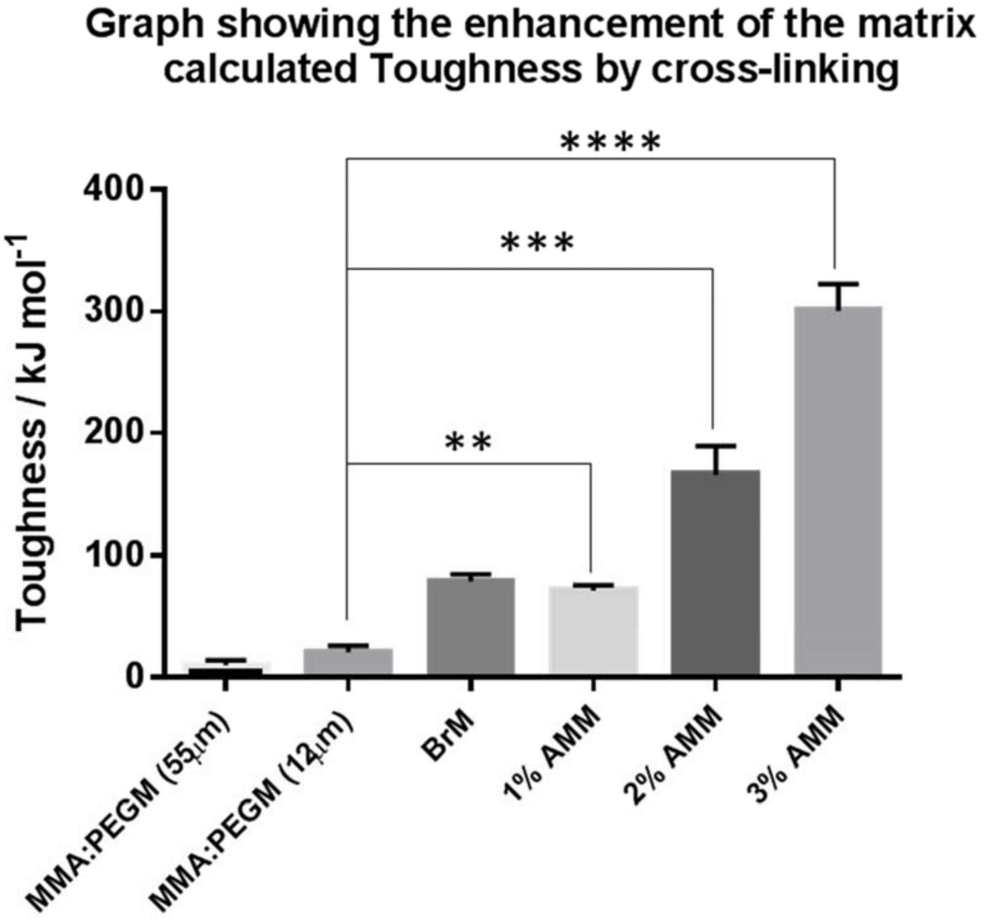

Figure 83: Graph showing the significant increase in membrane toughness when cross-linking is applied to the co-polymer matrix, highlighting the rising increase in the membrane's calculated toughness when AMM is applied and UV initiated.

Finally, the overall calculated toughness of AMM-2 was 166 ± 23.6 kJ mol^{-1}, compared to the previous generation of membranes (20.9 ± 5.24 kJ mol^{-1}) (Fig. 83), a significance of $p = 0.0001$. AMM-1 displayed a calculated toughness of 71.1 ± 4.61 kJ mol^{-1}, a significance of $p = 0.0022$, whilst AMM-3 displayed a calculated toughness of 300 ± 22.1 kJ mol^{-1}, a significance of $p < 0.0001$.

5.4.3 Testing the new generation of membranes for biocompatibility

With the observed increase in tensile strength, the new generation of co-polymer membranes were then tested for their biocompatibility, assessing any changes in RPE attachment or proliferation.

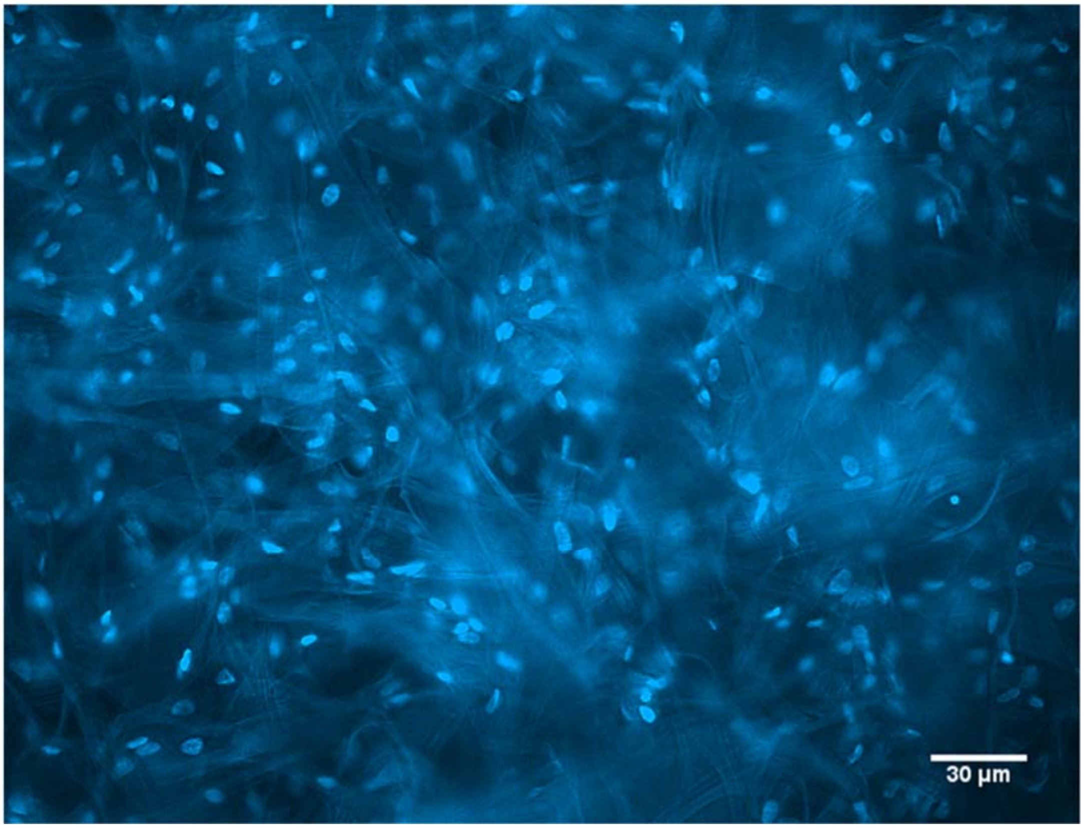

Figure 84: Representative immunofluorescent image of seeded ARPE-19 cells on the surface of an AMM-2 co-polymer fibrous mat, showing the extent of ARPE-19 cell distribution and proliferation after 10 days in cell culture. Cell nuclei stained with DAPI (light blue) and ARPE-19 cell seeded membrane imaged by fluorescent microscope.

Initial biocompatibility assays began with ARPE-19 cell seeding. As detailed previously (Chapter 3) ARPE-19, a spontaneously arising human RPE cell line, were seeded onto the surface of anthracenyl-infused co-polymer membranes and cultured for 10 days. Samples were then fixed (PFA) and stained with DAPI to highlight the cell nuclei (Fig. 84). Cells are shown to be well distributed across the membrane and highlight good proliferative activity across the anthracenyl-infused co-polymer membrane, comparable to the previous 60:40 co-polymer membranes.

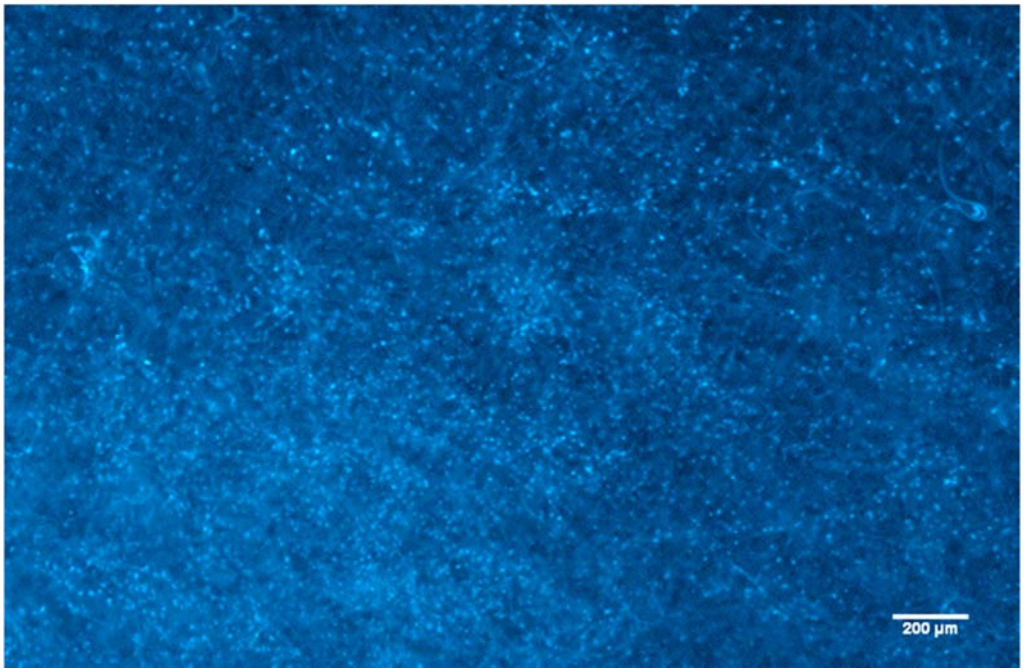

Figure 85: Representative immunofluorescent image of primary murine RPE cells seeded onto the surface of AMM-2 co-polymer fibres. Cell nuclei were stained with DAPI and image generated by fluorescent microscope.

After initial ARPE-19 assays were completed, a primary murine RPE cell culture was established on the surface of the new generation of co-polymer membranes. As described previously (Chapter 4), primary murine RPE cells were isolated from mouse eyes and seeded onto the surface of the anthracenyl-infused co-polymer membranes. Immunofluorescent DAPI staining showed good cell distribution and proliferation (Fig. 85). The extent of RPE cell coverage on the surface of the co-polymer membrane showed that there were no adverse effects of the anthracenyl incorporation into the co-polymer blend.

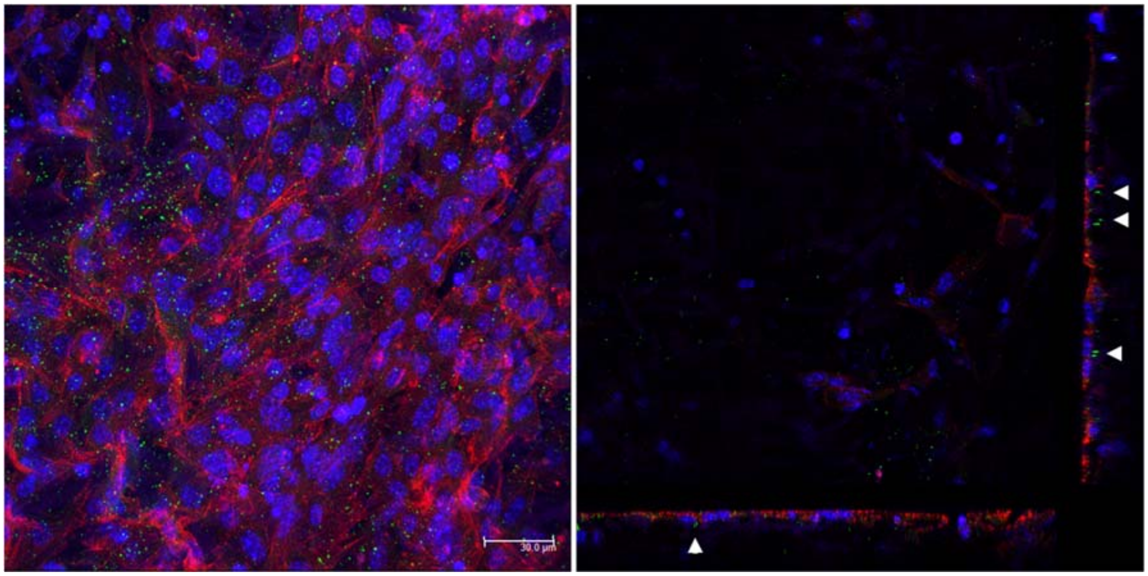

Figure 86: Representative mmunofluorescent images of primary RPE cells on the surface of AMM-2 co-polymer fibres, highlighting (left) the extent of RPE cell coverage (scale bar - 30µm) and (right) orthogonal sections showing the presence of focal adhesion kinase (FAK, punctate green marks highlighted by white arrows) throughout the RPE monolayer and indicating an established cell layer with focal adhesions to the anthracenyl-infused artificial BrM. Sample counterstained with DAPI (blue) and phalloidin (red).

Immunofluorescent focal adhesion kinase assays of RPE cells on the surface of the membrane indicated cell-to-substratum complexes were being formed with the matrix, highlighting an established RPE cell line on the anthracenyl-infused co-polymer matrix (Fig. 86).

After confirmation of cell proliferation and attachment to the surface of the co-polymer membrane, the expression of the RPE-specific protein (RPE-65) was characterised by immunofluorescent tagging with an anti-RPE65 antibody (Fig. 87).

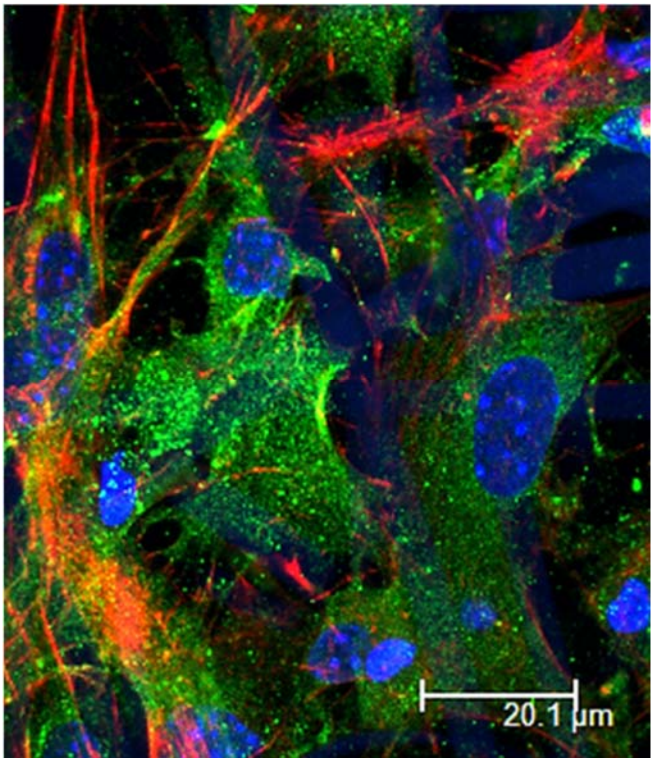

Figure 87: Representative immunofluorescent image of 3 month cultures of primary RPE cells on the surface of AMM-2 fibres, showing extensive expression of the RPE-specific protein RPE65 (green). Sample counterstained with DAPI (blue) and phalloidin (red).

Immunofluorescent analysis showed good distribution of RPE65 throughout the RPE layer, highlighting the presence of phenotypically-stable RPE cells.

Scanning electron microscopy (SEM) was utilised to show the distribution of the RPE layer on the surface of the anthracene co-polymer. Three month primary RPE samples on the surface of AMM-2 co-polymer fibres were incubated in 3% glutaraldehyde, 4% formaldehyde and 0.1M 1,4-piperazinediethanesulfonic acid (PIPES) in PBS for 1h at 4^{o}C, freeze-dried for 3h and then gold-sputtered (Fig. 88).

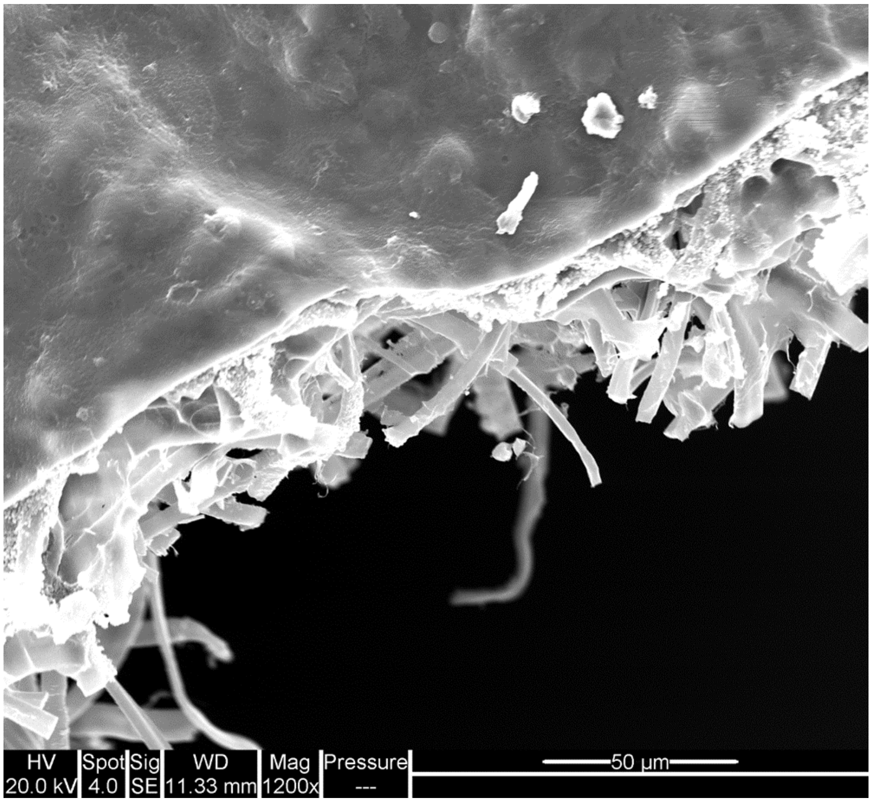

Figure 88: Side-on view of 3 month primary RPE cell layer on the surface of AMM-2 fibre mat, showing the continual fine layer overlaid on the AMM-2 matrix. Image generated by scanning electron microscopy (SEM).

SEM analysis showed a continual layer of RPE cells on the surface of the anthracenyl-infused co-polymer membrane (AMM-2), displaying the expected RPE surface morphology.

5.4.4 Diffusional properties of the anthracenyl-infused co-polymer matrix

With the biocompatibility of the co-polymer membranes established, showing good RPE attachment and expression of key RPE proteins, the ability of the membrane to provide a barrier to macromolecular diffusion was tested. As detailed previously with the previous generation of membranes (Chapter 3.5), a sample of the anthracenyl-infused co-polymer membrane was placed in the membrane casing inside the central reservoir of the Ussings chamber, and the diffusion of FITC-labelled dextran was measured using a colorimetric assay (Fig. 89).

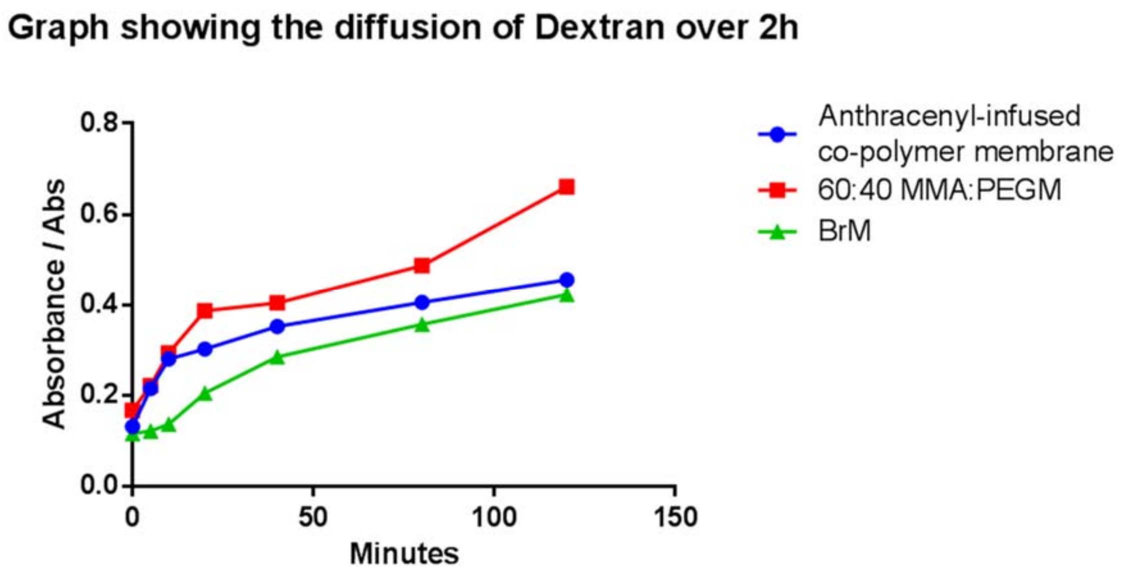

Figure 89: Graph showing a 2h diffusional study of the permeability of the anthracenyl-infused co-polymer membrane, measuring the amount of FITC-dextran passing through the membrane over time. The anthracenyl-infused membrane is shown to be more closely aligned to native BrM, reducing the permeability of the BrM mimetic by cross-linking.

After a period of 2h, it was clear that the amount of dextran diffused through the anthracenyl-infused co-polymer membranes had reduced, indicating a less permeable membrane and aligning it more closely to native BrM.

5.4.5 Curling of the co-polymer membranes *in vitro*

Anthracenyl-infused co-polymer membranes were tested to analyse the effect of curling in cell culture. The 60:40 MMA:PEGM co-polymer samples were previously found to curl and fold onto themselves after a long period in cell culture, and one of the requirements in strengthening the membrane was to ensure this effect did not continue.

Samples were monitored over 7 months in culture, with a comparison made from the new generation of anthracenyl-infused co-polymer membranes to the pre-existing 60:40 MMA:PEGM co-polymer membranes (Fig. 90).

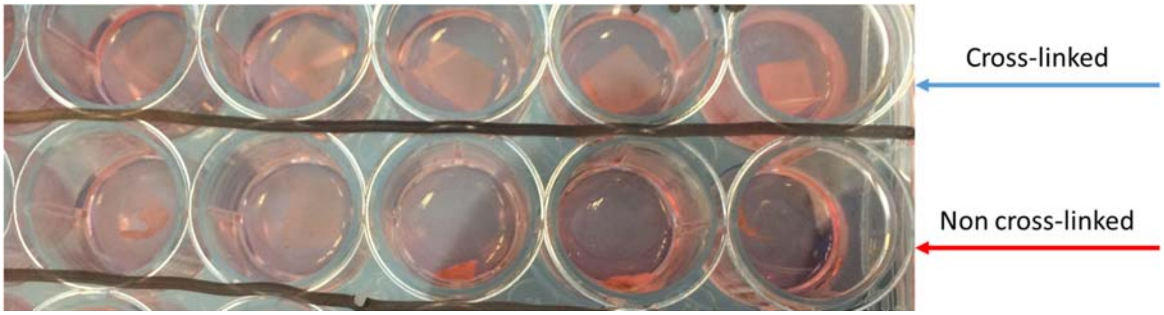

Figure 90: Image showing the effect of cross-linking on the membranes in tissue culture, showing (blue arrow) the row of cross-linked co-polymer membranes and (red arrow) the row of 60:40 MMA:PEGM co-polymer membranes. The cross-linked membranes retain their flat shape as cut, whereas the non-anthracenyl membranes curl.

The new generation of artificial BrM samples were found to be substantially better at retaining their flat-shape in tissue culture than compared to the previous non-cross-linked co-polymer membranes.

Chapter 6: Discussion, Conclusions and Future Work

6.1 General Introduction

Accumulating evidence and research has indicated that the transplantation of a polarised and intact RPE monolayer supported by a prosthetic BrM, as an alternative route to an injection of a RPE cell suspension, is a more reasonable approach in the design of a suitable treatment for geographic atrophy or dry AMD[84,148,150,151,289].

As such, there have been many artificial BrM designs, incorporating natural or synthetic materials which allow a RPE layer to form its required monolayer[148,151,154,168]. However, many of these prosthetic BrM substrates have disadvantages in terms of their biocompatible and biophysical properties.

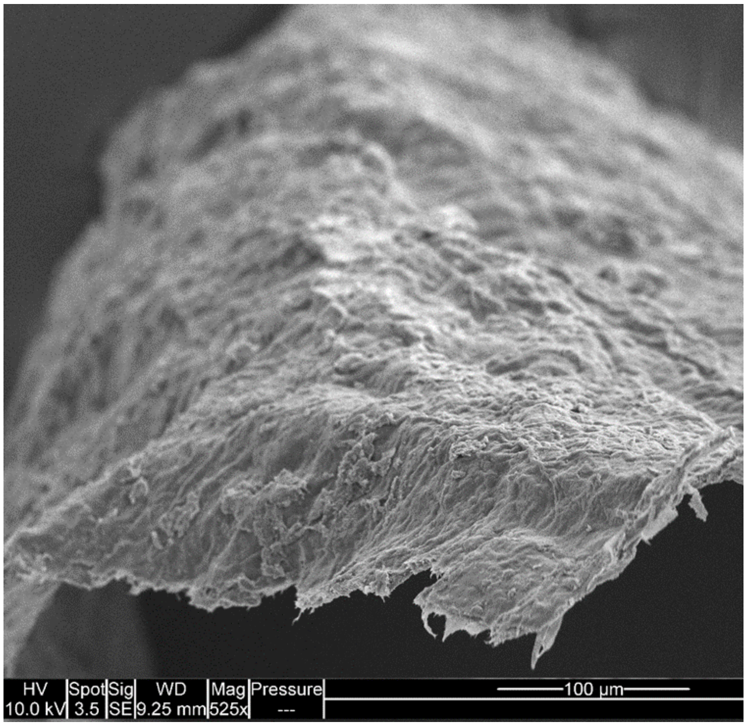

Figure 91: SEM of Bruch's membrane, highlighting the fibrous nature of the membrane.

A suitable artificial BrM should mimic the native BrM in: (i) its fibrous nature, to ensure good RPE cell attachment[149] (Fig. 91); (ii) its porosity, allowing a controlled diffusion of macromolecules; (iii) its thickness; (iv) its ability to show excellent biocompatibility; (v) maintaining integrity throughout the implantation process and thereby displaying good mechanical strength; and (vi) allowing a seeded layer of RPE cells to attach onto the substrate and perform all of its necessary physiological functions.

As detailed in Chapter 1.7, the aim of this project was to design an accurate artificial BrM onto which a layer of primary RPE cells could be seeded onto and maintain RPE-specific functionality. This mimetic would subsequently be the ideal carrier for a layer of regenerative RPE cells and would be required to maintain integrity during the implantation process.

Work carried out previously within the research group had designed a polymer blend which, when electrospun into a fibrous mat, had the potential to host a layer of RPE cells. Initial experimentation for this project started with the production of the existing generation of co-polymer membranes, synthesised using the same method as detailed previously (see Chapter 2.1.2 – 2.1.3)[127]. Once the co-polymer had been synthesised, it was electrospun (9.5ml/h; 15kV; 15cm distance to collector) into a polymer mat (Fig. 92). The generated mat was fibrous, which aligned it with the native ICL in BrM.

However, the thickness of the membrane was not known amongst other parameters and its efficacy as a suitable scaffold was not tested using the most suitable type of RPE cells.

6.2 Thickness measurements of the artificial BrM and native human BrM

Initial efforts on measuring the thickness of the artificial BrM were made *via* scanning electron microscopy (SEM). SEM was able to measure the individual fibre thickness by using the generated topographical images and comparing to the scale bar. Attempts were made to re-orientate the polymer fibre so that thickness measurements could be made using a side-on view (Fig. 92). However, due to the orientation of the membrane it would fold onto itself and cause a ‘buckling’ effect, making the co-polymer membrane thickness appear greater and the error associated with this method was too significant.

Therefore, alternative approaches were required. This led to the investigation into the use of an optical profilometer (ZeMetrics ZeScope). This technique was reported to be minimally invasive, had previously shown to measure samples at an angstrom-level resolution[190] and could measure samples with a flat orientation, removing the need to lie the sample on its side.

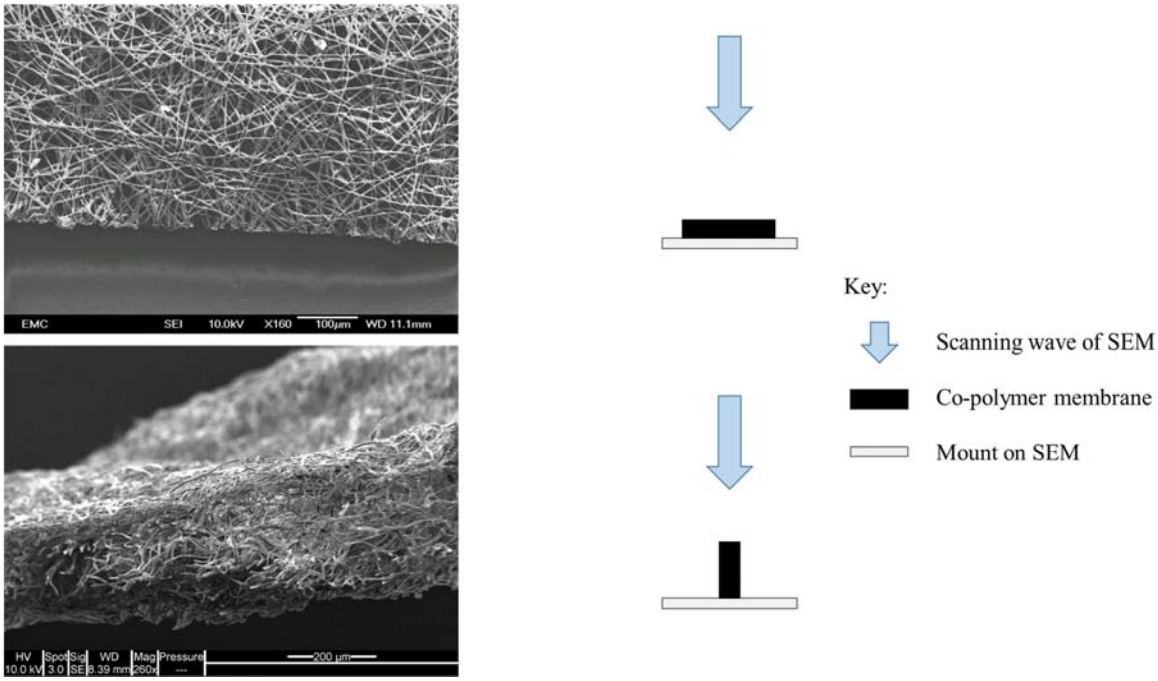

Figure 92: Representative SEM images of the first generation of prosthetic BrM, showing (top) the topographical view and (bottom) the side on view of the membrane. Representative diagrams are given alongside the SEM images showing the orientation of the membrane (black) with regards to the scanning wave (blue arrow).

A synthesised first generation artificial BrM was placed on a glass slide and analysed on the ZeScope optical profilometer. By comparing the membrane height to the base of the glass slide, a measurement in the difference in height gave the required thickness measurement. This was taken at a given point on the membrane (optical profile) and across the entire membrane (generating a histogram, see Chapter 3.2 Fig. 26). To understand the thickness of the co-polymer membrane generated, a histogram was produced to observe the overall thickness, giving a thickness of 51 ± 3µm. The fibre mats measured ranged from 48-54µm in thickness, leading to a large associated error. This could be due to the low voltage and high flow rate used in the electrospinning process, resulting in samples with individual fibre thickness' of 8-10µm. The range of fibres produced had a difference of 2µm, which can lead to large differences in the overall thickness of the membrane, whereas with thinner fibres these differences are reduced.

Use of the optical profilometer had allowed a further understanding into the properties of the first generation of synthesised co-polymer membranes. By orientating the membrane horizontally across a glass slide, the optical profilometer was able to generate a 3D map of the polymer mat and identify the edges of the membrane, thereby determining the thickness of the first generation of artificial BrM. A key component to any biocompatible synthetic tissue is its thickness; it influences the structural stability and diffusional properties and with the knowledge that the membrane was 51 ± 3μm in thickness, it could then be manipulated much more readily to mimic native BrM in a more accurate manner.

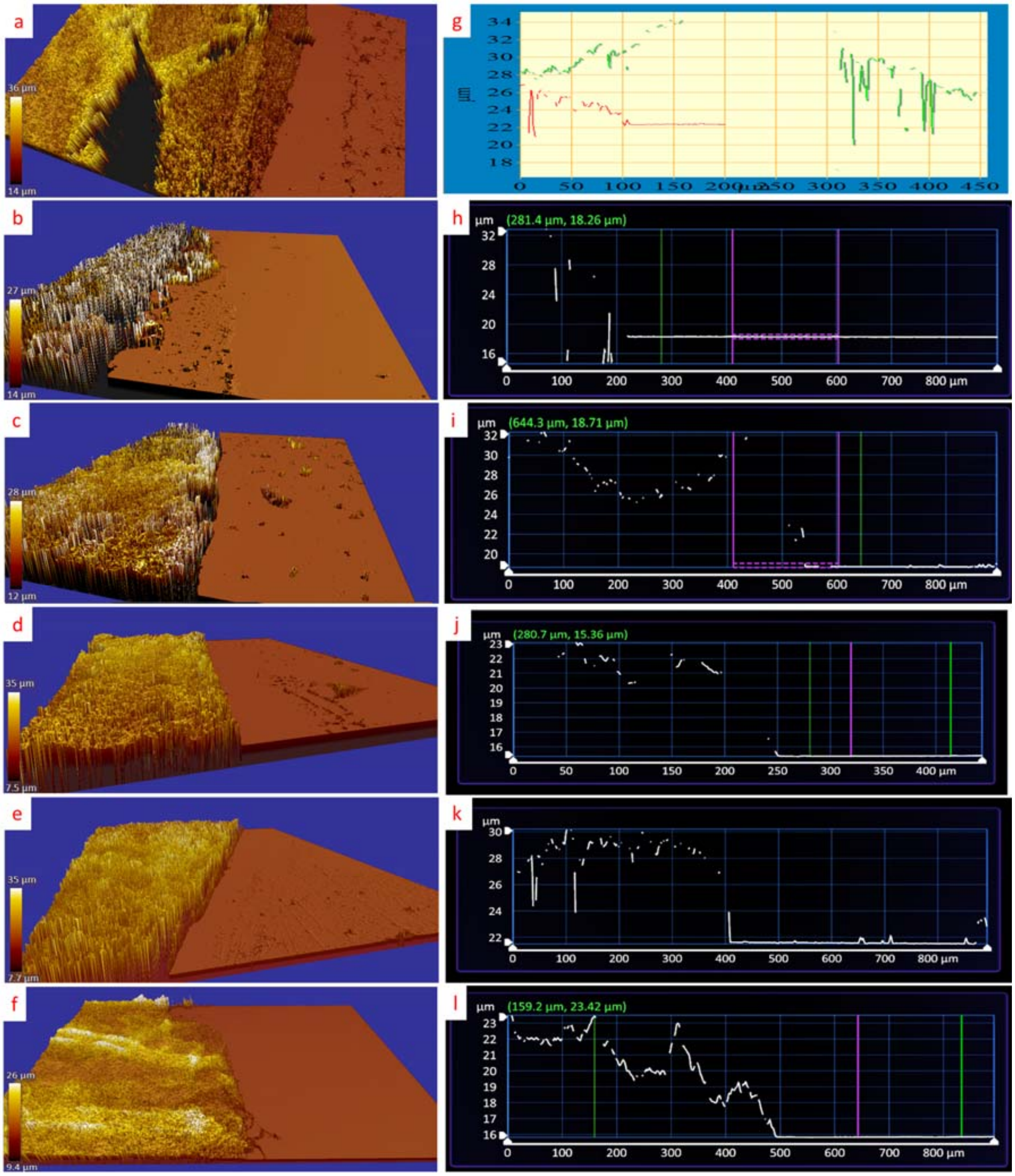

Figure 93: Summary of the BrM optical profilometer experiments, showing (a-f) the generated 3D image and (g-l) the optical profile of the membrane, with: (a, g) native BrM; (b, h) Coomassie brilliant blue-stained BrM; (c, i) Haematoxylin-stained BrM; (d, j) Oil red O-stained BrM; (e, k) Sudan black-stained BrM; and (f, l) gold-sputtered BrM sample.

However, in order to accurately mimic native BrM, thickness measurements of human BrM using the same optical profilometer method were required to allow a suitable comparison between the artificial membrane and native tissue. Therefore, suitable BrM samples needed to be isolated. Due to the difficulty in isolating BrM and to maintain the integrity of BrM[46,29], the BrM-choroid complex was collected.

Contrary to the co-polymer membrane, the ZeScope optical profilometer could not accurately detect the native BrM-choroid samples, generating ‘black spots’ in the spectra. These were potentially the result of light emissions not reflecting back to the optical profilometer, either through absorption into the membrane or by distorting the interference bands through reduction or total removal of the sample beam, resulting in a ‘gap’ in the generated profile and producing an incomplete 3D map (Fig. 93, a, g). As discussed in Chapter 3.2, the optical profilometer requires a suitable splitting of a light beam into two halves, one collected into a reference mirror and the other passing through the microscope objective. Failure of either of these beams of light to reflect into the correct path resulted in the distortion of the spectra, and this was occurring in the imaging of native BrM-choroid.

Therefore, to improve the reflection properties of the isolated tissue, a series of dyes were used. It was theorised that staining the native BrM would improve its reflectivity and subsequently the generated spectra, therefore an investigation was conducted into the use of protein-based stains to amplify the reflectivity and improve the clarity of the subsequent 3D optical profile images. Coomassie brilliant blue, haematoxylin, oil red o and sudan black were used in an attempt to generate clearer spectra. However, contrary to initial hypotheses the spectra did not improve (Fig. 93, b-e, h-k). The black spots generated in the non-stained BrM samples were still prevalent, and whilst there was a small improvement in the use of haematoxylin, it did not generate clean optical profiles. This was potentially down to insufficient staining of the membrane, a rejection of the stain from the BrM-choroid complex or an ineffective reflection from the stain for optical profilometry. Samples were stained for 20 minutes at room temperature as per manufactuer’s instructions, and therefore had sufficient time to dye the samples with the chosen protein stains. However, it was clear that the BrM-choroid samples were not dyed sufficiently for clean spectra on the optical profilometer.

The inability to produce a clean optical profile of the BrM-choroid complex using microscope-stains meant that an alternative method was required. Sputtering the BrM-choroid samples with an ultrathin layer of gold meant that the reflectivity of the membrane would be enhanced significantly, enabling the optical profilometer to detect the tissue fully.

Gold has a naturally reflective surface, and therefore the gold-sputtering of the BrM-choroid samples would provide the required reflective property to redirect the generated wavelength of light from the optical profilometer back towards the objective. Using this method produced a clean optical profile of human BrM-choroid (Fig. 93, f, l), and thickness measurement of 7.59 ± 0.04µm was taken.

This method was able to accurately quantify the thickness of native BrM-choroid, and whilst there are limitations to this technique (the need to retain the choroid to the BrM to maintain membrane integrity and the use of gold-sputtering), the use of an optical profilometer enabled the production of sub-nanometre thickness values. Other methods, such as OCT, TEM and light microscopy are unable to provide said accurate sub-nanometre measurements[195,196,204,206]. OCT is also unable to distinguish between the RPE and BrM[194,197], whilst the use of TEM and light microscopy requires the isolated BrM-choroid to be passed through a series of alcohol dehydration steps, which will reduce the thickness of the membranes through loss of water[201,207].

The thickness measurement taken by the optical profilometer for the gold-sputtered sample was from the central region of BrM. Further analysis of the thickness of the BrM-choroid complex across the macula was conducted looking at the change in thickness from the central region to the peripheral region (Chapter 3 Table 2). From the optical profilometer analysis it was found that the thickness increased from the central region to the peripheral region of the macula. As discussed by Chong *et al* the thickness of BrM decreases from the periphery (both the nasal and temporal sides) towards the fovea (central region)[218], caused by the thinning of the elastin layer, and this thickness variation is shown in the optical profilometer results, confirming its effectiveness in measuring the thickness of biological samples.

With the thickness measurement of the BrM-choroid complex ranging from 8µm to 17µm from the central region to the periphery, a comparison was made to the co-polymer BrM mimetic, which had a thickness of 51 ± 3µm. A thicker membrane could have profound complications during surgery and could increase the probability of metabolite build-up during the diffusion of macromolecules[290], further thickening the membrane[291] whilst also potentially preventing the diffusion of solutes between the RPE and choriocapillaris[292]. Therefore, steps were taken to reduce the thickness of the BrM mimic without compromising the existing fibrous nature and disrupting the mechanical strength of the membrane.

$$D = \left(\gamma c \frac{Q^2}{I^2} \frac{2}{\pi(2\ln\left(\frac{l}{d} - 3\right))} \right)^{\frac{1}{3}}$$

Equation 1: Analytical model of the effect of electrospinning parameters on the fibre thickness. D = diameter of fibre; γ = surface tension of the solution; *Q* = flow rate of the solution; *I* = current across needle; L = initial jet length; *d* = diameter of the nozzle[223].

Reducing the thickness of the artificial BrM without compromising the existing properties was carried out by modifying the parameters of the electrospinning procedure. As detailed in Chapter 3.4, the concentration and the amount of polymer solution used in the formation of the fibrous mat would be maintained; to reduce the risk of electrospraying and remove the potential generation of a brittle matrix. Therefore, the modification of the flow rate and the voltage applied in electrospinning was carried out to produce fibres of smaller diameter, thus reducing the thickness of the fibrous mat without compromising the fibrous nature or the amount of polymer used.

Polymer mat sample	Voltage (kV)	Flow Rate (ml/hr)	Distance to the collector (cm)	Average fibre thickness (μm)	Presence of polymeric beads	Obvious signs of breakage
1st Gen	15	9.5	15	8-12	No	No
1	15	0.05	15	0.5-2	Yes	Yes
2	15	0.1	15	1.5-3	Yes	No
5	15	1	15	3-5	Yes	Yes
7	20	0.05	15	0.1-1.5	Yes	No
10	35	0.05	15	0.1-0.8	No	No

Table 8: A summary table of the change in parameters affecting the production of fibres, showing the polymer mat samples (using Tables 3 & 4 located in Chapter 3) and the change in average fibre thickness compared to the 1st generation of membranes as the flow rate and voltage is changed.

Initial experiments looked at the effect of the flow rate on the fibre diameter, with a reduction in the fibre diameter noticed when the flow rate was reduced. Samples electrospun at a flow rate of 9.5ml/h (the parameter used in producing the 1st generation of fibres) generated fibres of 8-10μm in diameter, whereas a flow rate of 0.05ml/hr generated fibres of 0.5-2µm in diameter. This profound reduction in the fibre diameter displayed the influence of the flow rate on the fibre mat production. As shown in Equation 1, the flow rate of the solution, Q, directly affects the diameter of the fibre. An increase in the flow rate would therefore theoretically increase the fibre diameter, as the position of 'Q' influences the top half of the fraction.

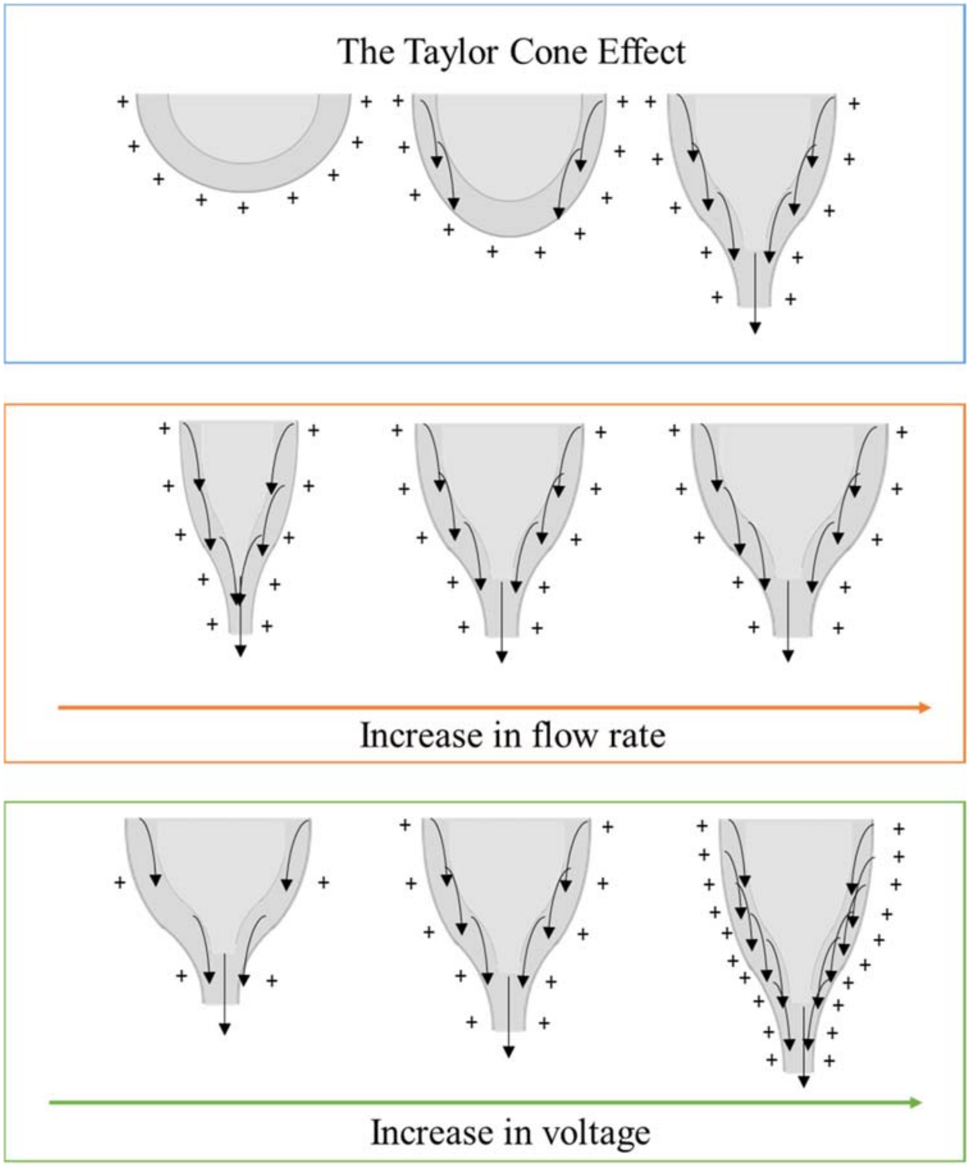

Figure 94: Schematic showing the effect of increasing the flow rate and voltage on the taylor cone of the electrospinning jet. As the flow rate increases, the amount of solution passing through the needle increases, creating a thicker jet. Increasing the voltage increases the potential across the jet, generating a thinner and elongated taylor cone.

This is confirmed in experimental investigations carried out by Cramariuc *et al*, and this work helped determine the result of the investigations carried out on the artificial BrM[130].

The reduction in the flow rate resulted in a slower release from the needle (Fig. 94). This, coupled with the maintaining of the current applied across the needle, ensured a greater electrostatic repulsion on the Taylor cone and a thinner jet. However, by reducing just the flow rate there was an increase in the formation of polymeric beads, due to a build up of polymer solution on the needle tip caused by the slower flow rate.

Therefore, the effect of the voltage used in the electrospinning process was investigated, looking in particular at the removal of polymeric beads alongside the slower flow rate. As shown in Table 8, by reducing the flow rate and increasing the electrospinning voltage, the presence of polymeric beads was removed whilst a decrease in the average fibre thickness was also observed (0.1-0.8µm). As shown in Equation 1, a theoretical increase in I (the current across the needle) reduces the value of D (the diameter of the fibre), and experiments carried out on the artificial BrM showed this decrease in fibre thickness. The removal of the polymeric beads was also achieved, and this was due to the increase in electrostatic repulsion. With an increase in the current across the needle, alongside a constant flow rate, the electrostatic repulsion of the Taylor cone increased (similar to the effect of reducing the flow rate), leading to a thinner jet (Fig. 94). The result of the change in fibre thickness was the reduction of the artificial BrM thickness, from 51µm to 12µm, aligning it more closely to native BrM.

This reduction in the thickness of the individual fibres had led to a decrease in the thickness of the artificial BrM. Recent publications carried out by researchers looking at generating the ideal prosthetic BrM have focused on the thickness of the artificial membrane. Liu *et al* proposed a poly(ethylene terephthalate) (PET) combined with poly(L-lactide-co-ε-caprolactone), which had individual fibres of 200nm in thickness[167]. This resulted in a fibrous mat with a thickness of 2-4µm. Whilst aligning it closely with native BrM, the artificial BrM required a 'secondary carrier' or a hydrogel coating to ensure it survived the implantation process, due to the membrane being frail in handling. This could also have complications in cell culture, with the handling of the membrane with a layer of RPE cells seeded on its surface potentially challenging. Haneef *et al* also designed an artificial BrM by electrospinning PET or polystyrene (PS)[165]. The thickness of these fibrous mats after production were 50.7 ± 2.96 µm and 180.7 ± 25.6µm thick respectively. The thickness of the PET artificial BrM was similar to that of the 1st generation of artificial BrM proposed in this project, and the subsequent thinning of the PET fibres led to a decrease in the tensile properties of the artificial membranes, making them unsuitable for handling and implantation.

Therefore, understanding the subsequent effect on the biophysical properties as a result of the thickness reduction of the 2nd generation of artificial membranes proposed by this project was required, looking at its mechanical strength, porosity and biocompatibility.

Reduction in the fibre thickness could have led to a fragile and difficult to handle membrane, as seen by Haneef *et al* and Liu *et al*[165,167]. Therefore an investigation into the change in tensile strength was carried out. This was achieved through the use of a DEBEN microtest tensile tester 300N, used in collaboration with the Bhaskar group at the University of Southampton.

In order to quantify the membrane tensile strength, the material was stretched horizontally. This was proposed as the most suitable method for accurately analysing the tensile strength of the material. This technique has been previously used within the literature to characterise the tensile strength of synthetic and electrospun membranes[142,293,294]; by stretching the membrane horizontally, the key mechanical characteristics of the artificial BrM could be quantified, whilst also allowing for a comparison to be made to native BrM. Using this technique, the Young's modulus, the stress at failure, the overall calculated toughness and the yield strength of the membrane were all analysed, allowing for a comprehensive understanding of the strength of the membrane and its ability to withstand stress and strain.

What was observed was an increase in all four tensile strength parameters investigated as the membrane developed from the first generation (51 ± 3µm in thickness) into the second generation (12µm in thickness). The individual fibre strength (the Young's modulus) increased from 13.6 ± 3.65 MPa to 26.0 ± 3.14 MPa. This indicated that by thinning the co-polymer fibres, the ability the individual fibres to withstand stress and strain increased. This could be as a result of the compressing of the polymer solution driven through the needle, as a result of the higher voltage applied to the electrospinning procedure (Fig. 94). By reducing the flow rate and increasing the voltage, the fibres produced were thinner but were not stretched (as a result of the slower flow rate). This could have resulted in a closely packed fibre, increasing the intermolecular forces between the polymer chains and thus increasing the resistance to stress and strain. This increase in resistance to stress and strain was seen in both the yield strength (from 1.40 ± 0.01 KPa to 3.48 ± 0.32 KPa) and the maximum stress at failure (from 23.5 ± 1.50 KPa to 38.7 ± 1.20 KPa) calculations, alongside an increase in the overall calculated toughness of the material (from 10.2 ± 3.98 kJ mol^{-1} to 20.1 ± 5.24 kJ mol^{-1}). This increase in tensile strength could also be due to the artificial BrM fibres forming a tighter weave of thin fibres, forming a fibrous matrix with a greater interwoven nature. The variability in the random alignment of the fibres produced using the electrospinning technique did not appear to cause severe fluctuations in the mechanical strength results, each sample was analysed 6 times with no significant deviations observed. This could be as a result of the interactions between adjacent fibres mitigating the effect of the random alignment, alongside the previously theorised 'tighter weave' in the generated, thinner matrices.

The mechanical studies carried out by Haneef *et al* showed that as the artificial BrM thickness decreased, the maximum stress before failure decreased[165]. PET membranes of 50.7 ± 2.96 µm thickness displayed a maximum stress before failure of 175 ± 25 Nm^2 (which converts to 0.175 ± 0.025 KPa), whereas PET membranes of 16 µm thickness displayed a maximum stress before failure of 40 ± 10 Nm^2 (which converts to 0.04 ± 0.01 KPa). This contrasts with the thinning of the artificial Bruch's membranes produced in this project, which display a maximum stress before failure improvement from 23.5 ± 1.50 KPa to 38.7 ± 1.20 KPa when the thickness is reduced to 12 µm. This is a clear improvement in tensile strength, and displays the effective approach in the modification of electrospinning parameters to reduce the thickness of the membrane. However, these values are not close to native human BrM (stress before failure: 90.3 ± 4.2 KPa), and the efforts taken to improve the tensile strength of the artificial BrM is discussed later.

With the noted change in mechanical strength shown, it was then important to assess the change in the porosity of the artificial BrM. By using the Ussings chamber, the diffusion of fluorescein isothyanate labelled dextran from one chamber, across the membrane and into the other chamber containing PBS was measured. Samples were measured over a 24h period, with the thinning of the membrane showing a less porous artificial BrM and aligning it more closely with native BrM. This could be caused by the apparent reduction in pore sizes of the new generation of the artificial BrM, caused by a tighter weave due to the thinning of the fibres. This tighter weave contributed to the thinning of the membrane and also, as shown in its porosity, reduced its diffusional properties. What was also interesting to note was the instant diffusion of dextran after 1h, then a slow, more controlled diffusion after 2h towards 24h. This spike in porosity may be caused by artificial BrM (which is immersed in PBS at first) adjusting to the conditions of the Ussings chamber and therefore initially allowing a small amount of dextran through.

It was also important to monitor any changes in biocompatibility, ensuring that a RPE layer could attach and proliferate on the surface of the new thinner artificial BrM. An immortalised ARPE-19 cell line showed good cell proliferation on the surface of the artificial BrM after 2 weeks in culture, and alongside the LDH assay of the ARPE-19 cells, looking at the integrity of the ARPE-19 cells after 3 weeks compared to a positive control, the biocompatibility of the new generation of artificial BrM was maintained. It was clear that after a period of 3 weeks the production of LDH was below the negative control, thereby showing that the ARPE-19 cells had not produced sufficient levels of LDH to indicate that they had not undergone apoptosis on the membrane. This showed that the thinner co-polymer membrane had not altered its initial biocompatability property.

In summary, accurate thickness measurements of the existing designed prosthetic BrM were achieved through the use of optical profilometry, and the subsequent comparison to native BrM showed a clear discrepancy between the two thickness measurements. An artificial BrM that is much larger in its thickness could have severe complications *in vivo* and therefore the reduction in its thickness was required. This was achieved through the modification of the electrospinning process, and subsequent test of the biophysical properties showed no deterioration of its existing biocompatibility, with improvements noticed in its tensile strength and diffusional properties.

However, in order to fully understand the prosthetic BrM in its ability to host a layer of RPE cells, ARPE-19 cells were not sufficient. Detailing the RPE cell functionality and behaviour on the membrane required a primary RPE cell line, and therefore the next chapter of this project looked at the seeding and analysis of a primary RPE cell layer on the surface of the second generation of BrM mimetics.

6.3 Observe and understand the behaviour of a primary RPE layer on the surface of the BrM mimetic

To understand the RPE cell functionality on the surface of the BrM mimetic and to analyse the potential of the new generation of membranes to host a layer of functional RPE cells, a primary RPE cell line was used. As discussed in Chapter 4.1, the spontaneously arising RPE cell line (ARPE-19) is a suitable test for the initial biocompatibility of a new substrate, however an ARPE-19 cell line does not provide the full range of morphological features found in healthy RPE *in vivo*, with the immortalised RPE cells unable to produce uniformly abundant apical microvilli and display differences to native RPE in its ion transport mechanisms in diffusional studies[155,159–163]. Therefore, to establish a clear understanding into the RPE cell functionality on the artificial BrM surface, primary mouse RPE cell lines were used.

Long-term cultures of primary RPE cells seeded on the artificial BrM were established to understand the RPE cell maturity on the prosthetic BrM. In order for the proposed artificial BrM to be successful in providing a potential therapy for AMD, the RPE must establish a mature monolayer on the co-polymer substrate whilst maintaining its functionality. Therefore, samples were established for up to 12 months, looking primarily at the RPE cell behaviour and functionality on the artificial BrM.

Initial experiments focused on the suitability of the prosthetic BrM to host a layer of RPE cells, and after 1 month in cell culture primary RPE cells were shown to be confluent, producing actin filaments (concurrent with RPE cells *in vivo*[295,296]) and arranged primarily on the artificial BrM apical surface. This compared well with the reported cell growth times in the literature, with primary human RPE cells taking 3-4 weeks to establish a confluent layer[232]. ARPE-19 cells are reported to take up to 2 weeks to establish a desired confluent RPE layer[166,297], and initial results from the primary murine RPE cells used in this project showed a RPE layer with good cell confluency.

Primary murine RPE cells seeded on the artificial BrM were maintained after 2 months, and continued experimentation focused on whether the RPE layer was continuing to remain predominantly on the apical surface of the artificial BrM, and not migrating into the centre of the membrane (Fig. 95).

As the initial experiments have indicated, the RPE layer was forming a predominantly apical arrangement on the artificial BrM surface after a period of 4-8 weeks. Long term cultures were analysed to understand the RPE layer arrangement over a period of 10 months, whilst also investigating the ability of the artificial BrM to prevent RPE cells from penetrating its surface over a longer period of time. 1, 2, 4, 7 and 10 month intervals were chosen as representative timepoints to highlight the progression of the RPE monolayer over a long period of time. Monthly intervals would have given a clearer insight, however finite samples of primary RPE seeded artificial membranes were able to be produced.

As shown in Figure 95, the use of orthogonal sections allowed the analysis of RPE cell penetration into the artificial BrM. After the first two months of imaging, the RPE layer had appeared to migrate slightly into the co-polymer membrane, with DAPI-labelled cell nuclei being shown on the 3rd Z-stack (within the co-polymer membrane). This could be the result of the seeding process, with cells falling through the membrane as they were applied to the artificial BrM. However, after 4 months and towards 10 months, the presence of RPE cells in the 3rd Z-stack had disappeared; the RPE layer was located in the

1st and 2nd Z-stack layers (i.e. above the co-polymer membrane). The RPE cells had either migrated towards the apical layer of the artificial BrM or had undergone cell apoptosis, leaving a RPE layer with an apical distribution across the surface of the artificial BrM. This trend was highlighted in the DAPI & Phalloidin location comparison between months 1 and 10, where the percentage cell coverage was significantly higher in Z-stack locations 1 and 2 and lower in the 3rd Z-stack (see Chapter 4.2 Figure 44).

This investigation into the migratory activity of the RPE monolayer into an electrospun artificial BrM is rarely discussed in the literature, where it is often reported that the chosen RPE model has formed a confluent monolayer but nothing on the migratory activity of the RPE monolayer. ARPE-19[165,166,297], primary human RPE[151] and fetal human RPE cells[167] are all discussed in great detail with regards to the apparent production of a confluent monolayer, however very little is reported about the potential of the RPE cells to migrate into the proposed artificial BrM. This is an interesting point of discussion, as an electrospun (and ultimately porous) artificial BrM could potentially allow the migration of RPE cells into the inner layers of the membrane, whilst native BrM does not allow the migration of RPE cells[35]. Within this project, the use of established long-term cultures allowed this investigation into the migration of the RPE monolayer to be carried out, showing the formation of a primary murine RPE monolayer after 10 months in cell culture.

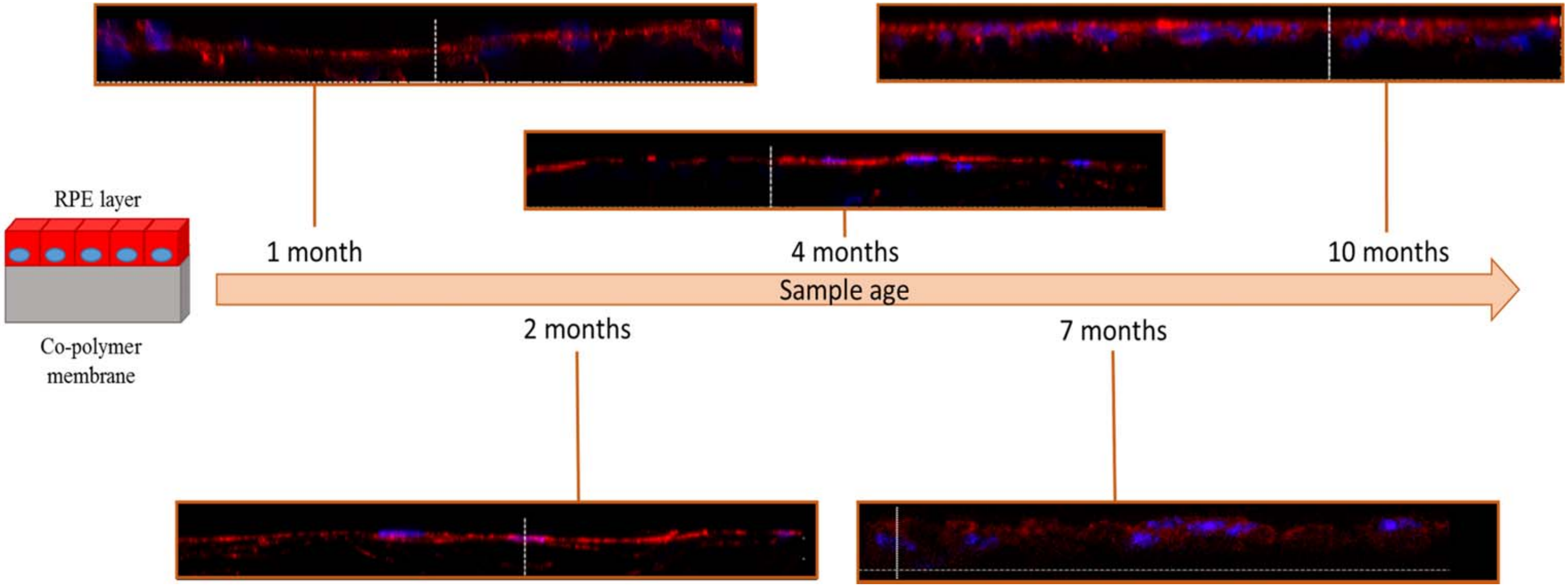

Figure 95: Respresentative orthogonal sections of confocal microscopy images highlighting the formation of a RPE monolayer arranged on the artificial BrM apical surface, with a schematic (left) showing the layout of the orthogonal sections. After 1 month post-seeding of RPE cells on the prosthetic BrM, the RPE cells appeared to have migrated into the centre of the membrane, and this was seen in samples after 2 and 4 months in culture. After 10 months however, the RPE cells were found predominantly on the surface of the co-polymer membrane, forming a distinct monolayer .

The primary murine RPE-artificial BrM samples proposed in this project are shown to be confluent after 4 weeks in culture, with the primary murine RPE cells forming a monolayer after 10 months in culture and displaying a reduction in the migration of RPE cells into the centre of the artificial membrane. These cultures also show the behaviour of the membranes and the primary murine RPE cells after 10 months at 37°C in tissue culture, allowing an understanding into the long-term capabilities of the RPE-artificial BrM.

Once the distribution and cell coverage of the RPE monolayer had been established, the next step was to analyse whether the RPE layer had attached and established focal adhesions with the artificial BrM. As discussed in Chapter 4.3, RPE cells are anchorage-dependant, and the integrity of the RPE layer required the formation of focal adhesions with the substrate (artificial BrM)[27]. In order to quantify the attachment of the RPE monolayer to a substrate, Lu *et al* reported that use of a calcein-ethidium bromide staining assay would determine cell vitality and thereby confirm cell attachment[219]. The calcein-ethidium bromide compound passively enters cells and is subsequently converted by metabolically active cells into a fluorescent molecule, calcein. This can then be observed using fluorescent microscopy and determine the number of vital cells. This method, used by Lu *et al*, required the assumption that RPE cells would undergo cell apoptosis when unable to form focal adhesions. It doesn't, however, account for the formation of contact points between the RPE monolayer and the substrate (artificial BrM).

Kearns *et al* quantified the attachment of the RPE layer to their proposed synthetic substrate through observation of the RPE cell shape, morphology and proliferative state, reporting that cells on earlier substrates 'had a rounded cell morphology indicating they were poorly attached' whereas the proposed membranes showed successful attachment due to the cell proliferation[298]. However the formation of focal adhesions was not quantified and therefore could not definitively confirm the presence of contact points between the substrate and the RPE monolayer.

In order to visualise the formation of focal adhesions, experiments were carried out using the specific tagging of proteins and kinases that are vital in the generation of said focal adhesions.

With the binding of the actin filaments to these attachment complexes, vinculin is key in providing the link (Chapter 4.3 Figure 46). An immunofluorescent assay of vinculin showed its distribution throughout the cytoskeletal network of the RPE layer, confirming its presence in the cell-substrate complexes through the RPE-artificial BrM connections.

The presence of vinculin within the cytoskeleton of the RPE cell is indicative of the cytoskeletal reorganisation occurring within the RPE monolayer[246], essential in allowing the actin filaments to bind to the focal adhesions and the attachment of the RPE to the substrate[299,300].

This confirmation gave an initial insight into the cell-substrate complexes being formed, and further analysis of focal adhesion kinase (FAK) binding in the focal adhesions *via* immunofluorescent analysis showed the presence of the focal adhesions. Using orthogonal sections, clear punctate focal adhesions could be seen in the RPE-artificial BrM interface which, when compared to a positive control (flatmount mouse eye), displayed the same arrangement as that of the RPE focal adhesions *in vivo*. This confirmed the RPE layer had generated focal adhesions with the artificial BrM (due to the presence of FAK which is colocalised with the focal adhesions[20]), interacting with the artificial BrM surface and using the co-polymer membrane as a substrate to attach to.

To determine that the RPE layer had settled on the membrane and was not constantly proliferating, FACS cell cycle was used. This would further confirm that the RPE layer had successfully formed focal adhesions with the artificial BrM, established a confluent monolayer and was not proliferating and migrating; an unwanted feature as a migratory RPE layer further highlights issues with the monolayer, as observed in diseases like proliferative vitreoretinopathy and proliferative diabetic retinopathy[301–303]. Using the cell cycle analysis, it was clear that the RPE cells on the surface of the artificial BrM were predominantly in their $G_{0/1}$ phase of the cell cycle (81.1%), displaying a non-proliferative nature whereas a proliferative RPE cell culture was found to be in its $G_{0/1}$ and G_2/M phases (47.2% and 43.4% respectively). This observation showed that the RPE cells on the artificial BrM were quiescent and established, aligning it to the native adult RPE monolayer in healthy human eyes[304]. To further determine the migratory state of the RPE cells, a study into the expression of cytokeratin 19 would be advantageous, as it has been reported that cytokeratin 19 is synthesised in migrating RPE cells, which is absent in native quiescent RPE and would be a good indicator of migratory RPE cells[300,305].

Cell cycle analysis further highlighted the established nature of the primary murine RPE cell monolayer on the co-polymer membrane which, when combined with the immunofluorescent assays of vinculin and FAK, further confirmed that it could form focal adhesions successfully with the substrate. The proposed artificial BrM substrate in this project has been shown to be interacting with the RPE monolayer, allowing the formation of essential focal adhesions in the basolateral RPE-apical artificial BrM interactions and displaying actin filament organisation as a result of focal adhesion formation.

Once the RPE monolayer had established focal adhesions and ceased migratory activity, the retention of the RPE phenotype was investigated. This was required to see if the RPE layer had not developed into fibroblastic-like arrangements and that the co-polymer membrane was allowing the RPE layer to remain epithelial. This was achieved through an investigation into a RPE-specific protein.

RPE65 has been discussed previously as being vital in the visual cycle. It is essential in the conversion of all-*trans*-retinol into 11-*cis*-retinal, allowing the regeneration of the light-sensitive molecule key to the generation of potential in the photoreceptors when stimulated with light. It is therefore important to observe the production of RPE65 within the RPE layer seeded onto the artificial BrM, as not only does it confirm the synthesis of the RPE-specific protein and therefore show that the RPE layer has retained its phenotype[232,306,307], it also further confirms that the artificial BrM is allowing the RPE layer to express its *in vivo*-like cell functionality[252].

An immunofluorescent analysis showed the clear expression of RPE65 in the RPE-artificial BrM sample, highlighting the expression of RPE65 throughout the cytoskeletal network, similar to what is reported in the literature for RPE cells on synthetic matrices[151,232] and human RPE cells[159]. The production of RPE65 by the 4 month RPE-artificial BrM cultures (and 3 month cultures on the anthracenyl-infused prosthetic Bruch's membranes) gave an initial confirmation that RPE layer had retained its phenotype over a long period in cell culture and was able to produce the necessary protein to complement the conversion of all-*trans*-retinol into 11-*cis*-retinal, a marker often used to determine the phenotype of the RPE cell[17,151,252].

RPE65 is an indicator that the RPE cells maintain morphology[308], but in order to completely determine that the RPE monolayer had retained its morphology, a study into the presence of the RPE-specific cellular retinaldehyde binding protein (CRALBP)[309] would be advantageous, given that it is often shown in the literature as a complimentary marker to indicate that the RPE monolayer does not undergo de-differentiation[308].

With the initial confirmation that the RPE layer had retained its phenotype, another RPE-specific marker was investigated, the formation of apical microvilli.

The ability of the RPE layer on an artificial BrM to produce apical microvilli has been well reported in the literature. Small clusters of apical microvilli are observed in ARPE-19 cells cultures on artificial BrM substrates[127,154], whereas uniformly arranged apical microvilli are reported on primary human RPE cells using SEM[151]. Therefore, in a primary murine RPE cell culture, it would be expected that the production of uniformly arranged apical microvilli would be apparent on a suitable artificial BrM substrate.

The presence of apical microvilli on the surface of the prosthetic BrM was confirmed by TEM analysis. Twelve month samples of primary murine RPE cells seeded on the artificial BrM were isolated, the RPE cells were trypsinised, fixed and embedded in algenate. The samples were unable to be run with the co-polymer membrane as the processing of the sample for TEM imaging resulted in the degradation of the artificial BrM, resulting in fragments of co-polymer membrane throughout the embedded sample and distorting the TEM images. Therefore the RPE cells were trypsinised from the co-polymer membrane, instantly placed in fixative and embedded in algenate. The images produced *via* TEM provided a detailed insight into the RPE ultrastructure, showing the expected cuboidal morphology and displaying the required apical microvilli. In contrast to the ARPE-19 cell cultures of apical microvilli[127,154], these appear to be well-formed with clearly identifiable, long microvilli on the apical surface of the RPE cell, as shown with reported primary cultures of RPE cells[151]. This is another confirmation that the RPE cells had maintained its phenotype over a long period in cell culture, with apical microvilli often seen as a key sign of RPE monolayer suitability and polarisation[295,310].

The presence of apical microvilli also indicated that the RPE layer had shown signs of polarity, pivotal for the RPE monolayer. Confirmation of this came from the immunofluorescent tagging for Na^+/K^+ ATPase, a gradient pump that is found specifically in the apical surface of the RPE monolayer[14]. In primary porcine RPE cultures reported in the literature, Na^+/K^+ ATPase has been shown to be apically localised after 3 weeks, displaying orthogonal immunofluorescent arrangements highlighting the polarity of the RPE monolayer and the extent of Na^+/K^+ ATPase production[311]. Subrizi *et al* also report the formation of Na^+/K^+ ATPase within their human embryonic stem cell-derived RPE monolayers on the surface of their proposed biodegradable artificial BrM[312]. The primary murine RPE monolayer seeded on the artificial BrM proposed in this project confirmed the presence of Na^+/K^+ ATPase *via* immunofluorescent orthogonal sections, showing an apical localisation of Na^+/K^+ ATPase across the surface of the RPE monolayer. The apical localisation of Na^+/K^+ ATPase is similar to that reported in the literature, showing a continuous line across the RPE monolayer[311]. The sample was counterstained with FAK to show the apical/basolateral orientation of the RPE layer on the artificial BrM, displaying both the punctate basolateral focal adhesions and the apical Na^+/K^+ ATPase pumps.

The combination of TEM and immunofluorescence confirmed the presence of apically distributed microvilli and the formation of a polarised monolayer of RPE cells, a key indicator of a biofunctional RPE layer.

Another indicator of a polarised RPE layer is in the basolateral secretion of VEGF. VEGF is essential in the maintenance of the choriocapillaris, and a suitable RPE-artificial BrM implant would be required to secrete VEGF to help maintain the underlying capillaries within the eye.

Initial investigations looked at the presence of VEGF in cell culture supernatant, using an ELISA to determine its concentration. After 1 month in culture, the RPE-artificial BrM was producing 66.5 ± 11.7 pg ml^{-1} of VEGF over a period of 3 days. This, compared to the reported primary human RPE VEGF concentrations in culture of 1000 pg ml^{-1}, is significantly less than native RPE tissue[254]. This is to be expected as the RPE cells are establishing the required monolayer of cells and, as observed earlier in the orthogonal sections (Fig. 95), have not formed a complete monolayer. After 5 months in culture, the RPE-artificial BrM was producing 528.8 ± 28.2 pg ml^{-1} of VEGF over a period of 3 days, a significant increase compared to the 1 month cultures ($p < 0.0001$). This increase in VEGF concentration is indicative of the development of the primary murine RPE monolayer on the surface of the artificial BrM, and after a period of 9 months the RPE layer was producing 702.4 ± 27.3 pg ml^{-1} of VEGF over a period of 3 days. This significant increase ($p <0.0001$ when compared to the 1 month samples and $p = 0.0032$ when compared to the 5 month samples) highlights an established and functional RPE layer on the artificial BrM. It is more closely aligned to the reported VEGF concentrations produced by primary human RPE cell cultures[254], displaying similar productivity to what is observed from within the eye.

These experiments confirmed the secretion of VEGF, however they were unable to confirm the polarity of the RPE monolayer. Terasaki *et al* were successful in analysing the effect of thrombin on the basolateral secretion of VEGF, using primary porcine RPE cells seeded on a transwell[239]. By using a transwell, two separate compartments divided the cell culture well into apical and basolateral sides.

Therefore, to achieve a similar arrangement, a Cell Crown^{TM} system was used to generate a polymer transwell, thereby separating the apical and basolateral sides of the RPE-artificial BrM. A 2 month culture was analysed on a VEGF ELISA, and showed a significant difference in VEGF production ($p = 0.0013$). The basolateral compartment of the RPE-artificial BrM was found to be producing 281.8 ± 28.0 pg ml^{-1} of VEGF whereas the apical compartment was producing 84.8 ± 20.2 pg ml^{-1} of VEGF, displaying a polarised membrane and indicating the RPE layer was establishing polarity after a period of 2 months in culture.

These results are again indicative of an established RPE layer on the surface of the artificial BrM, displaying a polarised monolayer and performing key physiological properties associated with the RPE within the eye.

Another key physiological role of the RPE within the retina is to control the flow of macromolecules from the choriocapillaris to the photoreceptors and *vice versa*. This controlled diffusion is facilitated by the BrM, and therefore it was necessary to test the barrier capabilities of the RPE-artificial BrM.

One method of testing the barrier properties of the RPE-artificial BrM was through diffusion studies. Research conducted by Hussain *et al* determined the diffusional capabilities of aged BrM-choroid samples through the use of a Ussings chamber and fluorescein-isothiocyanatge labelled dextran[46,313]. By using this method, they were able to identify a rapid decrease in the permeability of BrM-choroid as the samples age. Using this technique, the difference in macrmolecular diffusion through the RPE-artificial BrM complex could be determined by comparing native BrM samples, the artificial BrM without the RPE monolayer and the RPE-artificial BrM complex. What was observed was a decrease in the diffusion of dextran when the RPE layer was seeded on the surface of the co-polymer membrane. After a period of 2h, when compared to the co-polymer membrane without RPE cells, the influence of the RPE layer led to a more controlled diffusion of dextran, aligning it more closely to native BrM. This decrease in macromolecular diffusion can be explained by the formation of a RPE-barrier which, as discussed previously, is able to control the flow of solutes by forming a complete monolayer[13]. This experiment gave an initial insight into the formation of a RPE barrier.

What was also observed was the ability of the RPE-artificial BrM to form a barrier from its apical or basolateral side, an important property as native RPE-BrM controls diffusion from the photoreceptors on its apical side and from the choriocapillaris on its basolateral side[10,13]. As discussed in Chapter 6.1, there also appears to be an initial burst of dextran through the polymer samples, which again could be as a result of the artificial BrM adjusting to the Ussings apparatus.

To monitor the formation of the barrier over time, TEER was conducted. This allowed the continued measuring of the change in epithelial resistance as the RPE layer developed in culture without disturbing the samples. Using the Cell Crown^{TM} systems, changes in the apical and basolateral potential were measured, with a sharp increase in epithelial resistance over the first 28 days observed, finishing with a plateau in TEER from 29-42 days. The observed final TEER value was $72.4 \pm 0.95\ \Omega\ cm^2$, which showed similarity to human RPE-choroid measurements ($79 \pm 48\ \Omega\ cm^2$)[255]. This therefore indicated the formation of a RPE barrier across the artificial BrM.

Analysis of the formation of contact points between RPE cells allowed for the confirmation of barrier formation across the surface of the artificial BrM. The presence of ZO-1 within the RPE layer would indicate the formation of tight junctions, and initial experimentation looked at using western blotting to determine the generation of the ZO-1 protein. Researchers using ARPE-19 cultures have found a positive expression of ZO-1 on electrospun matrices in immunohistochemistry[154], with primary and hfRPE cell cultures also expressing ZO-1 tight junction formation in immunofluorescence analysis[151,167]. In this project, a band was observed at 195 kDa in western blotting analysis, indicative of ZO-1 protein expression. This confirmation of protein formation was then followed by immunofluorescent ZO-1 analysis, which showed the formation of initial contact points between RPE cells being formed, with the tight junctions being generated and forming the desired close-packed layer on the surface of the co-polymer matrix.

The ability to ingest and process photoreceptor outer segments (POS) is an essential role of the RPE layer in the human eye; failure of the RPE monolayer to phagocytose POS has been reported to cause unwanted complications within the eye, leading to problems such as retinal degeneration due to high photoreceptor density[314,315]. Therefore it was imperative to see this functionality in the primary murine RPE monolayer on the surface of the artificial BrM. Artificial substrates with seeded ARPE-19 cell layers have been widely reported in the literature as being able to phagocytose POS[150,154,166,219], using either immunofluorescence or FACS cell sorter analysis to quantify the POS ingestion by the ARPE-19 cell layer. Lu *et al* noted the phagocytotic activity of ARPE-19 cells on the surface of collagen scaffolds *via* fluorescently labelled POS[219], a technique also used by Xiang *et al*[154]. This technique allowed an understanding into the phagocytotic activity of the ARPE-19 cell line, whilst also showing the difference between internalised and extracellular POS. However, the progression of the phagocytotic activity of the RPE monolayer was not reported, with a single time-point taken for analysis.

The phagocytotic activity of primary human RPE cultures on the surface of a designed artificial BrM have also been investigated by Warnke *et al*, using latex beads as the substrate for ingestion[151]. Whilst providing an insight into the phagocytotic activity of the RPE layer, it has previously been reported that RPE cells do not selectively bind to latex beads, as noted by studies looking at the inhibition of the αVβ5 receptor[316]. This therefore does not account for the selective binding of POS by the αVβ5 receptor, and can not be used as a suitable assay of selective POS ingestion.

In this project, FITC-labelled porcine retinae were successfully fed to 4 month RPE-artificial BrM samples and subsequent immunofluorescent analysis showed the progressive ingestion over a 3h time period. Once samples were treated with FITC-POS for the allotted time period, they were washed repeatedly with PBS-CM, which removed any unused POS and terminated the phagocytotic activity. This therefore generated immunofluorescent images showing a frozen time point in the internalisation activity of POS by the RPE layer. The presence of internalised POS increased over time, reflecting the phagocytotic ability of the RPE layer to ingest POS, with the produced immunofluorescent images concurrent with the reported RPE behaviour *in vivo*[20,316,317]. The experiments were not carried out using a single-blind experiment set-up, due to the need to track the progression of POS internalisation time-frame and stop the process at the correct time points. Ideally, to remove potential sub-conscious bias, a single-blind experiment would be carried out, using two analysts to ensure bias was removed.

Orthogonal sections showed POS remaining within the RPE cytoskeleton, and this was confirmed by TEM, which highlighted the internalisation of multiple photoreceptor outer segments. By comparing the RPE-artificial BrM to isolated porcine retinae, the disk-like structures observed in the cytoskeleton of the RPE samples strongly resemble that of the procine photoreceptors, thereby confirming the successful internalisation of shed POS by the seeded RPE layer on the surface of the co-polymer membrane.

To ensure that the porcine POS were being selectively internalised by the RPE layer, an immunofluorescent investigation into the activity of MerTK and αVβ5 receptors was carried out. As discussed in Chapter 1.2.2, the RPE monolayer ingests shed POS through the apical membrane, facilitated by the MerTK and αVβ5 receptors[317,318]. This allowed a greater understanding into the ingeston pathway of the RPE-artificial BrM samples, highlighting its ability to selectively internalise POS. By labelling the MerTK and αVβ5, when FITC-POS interacted with the receptors the observed fluorescence changed, in this case turning the blue FITC-POS to purple. This then confirmed the selective binding of POS by the RPE receptors αVβ5 and MerTK, with the selective binding of POS initiated after 30 minutes.

Here, this project presents a detailed investigation into the phagocytotic activity of the primary murine RPE monolayer, showing the progression of internalised POS over time, confirmed by TEM, and the selective binding of POS by the MerTK and αVβ5 receptors. The initial immunofluorescent assay is similar to what is reported in the literature[154,219] however, with the detailed images generated from TEM showing clear disk-like structures within the RPE cell, and the immunofluorescent analysis of MerTK and αVβ5, we are able to confirm the successful selective internalisation of porcine POS by the primary murine RPE monolayer on the surface of the prosthetic BrM.

During the analysis of the photoreceptor internalisation by TEM, small granular melanosome-like structures were observed within the 12 month post-seeded primary RPE cells. As discussed by Schraermayer *et al*, melanin granules can have a speckled or ‘dotted’ arrangement, whereas other granules can have a more arranged morphology[258]. This indicates that the granular-like shapes observed within the cultured primary RPE cells in this project were melanin granules. The formation of melanosomes is a key physiological role of the RPE layer; the RPE layer forms a dark pigmented wall over the underlying choriocapillaris and BrM, preventing oxidative damage caused by the scattering of unabsorbed light from the retina. However, as discussed by Boulton[319], melanin formation occurs ‘during a brief window of embryogenesis and thereafter new melanin is formed at a very low level, if at all’. Alongside this, primary RPE cells have been reported to lose their pigmentation after proliferation[320]. Therefore, whilst TEM has shown an indication of melanosome formation, it is not sufficient in proving the synthesis of pigmented melanin granules. Gene expression analysis to confirm the synthesis of melanosomes and a suitable analysis of melanin accumulation (for example, NMR or MS) has been recommended in the literature to further define the production of melanin granules by the RPE monolayer, and would be recommended in future studies[319].

In summary, the aim of utilising primary murine RPE cells was to understand the RPE cell functionality and behaviour on the surface of the designed artificial BrM. By using this primary RPE cell line, an in-depth and detailed understanding of the ability of the RPE layer to perform key physiological roles on the surface of the prosthetic BrM was achieved.

As detailed in Chapter 1.2.2, the RPE layer within the human eye performs a number of key physiological roles: (i) it forms a barrier-like morphology to control the diffusion of macromolecules from the choriocapillaris to the photoreceptors and regulate the transport of water and ions from the retina to the choriocapillaris; (ii) it regenerates 11-*cis*-retinal through the use of RPE65 protein; (iii) it maintains the integrity of the photoreceptors with the continued selective ingestion of shed POS; (iv) it secrets VEGF to maintain the choriocapillaris underlying the RPE-BrM; (v) it interdigitises with the photoreceptors *via* its apical microvilli; and (vi) it helps prevent oxidative damage caused by the scattering of unabsorbed light from the retina.

These key physiological functions were observed from the primary RPE cell cultures on the artificial BrM, alongside the formation of key focal adhesions to the co-polymer membrane. This suggests that the designed prosthetic BrM has sufficient capability to provide a suitable substrate for the targeted delivery of functional RPE cells as a potential treatment for dry AMD.

In order to allow the delivery of the functional RPE cells, this biocompatible layer was required to withstand the implantation process and the choriocapillaris pulse within the sub-retinal space. Mechanical studies had shown that the blend of 60:40 MMA:PEGM was not as strong or as able to withstand stress as native human BrM, whilst curling of the membrane in cell culture was also observed. Therefore an improvement in the mechanical strength of the membrane was required.

6.4 Enhancement of the artificial BrM tensile strength

Throughout the experiments used to determine the biofunctionality of a primary RPE cell line seeded onto the artificial BrM, an observation was made into the structural integrity of the membranes after a prolonged period in cell culture. The co-polymer membranes were ‘curling’ in cell culture, folding onto themselves and not maintaining their flat shape. This phenomenon is not observed in the current literature of artificial BrM alternatives[150,289,297], and could be due to the co-polymer membrane losing its integrity after long-term cultures, potentially as a result of RPE constriction through the formation of tight junctions. Seeing as the proposed membrane is designed as a permanent prosthetic BrM, any changes in shape or curling of the membrane could lead to profound complications *in vivo*. This observation, coupled with the initial results of the mechanical studies which showed the first and second generations of artificial BrM having a lower tensile strength to native BrM, resulted in an investigation being conducted into the enhancement of the artificial BrM strength.

This improvement in the mechanical strength had to be achieved without compromising the porosity, the thickness and the biocompatibility of the artificial membrane. The use of nano-trusses, welding/soldering processes and volatile solvent exposure could not be incorporated into the membrane due to complications of potential carcinogenic reactions to volatile solvents and the risk of nanoparticle detatchment *in vivo*. Therefore, the co-polymer blend in the synthetic stages was altered to enhance its strength, looking at the use of cross-linking.

Initial experiments looked at the use of a solution-based cross-linking approach, whereby the synthesised co-polymer would be exposed to the cross-linking agent in solution. DSC and Diels-Alder cross-linking was investigated, in an attempt to enhance the strength of the membrane.

DSC cross-linking involved the use of the functional group di-succinimidyl carbonate used to provide an anchorage point for the RPE cell layer to adhere to. This was a continuation of an existing observation where the co-polymer synthetic process, if allowed to continue past the normal synthetic time, would result in a gel-like substance, indicative of a cross-linking effect. However, it is not possible to electrospin a gel, and so the investigation looked at a controlled method to the DSC chemical cross-linking approach. Unfortunately, a controlled approach was not possible, and further experimentation showed that the DSC cross-linked co-polymer system is not stable in aqueous environments, due to nucleophilic attack of H_2O to the carbonate-linking mechanism. Therefore, it was not suitable as a method for improving the strength of the artificial BrM.

Diels-Alder solution-based cross-linking was therefore investigated, looking at developing the co-polymer system to include a third monomer unit. The first and second generation of artificial BrM contained two monomer units, methyl methacrylate (MMA) and poly(ethylene glycol) methacrylate (PEGM). The incorporation of a third monomer unit, in this case a furfuryl methacrylate (FMA) monomer, had the potential to allow the specific cross-linking of the co-polymer membrane without disturbing the RPE-binding DSC side chain and allowing the co-polymer membrane to retain its previous properties. Diels-Alder chemistry also allows a thermoresponsive approach to cross-linking, therefore ensuring that the cross-linking only occurs at temperatures above 24°C (i.e. the temperature found within the human eye). However, as with the DSC cross-linking, the Diels-Alder approach generated a gel as a result of the cross-linking occurring within solution, incorporating the solvent to form a gel. However, the non-crosslinked MMA:PEGM:FMA co-polymer blend showed good fibrous morphology and biocompatibility, therefore indicating that the incorporation of a third monomeric unit, albeit at a small percentage infusion (58:40:2, MMA:PEGM:FMA) did not distort the existing biocompatible properties of the artificial BrM.

Due to the need to produce a fibrous mat, solution-based cross-linking was rejected and an investigation into cross-linking after the formation of the required fibrous matrix was carried out. Cross-linking the co-polymer mat after electrospinning required the incorporation of an element/compound that, when exposed to an external stimulus, cross-linked the fibrous mat into a mechanically stronger artificial BrM. External stimuli such as UV light or heat could provide the necessary reaction to enhance the strength of the membrane and research into the literature resulted in the UV cross-linking of anthracene[287,321,322] (see Chapter 5.3). Anthracene photodimerises under UV exposure and, due to its non-cytotoxic nature[288], could be incorporated into the co-polymer blend *via* its methacrylate form without complications *in vivo*. The ability to photodimerise also removed the use of a cross-linking agent, as the cross-linking was carried out by the anthracene molecule which is already incorporated into the co-polymer matrix. This prevented the presence of unused cross-linking agent and thereby remove further complications *in vivo*.

Synthesis of the electrospun anthracenyl-infused co-polymer matrix was successful, generating a fibrous mat. 1, 2 and 3% infusions were investigated, with the aim of identifying the optimal ratio of MMA:PEGM:AMM. Thickness measurements showed a range of 17-28μm across the three percentage infusions, with an increase in thickness observed when a greater ratio of anthracenyl methacrylate (AMM) was used. This could be due to an increased intermolecular repulsion from the non-polar aromatic AMM side-chains towards the more-polar PEGM side-chains, leading to a greater distance between fibres and resulting in a thicker membrane.

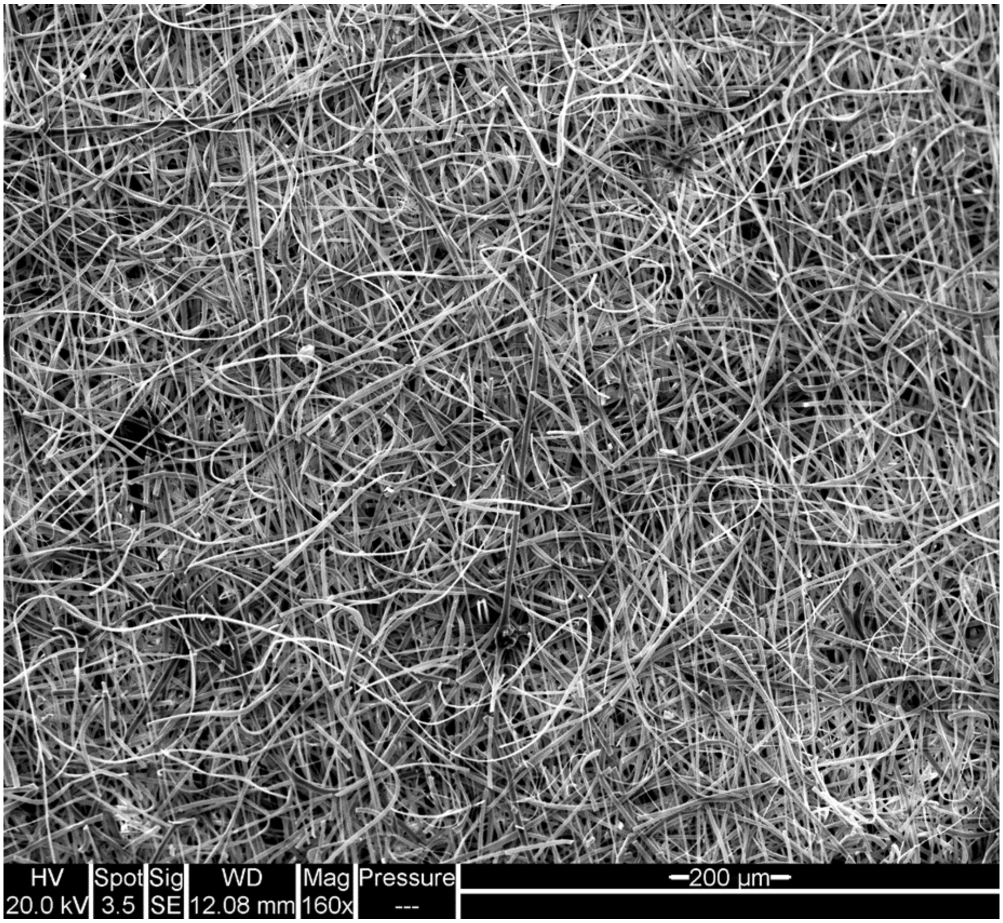

Figure 96: Representative scanning electron microscopy (SEM) image of AMM-2, showing the topography of the membranes after UV irradiation cross-linking. Fibres appear more aligned after cross-linking.

After UV irradiation of the electrospun membranes, there appeared to be a tightening effect observed, with the fibres re-orientating in a more aligned arrangement. This could have been as a result of the anthracene groups photodimerising, leading to the alignment of the fibres in parallel arrangements. The effect of this tightening led to a significant increase in mechanical strength (Fig. 96).

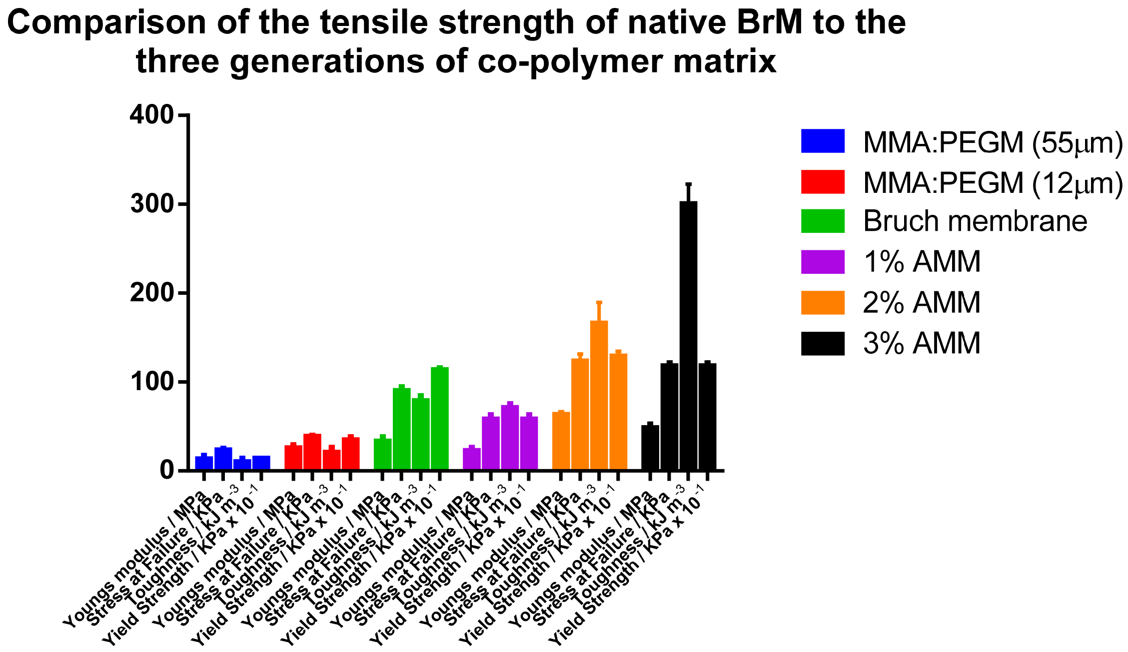

Figure 97: Summary of the improvement in mechanical strength, compared to the first generation of membranes (blue), the thinner artificial BrM (red) and native BrM (green). Significant increases in the Youngs modulus, stress at failure, toughness and yield strength were observed when AMM was applied to the co-polymer membrane.

When compared to the 2nd generation of co-polymer membranes, the 2% anthracenyl infused co-polymer membranes (AMM-2) had: (i) a significantly larger Young's modulus (63.4 ± 2.91 MPa compared to 25.9 ± 3.14 MPa, a significance of $p < 0.0001$); (ii) a greater resistance to stress before failure (123.7 ± 7.84 KPa compared to 38.7 ± 1.20 kPa, a significance of $p = 0.0004$); (iii) a significant improvement of the yield strength (1.29 ± 0.05 MPa compared to 0.348 ± 0.03 MPa, a significance of $p < 0.0001$]; and (iv) a larger calculated toughness (166 ± 23.6 kJ mol^{-1} compared to 20.9 ± 5.24 kJ mol^{-1}, a significance of $p = 0.0001$). The mechanical strength was not only improved on the co-polymer membrane but it had also aligned it more closely to native BrM (Fig. 97).

The increase in mechanical strength appeared to have been achieved due to the formation of covalent bonds (photodimerisation) between two neighbouring anthracenyl side-groups. However, a case could be made for the previously described alignment observations also improving the mechanical strength. Staudinger *et al* demonstrated the requirements for producing high strength membranes, one of which was the formation of 'fully extended and perfectly aligned fibres'[323]. The fibres would provide the 'ultimate stiffness' to the membrane, and so a combination of aligned and random fibres (demonstrated with the anthracenyl-infused prosthetic BrM) would display both flexibility and an increase in mechanical strength.

This improvement in the mechanical strength had been achieved without compromising the fibrous electrospun nature of the artificial BrM, allowing for an 'easier to handle' implant. Haneef *et al* noted that as the thickness reduced in their proposed prosthetic BrM, the maximum stress before failure also reduced[165]. The reported stress before failure values of 0.175 ± 0.025 KPa in the artificial BrM proposed by Haneef *et al* highlights the effect of selective cross-linking when compared to the stress before failure values of the AMM-2 membranes (123.7 ± 7.84 KPa). Lu *et al* reported a stress before failure of 17psi (117kPa) for their designed artificial BrM[289]. This value is close to what is reported in this project for the designed AMM-2 membranes, however the value demonstrated by Lu *et al* was for a membrane without a fibrous scaffold, and so the use of a continuous flat sheet significantly improves the mechanical strength of the membrane. By using anthracene-infused co-polymer membranes, the improvement in tensile strength had been achieved without compromising its fibrous nature. Alongside this, the remaining literature articles proposing artificial BrM alternatives do not specify the tensile strength of a fibrous matrix[154,167,168].

To ensure that this improvement in mechanical strength had not affected the artificial BrM in its ability to host a layer of RPE cells, a series of biocompatibility tests were carried out to assess any changes in RPE functionality.

Initial expriments looked at ARPE-19 cell proliferation on the surface of the new generation of prosthetic BrM. After 10 days, samples were analysed by immunofluorescent assay and ARPE-19 cells were shown to be well distributed and displayed good cell proliferation. With this confirmation, the anthracenyl-infused co-polymer membranes could be progressed to primary RPE cell cultures.

1 month samples of primary RPE-seeded cross-linked co-polymer showed good cell proliferation on the surface of the membrane, highlighting the lack of any adverse effects of the incorporation of AMM into the co-polymer blend. FAK was being produced alongside the RPE-specific RPE65 protein, further confirming the ability of the AMM co-polymer membrane to allow RPE cell functionality.

Diffusional studies showed another improvement in the addition of a cross-linked element to the prosthetic BrM. By cross-linking the co-polymer membrane, the diffusional properties of the membrane improved, aligning it more closely to native BrM. This could be due to the tightening of the membrane observed in SEM analysis (Fig. 96). As the cross-linked co-polymer membrane was exposed to UV light, it underwent a tightening effect, drawing the fibres closer together and this could have subsequently reduced the pore sizes of the membrane, resulting in a less diffuse artificial BrM.

The mechanical testing showed a single-plane improvement in the tensile strength; whilst this has been shown to characterise electrospun matrices in previously reported literature[142,293], it can only provide an understanding into the stretch-stress-strain properties of the membrane. An ideal improvement from this technique is to look at the three-dimensional mechanical strength of the membrane, not only looking at the single-plane strength but also the elasticity of the membrane[324].

Whilst there was a significant improvement in mechanical strength, there did appear to be an increase in the thickness of the cross-linked electrospun mat. This increase in thickness was of concern, as it could lead to the unwanted build up of lipids and macromolecules *in vivo*. It was therefore decided that AMM-2, which showed a significant increase in mechanical strength whilst maintaining a thickness below 20μm, was the best cross-linked candidate to progress the project.

6.5 Summary and Conclusions

The aim of this project was to produce an accurate artificial BrM to allow the transport of a layer of RPE cells into the sub-retinal space as a targeted approach towards the treatment of AMD. This prosthetic BrM needed to accurately mimic native BrM in: (i) its fibrous morphology; (ii) its thickness; (iii) its porosity; (iv) its ability to host a layer of RPE cells; and (v) its ability to allow full RPE cell functionality on its surface. Alongside these key properties, the biocompatible membrane also needed to be mechanically strong to ensure it survived both the implantation process and the choriocapillaris pulse *in vivo*.

By developing on the existing work carried out by Treharne *et al* in the research group[127], a suitable, accurate mimic of native BrM has been produced.

Use of the rotating stainless steel collector ensured that the electrospun co-polymer membrane was collected in an evenly distributed matrix, thus making sure that the collected fibres from the electrospinning polymer solution created a membrane with a greater uniformity in thickness in comparison to a flat metal collector[128,129]. The collector was maintained at a slow rotation rate to ensure that an evenly distributed, randomly aligned matrix of fibres were produced[122,129], mimicking native ICL within BrM and presenting the RPE monolayer with a surface similar to that of native BrM[39].

Through the use of an optical profilometer (ZeMetrics ZeScope), accurate thickness measurements of the 1st generation of artificial BrM was completed (Table 9). Due to the severe discrepancy in the thickness of the membrane when compared to native human BrM, an investigation into the reduction of the prosthetic BrM thickness was carried out. By altering the electrospinning parameters, the thickness reduction was achieved, producing the 2nd generation of artificial BrM and aligning it closely to native BrM.

Understanding the RPE cell functionality on the surface of the artificial BrM was achieved through the use of primary murine RPE cells. Primary RPE cells were shown to: (i) form an apical arrangement on the surface of the co-polymer membrane; (ii) form the required focal adhesions with the substrate and display an established layer (predominantly in the $G_{0/1}$phase of their cell cycle); (iii) generate the RPE-specific protein RPE65, vital in the visual cycle and an indication of the RPE layer retaining its phenotype on the artificial BrM surface; (iv) form apical microvilli, a key indicator of a polarised RPE layer and essential in allowing the ability to interdigitise with the photoreceptors; (v) secrete VEGF in a predominantly basolateral manner, confirming its polarity and another key role of RPE *in vivo*; (vi) form a barrier on the co-polymer membrane, essential in the regulation of macromolecules (confirmed by diffusional studies and TEER); (vii) ingest POS, a requirement of the epithelial layer *in vivo*; and (viii) appear to produce melanin granules, a key role of the RPE cell and again highlighting the RPE layer functionality on the surface of the artificial BrM.

And finally the mechanical strength of the prosthetic BrM was enhanced through the use of selective cross-linking. Anthracenyl methacrylate (AMM) was successfully infused into the co-polymer membrane *via* the methacrylate-based synthetic process, and subsequent cross-linking through the use of UV light led to a significant improvement in the artificial BrM mechanical strength. This facilitated the handling of the membrane, ensuring a tougher membrane which can potentially withstand the implantation process and the choriocapillaris pulse, whilst also maintaining its integrity in tissue culture.

The progression of the designed prosthetic BrM from the 1st generation to the 3rd anthracenyl-infused generation has resulted in the production of a membrane that: (i) maintains its biocompatibility, using methacrylate-based co-polymers that have been shown to have no cytotoxic effect within the human body[169,170,288]; (ii) has been enhanced in its mechanical strength using anthracenyl-based selective cross-linking, achieved without compromising the fibrous electrospun nature of the artificial BrM. The mechanical strength of the membrane is also significantly higher then that reported within the literature[165,289], with most proposed prosthetic membranes reported without the tensile strength[154,167,168]; (iii) has shown to successfully host a functional RPE monolayer on its surface, using multiple immunofluorescent assays and analytical techniques to highlight the extent of RPE functionality on the co-polymer matrix using primary RPE cells instead of an immortalised RPE cell line[154,165] and quantifying key components not often listed in the literature, such as the presence of cell attachment proteins Vinculin and FAK, alongside the selective internalisation of POS[151,165,289]; (iv) has a similar thickness to native BrM without affecting its fibrous nature or reducing its mechanical strength, as is observed within the literature on alternative BrM mimetics[165]; and (v) displays control over the diffusion of macromolecules similar to that of native BrM (essential as the ICL provides control over the diffusion of macromolecules[78]), assisting the RPE monolayer in allowing the transfer of key nutrients and ions.

By ensuring that these improvements do not affect the fibrous nature of the existing co-polymer matrix, the production of a stronger, thinner mimetic of native BrM has been achieved, resulting in an implant that can withstand the implantation process and provide a permanent biocompatible scaffold for a transplanted monolayer of regenerative RPE cells to facilitate in the potential prevention of reduced visual acuity. Maintaining the production of the fibrous matrix *via* electrospinning has allowed the artificial BrM to host a monolayer of RPE cells, similar to what is reported in the literature for electrospun matrices targeting different organs with fibrous grafts or substrates for specific cell delivery[138–140].

Whilst in native BrM the outer layers of the pentalaminar structure consist of the basement membranes of the choriocapillaris and RPE monolayer[51], the artificial BrM generated within this project has shown that seeded RPE cells can successfully attach, form a polarised monolayer and display *in vivo* functionality on the surface of the prosthetic BrM. The diffusional properties of the artificial membrane help maintain control over the transfer of macromolecules and solutes (comparable to native BrM, see Fig. 36), thereby providing a synthetic mimic of native BrM, able to withstand the implantation process, to allow the targeted delivery of an established RPE monolayer as a potential treatment to dry AMD.

These key improvements signify a significant development in the suitability of the artificial BrM, generating a fibrous prosthetic scaffold which is a more accurate mimic of native BrM.

	Native Human BrM	1st generation of artificial BrM	2nd generation of artificial BrM	3rd generation of artificial BrM
Polymer blend	N/A	60:40 MMA:PEGM	60:40 MMA:PEGM	58:40:2 MMA:PEGM:AMM
Thickness of the membrane	8-17 µm, increasing in thickness towards the periphery	51 ± 3 µm	10-12 µm	17-20 µm
Fibrous nature	Yes	Yes	Yes	Yes
Young's modulus	33.5 ± 4.78 MPa	13.6 ± 3.65 MPa	25.9 ± 3.14 MPa	63.4 ± 2.91 MPa
Stress at failure	90.3 ± 4.20 KPa	23.5 ± 1.50 KPa	38.7 ± 1.20 KPa	123.7 ± 7.84 KPa
Toughness	78.9 ± 5.67 kJ mol^{-1}	10.2 ± 3.98 kJ mol^{-1}	20.9 ± 5.24 kJ mol^{-1}	166 ± 23.6 kJ mol^{-1}
Yield Strength	1.14 ± 0.015 MPa	0.14 ± 0.00025 MPa	0.35 ± 0.03 MPa	1.29 ± 0.05 MPa
Diffusional properties	2h – 0.276 Abs 24h – 0.990 Abs	2h – 0.998 Abs 24h – 1.948 Abs	2h – 0.512 Abs 24h – 1.013 Abs	2h – 0.402 Abs
Fibre thickness	0.1-0.5 µm	8-10 µm	0.1-0.8 µm	0.1-0.8 µm

Table 9: Summary table displaying the evolution of the artificial BrM and how it compares to native BrM. As the project developed, the initial artificial BrM (1st gen) was tested for its thickness and found to be too thick (51 ± 3µm) when compared to native BrM (8-17µm). The membrane thickness was successfully reduced (12µm) and this led to the next generation of artificial BrM (2nd gen). Subsequent enhancement of the mechanical strength through cross-linking led to the evolution of the membrane (3rd gen) into a more accurate mimic of native BrM.

6.6 Future Work

For the continuation of this project, it would be important to implement a multi-layered complex into the prosthetic BrM. As native BrM is composed of a pentalaminar arrangement, consisting of multiple collagenous layers and a central elastin layer, this gives it a distinct advantage over the artificial BrM in terms of elasticity. By creating a 'sandwich' complex, composed of a central elastin layer with the designed co-polymer membranes on either side, a more accurate artificial BrM would be synthesised (Fig. 98).

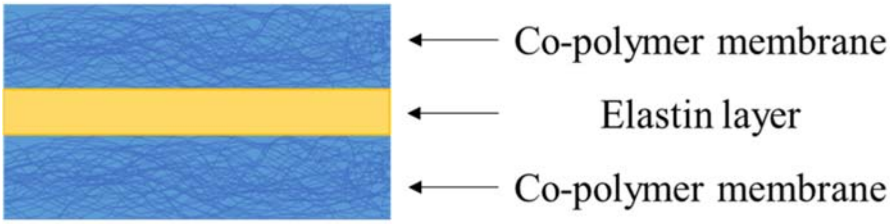

Figure 98: Representative schematic of the 'sandwich' complex, highlighting the tri-layered system. A central elastin layer would provide flexibility and allow a more accurate mimic of native BrM, whilst encasing it with two co-polymer membranes either side ensures RPE attachment and functionality.

Incorporation of a 'shape-memory' property into the prosthetic BrM would also be advantageous, and this could be achieved through further investigations into the cross-linking mechanisms. Linking into this, investigations into the artificial BrM elastic property would also be of interest.

Comprehensive *in vivo* experimentation is also required to understand the behaviour of the co-polymer membrane within the eye. Initial experimentation involving the implantation of the co-polymer membrane into rabbit eyes has been carried out, using RAMAN spectroscopy and haematoxylin & eosin (H&E) staining. Using these methods, the co-polymer membrane has been shown to implant successfully, with RAMAN spectroscopy confirming the presence of the AMM-2 artificial BrM in rabbit eyes after 1 month (Fig. 99).

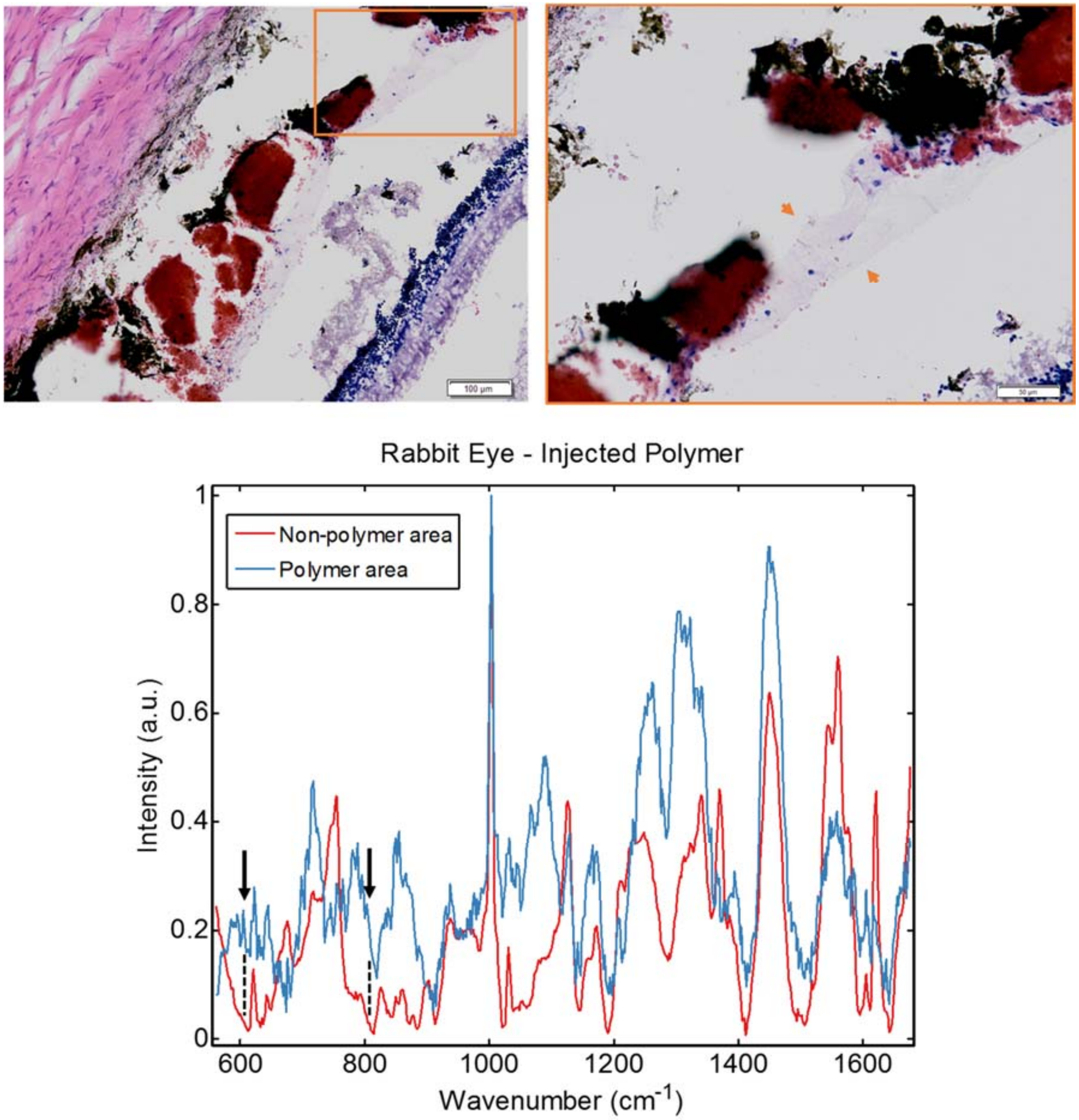

Figure 99: Summary of the initial *in vivo* experimentation, showing (bottom) RAMAN spectroscopy of the rabbit eye post-implantation and (top) the subsequent H&E staining of the rabbit eye. RAMAN confirmed the presence of the artificial BrM after 1 month *in vivo*, highlighted by the presence of typical methacrylate peaks at 600 cm^{-1} and 810 cm^{-1} (black arrows). H&E staining showed the presence of the prosthetic BrM (orange arrows), however due to a complication in surgery, leading to a retinal bleed and detatchment of the retina, the compatability of the artificial BrM could not be quantified.

RAMAN spectroscopy, carried out by Dr Mahajan at the University of Southampton, confirmed the presence of key methacrylate peaks at 600 cm^{-1} and 810 cm^{-1} (characteristic of a carbon-oxygen-carbon arrangement), indicating that the polymer was still present after 1 month *in vivo*.

Subsequent H&E staining confirmed the presence of the prosthetic BrM (Fig. 99, orange arrows), highlighting that the co-polymer membrane has not degraded after 1 month *in vivo*. However, due to complications in surgery the retina and RPE were severly damaged. This therefore did not allow an understanding into the compatability of the prosthetic BrM *in vivo*, and the continuation of this project should investigate this.

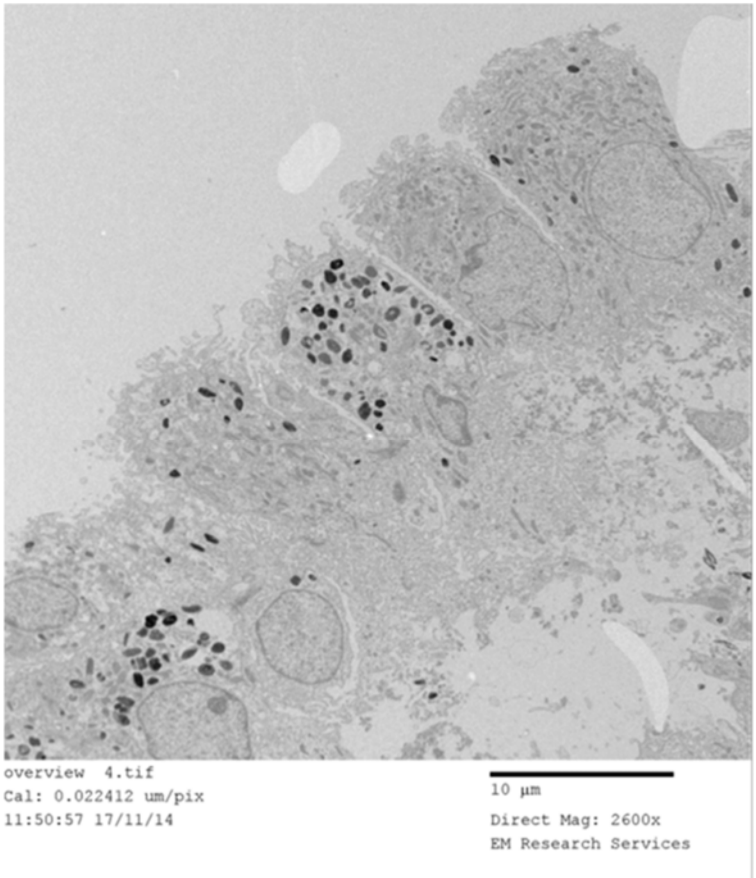

Figure 100: Transmission electron micrograph of iPS-derived RPE cells on the surface of the co-polymer membrane, displaying apical microvilli and melanin-pigments. Image curtosy of Valeria Chichagova at the University of Newcastle.

The behaviour of iPS-RPE cells on the surface of the co-polymer membrane has been looked at in collaboration with the Lako research group at the University of Newcastle, with initial results indicating that the iPS-derived RPE cells attach and proliferate on the surface of the co-polymer membrane (Fig. 100). Further work looking at the ability of the artificial BrM to host a layer of iPS-derived RPE cells on its surface would also be required.

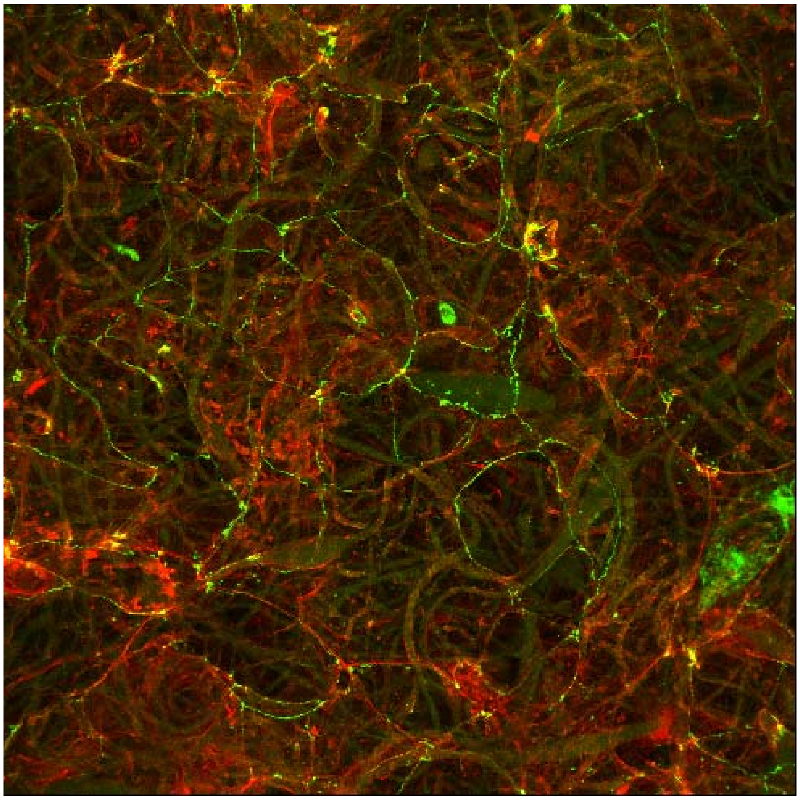

Figure 101: Confocal image of 16HBE (Human bronchial epithelial) cells on the surface of the co-polymer membrane, displaying (green) occludin tight junction formation. Counterstained with phalloidin (red).

Alongside this, in collaboration with the Davies research group at the University of Southampton, work has also been carried out on the use of the co-polymer membrane as a potential host for bronchial epithelial cells and fibroblastic cells as an *in vitro* model of the bronchial layer. The co-polymer membrane displayed good interaction with the bronchial epithelial cells, allowing it to establish an epithelial layer and form the necessary tight junctions (Fig. 101). Further work could develop into a suitable model for the alveolar lining in the human lung.

Appendices

Appendix A Publications

Patent applications

- Patent filed for anthracenyl-infused co-polymer membrane (May 2016, RIS 15298)

Paper presentations

- Ward G *et al*. Development of a novel bio-compatible polymer film for use as a Bruch's membrane substitute *ARVO Meeting Abstracts* **55,** 2997 (2014)

Presentations

- SET for Britian symposium
- OBCS Alliance meeting
- Bayreuth Electrospinning conference
- MEC BioEngineering conference
- Institute of Physics ‘Electrospinning, Principles, Possibilities and Practice’ conference

Appendix B Experimental data

NMR spectra

^{1}H NMR spectra

60:40 MMA:PEGM co-polymer unfuctionalised (1)

27/04/2016 10:27:55

Multiplets Integrals Sum 0.00	*Number of Nuclei*	6 H's / 24 H's (spectrum / structure)

Formula	$C_{13}H_{24}O_5$	*FW*	260.3267	*[M-H]-*	259.155097	*[M-H]+*	259.154000		
[M+H]-	261.170747			*[M+H]+*	261.169650	*M-*	260.162922		
M+	260.161825			*Monoisotopic Mass*	260.162374	*Nominal Mass*	260	*d_N(^{1}H)*	0.196
sd_N(^{1}H)	0.243	*max_d_N(^{1}H)*	0.498						

Acquisition Time (sec)	2.7329	*Comment*	GW/6749/1/1	*Date*	19 Oct 2012 16:51:28		
Date Stamp	19 Oct 2012 16:51:28						
File Name	\\soton.ac.uk\ude\PersonalFiles\Users\gw5g08\mydocuments\Postgraduate\NMR\oc1912hg02\10\PDATA\1\1					*Frequency (MHz)*	300.1300
Nucleus	1H	*Number of Transients*	16	*Origin*	av300	*Original Points Count*	16384
Owner	nmr	*Points Count*	16384	*Pulse Sequence*	zg30	*Receiver Gain*	812.70
SW(cyclical) (Hz)	5995.20	*Solvent*	CHLOROFORM-d			*Spectrum Offset (Hz)*	1500.0686
Spectrum Type	STANDARD	*Sweep Width (Hz)*	5994.84	*Temperature (degree C)*	25.160		

^{1}H NMR (300 MHz, CHLOROFORM-*d*) δ ppm 0.86 - 0.89 (m, 1 H) 1.02 - 1.06 (m, 1 H) 1.81 - 1.85 (m, 1 H) 3.60 - 3.63 (m, 1 H) 3.65 - 3.67 (m, 1 H) 4.11 - 4.15 (m, 1 H)

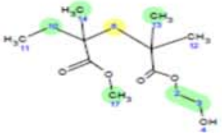

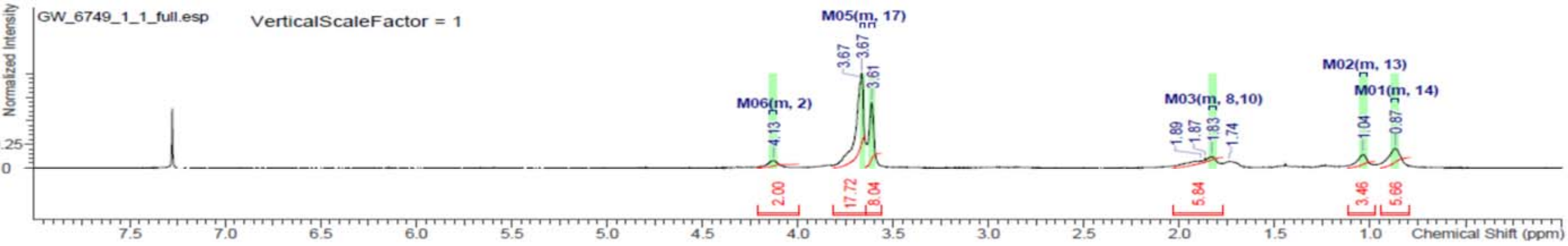

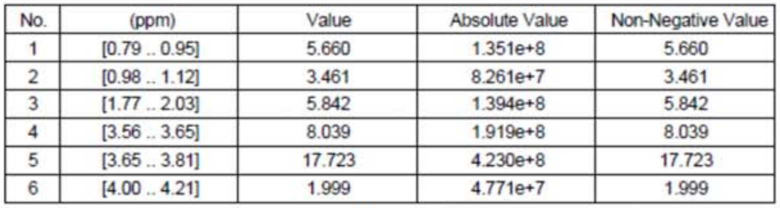

No.	(ppm)	Value	Absolute Value	Non-Negative Value
1	[0.79 .. 0.95]	5.660	1.351e+8	5.660
2	[0.98 .. 1.12]	3.461	8.261e+7	3.461
3	[1.77 .. 2.03]	5.842	1.394e+8	5.842
4	[3.56 .. 3.65]	8.039	1.919e+8	8.039
5	[3.65 .. 3.81]	17.723	4.230e+8	17.723
6	[4.00 .. 4.21]	1.999	4.771e+7	1.999

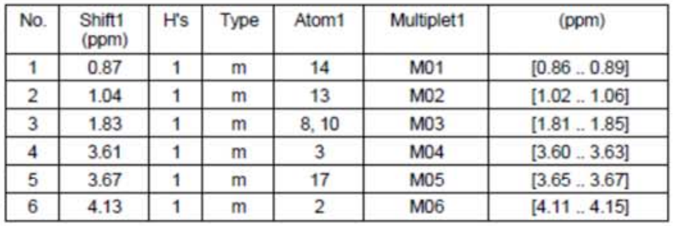

No.	Shift1 (ppm)	H's	Type	Atom1	Multiplet1	(ppm)
1	0.87	1	m	14	M01	[0.86 .. 0.89]
2	1.04	1	m	13	M02	[1.02 .. 1.06]
3	1.83	1	m	8, 10	M03	[1.81 .. 1.85]
4	3.61	1	m	3	M04	[3.60 .. 3.63]
5	3.67	1	m	17	M05	[3.65 .. 3.67]
6	4.13	1	m	2	M06	[4.11 .. 4.15]

No.	Atom	Exp. Shift (ppm)	Multiplet
1	14	0.87	M01
2	13	1.04	M02
3	8	1.83	M03
4	10	1.83	M03
5	3	3.61	M04
6	17	3.67	M05
7	2	4.13	M06

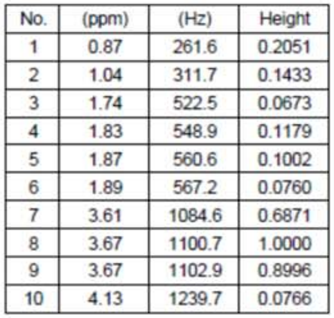

No.	(ppm)	(Hz)	Height
1	0.87	261.6	0.2051
2	1.04	311.7	0.1433
3	1.74	522.5	0.0673
4	1.83	548.9	0.1179
5	1.87	560.6	0.1002
6	1.89	567.2	0.0760
7	3.61	1084.6	0.6871
8	3.67	1100.7	1.0000
9	3.67	1102.9	0.8996
10	4.13	1239.7	0.0766

60:40 MMA:PEGM co-polymer fuctionalised (2)

27/04/2016 10:37:10

Multiplets Integrals Sum 0.00	*Number of Nuclei*	9 H's / 27 H's (spectrum / structure)

Formula	$C_{18}H_{27}NO_9$	*FW*	401.4083	*[M-H]-*	400.161305	*[M-H]+*	400.160208		
[M+H]-	402.176955			*[M+H]+*	402.175858	*M-*	401.169130		
M+	401.168033			*Monoisotopic Mass*	401.168581	*Nominal Mass*	401	*d_N(^1H)*	0.214
sd_N(^1H)	0.306	*max_d_N(^1H)*	0.607						

Acquisition Time (sec)	2.7329	*Comment*	GW/6749/2/5/2b	*Date*	01 Nov 2012 14:28:16		
Date Stamp	01 Nov 2012 14:28:16						
File Name	\\soton.ac.uk\ude\PersonalFiles\Users\gw5g08\mydocuments\Postgraduate\NMR\nv0112hg01\10\PDATA\1\1r					*Frequency (MHz)*	300.1300
Nucleus	1H	*Number of Transients*	16	*Origin*	av300	*Original Points Count*	16384
Owner	nmr	*Points Count*	16384	*Pulse Sequence*	zg30	*Receiver Gain*	1625.50
SW(cyclical) (Hz)	5995.20	*Solvent*	CHLOROFORM-d			*Spectrum Offset (Hz)*	1497.4951
Spectrum Type	STANDARD	*Sweep Width (Hz)*	5994.84	*Temperature (degree C)*	25.160		

^{1}H NMR (300 MHz, CHLOROFORM-*d*) δ ppm 0.85 - 0.88 (m, 1 H) 1.02 - 1.05 (m, 1 H) 1.58 - 1.61 (m, 1 H) 1.81 - 1.84 (m, 1 H) 2.84 - 2.87 (m, 1 H) 3.59 - 3.62 (m, 1 H) 3.64 - 3.68 (m, 1 H) 4.10 - 4.13 (m, 1 H) 4.45 - 4.48 (m, 1 H)

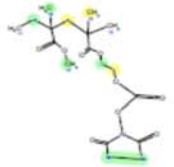

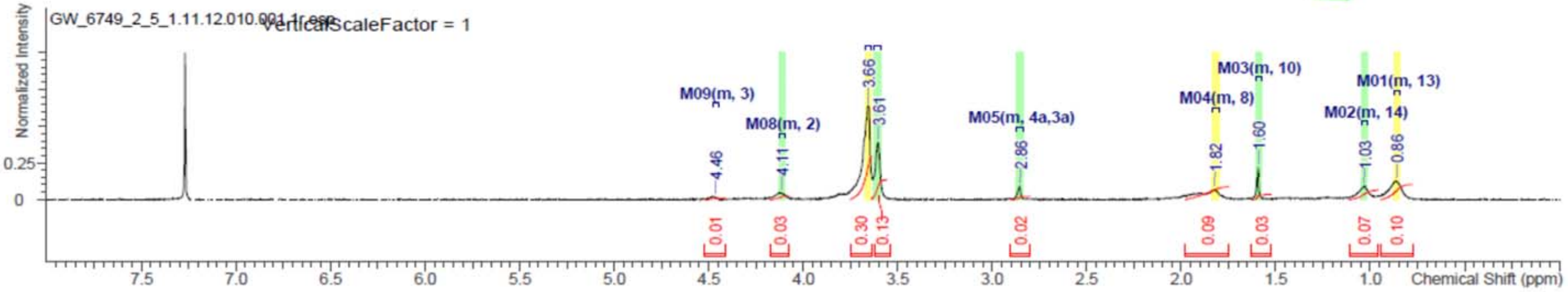

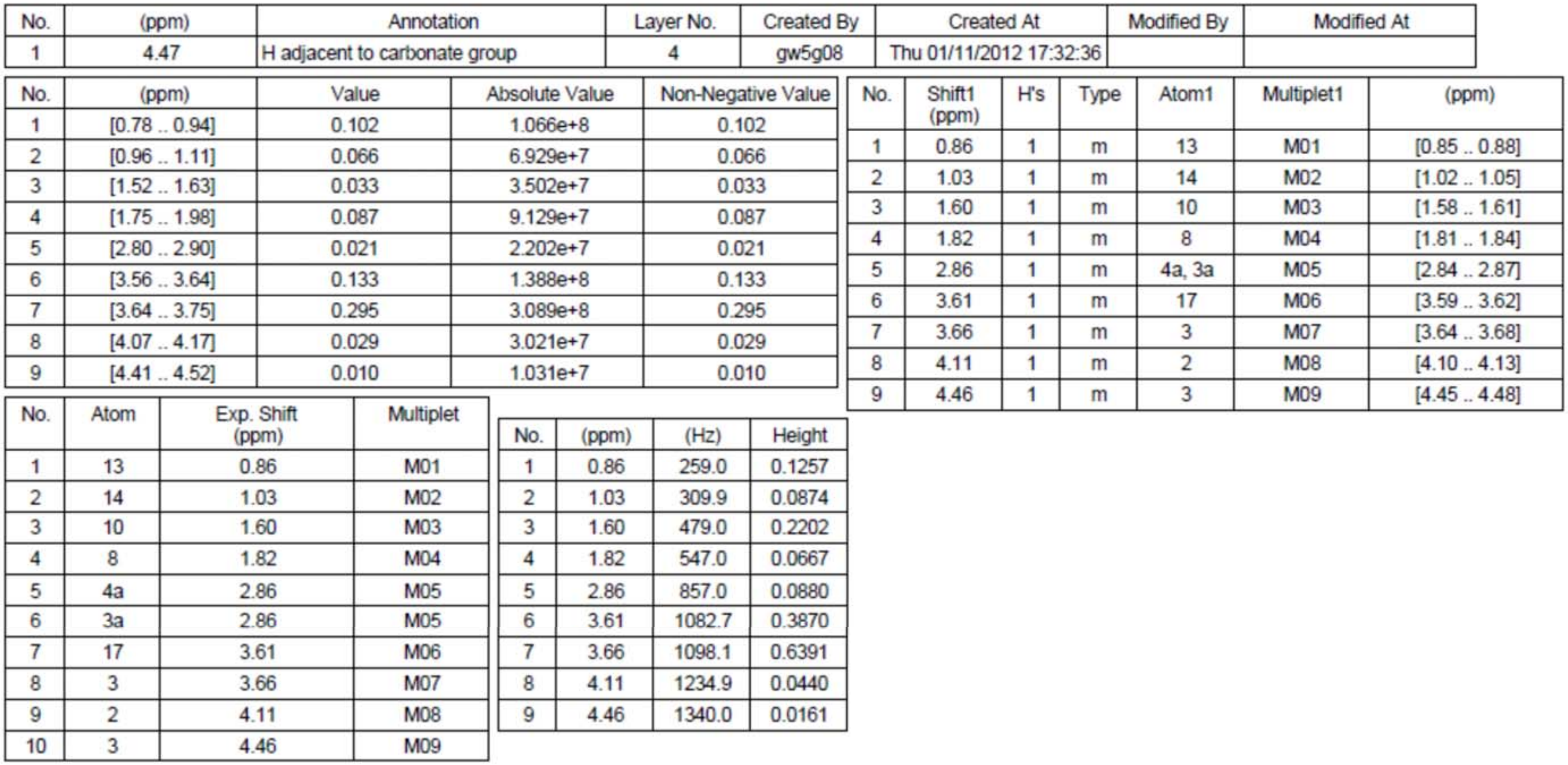

No.	(ppm)	Annotation	Layer No.	Created By	Created At	Modified By	Modified At
1	4.47	H adjacent to carbonate group	4	gw5g08	Thu 01/11/2012 17:32:36		

No.	(ppm)	Value	Absolute Value	Non-Negative Value
1	[0.78 .. 0.94]	0.102	1.066e+8	0.102
2	[0.96 .. 1.11]	0.066	6.929e+7	0.066
3	[1.52 .. 1.63]	0.033	3.502e+7	0.033
4	[1.75 .. 1.98]	0.087	9.129e+7	0.087
5	[2.80 .. 2.90]	0.021	2.202e+7	0.021
6	[3.56 .. 3.64]	0.133	1.388e+8	0.133
7	[3.64 .. 3.75]	0.295	3.089e+8	0.295
8	[4.07 .. 4.17]	0.029	3.021e+7	0.029
9	[4.41 .. 4.52]	0.010	1.031e+7	0.010

No.	Shift1 (ppm)	H's	Type	Atom1	Multiplet1	(ppm)
1	0.86	1	m	13	M01	[0.85 .. 0.88]
2	1.03	1	m	14	M02	[1.02 .. 1.05]
3	1.60	1	m	10	M03	[1.58 .. 1.61]
4	1.82	1	m	8	M04	[1.81 .. 1.84]
5	2.86	1	m	4a, 3a	M05	[2.84 .. 2.87]
6	3.61	1	m	17	M06	[3.59 .. 3.62]
7	3.66	1	m	3	M07	[3.64 .. 3.68]
8	4.11	1	m	2	M08	[4.10 .. 4.13]
9	4.46	1	m	3	M09	[4.45 .. 4.48]

No.	Atom	Exp. Shift (ppm)	Multiplet
1	13	0.86	M01
2	14	1.03	M02
3	10	1.60	M03
4	8	1.82	M04
5	4a	2.86	M05
6	3a	2.86	M05
7	17	3.61	M06
8	3	3.66	M07
9	2	4.11	M08
10	3	4.46	M09

No.	(ppm)	(Hz)	Height
1	0.86	259.0	0.1257
2	1.03	309.9	0.0874
3	1.60	479.0	0.2202
4	1.82	547.0	0.0667
5	2.86	857.0	0.0880
6	3.61	1082.7	0.3870
7	3.66	1098.1	0.6391
8	4.11	1234.9	0.0440
9	4.46	1340.0	0.0161

Appendix B

58:40:2 MMA:PEGM:FMA co-polymer unfunctionalised (3)

Number of Nuclei 5 H's / 32 H's (spectrum / structure)	

Formula	$C_{21}H_{32}O_8$	***FW***	412.4740	***[M-H]-***	411.202442	***[M-H]+***	411.201344		
[M+H]-	413.218092			***[M+H]+***	413.216994	***M-***	412.210267		
M+	412.209169			***Monoisotopic Mass***	412.209718	***Nominal Mass***	412	***d_N(¹H)***	1.479
sd_N(¹H)	2.351	***max_d_N(¹H)***	4.489						

Acquisition Time (sec)	4.0894	***Comment***	GW/6749/20/47	***Date***	02 Jun 2014 18:57:20		
Date Stamp	02 Jun 2014 18:57:20						
File Name	\\soton.ac.uk\ude\PersonalFiles\Users\gw5g08\mydocuments\Postgraduate\Analysis\NMR\ju0214ybj2\ju0214ybj2\10\PDATA\1\1r						
Frequency (MHz)	400.1300	***Nucleus***	1H	***Number of Transients***	16	***Origin***	AVII400
Original Points Count	32768	***Owner***	nmr	***Points Count***	65536	***Pulse Sequence***	zg30
Receiver Gain	70.50	***SW(cyclical) (Hz)***	8012.82	***Solvent***	CHLOROFORM-d		
Spectrum Offset (Hz)	2464.9363	***Spectrum Type***	STANDARD	***Sweep Width (Hz)***	8012.70	***Temperature (degree C)***	25.160

^{1}H NMR (400 MHz, CHLOROFORM-*d*) δ ppm 0.84 (br s, 1 H) 1.01 (br s, 1 H) 1.71 - 1.94 (m, 1 H) 3.59 (br s, 1 H) 4.10 (br s, 1 H)

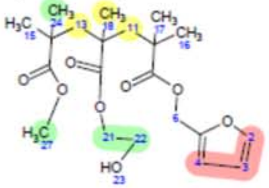

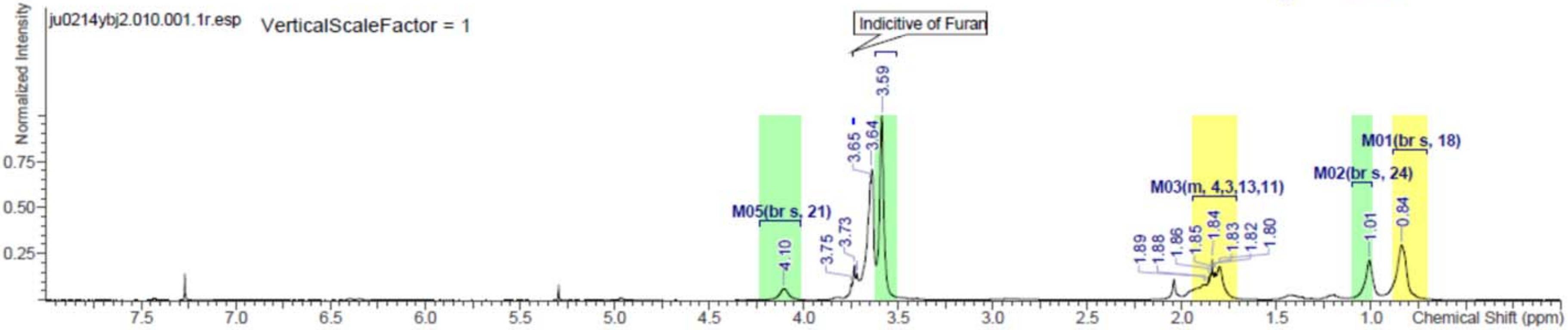

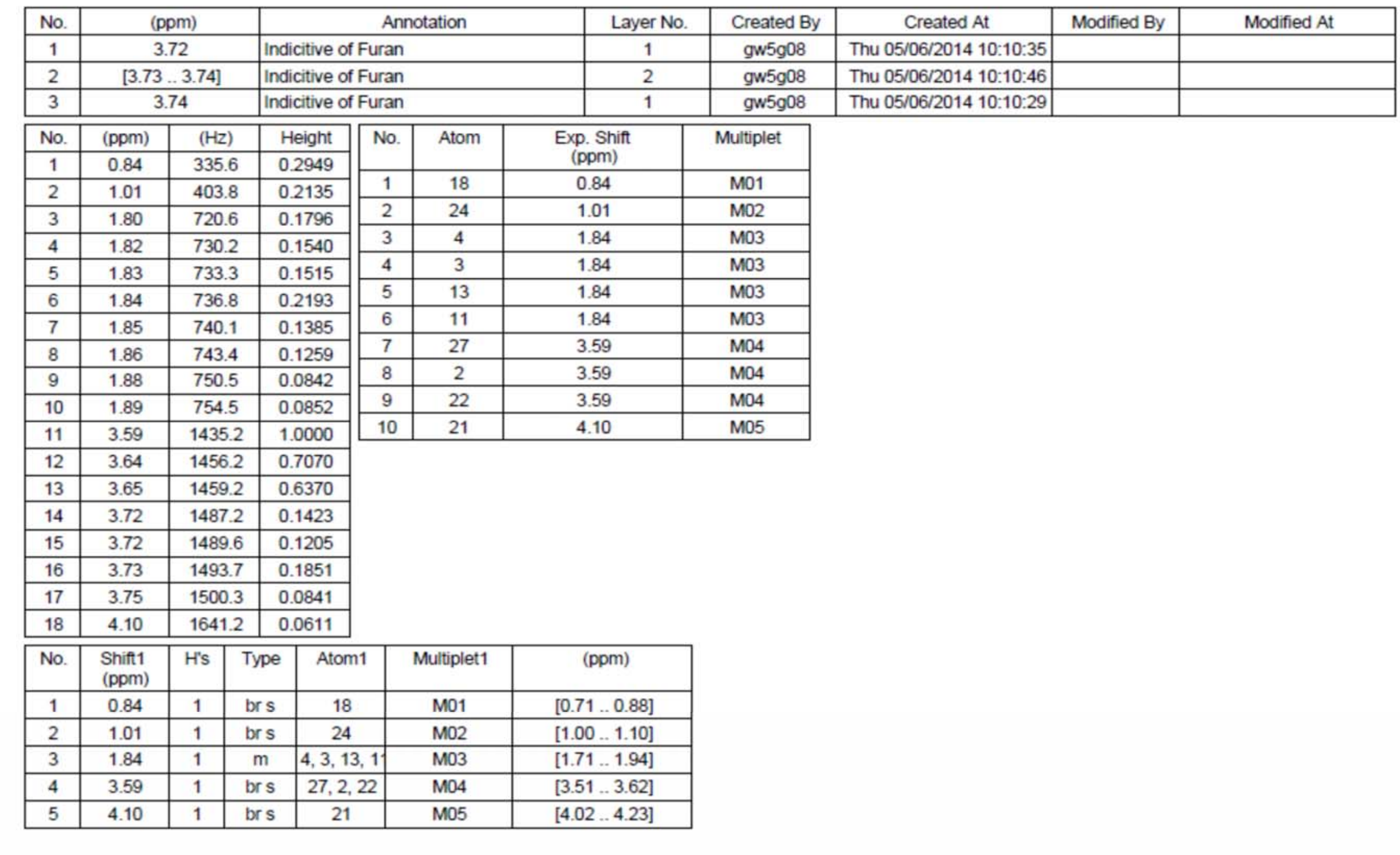

No.	(ppm)	Annotation	Layer No.	Created By	Created At	Modified By	Modified At
1	3.72	Indicitive of Furan	1	gw5g08	Thu 05/06/2014 10:10:35		
2	[3.73 .. 3.74]	Indicitive of Furan	2	gw5g08	Thu 05/06/2014 10:10:46		
3	3.74	Indicitive of Furan	1	gw5g08	Thu 05/06/2014 10:10:29		

No.	(ppm)	(Hz)	Height
1	0.84	335.6	0.2949
2	1.01	403.8	0.2135
3	1.80	720.6	0.1796
4	1.82	730.2	0.1540
5	1.83	733.3	0.1515
6	1.84	736.8	0.2193
7	1.85	740.1	0.1385
8	1.86	743.4	0.1259
9	1.88	750.5	0.0842
10	1.89	754.5	0.0852
11	3.59	1435.2	1.0000
12	3.64	1456.2	0.7070
13	3.65	1459.2	0.6370
14	3.72	1487.2	0.1423
15	3.72	1489.6	0.1205
16	3.73	1493.7	0.1851
17	3.75	1500.3	0.0841
18	4.10	1641.2	0.0611

No.	Atom	Exp. Shift (ppm)	Multiplet
1	18	0.84	M01
2	24	1.01	M02
3	4	1.84	M03
4	3	1.84	M03
5	13	1.84	M03
6	11	1.84	M03
7	27	3.59	M04
8	2	3.59	M04
9	22	3.59	M04
10	21	4.10	M05

No.	Shift1 (ppm)	H's	Type	Atom1	Multiplet1	(ppm)
1	0.84	1	br s	18	M01	[0.71 .. 0.88]
2	1.01	1	br s	24	M02	[1.00 .. 1.10]
3	1.84	1	m	4, 3, 13, 1	M03	[1.71 .. 1.94]
4	3.59	1	br s	27, 2, 22	M04	[3.51 .. 3.62]
5	4.10	1	br s	21	M05	[4.02 .. 4.23]

58:40:2 MMA:PEGM:FMA co-polymer functionalised (4)

Number of Nuclei 10 H's / 35 H's (spectrum / structure)

Formula	$C_{26}H_{35}NO_{12}$	***FW***	553.5556	***[M-H]-***	552.208649	***[M-H]+***	552.207552
[M+H]-	554.224299	***[M+H]+***	554.223202	***M-***	553.216474		
M+	553.215377	***Monoisotopic Mass***	553.215926	***Nominal Mass***	553	***d_N(^{1}H)***	1.303
sd_N(^{1}H)	2.117	***max_d_N(^{1}H)***	4.450				

Acquisition Time (sec)	4.0894	***Comment***	GW/6749/21/49	***Date***	02 Jun 2014 19:35:44		
Date Stamp	02 Jun 2014 19:35:44						
File Name	\\soton.ac.uk\ude\PersonalFiles\Users\gw5g08\mydocuments\Postgraduate\Analysis\NMR\ju0214ybj3\ju0214ybj3\10\PDATA\1\1r						
Frequency (MHz)	400.1300	***Nucleus***	1H	***Number of Transients***	16	***Origin***	AVII400
Original Points Count	32768	***Owner***	nmr	***Points Count***	65536	***Pulse Sequence***	zg30
Receiver Gain	70.50	***SW(cyclical) (Hz)***	8012.82	***Solvent***	CHLOROFORM-d		
Spectrum Offset (Hz)	2464.8140	***Spectrum Type***	STANDARD	***Sweep Width (Hz)***	8012.70	***Temperature (degree C)***	25.160

^{1}H NMR (400 MHz, CHLOROFORM-*d*) δ ppm 0.82 - 0.85 (m, 1 H) 0.99 - 1.02 (m, 1 H) 1.78 - 1.81 (m, 1 H) 1.87 - 1.89 (m, 1 H) 2.82 - 2.85 (m, 1 H) 3.57 - 3.60 (m, 1 H) 3.64 - 3.67 (m, 1 H) 3.78 - 3.80 (m, 1 H) 4.08 - 4.11 (m, 1 H) 4.44 - 4.46 (m, 1 H)

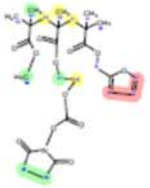

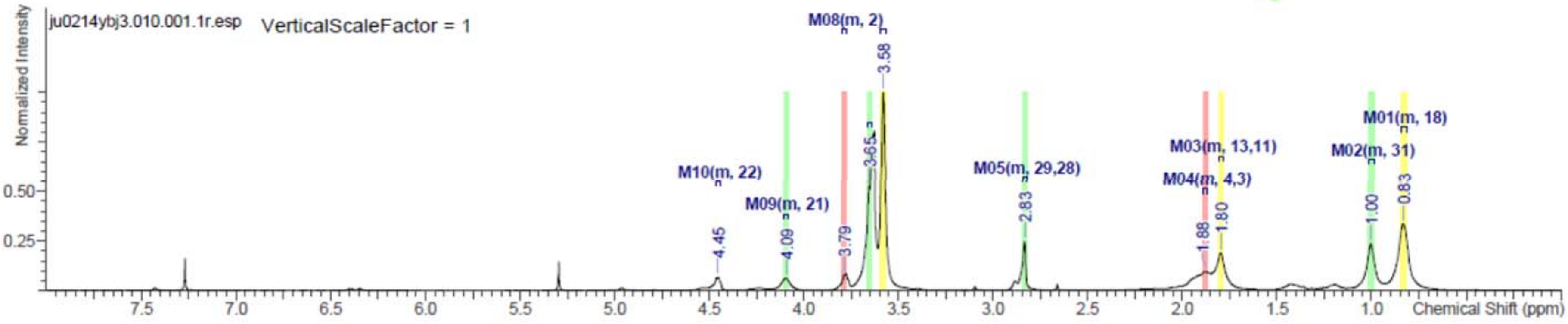

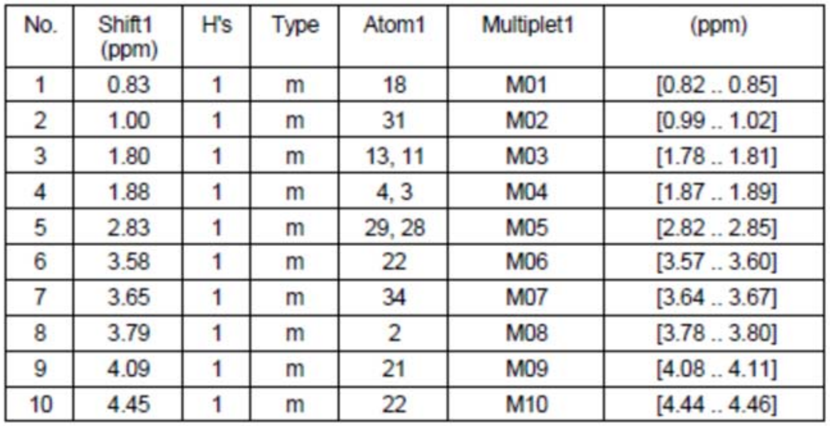

No.	Shift1 (ppm)	H's	Type	Atom1	Multiplet1	(ppm)
1	0.83	1	m	18	M01	[0.82 .. 0.85]
2	1.00	1	m	31	M02	[0.99 .. 1.02]
3	1.80	1	m	13, 11	M03	[1.78 .. 1.81]
4	1.88	1	m	4, 3	M04	[1.87 .. 1.89]
5	2.83	1	m	29, 28	M05	[2.82 .. 2.85]
6	3.58	1	m	22	M06	[3.57 .. 3.60]
7	3.65	1	m	34	M07	[3.64 .. 3.67]
8	3.79	1	m	2	M08	[3.78 .. 3.80]
9	4.09	1	m	21	M09	[4.08 .. 4.11]
10	4.45	1	m	22	M10	[4.44 .. 4.46]

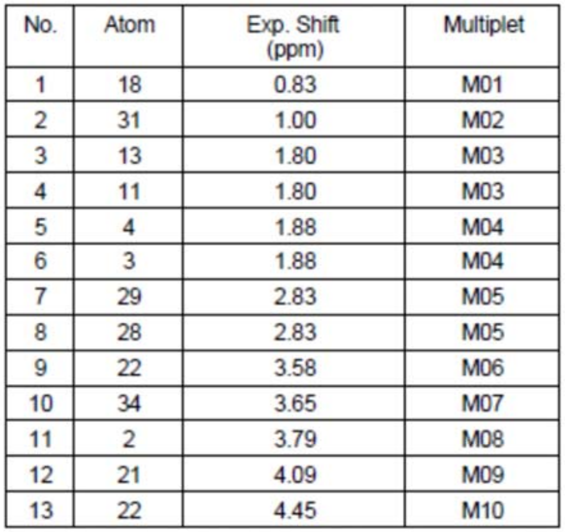

No.	Atom	Exp. Shift (ppm)	Multiplet
1	18	0.83	M01
2	31	1.00	M02
3	13	1.80	M03
4	11	1.80	M03
5	4	1.88	M04
6	3	1.88	M04
7	29	2.83	M05
8	28	2.83	M05
9	22	3.58	M06
10	34	3.65	M07
11	2	3.79	M08
12	21	4.09	M09
13	22	4.45	M10

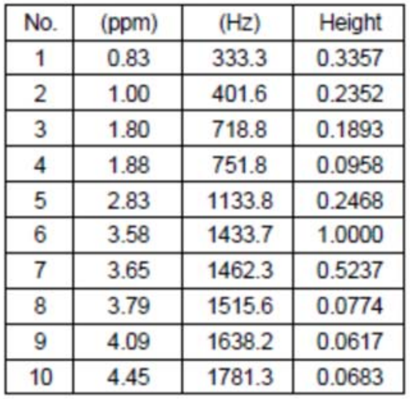

No.	(ppm)	(Hz)	Height
1	0.83	333.3	0.3357
2	1.00	401.6	0.2352
3	1.80	718.8	0.1893
4	1.88	751.8	0.0958
5	2.83	1133.8	0.2468
6	3.58	1433.7	1.0000
7	3.65	1462.3	0.5237
8	3.79	1515.6	0.0774
9	4.09	1638.2	0.0617
10	4.45	1781.3	0.0683

Appendix B

9-anthryl methyl methacrylate (5)

Multiplets Integrals Sum 0.00		***Number of Nuclei***	9 H's / 16 H's (spectrum / structure)

Formula	$C_{19}H_{16}O_2$	***FW***	276.3291	***[M-H]-***	275.107753	***[M-H]+***	275.106656		
[M+H]-	277.123403			***[M+H]+***	277.122306	***M-***	276.115578		
M+	276.114481			***Monoisotopic Mass***	276.115030	***Nominal Mass***	276	***d_N(¹H)***	0.328
sd_N(¹H)	0.544	***max_d_N(¹H)***	1.743						

Acquisition Time (sec)	4.0894	***Comment***	GW/6749/16	***Date***	27 Nov 2013 14:49:36		
Date Stamp	27 Nov 2013 14:49:36						
File Name	\\soton.ac.uk\ude\PersonalFiles\Users\gw5g08\mydocuments\Postgraduate\Analysis\NMR\GW_6749_16\nv2713alf1\10\PDATA\1\1r						
Frequency (MHz)	400.1300	***Nucleus***	1H	***Number of Transients***	16	***Origin***	AVII400
Original Points Count	32768	***Owner***	nmr	***Points Count***	65536	***Pulse Sequence***	zg30
Receiver Gain	271.00	***SW(cyclical) (Hz)***	8012.82	***Solvent***	CHLOROFORM-d	***Spectrum Offset (Hz)***	2465.1812
Spectrum Type	STANDARD	***Sweep Width (Hz)***	8012.70	***Temperature (degree C)***	25.160		

^{1}H NMR (400 MHz, CHLOROFORM-*d*) δ ppm 1.92 - 1.94 (m, 1 H) 5.52 (t, *J*=1.59 Hz, 1 H) 6.07 (d, *J*=0.61 Hz, 1 H) 6.24 (s, 1 H) 7.46 - 7.54 (m, 1 H) 7.56 - 7.62 (m, 1 H) 8.05 (d, *J*=8.44 Hz, 1 H) 8.32 - 8.42 (m, 1 H) 8.53 (s, 1 H)

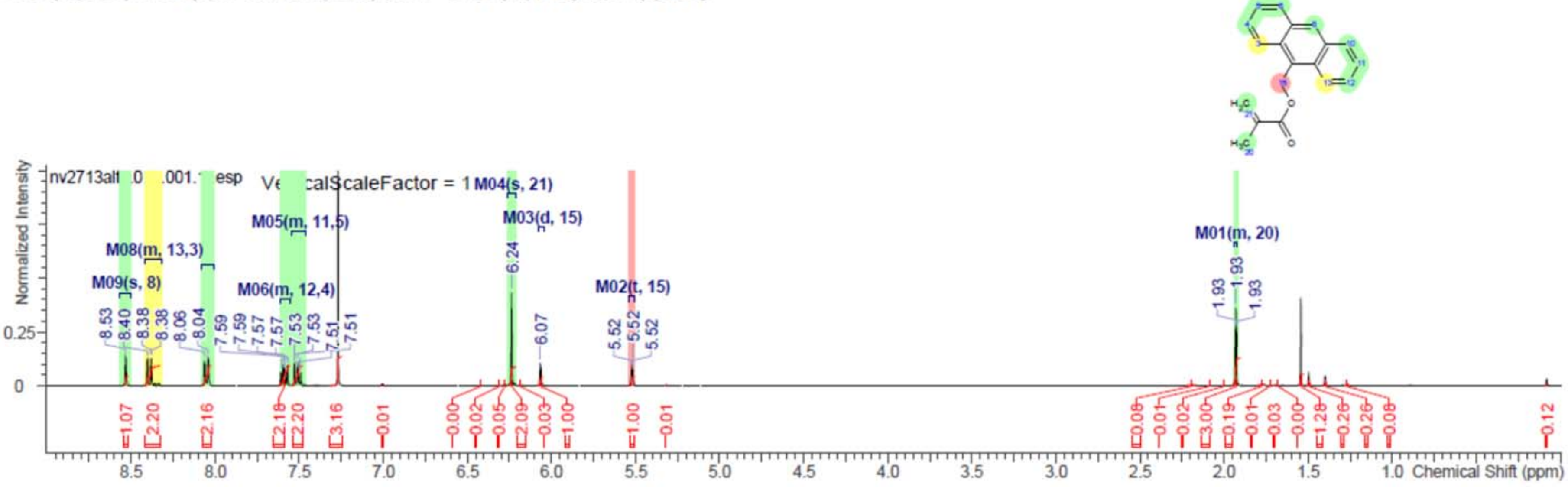

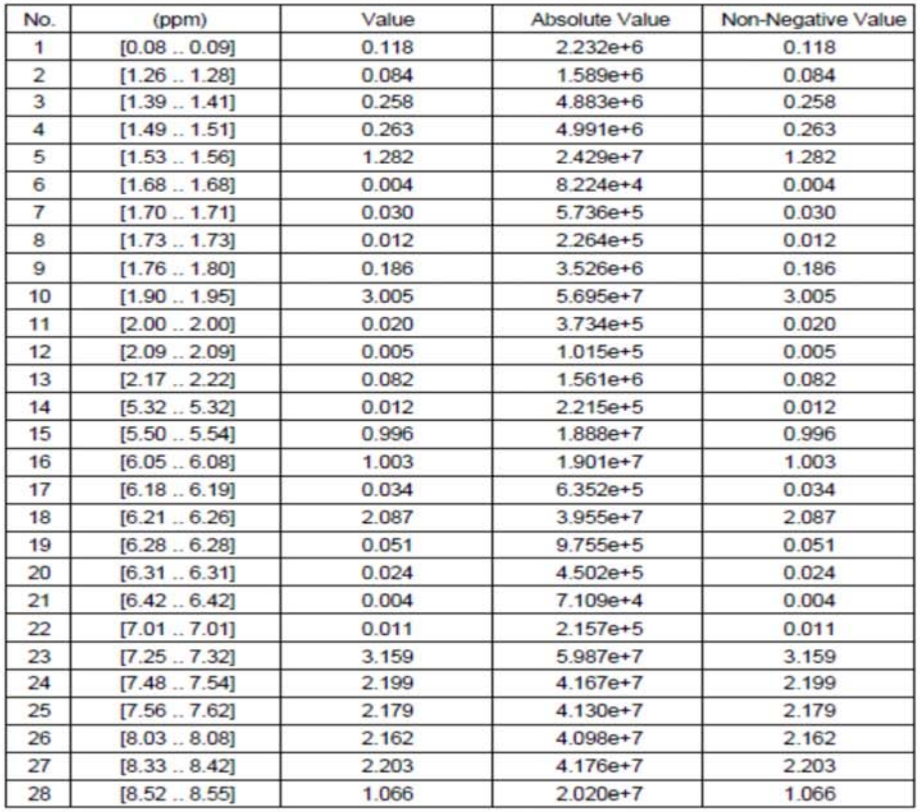

No.	(ppm)	Value	Absolute Value	Non-Negative Value
1	[0.08 .. 0.09]	0.118	2.232e+6	0.118
2	[1.26 .. 1.28]	0.084	1.589e+6	0.084
3	[1.39 .. 1.41]	0.258	4.883e+6	0.258
4	[1.49 .. 1.51]	0.263	4.991e+6	0.263
5	[1.53 .. 1.56]	1.282	2.429e+7	1.282
6	[1.68 .. 1.68]	0.004	8.224e+4	0.004
7	[1.70 .. 1.71]	0.030	5.736e+5	0.030
8	[1.73 .. 1.73]	0.012	2.264e+5	0.012
9	[1.76 .. 1.80]	0.186	3.526e+6	0.186
10	[1.90 .. 1.95]	3.005	5.695e+7	3.005
11	[2.00 .. 2.00]	0.020	3.734e+5	0.020
12	[2.09 .. 2.09]	0.005	1.015e+5	0.005
13	[2.17 .. 2.22]	0.082	1.561e+6	0.082
14	[5.32 .. 5.32]	0.012	2.215e+5	0.012
15	[5.50 .. 5.54]	0.996	1.888e+7	0.996
16	[6.05 .. 6.08]	1.003	1.901e+7	1.003
17	[6.18 .. 6.19]	0.034	6.352e+5	0.034
18	[6.21 .. 6.26]	2.087	3.955e+7	2.087
19	[6.28 .. 6.28]	0.051	9.755e+5	0.051
20	[6.31 .. 6.31]	0.024	4.502e+5	0.024
21	[6.42 .. 6.42]	0.004	7.109e+4	0.004
22	[7.01 .. 7.01]	0.011	2.157e+5	0.011
23	[7.25 .. 7.32]	3.159	5.987e+7	3.159
24	[7.48 .. 7.54]	2.199	4.167e+7	2.199
25	[7.56 .. 7.62]	2.179	4.130e+7	2.179
26	[8.03 .. 8.08]	2.162	4.098e+7	2.162
27	[8.33 .. 8.42]	2.203	4.176e+7	2.203
28	[8.52 .. 8.55]	1.066	2.020e+7	1.066

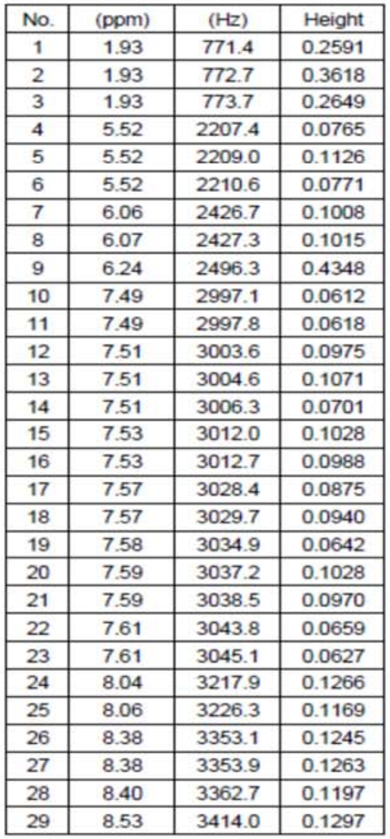

No.	(ppm)	(Hz)	Height
1	1.93	771.4	0.2591
2	1.93	772.7	0.3618
3	1.93	773.7	0.2649
4	5.52	2207.4	0.0765
5	5.52	2209.0	0.1126
6	5.52	2210.6	0.0771
7	6.06	2426.7	0.1008
8	6.07	2427.3	0.1015
9	6.24	2496.3	0.4348
10	7.49	2997.1	0.0612
11	7.49	2997.8	0.0618
12	7.51	3003.6	0.0975
13	7.51	3004.6	0.1071
14	7.51	3006.3	0.0701
15	7.53	3012.0	0.1028
16	7.53	3012.7	0.0988
17	7.57	3028.4	0.0875
18	7.57	3029.7	0.0940
19	7.58	3034.9	0.0642
20	7.59	3037.2	0.1028
21	7.59	3038.5	0.0970
22	7.61	3043.8	0.0659
23	7.61	3045.1	0.0627
24	8.04	3217.9	0.1266
25	8.06	3226.3	0.1169
26	8.38	3353.1	0.1245
27	8.38	3353.9	0.1263
28	8.40	3362.7	0.1197
29	8.53	3414.0	0.1297

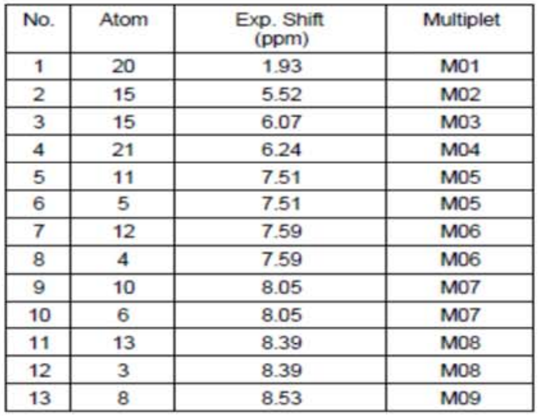

No.	Atom	Exp. Shift (ppm)	Multiplet
1	20	1.93	M01
2	15	5.52	M02
3	15	6.07	M03
4	21	6.24	M04
5	11	7.51	M05
6	5	7.51	M05
7	12	7.59	M06
8	4	7.59	M06
9	10	8.05	M07
10	6	8.05	M07
11	13	8.39	M08
12	3	8.39	M08
13	8	8.53	M09

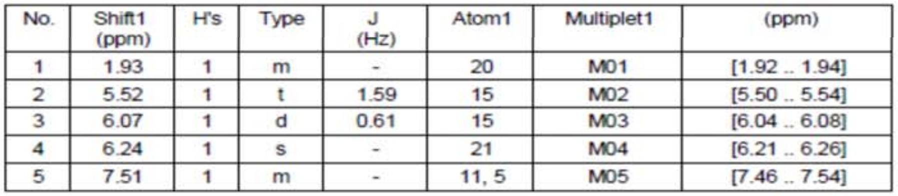

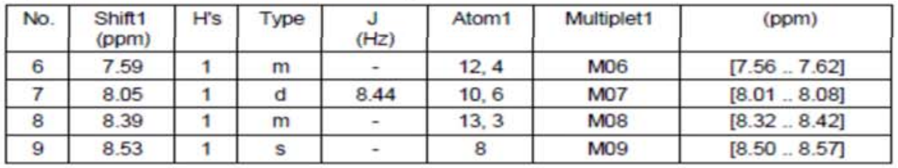

No.	Shift1 (ppm)	H's	Type	J (Hz)	Atom1	Multiplet1	(ppm)
1	1.93	1	m	-	20	M01	[1.92 .. 1.94]
2	5.52	1	t	1.59	15	M02	[5.50 .. 5.54]
3	6.07	1	d	0.61	15	M03	[6.04 .. 6.08]
4	6.24	1	s	-	21	M04	[6.21 .. 6.26]
5	7.51	1	m	-	11, 5	M05	[7.46 .. 7.54]
6	7.59	1	m	-	12, 4	M06	[7.56 .. 7.62]
7	8.05	1	d	8.44	10, 6	M07	[8.01 .. 8.08]
8	8.39	1	m	-	13, 3	M08	[8.32 .. 8.42]
9	8.53	1	s	-	8	M09	[8.50 .. 8.57]

58:40:2 MMA:PEGM:AMM co-polymer unfunctionalised (6)

Multiplets Integrals Sum	0.00	*Number of Nuclei*	8 H's / 40 H's (spectrum / structure)

Formula	$C_{32}H_{40}O_7$	*FW*	536.6558	*[M-H]-*	535.270127	*[M-H]+*	535.269030		
[M+H]-	537.285777			*[M+H]+*	537.284680	*M-*	536.277952		
M+	536.276855			*Monoisotopic Mass*	536.277404	*Nominal Mass*	536	*$d_N(^1H)$*	0.263
$sd_N(^1H)$	0.344	*$max\_d_N(^1H)$*	0.617						

Acquisition Time (sec)	4.0894	*Comment*	GW/6749/17	*Date*	05 Feb 2014 16:57:36		
Date Stamp	05 Feb 2014 16:57:36						
File Name	\\soton.ac.uk\ude\PersonalFiles\Users\gw5g08\mydocuments\Postgraduate\Analysis\NMR\GW_6749_18\fe0514alya1\10\PDATA\1\1r						
Frequency (MHz)	400.1300	*Nucleus*	1H	*Number of Transients*	16	*Origin*	AVII400
Original Points Count	32768	*Owner*	nmr	*Points Count*	65536	*Pulse Sequence*	zg30
Receiver Gain	165.26	*SW(cyclical) (Hz)*	8012.82	*Solvent*	CHLOROFORM-d	*Spectrum Offset (Hz)*	2466.0371
Spectrum Type	STANDARD	*Sweep Width (Hz)*	8012.70	*Temperature (degree C)*	25.160		

^{1}H NMR (400 MHz, CHLOROFORM-*d*) δ ppm 0.86 (br s, 1 H) 1.03 (br s, 1 H) 1.14 - 1.28 (m, 1 H) 1.75 - 2.09 (m, 1 H) 3.61 (br s, 1 H) 3.67 (br s, 1 H) 4.12 (br s, 1 H) 5.31 (s, 1 H)

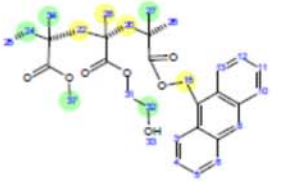

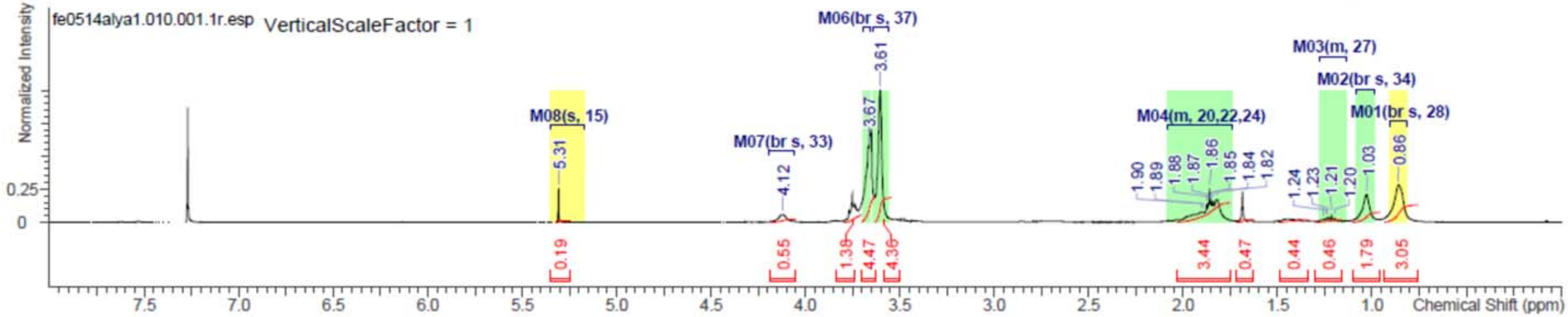

No.	(ppm)	Value	Absolute Value	Non-Negative Value
1	[0.76 .. 0.93]	3.050	1.777e+8	3.050
2	[0.96 .. 1.10]	1.794	1.045e+8	1.794
3	[1.16 .. 1.30]	0.457	2.664e+7	0.457
4	[1.34 .. 1.49]	0.436	2.538e+7	0.436
5	[1.63 .. 1.72]	0.475	2.768e+7	0.475
6	[1.75 .. 2.03]	3.437	2.003e+8	3.437
7	[3.54 .. 3.63]	4.365	2.543e+8	4.365
8	[3.63 .. 3.70]	4.470	2.605e+8	4.470
9	[3.70 .. 3.79]	1.378	8.030e+7	1.378
10	[4.05 .. 4.19]	0.554	3.228e+7	0.554
11	[5.25 .. 5.35]	0.189	1.102e+7	0.189

No.	Shift1 (ppm)	H's	Type	Atom1	Multiplet1	(ppm)
1	0.86	1	br s	28	M01	[0.82 .. 0.90]
2	1.03	1	br s	34	M02	[0.99 .. 1.09]
3	1.22	1	m	27	M03	[1.14 .. 1.28]
4	1.86	1	m	20, 22, 24	M04	[1.75 .. 2.09]
5	3.61	1	br s	32	M05	[3.56 .. 3.64]
6	3.67	1	br s	37	M06	[3.66 .. 3.69]
7	4.12	1	br s	33	M07	[4.06 .. 4.19]
8	5.31	1	s	15	M08	[5.17 .. 5.35]

No.	(ppm)	(Hz)	Height
1	0.86	343.6	0.2827
2	1.03	411.7	0.2078
3	1.20	478.8	0.0352
4	1.21	485.9	0.0626
5	1.23	492.8	0.0433
6	1.24	497.5	0.0286
7	1.26	504.5	0.0209
8	1.82	728.0	0.1723
9	1.84	737.1	0.1619
10	1.85	740.4	0.1582
11	1.86	743.9	0.2557
12	1.87	747.3	0.1424
13	1.88	750.5	0.1318
14	1.89	757.7	0.0761
15	1.90	761.8	0.0782
16	3.61	1442.7	1.0000
17	3.67	1467.4	0.5735
18	4.12	1648.0	0.0577
19	5.31	2123.5	0.2594

No.	Atom	Exp. Shift (ppm)	Multiplet
1	28	0.86	M01
2	34	1.03	M02
3	27	1.22	M03
4	20	1.86	M04
5	22	1.86	M04
6	24	1.86	M04
7	32	3.61	M05
8	37	3.67	M06
9	33	4.12	M07
10	15	5.31	M08

58:40:2 MMA:PEGM:AMM co-polymer functionalised (7)

Multiplets Integrals Sum	0.36	*Number of Nuclei*	9 H's / 43 H's (spectrum / structure)

Formula	$C_{37}H_{43}NO_{11}$	*FW*	677.7374	*[M-H]-*	676.276335	*[M-H]+*	676.275238
[M+H]-	678.291985	*[M+H]+*	678.290888	*M-*	677.284160		
M+	677.283063	*Monoisotopic Mass*	677.283611	*Nominal Mass*	677	*$d_N(^1H)$*	0.337
$sd_N(^1H)$	0.412	*$max\_d_N(^1H)$*	0.627				

Acquisition Time (sec)	2.7329	*Comment*	GW/6749/3/5	*Date*	31 Oct 2012 18:50:40		
Date Stamp	31 Oct 2012 18:50:40						
File Name	\\soton.ac.uk\ude\PersonalFiles\Users\gw5g08\mydocuments\Postgraduate\NMR\oc3112hg01\10\PDATA\1\1r					*Frequency (MHz)*	300.1300
Nucleus	1H	*Number of Transients*	16	*Origin*	av300	*Original Points Count*	16384
Owner	nmr	*Points Count*	16384	*Pulse Sequence*	zg30	*Receiver Gain*	912.30
SW(cyclical) (Hz)	5995.20	*Solvent*	CHLOROFORM-d			*Spectrum Offset (Hz)*	1497.4951
Spectrum Type	STANDARD	*Sweep Width (Hz)*	5994.84	*Temperature (degree C)*	25.160		

^{1}H NMR (300 MHz, CHLOROFORM-*d*) δ ppm 0.86 (s, 1 H) 1.03 (s, 1 H) 1.82 (s, 1 H) 1.92 (s, 1 H) 2.85 (s, 1 H) 3.60 (s, 1 H) 3.65 (s, 1 H) 4.15 (s, 1 H) 5.32 (s, 1 H)

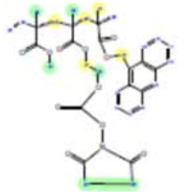

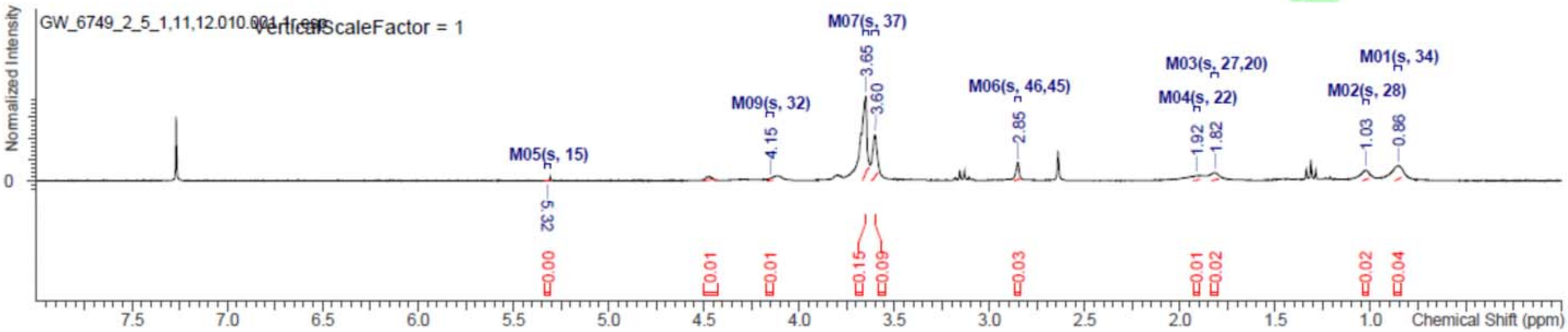

No.	(ppm)	Value	Absolute Value	Non-Negative Value
1	[0.84 .. 0.87]	0.037	4.106e+7	0.037
2	[1.01 .. 1.04]	0.025	2.728e+7	0.025
3	[1.80 .. 1.83]	0.019	2.128e+7	0.019
4	[1.90 .. 1.93]	0.013	1.382e+7	0.013
5	[2.83 .. 2.87]	0.026	2.913e+7	0.026
6	[3.59 .. 3.62]	0.090	9.901e+7	0.090
7	[3.63 .. 3.67]	0.147	1.624e+8	0.147
8	[4.14 .. 4.17]	0.006	6.352e+6	0.006
9	[4.43 .. 4.50]	0.013	1.400e+7	0.013
10	[5.30 .. 5.34]	0.002	1.689e+6	0.002

No.	Shift1 (ppm)	H's	Type	Atom1	Multiplet1	(ppm)
1	0.86	1	s	34	M01	[0.84 .. 0.87]
2	1.03	1	s	28	M02	[1.01 .. 1.04]
3	1.82	1	s	20, 27	M03	[1.80 .. 1.83]
4	1.92	1	s	22	M04	[1.90 .. 1.93]
5	2.85	1	s	46, 45	M06	[2.83 .. 2.87]
6	3.60	1	s	31	M08	[3.59 .. 3.62]
7	3.65	1	s	37	M07	[3.63 .. 3.67]
8	4.15	1	s	32	M09	[4.14 .. 4.17]
9	5.32	1	s	15	M05	[5.30 .. 5.34]

No.	Atom	Exp. Shift (ppm)	Multiplet
1	34	0.86	M01
2	28	1.03	M02
3	20	1.82	M03
4	27	1.82	M03
5	22	1.92	M04
6	46	2.85	M06
7	45	2.85	M06
8	31	3.60	M08
9	37	3.65	M07
10	32	4.15	M09
11	15	5.32	M05

No.	(ppm)	(Hz)	Height
1	0.86	257.2	0.1787
2	1.03	308.4	0.1239
3	1.82	545.6	0.0946
4	1.92	574.8	0.0575
5	2.85	855.9	0.2182
6	3.60	1081.3	0.5449
7	3.65	1095.5	1.0000
8	4.15	1246.7	0.0258
9	5.32	1596.5	-0.0011

59:40:1 MMA:PEGM:AMM co-polymer unfunctionalised (8)

Multiplets Integrals Sum	0.51	*Number of Nuclei*	12 H's / 40 H's (spectrum / structure)

Formula	$C_{32}H_{40}O_7$	*FW*	536.6558	*[M-H]-*	535.270127	*[M-H]+*	535.269030		
[M+H]-	537.285777			*[M+H]+*	537.284680	*M-*	536.277952		
M+	536.276855			*Monoisotopic Mass*	536.277404	*Nominal Mass*	536	*$d_N(^1H)$*	0.205
$sd_N(^1H)$	0.257	*$max\_d_N(^1H)$*	0.520						

Acquisition Time (sec)	2.7329	*Comment*	gw/6749/1/1c	*Date*	26 Oct 2012 17:38:24		
Date Stamp	26 Oct 2012 17:38:24						
File Name	\\soton.ac.uk\ude\personalfiles\users\gw5g08\mydocuments\Postgraduate\NMR\GW_6749_1_1\1c\GW_6749_1_1_29.10.12\10\PDATA\1\1r						
Frequency (MHz)	300.1300	*Nucleus*	1H	*Number of Transients*	16	*Origin*	av300
Original Points Count	16384	*Owner*	nmr	*Points Count*	16384	*Pulse Sequence*	zg30
Receiver Gain	645.10	*SW(cyclical) (Hz)*	5995.20	*Solvent*	CHLOROFORM-d	*Spectrum Offset (Hz)*	1497.4951
Spectrum Type	STANDARD	*Sweep Width (Hz)*	5994.84	*Temperature (degree C)*	25.160		

^{1}H NMR (300 MHz, CHLOROFORM-*d*) δ ppm 0.86 (s, 1 H) 0.85 - 0.88 (m, 1 H) 1.01 - 1.05 (m, 1 H) 1.23 (s, 1 H) 1.82 - 1.85 (m, 1 H) 1.95 (s, 1 H) 1.97 (s, 1 H) 3.58 - 3.62 (m, 1 H) 3.65 - 3.68 (m, 1 H) 4.10 - 4.13 (m, 1 H) 4.29 (s, 1 H) 5.58 (s, 1 H)

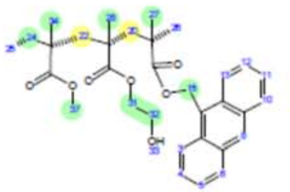

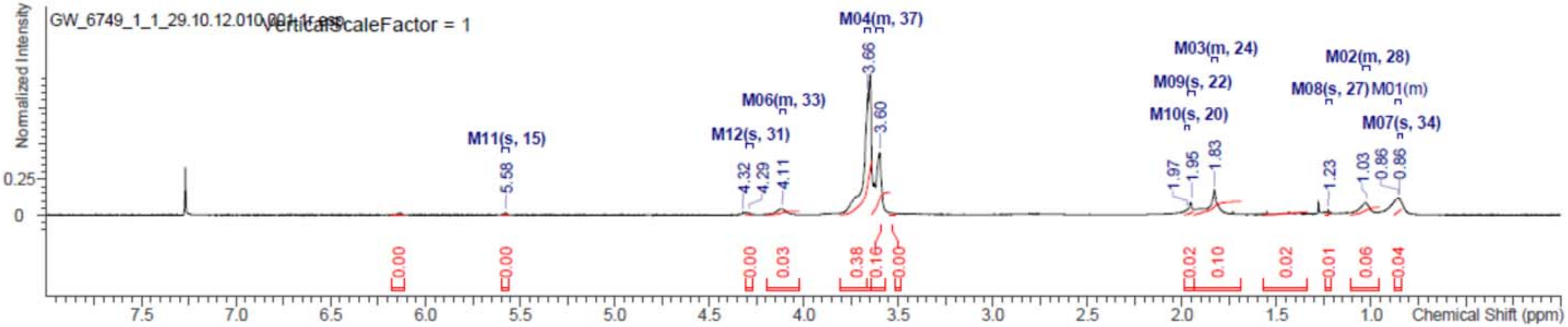

No.	(ppm)	Value	Absolute Value	Non-Negative Value
1	[0.84 .. 0.88]	0.040	4.998e+7	0.040
2	[0.96 .. 1.11]	0.058	7.267e+7	0.058
3	[1.21 .. 1.24]	0.006	8.077e+6	0.006
4	[1.34 .. 1.57]	0.021	2.680e+7	0.021
5	[1.69 .. 1.94]	0.096	1.213e+8	0.096
6	[1.94 .. 1.99]	0.023	2.944e+7	0.023
7	[3.51 .. 3.54]	0.004	5.081e+6	0.004
8	[3.54 .. 3.64]	0.161	2.032e+8	0.161
9	[3.64 .. 3.81]	0.380	4.803e+8	0.380
10	[4.03 .. 4.20]	0.027	3.454e+7	0.027
11	[4.27 .. 4.30]	0.003	3.573e+6	0.003
12	[5.56 .. 5.59]	0.003	3.354e+6	0.003
13	[6.11 .. 6.18]	0.003	3.967e+6	0.003

No.	Shift1 (ppm)	H's	Type	Atom1	Multiplet1	(ppm)
1	0.86	1	s	34	M07	[0.84 .. 0.86]
2	0.86	1	m		M01	[0.85 .. 0.88]
3	1.03	1	m	28	M02	[1.01 .. 1.05]
4	1.23	1	s	27	M08	[1.21 .. 1.24]
5	1.83	1	m	24	M03	[1.82 .. 1.85]
6	1.95	1	s	22	M09	[1.94 .. 1.97]
7	1.97	1	s	20	M10	[1.96 .. 1.99]
8	3.60	1	m	37	M04	[3.58 .. 3.62]
9	3.66	1	m	32	M05	[3.65 .. 3.68]
10	4.11	1	m	33	M06	[4.10 .. 4.13]
11	4.29	1	s	31	M12	[4.27 .. 4.30]
12	5.58	1	s	15	M11	[5.56 .. 5.59]

No.	Atom	Exp. Shift (ppm)	Multiplet
1	34	0.86	M07
2	28	1.03	M02
3	27	1.23	M08
4	24	1.83	M03
5	22	1.95	M09
6	20	1.97	M10
7	37	3.60	M04
8	32	3.66	M05
9	33	4.11	M06
10	31	4.29	M12
11	15	5.58	M11

No.	(ppm)	(Hz)	Height
1	0.86	257.2	0.1175
2	0.86	258.7	0.1172
3	1.03	308.8	0.0852
4	1.23	368.1	0.0368
5	1.83	549.9	0.1749
6	1.95	586.5	0.0939
7	1.97	591.7	0.0402
8	3.60	1080.9	0.4364
9	3.66	1099.6	0.8516
10	4.11	1234.9	0.0428
11	4.29	1286.9	0.0159
12	4.32	1296.8	0.0172
13	5.58	1674.1	0.0161

59:40:1 MMA:PEGM:AMM co-polymer functionalised (9)

Multiplets Integrals Sum	0.35	*Number of Nuclei*	9 H's / 43 H's (spectrum / structure)

Formula	$C_{37}H_{43}NO_{11}$	*FW*	677.7374	*[M-H]-*	676.276335	*[M-H]+*	676.275238
[M+H]-	678.291985	*[M+H]+*	678.290888	*M-*	677.284160		
M+	677.283063	*Monoisotopic Mass*	677.283611	*Nominal Mass*	677	*$d_N(^1H)$*	0.420
$sd_N(^1H)$	0.542	*$max\_d_N(^1H)$*	1.053				

Acquisition Time (sec)	2.7329	*Comment*	GW/6749/25/3	*Date*	24 Oct 2012 19:16:32		
Date Stamp	24 Oct 2012 19:16:32						
File Name	\\soton.ac.uk\ude\PersonalFiles\Users\gw5g08\mydocuments\Postgraduate\NMR\GW_6749_2_3\GW_6749_2_3_24.10.12\10\PDATA\1\1r						
Frequency (MHz)	300.1300	*Nucleus*	1H	*Number of Transients*	16	*Origin*	av300
Original Points Count	16384	*Owner*	nmr	*Points Count*	16384	*Pulse Sequence*	zg30
Receiver Gain	1625.50	*SW(cyclical) (Hz)*	5995.20	*Solvent*	CHLOROFORM-d	*Spectrum Offset (Hz)*	1497.4951
Spectrum Type	STANDARD	*Sweep Width (Hz)*	5994.84	*Temperature (degree C)*	25.160		

^{1}H NMR (300 MHz, CHLOROFORM-*d*) δ ppm 1.24 (s, 1 H) 1.48 (t, *J*=7.14 Hz, 1 H) 1.69 (s, 1 H) 1.70 (s, 1 H) 2.62 (s, 1 H) 3.61 (d, *J*=7.32 Hz, 1 H) 3.55 - 5.16 (m, 1 H) 3.61 (s, 1 H) 5.65 (s, 1 H)

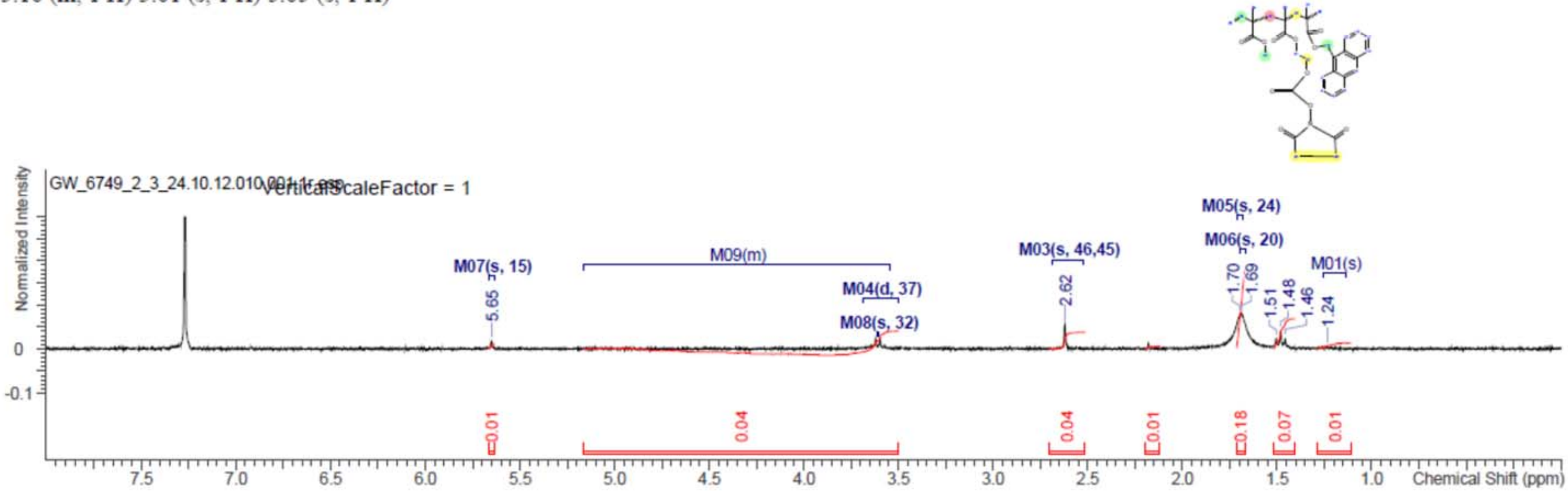

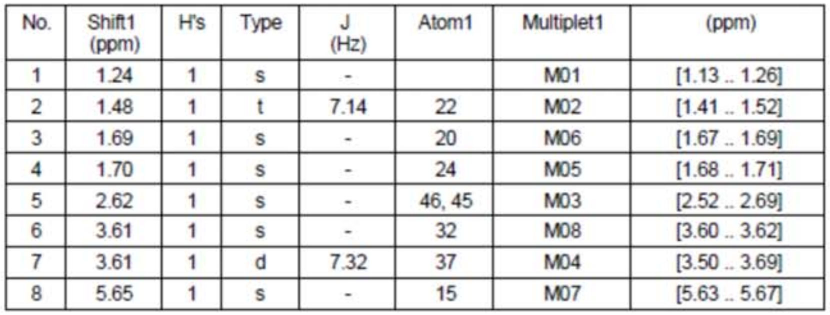

No.	Shift1 (ppm)	H's	Type	J (Hz)	Atom1	Multiplet1	(ppm)
1	1.24	1	s	-		M01	[1.13 .. 1.26]
2	1.48	1	t	7.14	22	M02	[1.41 .. 1.52]
3	1.69	1	s	-	20	M06	[1.67 .. 1.69]
4	1.70	1	s	-	24	M05	[1.68 .. 1.71]
5	2.62	1	s	-	46, 45	M03	[2.52 .. 2.69]
6	3.61	1	s	-	32	M08	[3.60 .. 3.62]
7	3.61	1	d	7.32	37	M04	[3.50 .. 3.69]
8	5.65	1	s	-	15	M07	[5.63 .. 5.67]

No.	(ppm)	Value	Absolute Value	Non-Negative Value
1	[1.11 .. 1.28]	0.013	2.465e+6	0.013
2	[1.41 .. 1.52]	0.069	1.305e+7	0.069
3	[1.67 .. 1.71]	0.179	3.363e+7	0.179
4	[2.12 .. 2.20]	0.006	1.111e+6	0.006
5	[2.52 .. 2.70]	0.038	7.112e+6	0.038
6	[3.50 .. 3.69]	0.049	9.258e+6	0.049
7	[5.63 .. 5.67]	0.011	2.032e+6	0.011

No.	Atom	Exp. Shift (ppm)	Multiplet
1	22	1.48	M02
2	20	1.69	M06
3	24	1.70	M05
4	46	2.62	M03
5	45	2.62	M03
6	32	3.61	M08
7	37	3.61	M04
8	15	5.65	M07

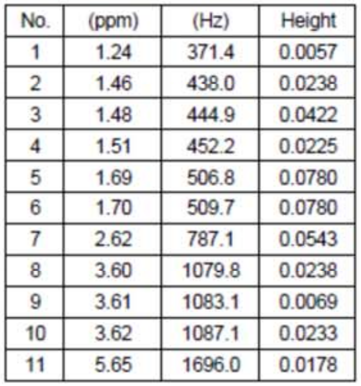

No.	(ppm)	(Hz)	Height
1	1.24	371.4	0.0057
2	1.46	438.0	0.0238
3	1.48	444.9	0.0422
4	1.51	452.2	0.0225
5	1.69	506.8	0.0780
6	1.70	509.7	0.0780
7	2.62	787.1	0.0543
8	3.60	1079.8	0.0238
9	3.61	1083.1	0.0069
10	3.62	1087.1	0.0233
11	5.65	1696.0	0.0178

57:40:3 MMA:PEGM:AMM co-polymer unfunctionalised (10)

OriginalDateForRelativeTime	2012-12-08T01:18:05	Multiplets Integrals Sum	32.92	Number of Nuclei	32 H's / 40 H's (spectrum / structure)

Formula	$C_{32}H_{40}O_7$	FW	536.6558	[M-H]-	535.270127	[M-H]+	535.269030		
[M+H]-	537.285777			[M+H]+	537.284680	M-	536.277952		
M+	536.276855			Monoisotopic Mass	536.277404	Nominal Mass	536	$d_N(^1H)$	0.355
$sd_N(^1H)$	0.606	$max\_d_N(^1H)$	1.739						

Acquisition Time (sec)	2.7329	Comment	GW/6749/1C	D	0.06	DE	6	DS	2
Date	08 Dec 2012 01:18:05			Date Stamp	08 Dec 2012 01:18:05				
File Name	\\soton.ac.uk\ude\personalfiles\users\gw5g08\mydocuments\Postgraduate\Experimental & Analysis\NMR\GW_6749_1\1e\dc0712hg02\10\fid							Frequency (MHz)	300.1300
GB	0	INSTRUM	<spect>	LB	0.3	NS	16	Nucleus	1H
Number of Transients	16	Origin	spect	Original Points Count	16384	Owner	nmr	PC	1
PROBHD	<5 mm QNP 1H/13C/31P/19F Z3246/0118 >			PULPROG	<zg30>	Points Count	16384	Pulse Sequence	zg30
Receiver Gain	287.40	SF	300.13	SFO1	300.1315006499			SI	16384
SSB	0	SW(cyclical) (Hz)	5995.20	SWH	5995.20383693046			Solvent	CHLOROFORM-d
Spectrum Offset (Hz)	1500.6508	Spectrum Type	standard	Sweep Width (Hz)	5994.84	TD	32768	TD0	1
TE	298.16	Temperature (degree C)	25.160	WDW	1				

^{1}H NMR (300 MHz, CHLOROFORM-*d*) δ ppm 0.86 (br s, 3 H) 0.95 - 1.11 (m, 3 H) 1.33 (s, 1 H) 1.82 (br s, 1 H) 1.86 - 2.04 (m, 2 H) 3.52 - 3.78 (m, 21 H) 4.11 (s, 1 H)

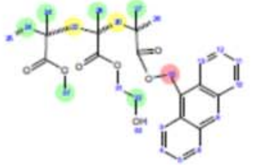

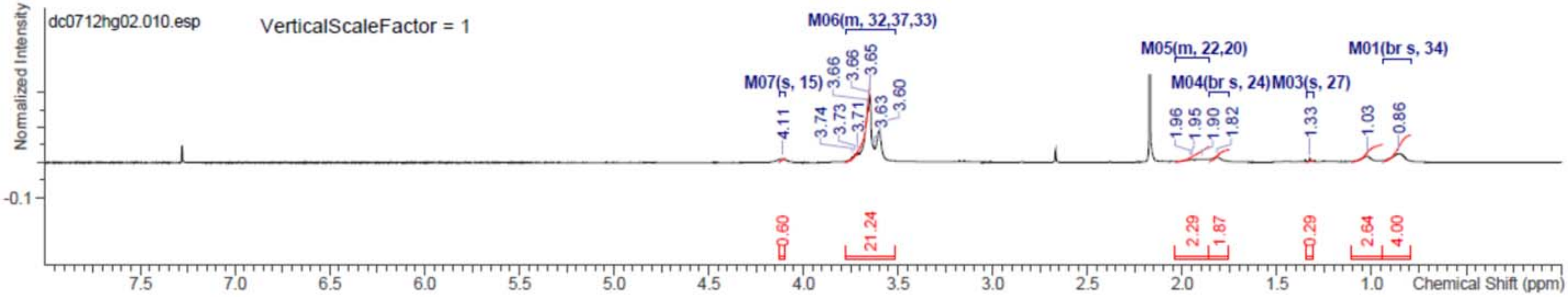

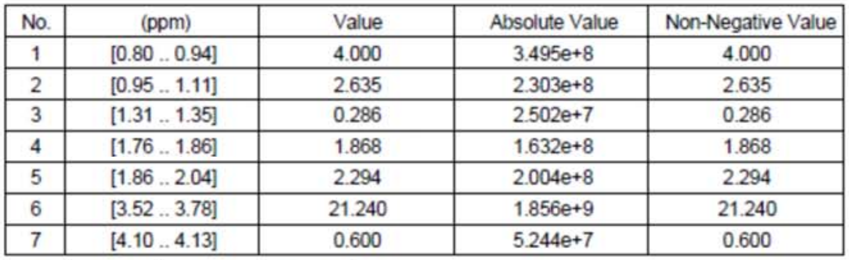

No.	(ppm)	Value	Absolute Value	Non-Negative Value
1	[0.80 .. 0.94]	4.000	3.495e+8	4.000
2	[0.95 .. 1.11]	2.635	2.303e+8	2.635
3	[1.31 .. 1.35]	0.286	2.502e+7	0.286
4	[1.76 .. 1.86]	1.868	1.632e+8	1.868
5	[1.86 .. 2.04]	2.294	2.004e+8	2.294
6	[3.52 .. 3.78]	21.240	1.856e+9	21.240
7	[4.10 .. 4.13]	0.600	5.244e+7	0.600

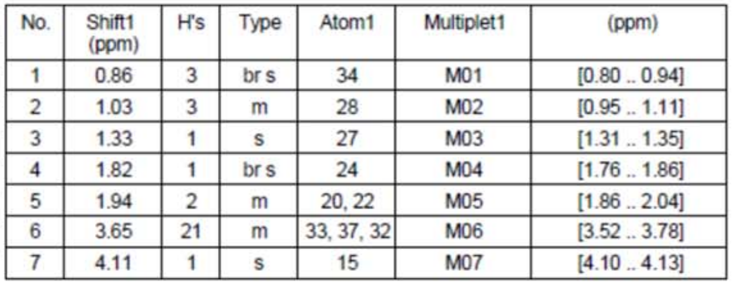

No.	Shift1 (ppm)	H's	Type	Atom1	Multiplet1	(ppm)
1	0.86	3	br s	34	M01	[0.80 .. 0.94]
2	1.03	3	m	28	M02	[0.95 .. 1.11]
3	1.33	1	s	27	M03	[1.31 .. 1.35]
4	1.82	1	br s	24	M04	[1.76 .. 1.86]
5	1.94	2	m	20, 22	M05	[1.86 .. 2.04]
6	3.65	21	m	33, 37, 32	M06	[3.52 .. 3.78]
7	4.11	1	s	15	M07	[4.10 .. 4.13]

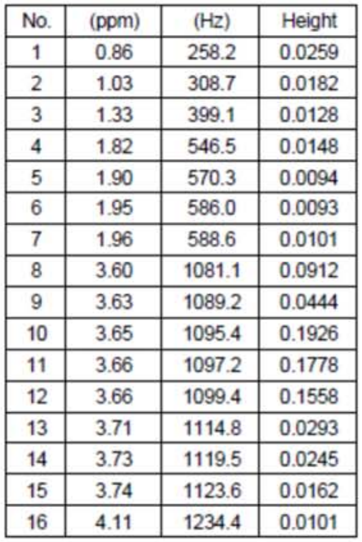

No.	(ppm)	(Hz)	Height
1	0.86	258.2	0.0259
2	1.03	308.7	0.0182
3	1.33	399.1	0.0128
4	1.82	546.5	0.0148
5	1.90	570.3	0.0094
6	1.95	586.0	0.0093
7	1.96	588.6	0.0101
8	3.60	1081.1	0.0912
9	3.63	1089.2	0.0444
10	3.65	1095.4	0.1926
11	3.66	1097.2	0.1778
12	3.66	1099.4	0.1558
13	3.71	1114.8	0.0293
14	3.73	1119.5	0.0245
15	3.74	1123.6	0.0162
16	4.11	1234.4	0.0101

No.	Atom	Exp. Shift (ppm)	Multiplet
1	34	0.86	M01
2	28	1.03	M02
3	27	1.33	M03
4	24	1.82	M04
5	20	1.94	M05
6	22	1.94	M05
7	33	3.65	M06
8	37	3.65	M06
9	32	3.65	M06
10	15	4.11	M07

57:40:3 MMA:PEGM:AMM co-polymer functionalised (11)

OriginalDateForRelativeTime	2012-11-03T00:31:51	*Multiplets Integrals Sum*	41.62	*Number of Nuclei*	42 H's / 43 H's (spectrum / structure)

Formula	$C_{37}H_{43}NO_{11}$	*FW*	677.7374	*[M-H]-*	676.276335	*[M-H]+*	676.275238
[M+H]-	678.291985	*[M+H]+*	678.290888	*M-*	677.284160		
M+	677.283063	*Monoisotopic Mass*	677.283611	*Nominal Mass*	677	*$d_N(^1H)$*	0.526
$sd_N(^1H)$	0.741	*$max\_d_N(^1H)$*	1.913				

Acquisition Time (sec)	2.7329	*Comment*	GW/6749/26	*D*	0.06	*DE*	6	*DS*	2
Date	03 Nov 2012 00:31:51			*Date Stamp*	03 Nov 2012 00:31:51				
File Name	\\soton.ac.uk\ude\personalfiles\users\gw5g08\mydocuments\Postgraduate\Experimental & Analysis\NMR\GW_6749_2\2b\GW_6749_2_5_2.11.12\10\fid								
Frequency (MHz)	300.1301	*GB*	0	*INSTRUM*	<av300>	*LB*	0.3	*NS*	16
Nucleus	1H	*Number of Transients*	16	*Origin*	av300	*Original Points Count*	16384	*Owner*	nmr
PC	1	*PROBHD*	<5 mm QNP 1H/13C/31P/19F Z3246/0118 >			*PULPROG*	<zg30>	*Points Count*	16384
Pulse Sequence	zg30	*Receiver Gain*	287.40	*SF*	300.130052738867			*SFO1*	300.1315006499
SI	16384	*SSB*	0	*SW(cyclical) (Hz)*	5995.20	*SWH*	5995.20383693046		
Solvent	CHLOROFORM-d			*Spectrum Offset (Hz)*	1447.9128	*Spectrum Type*	standard	*Sweep Width (Hz)*	5994.84
TD	32768	*TD0*	1	*TE*	298.16	*Temperature (degree C)*	25.160	*WDW*	1

^{1}H NMR (300 MHz, CHLOROFORM-*d*) δ ppm 0.68 (br s, 6 H) 0.85 (br s, 2 H) 1.07 (s, 1 H) 1.65 (br s, 3 H) 1.69 - 1.81 (m, 3 H) 2.68 (s, 1 H) 3.37 - 3.58 (m, 25 H) 3.94 (br s, 1 H)

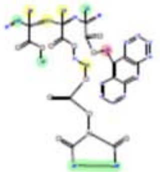

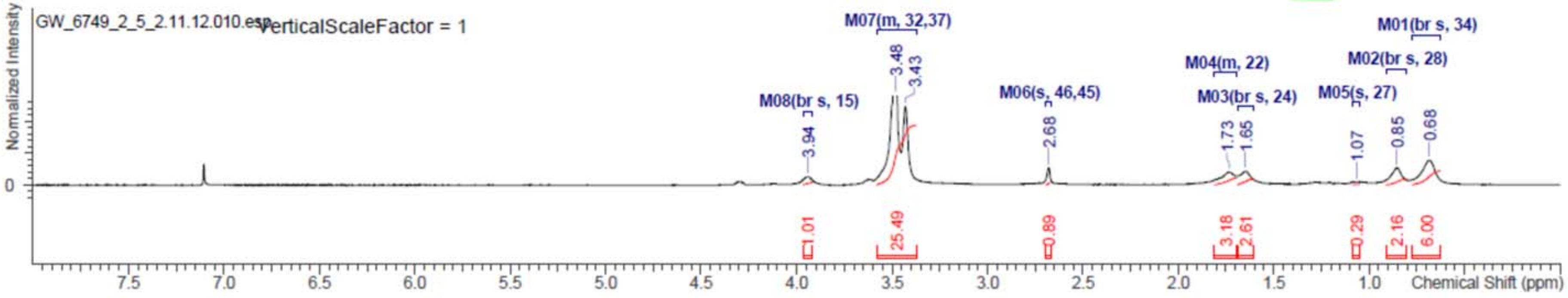

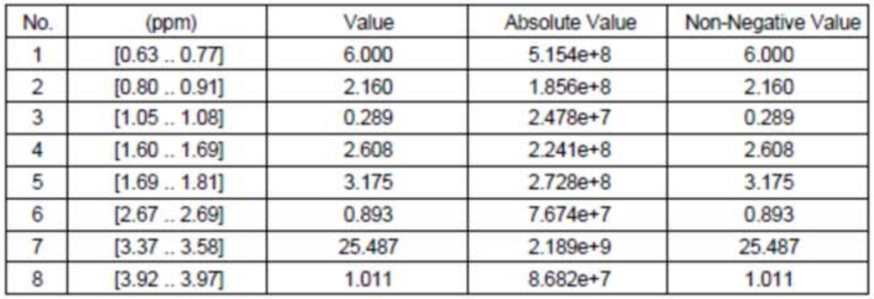

No.	(ppm)	Value	Absolute Value	Non-Negative Value
1	[0.63 .. 0.77]	6.000	5.154e+8	6.000
2	[0.80 .. 0.91]	2.160	1.856e+8	2.160
3	[1.05 .. 1.08]	0.289	2.478e+7	0.289
4	[1.60 .. 1.69]	2.608	2.241e+8	2.608
5	[1.69 .. 1.81]	3.175	2.728e+8	3.175
6	[2.67 .. 2.69]	0.893	7.674e+7	0.893
7	[3.37 .. 3.58]	25.487	2.189e+9	25.487
8	[3.92 .. 3.97]	1.011	8.682e+7	1.011

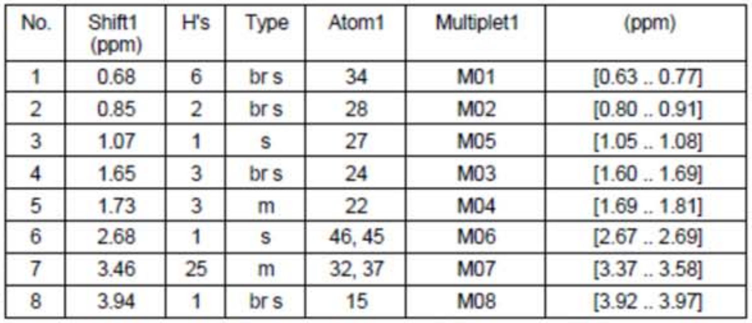

No.	Shift1 (ppm)	H's	Type	Atom1	Multiplet1	(ppm)
1	0.68	6	br s	34	M01	[0.63 .. 0.77]
2	0.85	2	br s	28	M02	[0.80 .. 0.91]
3	1.07	1	s	27	M05	[1.05 .. 1.08]
4	1.65	3	br s	24	M03	[1.60 .. 1.69]
5	1.73	3	m	22	M04	[1.69 .. 1.81]
6	2.68	1	s	46, 45	M06	[2.67 .. 2.69]
7	3.46	25	m	32, 37	M07	[3.37 .. 3.58]
8	3.94	1	br s	15	M08	[3.92 .. 3.97]

No.	Atom	Exp. Shift (ppm)	Multiplet
1	34	0.68	M01
2	28	0.85	M02
3	27	1.07	M05
4	24	1.65	M03
5	22	1.73	M04
6	46	2.68	M06
7	45	2.68	M06
8	32	3.46	M07
9	37	3.46	M07
10	15	3.94	M08

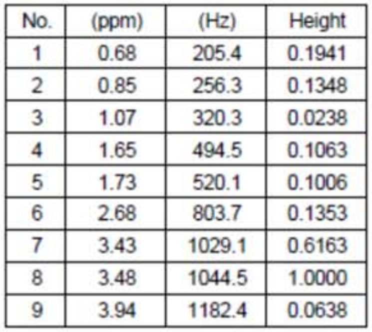

No.	(ppm)	(Hz)	Height
1	0.68	205.4	0.1941
2	0.85	256.3	0.1348
3	1.07	320.3	0.0238
4	1.65	494.5	0.1063
5	1.73	520.1	0.1006
6	2.68	803.7	0.1353
7	3.43	1029.1	0.6163
8	3.48	1044.5	1.0000
9	3.94	1182.4	0.0638

^{13}C NMR spectra

60:40 MMA:PEGM co-polymer unfuctionalised (1)

27/04/2016 10:35:32

Number of Nuclei 2 C's / 13 C's (spectrum / structure)

Formula	$C_{13}H_{24}O_5$	*FW*	260.3267	*[M-H]-*	259.155097	*[M-H]+*	259.154000		
[M+H]-	261.170747			*[M+H]+*	261.169650	*M-*	260.162922		
M+	260.161825			*Monoisotopic Mass*	260.162374	*Nominal Mass*	260	*d_N(^{13}C)*	6.021
sd_N(^{13}C)	9.647	*max_d_N(^{13}C)*	22.279						

Acquisition Time (sec)	0.9044	*Comment*	GW/6749/1d	*Date*	08 Nov 2012 21:43:28		
Date Stamp	08 Nov 2012 21:43:28						
File Name	\\soton.ac.uk\ude\PersonalFiles\Users\gw5g08\mydocuments\Postgraduate\NMR\nv0812hg02\11\PDATA\1\1					*Frequency (MHz)*	75.4678
Nucleus	13C	*Number of Transients*	512	*Origin*	av300	*Original Points Count*	16384
Owner	nmr	*Points Count*	16384	*Pulse Sequence*	zgpg30	*Receiver Gain*	29193.00
SW(cyclical) (Hz)	18115.94	*Solvent*	CHLOROFORM-d			*Spectrum Offset (Hz)*	8301.4531
Spectrum Type	STANDARD	*Sweep Width (Hz)*	18114.84	*Temperature (degree C)*	25.160		

^{13}C NMR (75 MHz, CHLOROFORM-*d*) δ ppm 54.10 (br s, 1 C) 177.20 (s, 1 C)

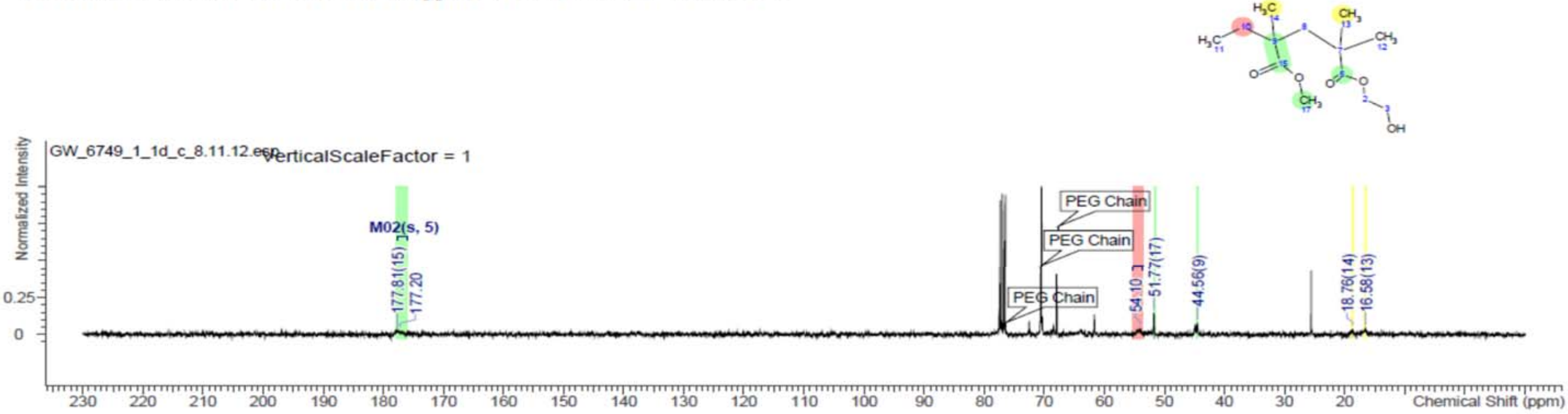

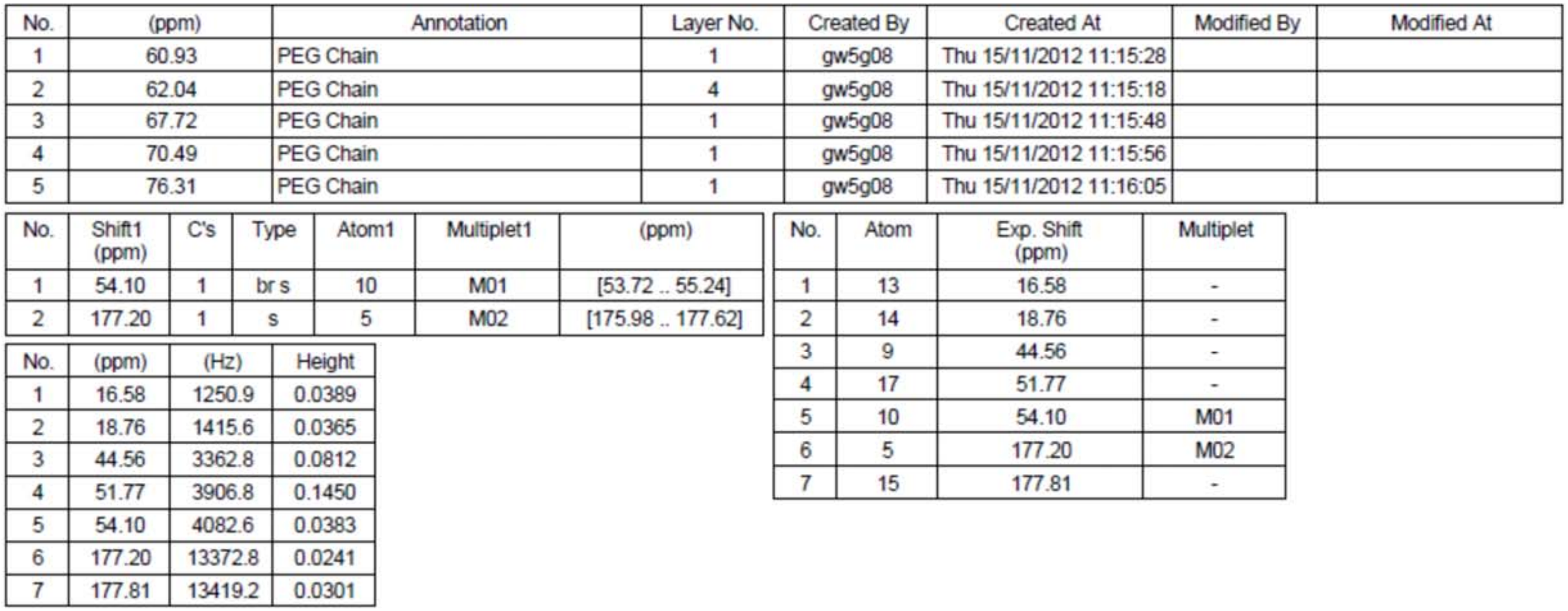

No.	(ppm)	Annotation	Layer No.	Created By	Created At	Modified By	Modified At
1	60.93	PEG Chain	1	gw5g08	Thu 15/11/2012 11:15:28		
2	62.04	PEG Chain	4	gw5g08	Thu 15/11/2012 11:15:18		
3	67.72	PEG Chain	1	gw5g08	Thu 15/11/2012 11:15:48		
4	70.49	PEG Chain	1	gw5g08	Thu 15/11/2012 11:15:56		
5	76.31	PEG Chain	1	gw5g08	Thu 15/11/2012 11:16:05		

No.	Shift1 (ppm)	C's	Type	Atom1	Multiplet1	(ppm)
1	54.10	1	br s	10	M01	[53.72 .. 55.24]
2	177.20	1	s	5	M02	[175.98 .. 177.62]

No.	Atom	Exp. Shift (ppm)	Multiplet
1	13	16.58	-
2	14	18.76	-
3	9	44.56	-
4	17	51.77	-
5	10	54.10	M01
6	5	177.20	M02
7	15	177.81	-

No.	(ppm)	(Hz)	Height
1	16.58	1250.9	0.0389
2	18.76	1415.6	0.0365
3	44.56	3362.8	0.0812
4	51.77	3906.8	0.1450
5	54.10	4082.6	0.0383
6	177.20	13372.8	0.0241
7	177.81	13419.2	0.0301

60:40 MMA:PEGM co-polymer fuctionalised (2)

27/04/2016 10:38:16

Multiplets Integrals Sum 0.00	*Number of Nuclei* 7 C's / 18 C's (spectrum / structure)

Formula	$C_{18}H_{27}NO_9$	*FW*	401.4083	*[M-H]-*	400.161305	*[M-H]+*	400.160208		
[M+H]-	402.176955			*[M+H]+*	402.175858	*M-*	401.169130		
M+	401.168033			*Monoisotopic Mass*	401.168581	*Nominal Mass*	401	*d_N(^{13}C)*	5.172
sd_N(^{13}C)	8.785	*max_d_N(^{13}C)*	22.501						

Acquisition Time (sec)	0.9044	*Comment*	GW/6749/26	*Date*	03 Nov 2012 00:49:04		
Date Stamp	03 Nov 2012 00:49:04						
File Name	\\soton.ac.uk\ude\PersonalFiles\Users\gw5g08\mydocuments\Postgraduate\NMR\nv1012hg01\11\PDATA\1\1r					*Frequency (MHz)*	75.4678
Nucleus	13C	*Number of Transients*	512	*Origin*	av300	*Original Points Count*	16384
Owner	nmr	*Points Count*	16384	*Pulse Sequence*	zgpg30	*Receiver Gain*	29193.00
SW(cyclical) (Hz)	18115.94	*Solvent*	CHLOROFORM-d			*Spectrum Offset (Hz)*	8299.4150
Spectrum Type	STANDARD	*Sweep Width (Hz)*	18114.84	*Temperature (degree C)*	25.160		

^{13}C NMR (75 MHz, CHLOROFORM-*d*) δ ppm 16.39 (br s, 1 C) 18.72 (br s, 1 C) 25.44 (s, 1 C) 44.58 (br s, 1 C) 51.77 (br s, 1 C) 54.32 (br s, 1 C) 177.76 (br s, 1 C)

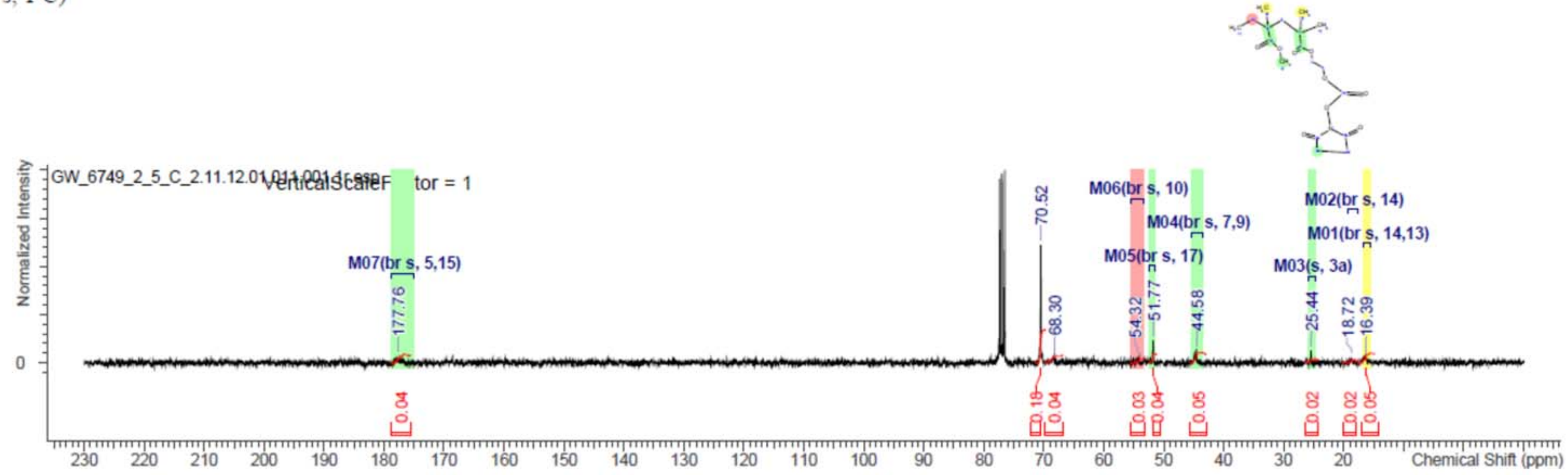

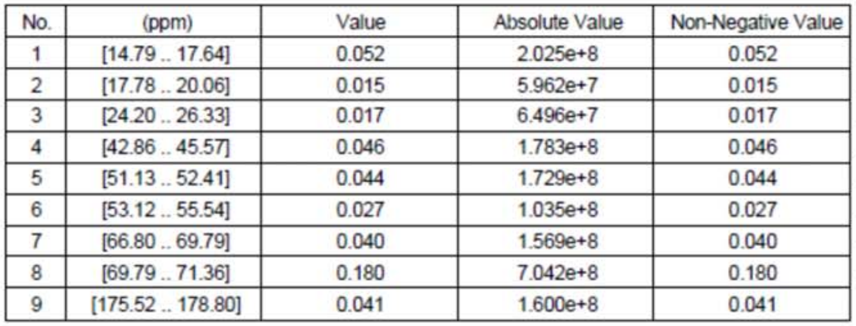

No.	(ppm)	Value	Absolute Value	Non-Negative Value
1	[14.79 .. 17.64]	0.052	2.025e+8	0.052
2	[17.78 .. 20.06]	0.015	5.962e+7	0.015
3	[24.20 .. 26.33]	0.017	6.496e+7	0.017
4	[42.86 .. 45.57]	0.046	1.783e+8	0.046
5	[51.13 .. 52.41]	0.044	1.729e+8	0.044
6	[53.12 .. 55.54]	0.027	1.035e+8	0.027
7	[66.80 .. 69.79]	0.040	1.569e+8	0.040
8	[69.79 .. 71.36]	0.180	7.042e+8	0.180
9	[175.52 .. 178.80]	0.041	1.600e+8	0.041

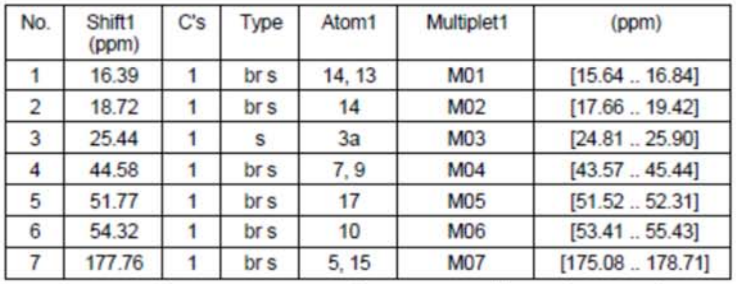

No.	Shift1 (ppm)	C's	Type	Atom1	Multiplet1	(ppm)
1	16.39	1	br s	14, 13	M01	[15.64 .. 16.84]
2	18.72	1	br s	14	M02	[17.66 .. 19.42]
3	25.44	1	s	3a	M03	[24.81 .. 25.90]
4	44.58	1	br s	7, 9	M04	[43.57 .. 45.44]
5	51.77	1	br s	17	M05	[51.52 .. 52.31]
6	54.32	1	br s	10	M06	[53.41 .. 55.43]
7	177.76	1	br s	5, 15	M07	[175.08 .. 178.71]

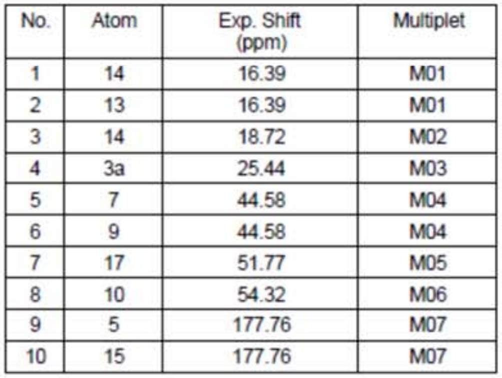

No.	Atom	Exp. Shift (ppm)	Multiplet
1	14	16.39	M01
2	13	16.39	M01
3	14	18.72	M02
4	3a	25.44	M03
5	7	44.58	M04
6	9	44.58	M04
7	17	51.77	M05
8	10	54.32	M06
9	5	177.76	M07
10	15	177.76	M07

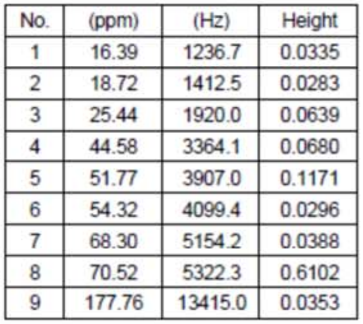

No.	(ppm)	(Hz)	Height
1	16.39	1236.7	0.0335
2	18.72	1412.5	0.0283
3	25.44	1920.0	0.0639
4	44.58	3364.1	0.0680
5	51.77	3907.0	0.1171
6	54.32	4099.4	0.0296
7	68.30	5154.2	0.0388
8	70.52	5322.3	0.6102
9	177.76	13415.0	0.0353

58:40:2 MMA:PEGM:FMA co-polymer unfunctionalised (3)

OriginalDateForRelativeTime	2014-06-02T19:28:38	*Multiplets Integrals Sum*	0.00	*Number of Nuclei*	11 C's / 21 C's (spectrum / structure)

Formula	$C_{21}H_{32}O_8$	*FW*	412.4740	*[M-H]-*	411.202442	*[M-H]+*	411.201344		
[M+H]-	413.218092			*[M+H]+*	413.216994	*M-*	412.210267		
M+	412.209169			*Monoisotopic Mass*	412.209718	*Nominal Mass*	412	*$d_N(^{13}C)$*	10.782
$sd_N(^{13}C)$	23.627	*$max\_d_N(^{13}C)$*	87.455						

Acquisition Time (sec)	1.3631	*Comment*	GW/6749/20/47			*D*	0.03	*DE*	6.5
DS	4	*Date*	02 Jun 2014 19:28:38			*Date Stamp*	02 Jun 2014 19:28:38		
File Name	\\soton.ac.uk\ude\personalfiles\users\gw5g08\mydocuments\Postgraduate\Experimental & Analysis\NMR\GW_6749_20\ju0214ybj2\ju0214ybj2\11\fi							*Frequency (MHz)*	100.6128
GB	0	*INSTRUM*	<AVII400>	*LB*	1	*NS*	512	*Nucleus*	13C
Number of Transients	512	*Origin*	AVII400	*Original Points Count*	32768	*Owner*	nmr	*PC*	1.4
PROBHD	<5 mm PABBO BB/19F-1H/D Z-GRD Z108618/0664 >			*PULPROG*	<zgpg30>	*Points Count*	32768	*Pulse Sequence*	zgpg30
Receiver Gain	309.31	*SF*	100.612769	*SFO1*	100.622829328806			*SI*	32768
SSB	0	*SW(cyclical) (Hz)*	24038.46	*SWH*	24038.4615384615				
Solvent	CHLOROFORM-d			*Spectrum Offset (Hz)*	10060.3320	*Spectrum Type*	standard	*Sweep Width (Hz)*	24037.73
TD	65536	*TD0*	1	*TE*	298.16	*Temperature (degree C)*	25.160	*UNC1*	<13C>
WDW	1								

^{13}C NMR (101 MHz, CHLOROFORM-*d*) δ ppm 16.57 (s, 1 C) 18.68 (s, 1 C) 25.60 (s, 1 C) 44.57 (s, 1 C) 44.91 (s, 1 C) 51.79 (s, 1 C) 61.71 (s, 1 C) 67.96 (s, 1 C) 70.56 (s, 1 C) 72.60 (s, 1 C) 177.78 (s, 1 C)

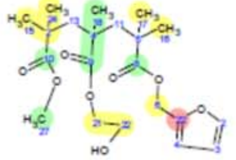

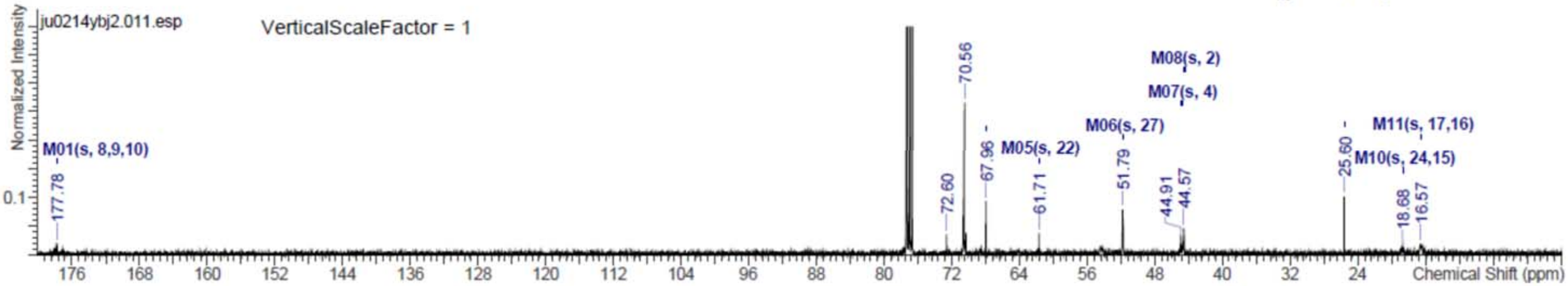

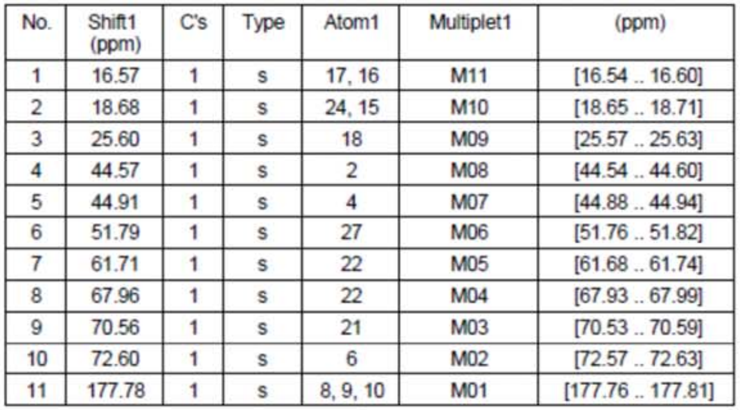

No.	Shift1 (ppm)	C's	Type	Atom1	Multiplet1	(ppm)
1	16.57	1	s	17, 16	M11	[16.54 .. 16.60]
2	18.68	1	s	24, 15	M10	[18.65 .. 18.71]
3	25.60	1	s	18	M09	[25.57 .. 25.63]
4	44.57	1	s	2	M08	[44.54 .. 44.60]
5	44.91	1	s	4	M07	[44.88 .. 44.94]
6	51.79	1	s	27	M06	[51.76 .. 51.82]
7	61.71	1	s	22	M05	[61.68 .. 61.74]
8	67.96	1	s	22	M04	[67.93 .. 67.99]
9	70.56	1	s	21	M03	[70.53 .. 70.59]
10	72.60	1	s	6	M02	[72.57 .. 72.63]
11	177.78	1	s	8, 9, 10	M01	[177.76 .. 177.81]

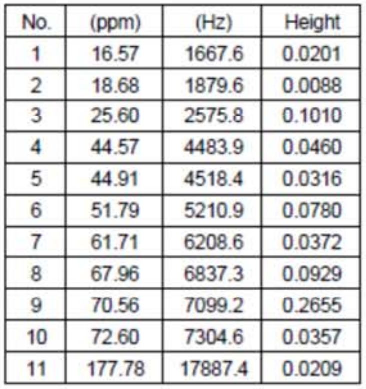

No.	(ppm)	(Hz)	Height
1	16.57	1667.6	0.0201
2	18.68	1879.6	0.0088
3	25.60	2575.8	0.1010
4	44.57	4483.9	0.0460
5	44.91	4518.4	0.0316
6	51.79	5210.9	0.0780
7	61.71	6208.6	0.0372
8	67.96	6837.3	0.0929
9	70.56	7099.2	0.2655
10	72.60	7304.6	0.0357
11	177.78	17887.4	0.0209

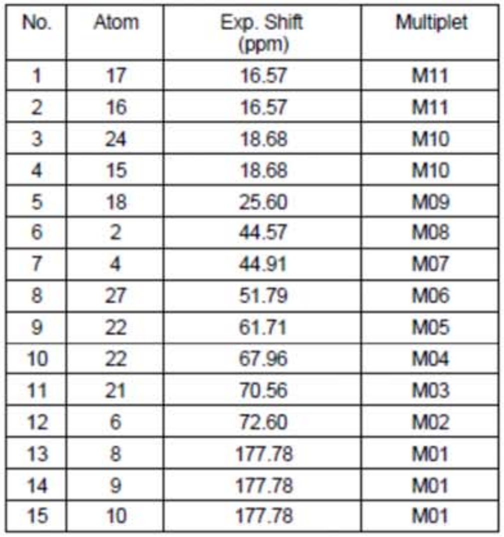

No.	Atom	Exp. Shift (ppm)	Multiplet
1	17	16.57	M11
2	16	16.57	M11
3	24	18.68	M10
4	15	18.68	M10
5	18	25.60	M09
6	2	44.57	M08
7	4	44.91	M07
8	27	51.79	M06
9	22	61.71	M05
10	22	67.96	M04
11	21	70.56	M03
12	6	72.60	M02
13	8	177.78	M01
14	9	177.78	M01
15	10	177.78	M01

Appendix B

58:40:2 MMA:PEGM:FMA co-polymer functionalised (4)

OriginalDateForRelativeTime	2014-06-02T20:06:16	*Multiplets Integrals Sum*	0.00	*Number of Nuclei*	12 C's / 26 C's (spectrum / structure)

Formula	$C_{26}H_{35}NO_{12}$	*FW*	553.5556	*[M-H]-*	552.208649	*[M-H]+*	552.207552
[M+H]-	554.224299	*[M+H]+*	554.223202	*M-*	553.216474		
M+	553.215377	*Monoisotopic Mass*	553.215926	*Nominal Mass*	553	*$d_N(^{13}C)$*	4.913
$sd_N(^{13}C)$	6.640	*$max\_d_N(^{13}C)$*	12.744				

Acquisition Time (sec)	1.3631	*Comment*	GW/6749/21/49			*D*	0.03	*DE*	6.5
DS	4	*Date*	02 Jun 2014 20:06:16			*Date Stamp*	02 Jun 2014 20:06:16		
File Name	\\soton.ac.uk\ude\personalfiles\users\gw5g08\mydocuments\Postgraduate\Experimental & Analysis\NMR\GW_6749_21\ju0214ybj3\ju0214ybj3\11\fi							*Frequency (MHz)*	100.6128
GB	0	*INSTRUM*	<AVII400>	*LB*	1	*NS*	512	*Nucleus*	13C
Number of Transients	512	*Origin*	AVII400	*Original Points Count*	32768	*Owner*	nmr	*PC*	1.4
PROBHD	<5 mm PABBO BB/19F-1H/D Z-GRD Z108618/0664 >			*PULPROG*	<zgpg30>	*Points Count*	32768	*Pulse Sequence*	zgpg30
Receiver Gain	309.31	*SF*	100.612769	*SFO1*	100.622829328806			*SI*	32768
SSB	0	*SW(cyclical) (Hz)*	24038.46	*SWH*	24038.4615384615				
Solvent	CHLOROFORM-d			*Spectrum Offset (Hz)*	10060.3320	*Spectrum Type*	standard	*Sweep Width (Hz)*	24037.73
TD	65536	*TD0*	1	*TE*	298.16	*Temperature (degree C)*	25.160	*UNC1*	<13C>
WDW	1								

^{13}C NMR (101 MHz, CHLOROFORM-*d*) δ ppm 0.00 - 0.00 (m, 1 C) 15.98 (s, 1 C) 16.48 (s, 1 C) 25.47 (s, 1 C) 44.58 (s, 1 C) 44.92 (s, 1 C) 51.78 (s, 1 C) 68.34 (s, 1 C) 70.56 (s, 1 C) 151.65 (s, 1 C) 168.61 (s, 1 C) 177.78 (s, 1 C)

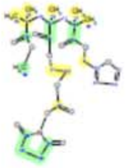

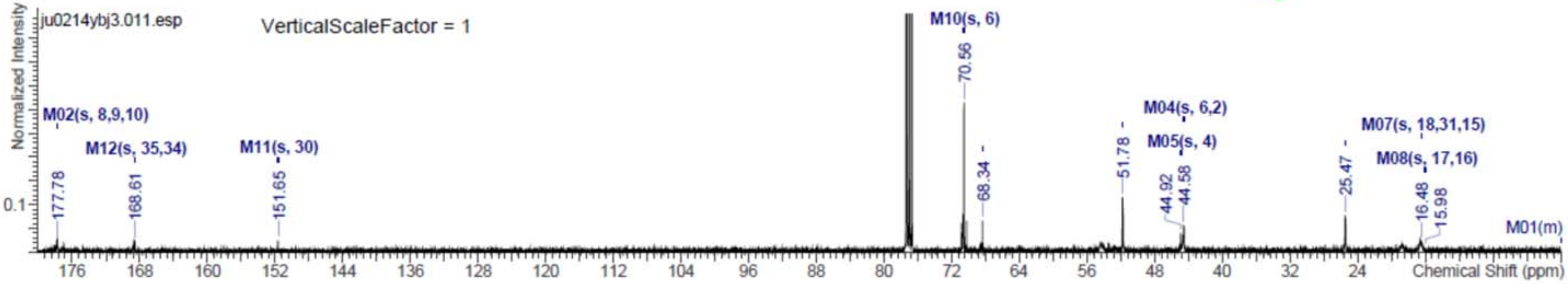

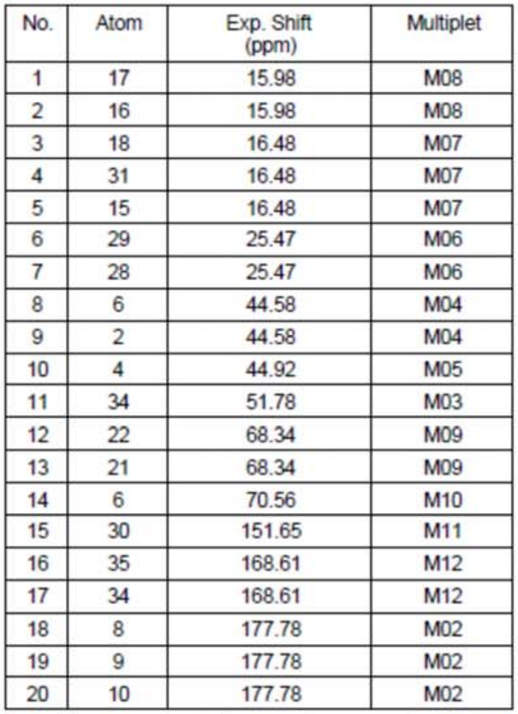

No.	Atom	Exp. Shift (ppm)	Multiplet
1	17	15.98	M08
2	16	15.98	M08
3	18	16.48	M07
4	31	16.48	M07
5	15	16.48	M07
6	29	25.47	M06
7	28	25.47	M06
8	6	44.58	M04
9	2	44.58	M04
10	4	44.92	M05
11	34	51.78	M03
12	22	68.34	M09
13	21	68.34	M09
14	6	70.56	M10
15	30	151.65	M11
16	35	168.61	M12
17	34	168.61	M12
18	8	177.78	M02
19	9	177.78	M02
20	10	177.78	M02

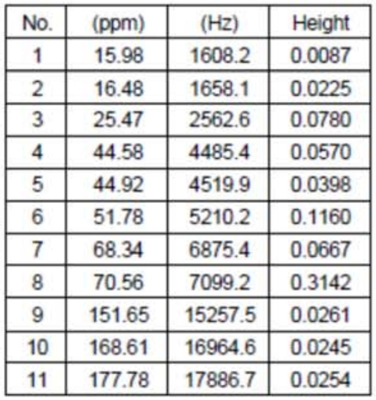

No.	(ppm)	(Hz)	Height
1	15.98	1608.2	0.0087
2	16.48	1658.1	0.0225
3	25.47	2562.6	0.0780
4	44.58	4485.4	0.0570
5	44.92	4519.9	0.0398
6	51.78	5210.2	0.1160
7	68.34	6875.4	0.0667
8	70.56	7099.2	0.3142
9	151.65	15257.5	0.0261
10	168.61	16964.6	0.0245
11	177.78	17886.7	0.0254

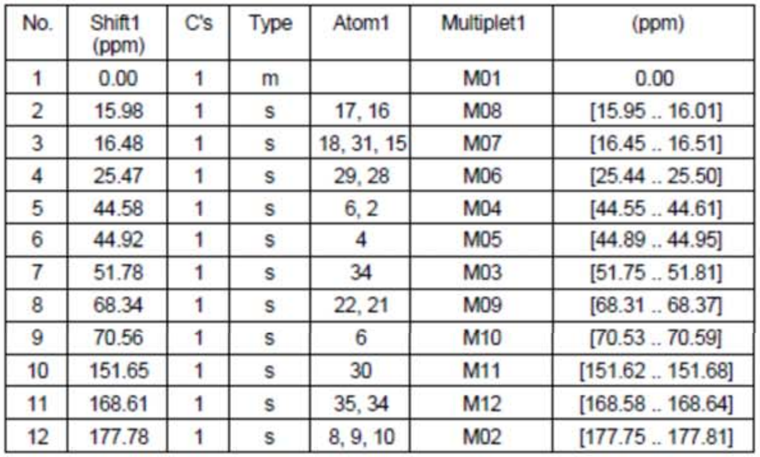

No.	Shift1 (ppm)	C's	Type	Atom1	Multiplet1	(ppm)
1	0.00	1	m		M01	0.00
2	15.98	1	s	17, 16	M08	[15.95 .. 16.01]
3	16.48	1	s	18, 31, 15	M07	[16.45 .. 16.51]
4	25.47	1	s	29, 28	M06	[25.44 .. 25.50]
5	44.58	1	s	6, 2	M04	[44.55 .. 44.61]
6	44.92	1	s	4	M05	[44.89 .. 44.95]
7	51.78	1	s	34	M03	[51.75 .. 51.81]
8	68.34	1	s	22, 21	M09	[68.31 .. 68.37]
9	70.56	1	s	6	M10	[70.53 .. 70.59]
10	151.65	1	s	30	M11	[151.62 .. 151.68]
11	168.61	1	s	35, 34	M12	[168.58 .. 168.64]
12	177.78	1	s	8, 9, 10	M02	[177.75 .. 177.81]

9-anthryl methyl methacrylate (5)

Number of Nuclei	6 C's / 19 C's (spectrum / structure)	Multiplets Integrals Sum	0.00

Formula	$C_{19}H_{16}O_2$	FW	276.3291	[M-H]-	275.107753	[M-H]+	275.106656		
[M+H]-	277.123403			[M+H]+	277.122306	M-	276.115578		
M+	276.114481			Monoisotopic Mass	276.115030	Nominal Mass	276	$d_N(^{13}C)$	3.551
$sd_N(^{13}C)$	4.050	$max\_d_N(^{13}C)$	6.792						

Acquisition Time (sec)	1.3631	Comment	GW/6749/16	Date	27 Nov 2013 15:19:28		
Date Stamp	27 Nov 2013 15:19:28						
File Name	\\soton.ac.uk\ude\PersonalFiles\Users\gw5g08\mydocuments\Postgraduate\Analysis\NMR\GW_6749_16\nv2713alf1\11\PDATA\1\1r						
Frequency (MHz)	100.6128	Nucleus	13C	Number of Transients	512	Origin	AVII400
Original Points Count	32768	Owner	nmr	Points Count	32768	Pulse Sequence	zgpg30
Receiver Gain	309.31	SW(cyclical) (Hz)	24038.46	Solvent	CHLOROFORM-d	Spectrum Offset (Hz)	10091.3877
Spectrum Type	STANDARD	Sweep Width (Hz)	24037.73	Temperature (degree C)	25.160		

^{13}C NMR (101 MHz, CHLOROFORM-*d*) δ ppm 18.66 (s, 1 C) 124.36 (s, 1 C) 125.41 (s, 1 C) 126.30 (s, 1 C) 126.90 (s, 1 C) 129.40 (s, 1 C)

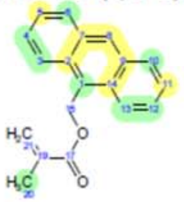

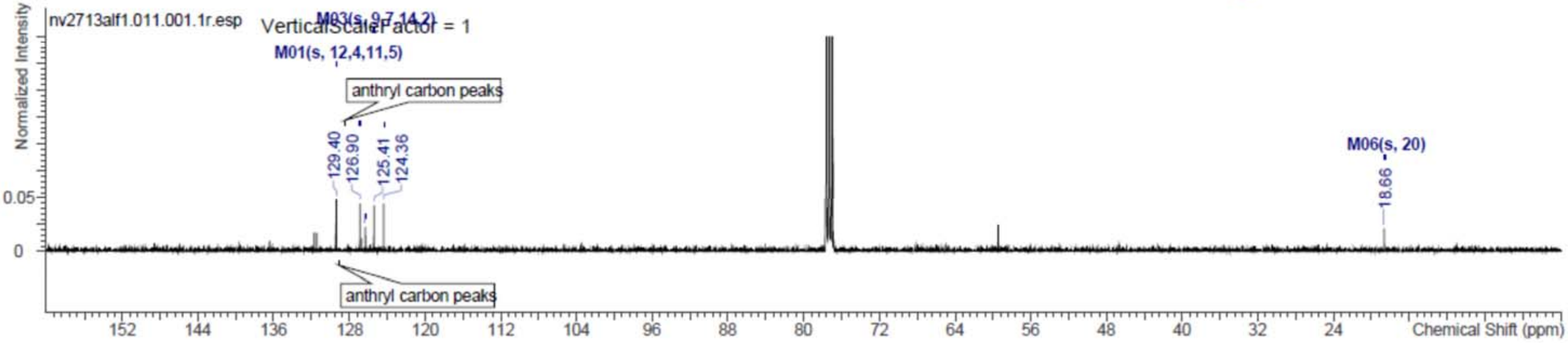

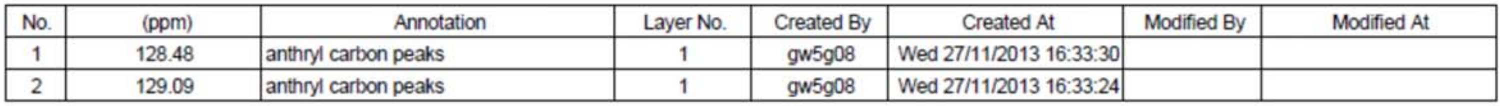

No.	(ppm)	Annotation	Layer No.	Created By	Created At	Modified By	Modified At
1	128.48	anthryl carbon peaks	1	gw5g08	Wed 27/11/2013 16:33:30		
2	129.09	anthryl carbon peaks	1	gw5g08	Wed 27/11/2013 16:33:24		

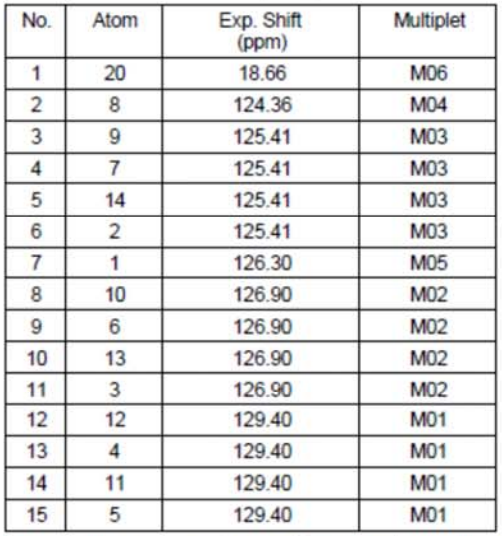

No.	Atom	Exp. Shift (ppm)	Multiplet
1	20	18.66	M06
2	8	124.36	M04
3	9	125.41	M03
4	7	125.41	M03
5	14	125.41	M03
6	2	125.41	M03
7	1	126.30	M05
8	10	126.90	M02
9	6	126.90	M02
10	13	126.90	M02
11	3	126.90	M02
12	12	129.40	M01
13	4	129.40	M01
14	11	129.40	M01
15	5	129.40	M01

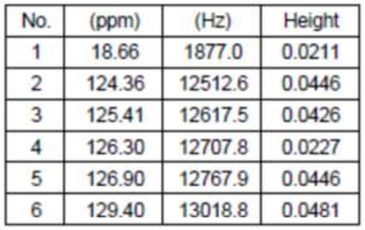

No.	(ppm)	(Hz)	Height
1	18.66	1877.0	0.0211
2	124.36	12512.6	0.0446
3	125.41	12617.5	0.0426
4	126.30	12707.8	0.0227
5	126.90	12767.9	0.0446
6	129.40	13018.8	0.0481

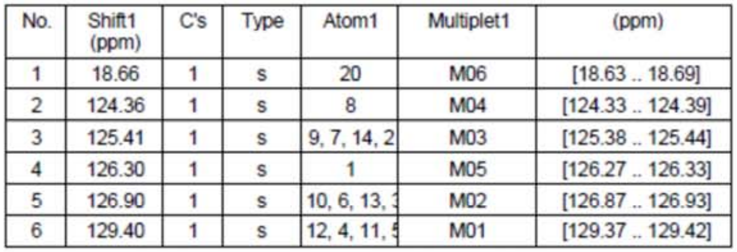

No.	Shift1 (ppm)	C's	Type	Atom1	Multiplet1	(ppm)
1	18.66	1	s	20	M06	[18.63 .. 18.69]
2	124.36	1	s	8	M04	[124.33 .. 124.39]
3	125.41	1	s	9, 7, 14, 2	M03	[125.38 .. 125.44]
4	126.30	1	s	1	M05	[126.27 .. 126.33]
5	126.90	1	s	10, 6, 13,	M02	[126.87 .. 126.93]
6	129.40	1	s	12, 4, 11,	M01	[129.37 .. 129.42]

Appendix B

IR Spectra

Appendix B

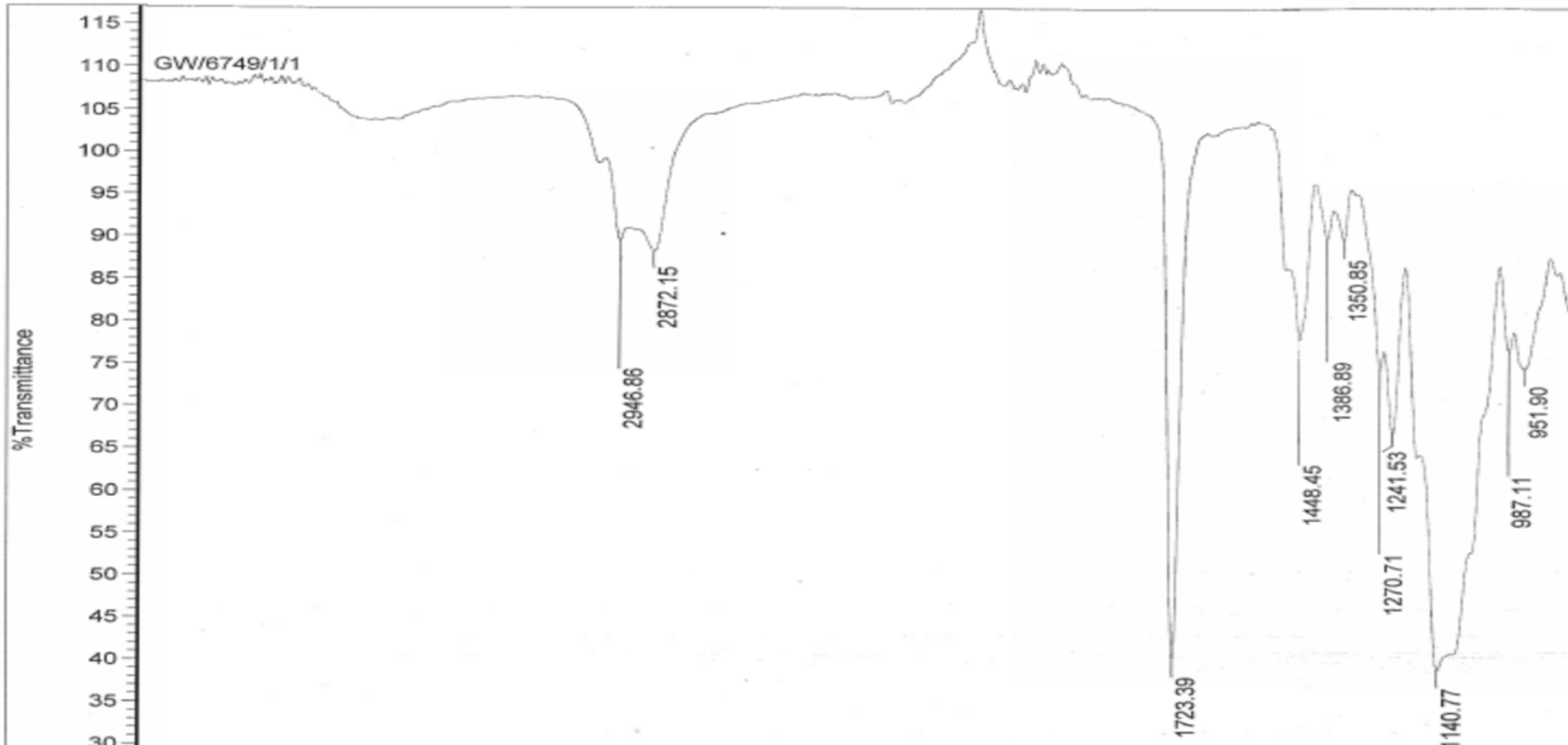
GW/6749/1/1
% Transmittance
115
110
105
100
95
90
85
80
75
70
65
60
55
50
45
40
35
30
2946.86
2872.15
1723.39
1448.45
1386.89
1350.85
1270.71
1241.53
1140.77
987.11
951.90

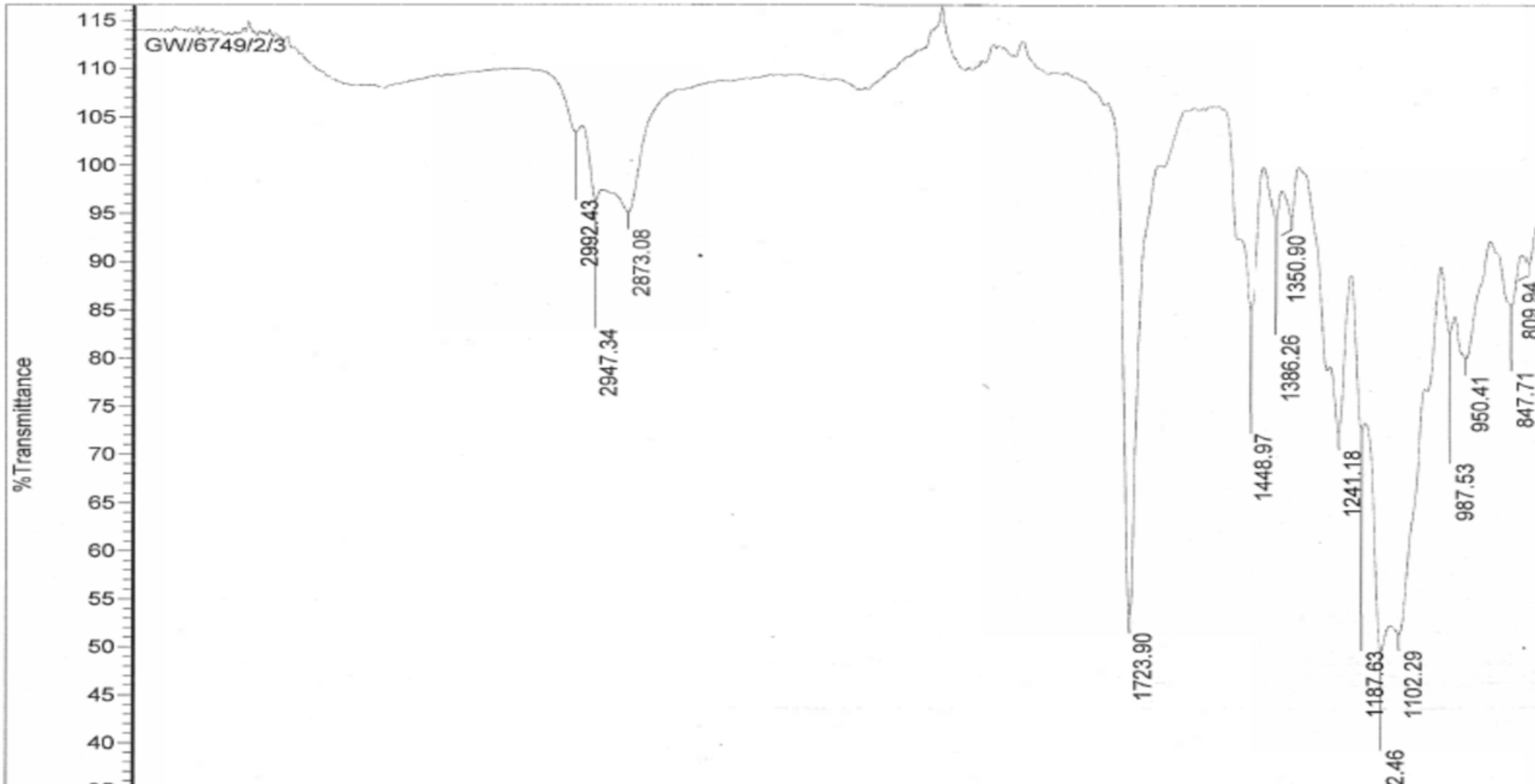
GW/6749/2/3
%Transmittance
115
110
105
100
95
90
85
80
75
70
65
60
55
50
45
40
2992.43
2947.34
2873.08
1723.90
1448.97
1386.26
1350.90
1241.18
1187.63
1102.29
987.53
950.41
847.71
809.94
2.46

MMA:PEGM:FMA co-polymer unfunctionalised (3)

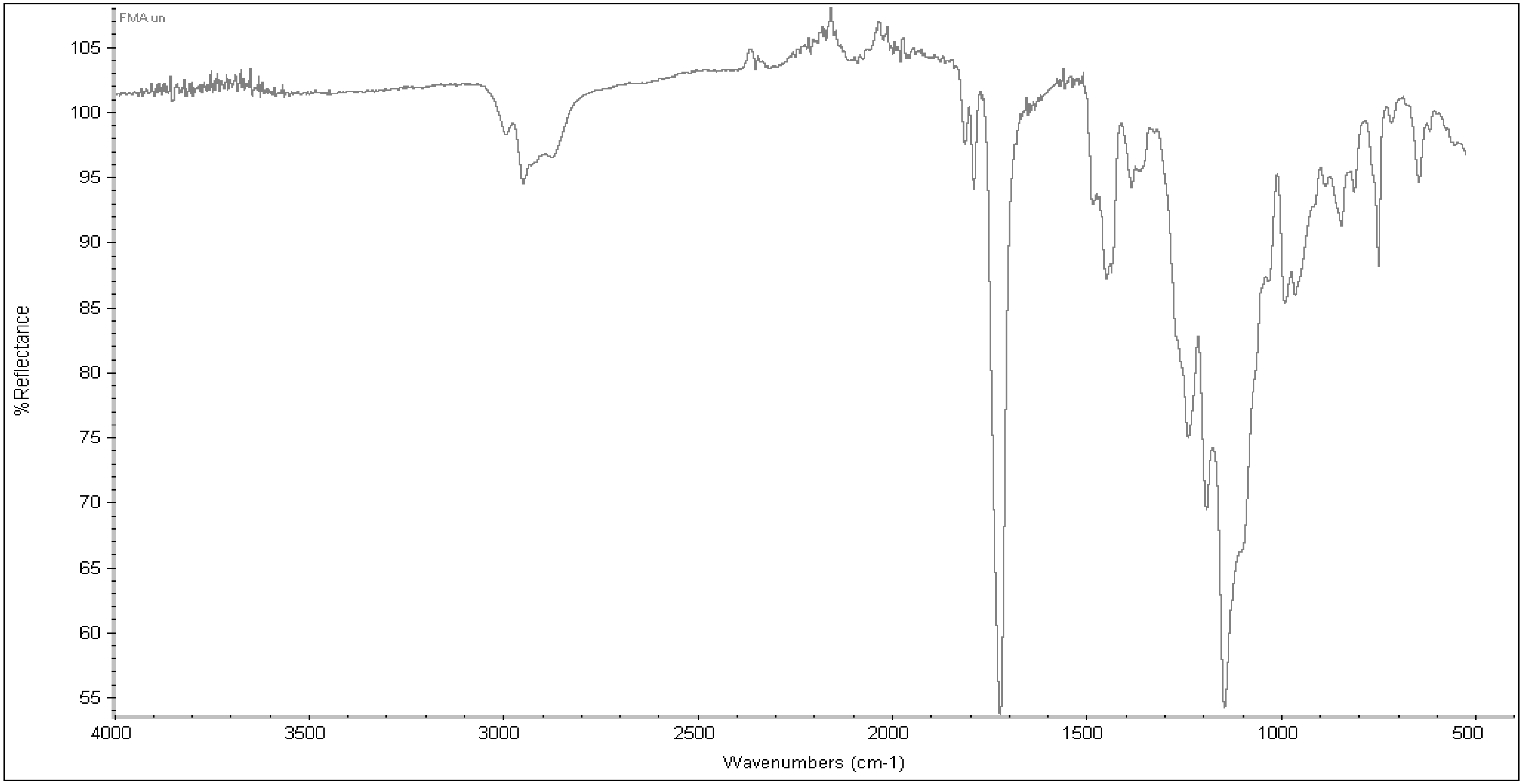

MMA:PEGM:FMA co-polymer functionalised (4)

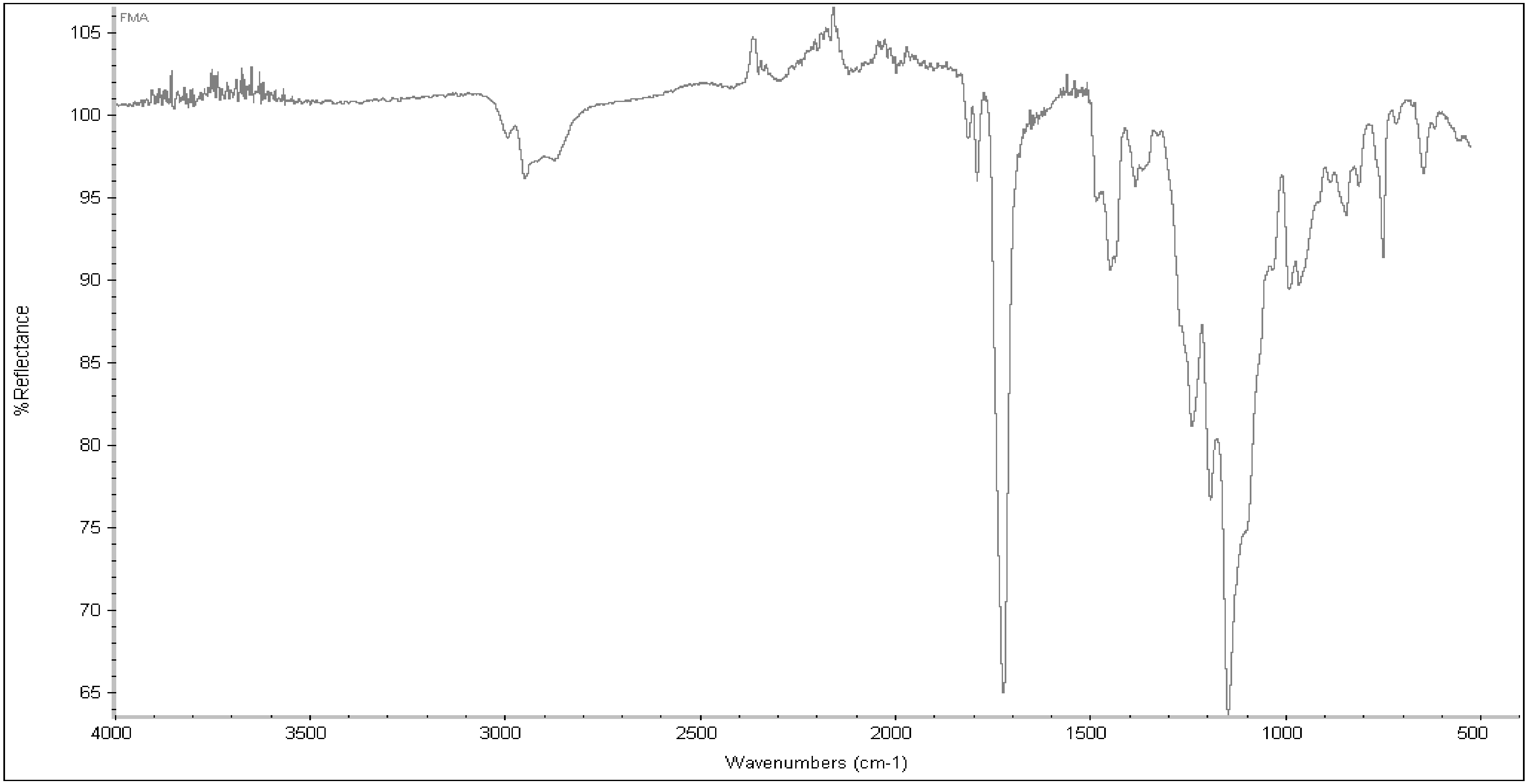

MMA:PEGM:AMM co-polymer unfunctionalised (6)

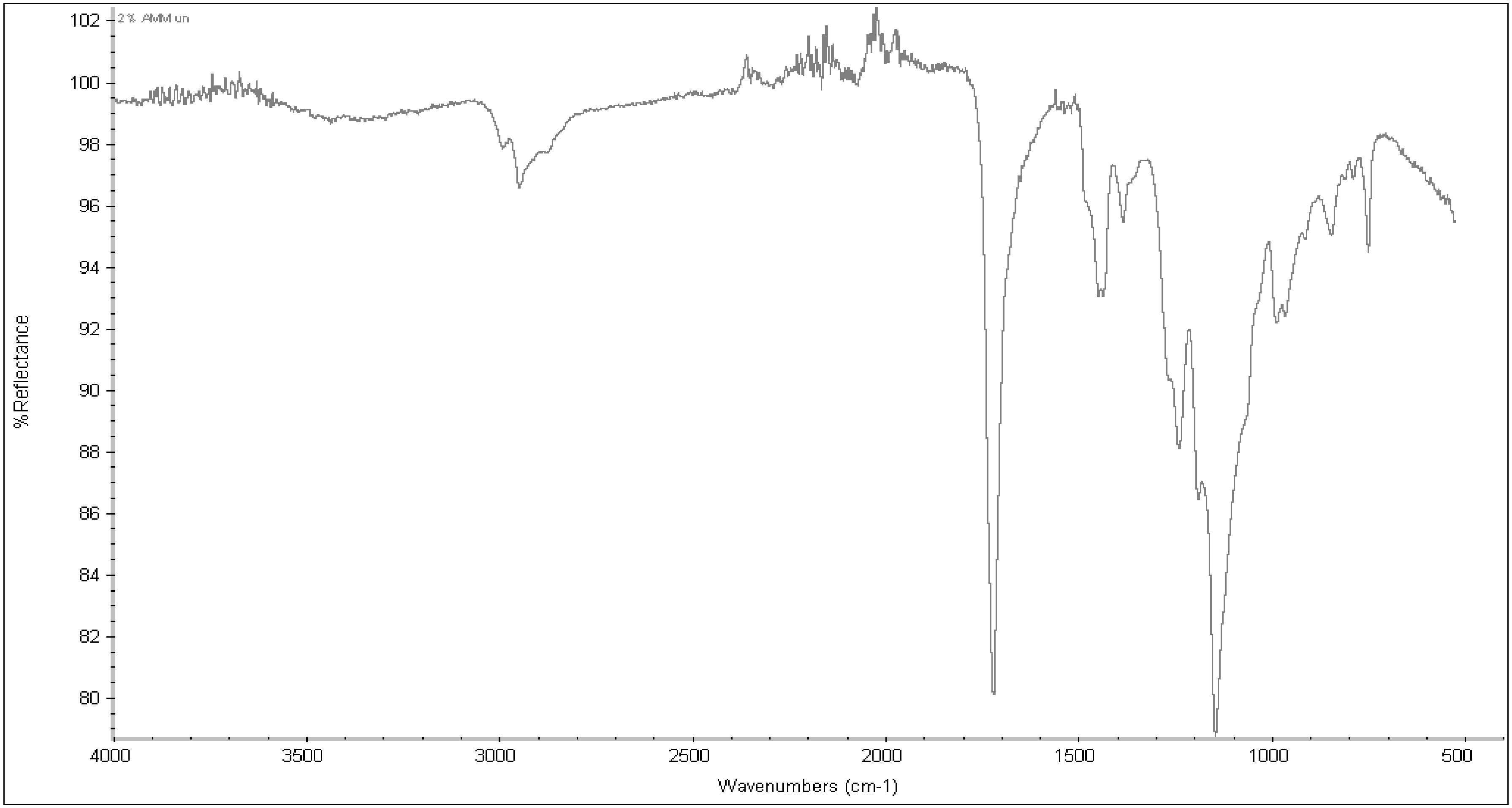

MMA:PEGM:AMM co-polymer functionalised (7)

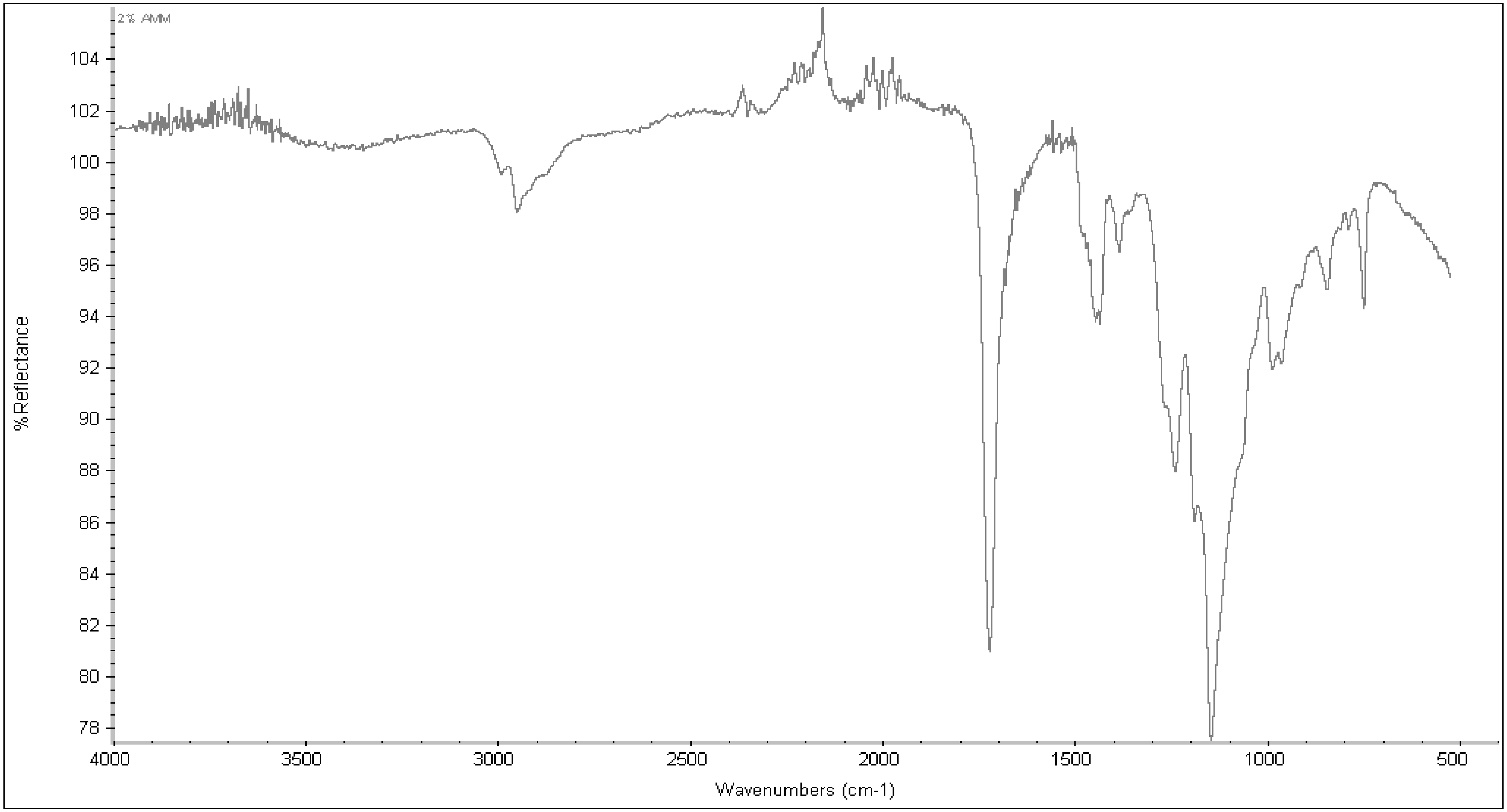

MMA:PEGM:AMM co-polymer unfunctionalised (8)

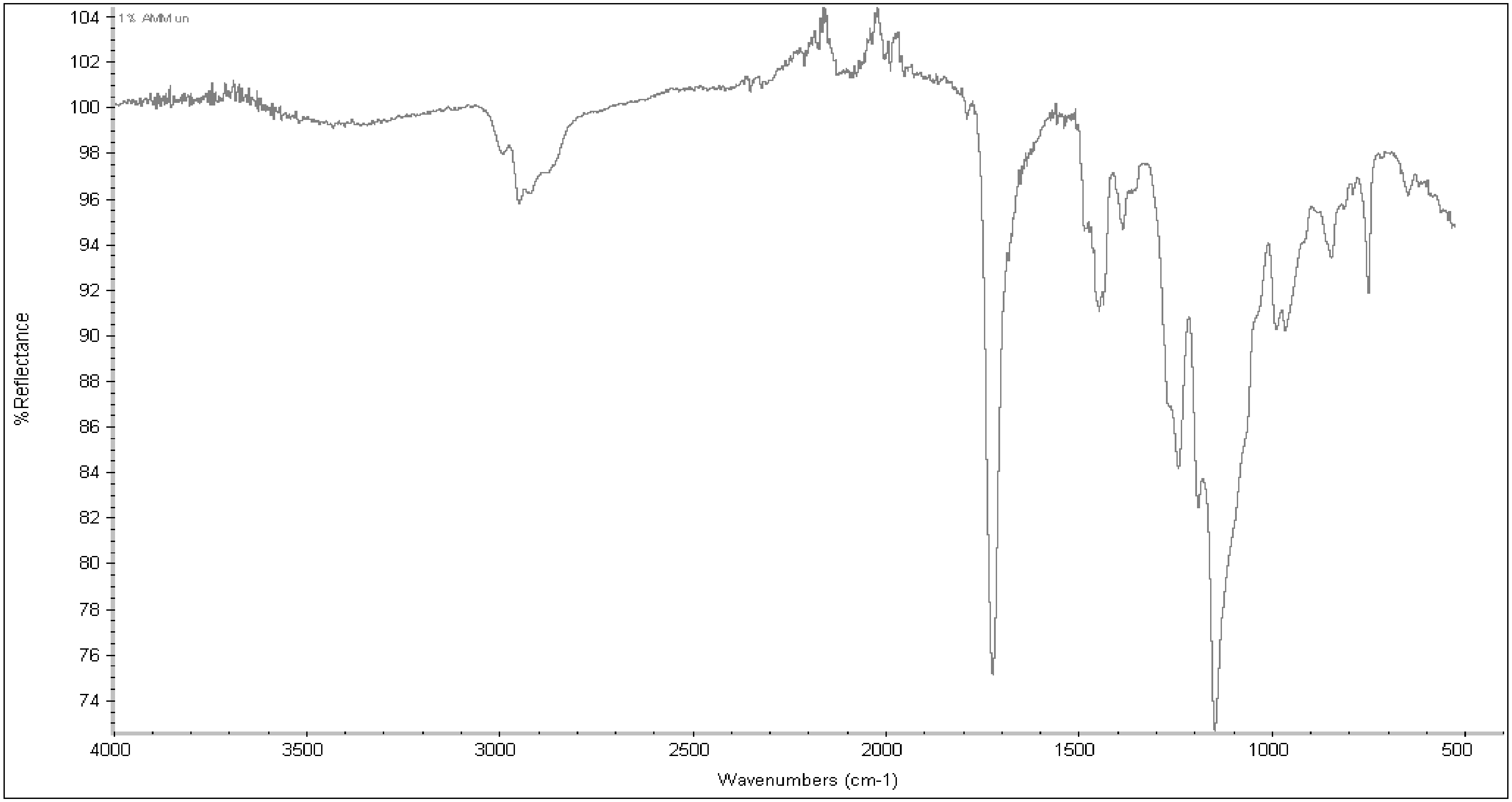

MMA:PEGM:AMM co-polymer functionalised (9)

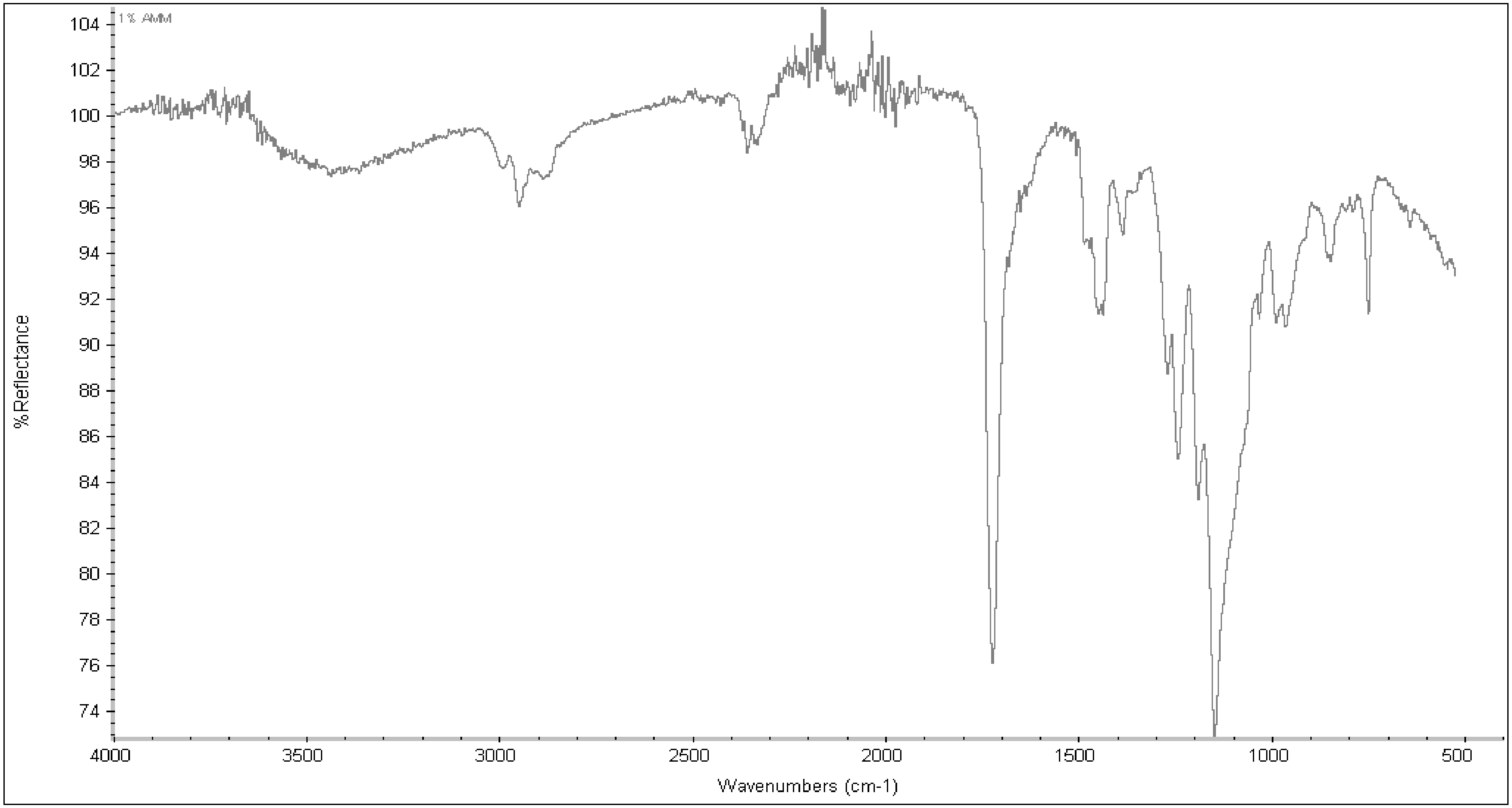

MMA:PEGM:AMM co-polymer unfunctionalised (10)

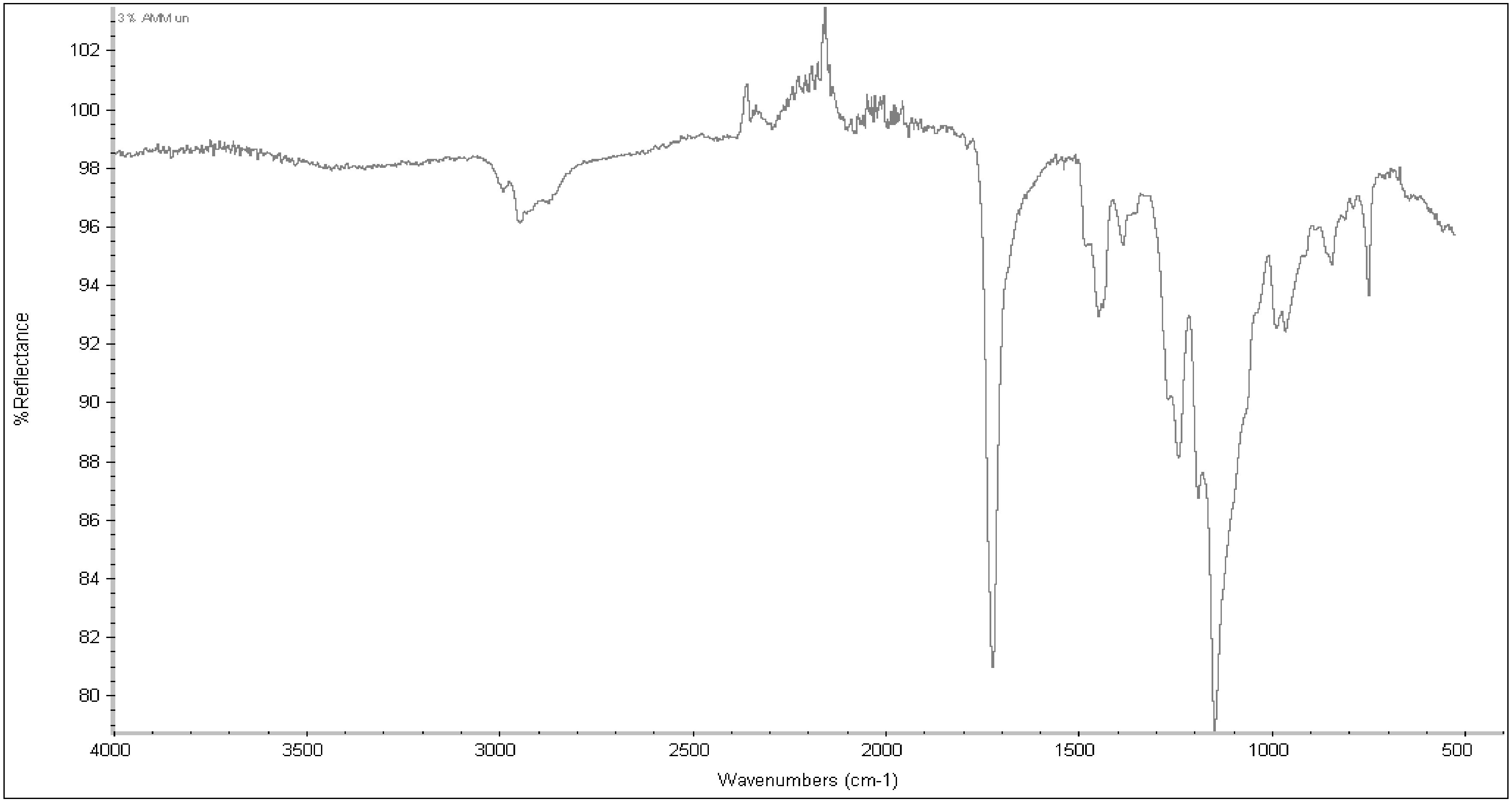

MMA:PEGM:AMM co-polymer functionalised (11)

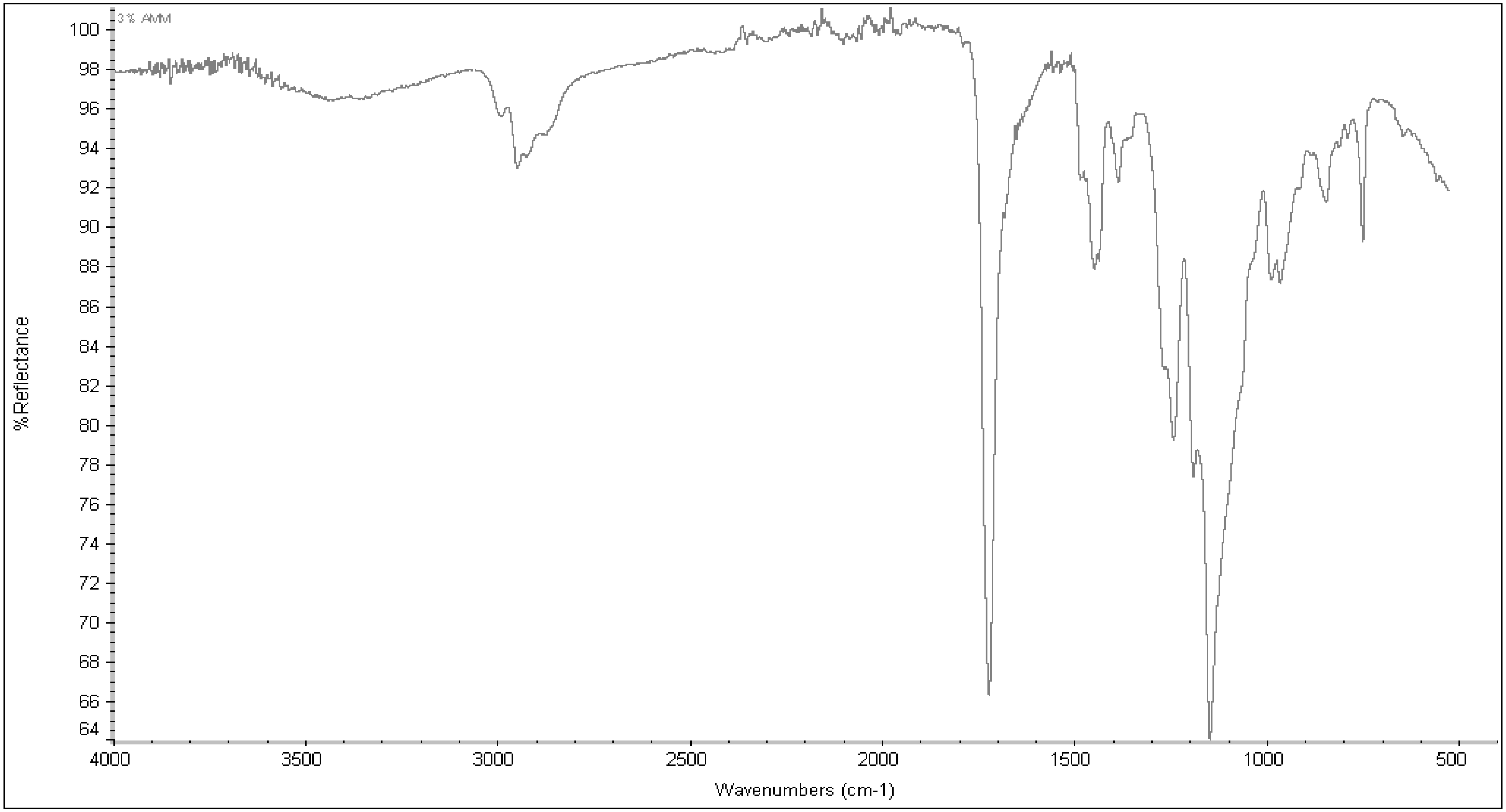

MS Spectra MMA:PEGM co-polymer unfunctionalised (1)

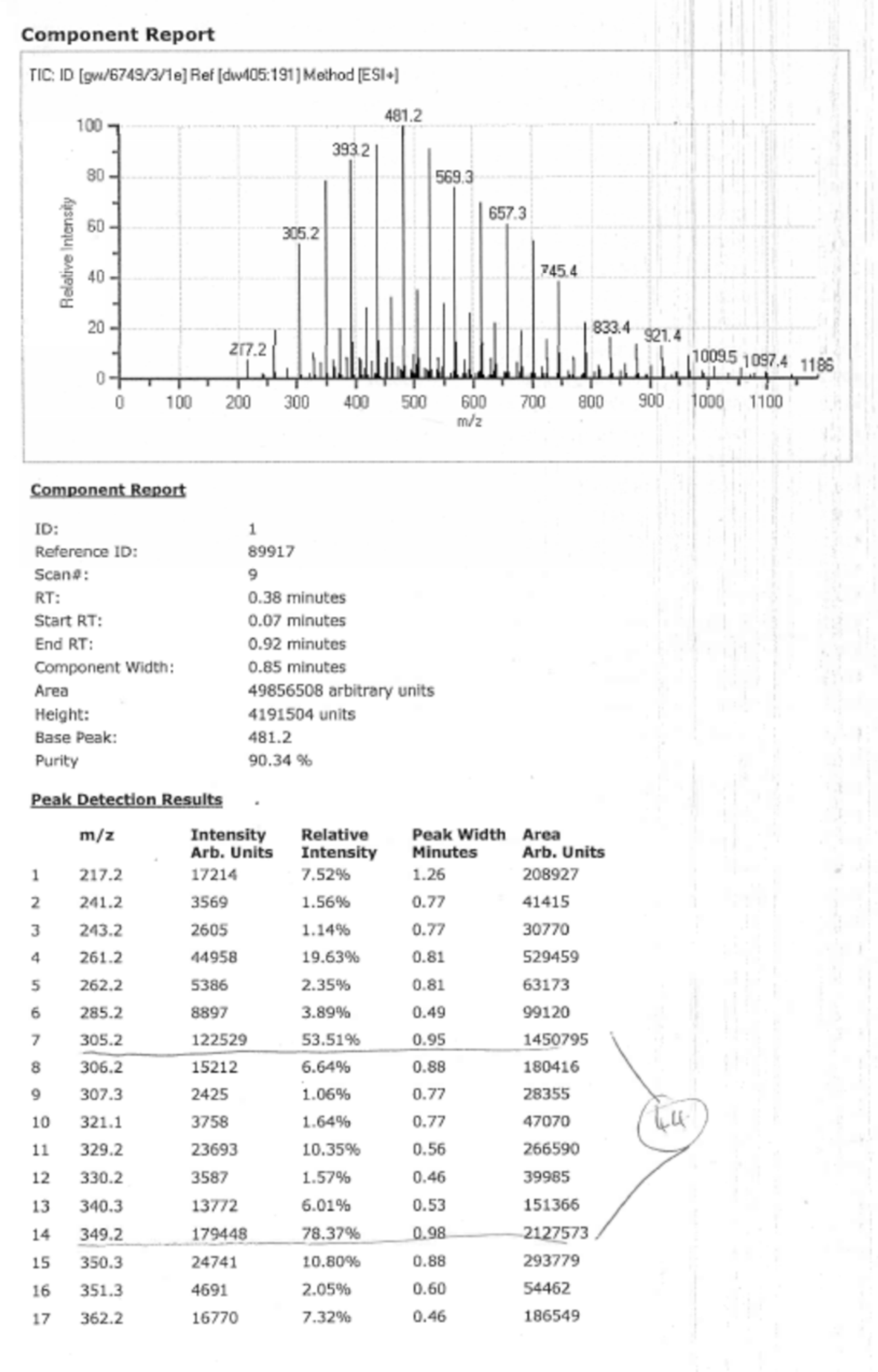

Component Report

TIC: ID [gw/6749/3/1e] Ref [dw405:191] Method [ESI+]

Component Report

ID:	1
Reference ID:	89917
Scan#:	9
RT:	0.38 minutes
Start RT:	0.07 minutes
End RT:	0.92 minutes
Component Width:	0.85 minutes
Area	49856508 arbitrary units
Height:	4191504 units
Base Peak:	481.2
Purity	90.34 %

Peak Detection Results

	m/z	Intensity Arb. Units	Relative Intensity	Peak Width Minutes	Area Arb. Units
1	217.2	17214	7.52%	1.26	208927
2	241.2	3569	1.56%	0.77	41415
3	243.2	2605	1.14%	0.77	30770
4	261.2	44958	19.63%	0.81	529459
5	262.2	5386	2.35%	0.81	63173
6	285.2	8897	3.89%	0.49	99120
7	305.2	122529	53.51%	0.95	1450795
8	306.2	15212	6.64%	0.88	180416
9	307.3	2425	1.06%	0.77	28355
10	321.1	3758	1.64%	0.77	47070
11	329.2	23693	10.35%	0.56	266590
12	330.2	3587	1.57%	0.46	39985
13	340.3	13772	6.01%	0.53	151366
14	349.2	179448	78.37%	0.98	2127573
15	350.3	24741	10.80%	0.88	293779
16	351.3	4691	2.05%	0.60	54462
17	362.2	16770	7.32%	0.46	186549

44

9-anthryl methyl methacrylate (5)

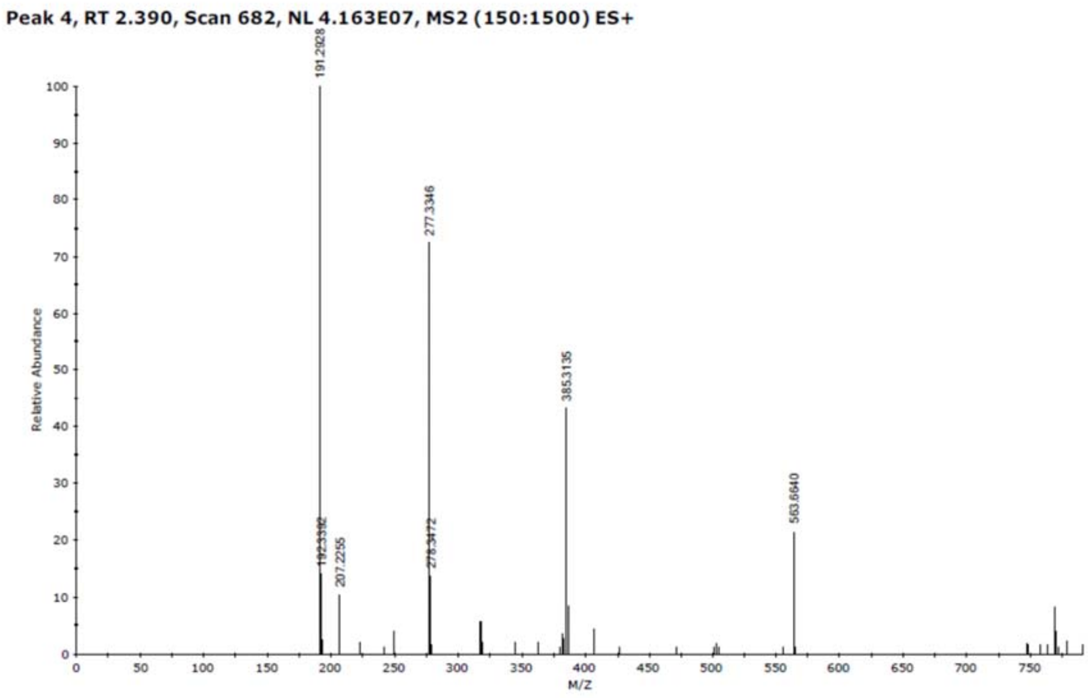

List of References

1. Chen, F. K. *et al.* Long-term visual and microperimetry outcomes following autologous retinal pigment epithelium choroid graft for neovascular age-related macular degeneration. *Clin. Experiment. Ophthalmol.* **37,** 275–85 (2009).
2. Schwartz, S. D., Regillo, C. D. & Lanza, R. Human embryonic stem cell-derived retinal pigment epithelium in patients with age-related macular degeneration and Stargardt's macular dystrophy: follow-up of two open-label phase 1/2 studies. *Lancet* **385,** 509–516 (2015).
3. Schwartz, S. D. *et al.* Embryonic stem cell trials for macular degeneration: a preliminary report. *Lancet* **379,** 713–720 (2012).
4. Thomson, H. a J., Treharne, A. J., Walker, P., Grossel, M. C. & Lotery, A. J. Optimisation of polymer scaffolds for retinal pigment epithelium (RPE) cell transplantation. *Br. J. Ophthalmol.* **95,** 563–8 (2011).
5. Davson, H. *The Eye*. (Academic Press Ltd Elseiver Science Ltd, 1984).
6. Lamb, T. D. & Pugh, E. N. Dark adaptation and the retinoid cycle of vision. *Prog. Retin. Eye Res.* **23,** 307–80 (2004).
7. Yokoyama, S. *Molecular evolution of vertebrate visual pigments. Progress in retinal and eye research* **19,** (2000).
8. Baino, F. The Use of Polymers in the Treatment of Retinal Detachment: Current Trends and Future Perspectives. *Polymers (Basel).* **2,** 286–322 (2010).
9. Rizzolo, L. J., Chen, X., Weitzman, M., Sun, R. & Zhang, H. Analysis of the RPE transcriptome reveals dynamic changes during the development of the outer blood-retinal barrier. *Mol. Vis.* **13,** 1259–1273 (2007).
10. Strauss, O. The Retinal Pigment Epithelium in Visual Function. *Physiol Rev* **85,** 845–881 (2005).
11. Boulton, M. & Dayhaw-Barker, P. The role of the retinal pigment epithelium: topographical variation and ageing changes. *Eye (Lond).* **15,** 384–389 (2001).
12. Boulton, M. in *The Retinal Pigment Epithelium* 68–65 (1998).
13. Strauss, O. Transport mechanisms of the retinal pigment epithelium to maintain of visual function. *Heat Mass Transf.* **50,** 303–313 (2013).
14. Gundersen, D., Orlowski, J. & Rodriguez-Boulan, E. Apical Polarity of Na,K-ATPase in Retinal Pigment Epithelium Is Linked to a Reversal of the Ankyrin-Fodrin Submembrane Cytoskeleton. *Mol. Genet.* **112,** 863–872 (1991).
15. Hargrave, P. A. Rhodopsin Structure, Function, and Topography. *Invest. Ophthalmol. Vis. Sci.* **42,** 3–9 (2001).
16. Papermaster, D. S. & Dreyer, W. J. Rhodopsin Content in the Outer Segment Membranes. *Biochemistry* **13,** 2438–2444 (1974).
17. Mata, N. L. *et al.* Rpe65 is a retinyl ester binding protein that presents insoluble substrate to the isomerase in retinal pigment epithelial cells. *J. Biol. Chem.* **279,** 635–43 (2004).
18. Beatty, S., Koh, H.-H., Phil, M., Henson, D. & Boulton, M. The Role of Oxidative Stress in the Pathogenesis of Age-Related Macular Degeneration. *Surv. Ophthalmol.* **45,** 115–134 (2000).
19. Kevany, B. M. & Palczewski, K. Phagocytosis of retinal rod and cone photoreceptors. *Physiology (Bethesda).* **25,** 8–15 (2010).
20. Finnemann, S. C. Focal adhesion kinase signaling promotes phagocytosis of integrin-bound photoreceptors. *EMBO J.* **22,** 4143–54 (2003).

21. Hamel, C. Retinitis pigmentosa. *Orphanet J. Rare Dis.* **1,** 40 (2006).

22. Hartong, D. T., Berson, E. L. & Dryja, T. P. Retinitis pigmentosa. *Lancet* **368,** 1795–1809 (2006).

23. Niemann, S. *et al.* Mutations in MERTK , the human orthologue of the RCS rat retinal dystrophy gene , cause retinitis pigmentosa. *Nat. Genet.* **26,** 270–271 (2000).

24. Kay, P., Yang, Y. C. & Paraoan, L. Directional protein secretion by the retinal pigment epithelium: roles in retinal health and the development of age-related macular degeneration. *J. Cell. Mol. Med.* **17,** 833–43 (2013).

25. Baffi, J., Byrnes, G., Chan, C. C. & Csaky, K. G. Choroidal neovascularization in the rat induced by adenovirus mediated expression of vascular endothelial growth factor. *Investig. Ophthalmol. Vis. Sci.* **41,** 3582–3589 (2000).

26. Kwak, N., Okamoto, N., Wood, J. M. & Campochiaro, P. A. VEGF is major stimulator in model of choroidal neovascularization. *Investig. Ophthalmol. Vis. Sci.* **41,** 3158–3164 (2000).

27. Tezel, T. H. & Del Priore, L. V. Reattachment to a substrate prevents apoptosis of human retinal pigment epithelium. *Graefes Arch. Clin. Exp. Ophthalmol.* **235,** 41–7 (1997).

28. Hussain, A., Starita, C. & Marshall, J. in *Focus on macular degeneration research* (Nova Biomedical Books, 2004).

29. Moore, D. J., Hussain, A. A. & Marshall, J. Age-Related Variation in the Hydraulic Conductivity of Bruch's Membrane. *Invest. Ophthalmol. Vis. Sci.* **36,** 1290–7 (1995).

30. Hogan, M. J., Alvarado, J. & Weddell, J. E. *Histology of the Human Eye: An Atlas and Textbook*. (WB Saunders, 1971).

31. Hogan, M. J. & Alvarado, J. Studies on the Human Macula IV. Aging Changes in Bruch's Membrane. *Arch. Ophthalmol.* **77,** 410–420 (1967).

32. Booij, J. C., Baas, D. C., Beisekeeva, J., Gorgels, T. G. M. F. & Bergen, a a B. The dynamic nature of Bruch's membrane. *Prog. Retin. Eye Res.* **29,** 1–18 (2010).

33. Chen, L., Miyamura, N., Ninomiya, Y. & Handa, J. T. Distribution of the collagen IV isoforms in human Bruch's membrane. *Br J Ophthalmol* **87,** 212–215 (2003).

34. Marshall, G. E., Konstas, a G., Reid, G. G., Edwards, J. G. & Lee, W. R. Type IV collagen and laminin in Bruch's membrane and basal linear deposit in the human macula. *Br J Ophthalmol* **76,** 607–614 (1992).

35. Aisenbrey, S. *et al.* Retinal Pigment Epithelial Cells Synthesize Laminins , Including Laminin 5 , and Adhere to Them through. *Invest. Ophthalmol. Vis. Sci.* **47,** 5537–5544 (2006).

36. McKay, B., Irving, P. E., Skumatz, C. M. B. & Burke, J. M. Cell – Cell Adhesion Molecules and the Development of an Epithelial Phenotype in Cultured Human Retinal Pigment. *Exp. Eye Res.* **65,** 661–671 (1997).

37. Lutty, G. A., Hasegawa, T. & McLeod, D. S. Development of the human choriocapillaris. *Eye (Lond).* **24,** 408–415 (2010).

38. Marshall, G. E., Konstas, A. G. & Lee, W. R. Collagens in ocular tissues. *Br. J. Ophthalmol.* **77,** 515–524 (1993).

39. Wang, H., Ninomiya, Y., Sugino, I. K. & Zarbin, M. a. Retinal pigment epithelium wound healing in human Bruch's membrane explants. *Investig. Ophthalmol. Vis. Sci.* **44,** 2199–2210 (2003).

40. Marshall, G. E., Konstas, a G., Reid, G. G., Edwards, J. G. & Lee, W. R. Type IV collagen and laminin in Bruch's membrane and basal linear deposit in the human macula. *Br. J. Ophthalmol.* **76,** 607–614 (1992).

41. Starita, C., Hussain, A. A., Patmore, A. & Marshall, J. Localization of the Site of Major Resistance to Fluid Transport in Bruch's Membrane. *Invest. Ophthalmol. Vis. Sci.* **38,** 762–7

(1997).

42. Beers, A. & Van Der Heijde, G. In vivo determination of the biomechanical properties of the component elements of the accommodation mechanism. *Vision Res.* **34,** 2897–905 (1994).

43. Charman, W. N. The eye in focus : accommodation and presbyopia. *Clin. Experiment. Ophthalmol.* **91,** 207–225 (2008).

44. Ugarte, M., Hussain, a a & Marshall, J. An experimental study of the elastic properties of the human Bruch's membrane-choroid complex: relevance to ageing. *Br. J. Ophthalmol.* **90,** 621–6 (2006).

45. Korte, G. E. & D'Aversa, G. The elastic tissue of Bruch's membrane. *Arch. Ophthalmol.* **107,** 1654–1658 (1989).

46. Hussain, A. A., Starita, C., Hodgetts, A. & Marshall, J. Macromolecular diffusion characteristics of ageing human Bruch's membrane: Implications for age-related macular degeneration (AMD). *Exp. Eye Res.* **90,** 703–710 (2010).

47. Marshall, J. The ageing retina: physiology or pathology. *Eye (Lond).* **1 (Pt 2),** 282–295 (1987).

48. Olson, M. D. Development of Bruch's membrane in the chick: An electron microscopic study. *Investig. Ophthalmol. Vis. Sci.* **18,** 329–338 (1979).

49. Takei, Y. & Ozanics, V. Origin and development of Bruch's membrane in monkey fetuses: an electron microscopic study. *Investig. Ophthalmol. Vis. Sci.* **14,** 903–916 (1975).

50. Campochiaro, P. A., Jerdan, J. A. & Glaser, B. M. The Extracellular Matrix of Human Retinal Pigment Epithelial Cells In Vivo and its Synthesis In Vitro. *Investig. Ophthalmol. Vis. Sci.* **27,** 1615–1621 (1986).

51. Curcio, C. A. & Johnson, M. in *Retina* 465–481 (2012).

52. Scales, D., Fryczkowski, A. & Opremcak, E. in *Principle and practices of ophthalmology* 252–61 (1994).

53. Ford, K. M., Saint-Geniez, M., Walshe, T., Zahr, A. & D'Amore, P. a. Expression and role of VEGF in the adult retinal pigment epithelium. *Invest. Ophthalmol. Vis. Sci.* **52,** 9478–87 (2011).

54. Pascolini, D. & Mariotti, S. P. Global estimates of visual impairment: 2010. *Br. J. Ophthalmol.* **96,** 614–618 (2012).

55. Resnikoff, S. *et al.* Global data on visual impairment in the year 2002. **82,** 844–851 (2004).

56. Farkas, T. G. The ultrastructure of drusen. *Am. J. Ophthalmol.* **71,** 1196–1205 (1971).

57. Curcio, C. a, Presley, J. B., Millican, C. L. & Medeiros, N. E. Basal deposits and drusen in eyes with age-related maculopathy: evidence for solid lipid particles. *Exp. Eye Res.* **80,** 761–75 (2005).

58. Pauleikhoff, D. *et al.* Drusen and their significance in age related macular degeneration. *Fortschritte der Ophthalmol. Zeitschrift der Dtsch. Ophthalmol. Gesellschaft* **87,** 429–432 (1990).

59. Donald, J. & Gass, M. Drusen and Disciform Macular Detachment and Degeneration. *Arch. Ophthalmol.* **90,** 206–217 (1973).

60. Spilsbury, K., Garrett, K. L., Shen, W. Y., Constable, I. J. & Rakoczy, P. E. Overexpression of vascular endothelial growth factor (VEGF) in the retinal pigment epithelium leads to the development of choroidal neovascularization. *Am. J. Pathol.* **157,** 135–144 (2000).

61. Krzystolik, M. G. *et al.* Prevention of experimental choroidal neovascularization with intravitreal anti-vascular endothelial growth factor antibody fragment. *Arch. Ophthalmol.* **120,** 338–346 (2002).

62. Madhusudhana, K. C. *et al.* Intravitreal bevacizumab (Avastin) for the treatment of choroidal neovascularization in age-related macular degeneration: results from 118 cases.

Br. J. Ophthalmol. **91,** 1716–7 (2007).

63. Heier, J. S. *et al.* Intravitreal aflibercept (VEGF trap-eye) in wet age-related macular degeneration. *Ophthalmology* **119,** 2537–2548 (2012).

64. Mitchell, P. *et al.* Ranibizumab (Lucentis) in neovascular age-related macular degeneration: evidence from clinical trials. *Br. J. Ophthalmol.* **94,** 2–13 (2010).

65. Rosenfeld, P. J. *et al.* Ranibizumab for Neovascular Age-Related Macular Degeneration. *N. Engl. J. Med.* **355,** 1419–1431 (2006).

66. Martin, D. F. *et al.* Ranibizumab and bevacizumab for treatment of neovascular age-related macular degeneration: Two-year results. *Ophthalmology* **119,** 1388–1398 (2012).

67. Grunwald, J. E. *et al.* Growth of geographic atrophy in the comparison of age-related macular degeneration treatments trials. *Ophthalmology* **122,** 809–816 (2015).

68. Charbel Issa, P., Chong, N. V. & Scholl, H. P. N. The significance of the complement system for the pathogenesis of age-related macular degeneration - current evidence and translation into clinical application. *Graefes Arch. Clin. Exp. Ophthalmol.* **249,** 163–74 (2011).

69. Donoso, L. a, Vrabec, T. & Kuivaniemi, H. The role of complement Factor H in age-related macular degeneration: a review. *Surv. Ophthalmol.* **55,** 227–46 (2010).

70. Wyatt, M. K. *et al.* Interaction of complement factor h and fibulin3 in age-related macular degeneration. *PLoS One* **8,** e68088 (2013).

71. Ferreira, S. T., Vieira, M. N. N. & De Felice, F. G. Soluble protein oligomers as emerging toxins in alzheimer's and other amyloid diseases. *IUBMB Life* **59,** 332–345 (2007).

72. Dentchev, T., Milam, A. H., Lee, V. M.-Y., Trojanowski, J. Q. & Dunaief, J. L. Amyloid-beta is found in drusen from some age-related macular degeneration retinas, but not in drusen from normal retinas. *Mol. Vis.* **9,** 184–90 (2003).

73. Yoshida, T. *et al.* The potential role of amyloid β in the pathogenesis of age-related macular degeneration. *J. Clin. Invest.* **115,** 2793–2800 (2005).

74. Guymer, R., Luthert, P. & Bird, A. Changes in Bruch's Membrane and Related Structures with Age. *Prog. Retin. Eye Res.* **18,** 59–90 (1998).

75. Pauleikhoff, D., Harper, C. A., Marshall, J. & Bird, A. C. Aging changes in Bruch's membrane. A histochemical and morphologic study. *Ophthalmology* **97,** 171–178 (1990).

76. Bhutto, I. & Lutty, G. Understanding age-related macular degeneration (AMD): relationships between the photoreceptor/retinal pigment epithelium/Bruch's membrane/choriocapillaris complex. *Mol. Aspects Med.* **33,** 295–317 (2012).

77. Moore, D. J. & Clover, G. M. The Effect of Age on the Macromolecular Permeability of Human Bruch's Membrane. *Invest. Ophthalmol. Vis. Sci.* **42,** 2970–2975 (2001).

78. Starita, C., Hussain, A., Pagliarinin, S. & Marshall, J. Hydrodynamics of Ageing Bruch's Membrane : Implications for Macular Disease. *Exp. Eye Res.* **62,** 565–571 (1996).

79. Hollyfield, J. G. *et al.* Oxidative damage-induced inflammation initiates age-related macular degeneration. *Nat. Med.* **14,** 194–8 (2008).

80. Jarrett, S. & Boulton, M. Consequences of oxidative stress in age-related macular degeneration. *Mol Asp. Med.* **33,** 399–417 (2012).

81. Crabb, J. W. *et al.* Drusen proteome analysis: an approach to the etiology of age-related macular degeneration. *Proc. Natl. Acad. Sci. U. S. A.* **99,** 14682–7 (2002).

82. Binder, S. *et al.* Transplantation of Autologous Retinal Pigment Epithelium in Eyes With Foveal Neovascularization Resulting From Age-related Macular Degeneration: A Pilot Study. *Am. J. Ophthalmol.* **133,** 215–225 (2002).

83. Binder, S. *et al.* Outcome of transplantation of autologous retinal pigment epithelium in age-related macular degeneration: A prospective trial. *Investig. Ophthalmol. Vis. Sci.* **45,** 4151–4160 (2004).

84. Binder, S., Stanzel, B. V, Krebs, I. & Glittenberg, C. Transplantation of the RPE in AMD. *Prog. Retin. Eye Res.* **26,** 516–54 (2007).

85. Gullapalli, V. K., Sugino, I. K., Van Patten, Y., Shah, S. & Zarbin, M. a. Impaired RPE survival on aged submacular human Bruch's membrane. *Exp. Eye Res.* **80,** 235–248 (2005).

86. Kamao, H. *et al.* Characterization of human induced pluripotent stem cell-derived retinal pigment epithelium cell sheets aiming for clinical application. *Stem Cell Reports* **2,** 205–218 (2014).

87. Daiger, S. P., Sullivan, L. S. & Bowne, S. J. Genes and mutations causing retinitis pigmentosa. *Clin. Genet.* **84,** 132–141 (2013).

88. Lotery, A. J., Namperumalsamy, P., Jacobsen, S. G. & Al, E. Mutation Analysis of 3 Genes in Patients With Leber Congenital Amaurosis. *Ophthalmic Mol. Genet.* **118,** 538–543 (2000).

89. Berson, E. L., Sandberg, M. A., Rosner, B., Birch, D. G. & Hanson, A. H. Natural course of retinitis pigmentosa over a three-year interval. *Am. J. Ophthalmol.* **99,** 240–51 (1985).

90. Busskamp, V., Picaud, S., Sahel, J. a & Roska, B. Optogenetic therapy for retinitis pigmentosa. *Gene Ther.* **19,** 169–175 (2012).

91. Barker, S. S. *et al.* Effect of Gene Therapy on Visual Function in Leber's Congenital Amaurosis. *N. Engl. J. Med.* 2231–2239 (2008).

92. Maguire, A. M. *et al.* Safety and efficacy of gene transfer for Leber's congenital amaurosis. *N. Engl. J. Med.* **358,** 2240–8 (2008).

93. Beltran, W. a. *et al.* Gene therapy rescues photoreceptor blindness in dogs and paves the way for treating human X-linked retinitis pigmentosa. *Proc. Natl. Acad. Sci.* **109,** 2132–2137 (2012).

94. IUPAC. Basic definitions of terms relating to polymers. *Pure Appl. Chem.* **40,** 477–491 (1974).

95. Brazel, C. S. & Rosen, S. L. *Fundamental Principles of Polymeric Materials.* (2012).

96. Norman, R. O. C. & Waddington, D. J. in *Modern Organic Chemistry* 281–300 (1972).

97. Boyle, M. & Senior, K. in *Biology* 38–66 (2002).

98. Norman, R. O. C. & Waddington, D. J. in *Modern Organic Chemistry* 327–347 (1972).

99. Allsopp, M. W. & Vianello, G. in *Ullmann's Encyclopedia of Industrial Chemistry* (2000).

100. Cowie, J. M. G. & Arrighi, V. *Polymers: Chemistry and Physics of Modern Materials.* (CRC Press, 2008).

101. Carraher, C. E. Synthesis of caprolactam and Nylon 6. *J. Chem. Educ.* **55,** 51 (1978).

102. Mera, H. & Takata, T. in *Ullmann's Encyclopedia of Industrial Chemistry* (2000).

103. Kwoleck, S. L. Wholly aromatic carbocyclic polycarbonamide fiber having orientation angle of less than about 45 degrees. (1971).

104. Habaue, S., Takahashi, Y., Hosogoe, Y., Yamashita, H. & Kajiwara, M. Poly (ethylene terephthalate) synthesis with catalysts derived from chrysotile asbestos. *Nat. Sci.* **2,** 557–562 (2010).

105. Szwarc, M. 'Living' Polymers. *Nature* **178,** 1168 (1956).

106. Szwarc, M., Levy, M. & Milkovich, R. Polymerization Initiated By Electron Transfer To Monomer. A New Method Of Formation Of Block Polymers. *J. Am. Chem. Soc.* **78,** 2657 (1956).

107. Dreyfuss, M. P. & Dreyfuss, P. A 'living' polymer after cationic initiation. *Polymer (Guildf).* **6,** 93–95 (1965).

108. Abrol, S., Caul, M. J., Qiao, G. G. & Solomon, D. H. Studies on microgels . 5 . Synthesis of microgels via living free radical polymerisation. *Polymer (Guildf).* **42,** 5987–5991 (2001).

109. Prajapati, K. & Varshney, A. Free Radical Polymerisation of Methylmethacrylate Using p-nitrobenzyltriphenyl Phosphonium Ylide as Novel Initiator. *J. Polym. Res.* **13,** 97–105 (2005).

110. Karjalainen, E. *et al.* An enzymatic biomimetic system: enhancement of catalytic efficiency with new polymeric chiral ionic liquids synthesised by controlled radical polymerisation. *Polym. Chem.* **5,** 1437 (2014).

111. Baann, H. V & Lindahl, A. K. Injection Molding Polymer. **1,** 2–6 (2004).

112. Schift, H. *et al.* Nanoreplication in polymers using hot embossing and injection molding. *Microelectron. Eng.* **53,** 171–174 (2000).

113. Lawrence, C. J. The mechanics of spin coating of polymer films. *Phys. Fluids* **31,** 2786–2795 (1988).

114. Cooley, J. F. Improved methods of and apparatus for electrically separating the relatively volatile liquid component from the component of relatively fixed substances of composite fluids. (1900).

115. Bhardwaj, N. & Kundu, S. C. Electrospinning: a fascinating fiber fabrication technique. *Biotechnol. Adv.* **28,** 325–47 (2010).

116. Taylor, G. Disintegration of Water Drops in an Electric Field. *Proc. R. Soc. A* **280,** 383–397 (1964).

117. Lee, S. J. *et al.* In vitro evaluation of electrospun nanofiber scaffolds for vascular graft application. *J. Biomed. Mater. Res. part a* **83A,** 999–1008 (2007).

118. Tao, S. L. & Desai, T. a. Aligned arrays of biodegradable poly(epsilon-caprolactone) nanowires and nanofibers by template synthesis. *Nano Lett.* **7,** 1463–8 (2007).

119. Rnjak, J., Li, Z., Maitz, P. K. M., Wise, S. G. & Weiss, A. S. Primary human dermal fibroblast interactions with open weave three-dimensional scaffolds prepared from synthetic human elastin. *Biomaterials* **30,** 6469–77 (2009).

120. Rnjak-Kovacina, J. *et al.* Electrospun synthetic human elastin:collagen composite scaffolds for dermal tissue engineering. *Acta Biomater.* **8,** 3714–22 (2012).

121. Rnjak-Kovacina, J. *et al.* Tailoring the porosity and pore size of electrospun synthetic human elastin scaffolds for dermal tissue engineering. *Biomaterials* **32,** 6729–36 (2011).

122. Theron, A., Zussman, E. & Yarin, A. L. Electrostatic field-assisted alignment of electrospun nanofibres. *Nanotechnology* **12,** 384–390 (2001).

123. Piperno, S., Lozzi, L., Rastelli, R., Passacantando, M. & Santucci, S. PMMA nanofibers production by electrospinning. *Appl. Surf. Sci.* **252,** 5583–5586 (2006).

124. Uyar, T., Balan, A., Toppare, L. & Besenbacher, F. Electrospinning of cyclodextrin functionalized poly(methyl methacrylate) (PMMA) nanofibers. *Polymer (Guildf).* **50,** 475–480 (2009).

125. Uyar, T. *et al.* Cyclodextrin functionalized poly(methyl methacrylate) (PMMA) electrospun nanofibers for organic vapors waste treatment. *J. Memb. Sci.* **365,** 409–417 (2010).

126. Xu, X., Zhang, J. F. & Fan, Y. Fabrication of cross-linked polyethyleneimine microfibers by reactive electrospinning with in situ photo-cross-linking by UV radiation. *Biomacromolecules* **11,** 2283–2289 (2010).

127. Treharne, A. J., Thomson, H. a J., Grossel, M. C. & Lotery, A. J. Developing methacrylate-based copolymers as an artificial Bruch's membrane substitute. *J. Biomed. Mater. Res. A* **100,** 2358–64 (2012).

128. Huang, Z.-M., Zhang, Y.-Z., Kotaki, M. & Ramakrishna, S. A review on polymer nanofibers by electrospinning and their applications in nanocomposites. *Compos. Sci. Technol.* **63,** 2223–2253 (2003).

129. Boland, E. D. *et al.* Tailoring Tissue Enginerring Scaffolds using Electrostatic Processing Techniques: A Study of Poly(glycolic acid) Electrospinning. *J. Macromol. Sci. - Pure Appl.*

Chem. **38,** 1231–1243 (2001).

130. Cramariuc, B. *et al.* Fiber diameter in electrospinning process. *J. Electrostat.* **71,** 189–198 (2013).

131. Yu, N. Y. C., Schindeler, A., Little, D. G. & Ruys, A. J. Biodegradable poly(alpha-hydroxy acid) polymer scaffolds for bone tissue engineering. *J. Biomed. Mater. Res. B. Appl. Biomater.* **93,** 285–95 (2010).

132. Davis, M. W. & Vacanti, J. P. Toward development of an implantable tissue engineered liver. *Biomaterials* **17,** 365–72 (1996).

133. Chen, Q.-Z., Ishii, H. & Harding, S. E. An elastomeric patch derived from poly(glycerol sebacate) for delivery of embryonic stem cells to the heart. *Biomaterials* **31,** 3885–3893 (2010).

134. Young, C.-D., Wu, J.-R. & Tsou, T.-L. Fabrication and characteristics of polyHEMA artificial skin with improved tensile properties. *J. Memb. Sci.* **146,** 83–93 (1998).

135. Ghasemi-Mobarakeh, L., Prabhakaran, M. & Ramakrishna, S. Electrospun poly(ε-caprolactone)/gelatin nanofibrous scaffolds for nerve tissue engineering. *Biomaterials* **29,** 4532–4539 (2008).

136. Sell, S. A., Mcclure, M. J. & Bowlin, G. L. Electrospun polydioxanone–elastin blends: potential for bioresorbable vascular grafts. *Biomed. Mater.* **1,** 72–80 (2006).

137. Wise, S. G. *et al.* A multilayered synthetic human elastin/polycaprolactone hybrid vascular graft with tailored mechanical properties. *Acta Biomater.* **7,** 295–303 (2011).

138. Han, D. & Gouma, P.-I. Electrospun bioscaffolds that mimic the topology of extracellular matrix. *Nanomedicine* **2,** 37–41 (2006).

139. Gu, B. K., Ismail, Y. A. & Kim, S. J. A linear actuation of polymeric nanofibrous bundle for artificial muscles. *Chem. Mater.* **21,** 511–515 (2009).

140. Yang, F., Murugan, R. & Wang, S. Fabrication of nano-structured porous PLLA scaffold intended for nerve tissue engineering. *Biomaterials* **25,** 1891–1900 (2004).

141. Jay, B., Apple, D. J. & Sims, J. Remembrances of things past: Harold Ridley and the Invention of the Intraocular Lens. *Surv. Ophthalmol.* **40,** 279–292 (1996).

142. Tonsomboon, K. & Oyen, M. L. Composite electrospun gelatin fiber-alginate gel scaffolds for mechanically robust tissue engineered cornea. *J. Mech. Behav. Biomed. Mater.* **21,** 185–94 (2013).

143. Liu, Y., Ren, L. & Wang, Y. Crosslinked collagen–gelatin–hyaluronic acid biomimetic film for cornea tissue engineering applications. *Mater. Sci. Eng. C* **33,** 196–201 (2013).

144. Aksungur, P. *et al.* Development and characterization of Cyclosporine A loaded nanoparticles for ocular drug delivery: Cellular toxicity, uptake, and kinetic studies. *J. Control. Release* **151,** 286–294 (2011).

145. Nagarwal, R. C., Kant, S., Singh, P. N., Maiti, P. & Pandit, J. K. Polymeric nanoparticulate system: a potential approach for ocular drug delivery. *J. Control. Release* **136,** 2–13 (2009).

146. Bakhshandeh, H. *et al.* Poly (epsilon-caprolactone) nanofibrous ring surrounding a polyvinyl alcohol hydrogel for the development of a biocompatible two-part artificial cornea. *Int. J. Nanomedicine* **6,** 1509–15 (2011).

147. Myung, D. *et al.* Design and fabrication of an artificial cornea based on a photolithographically patterned hydrogel construct. *Biomed. Microdevices* **9,** 911–22 (2007).

148. Binder, S. Scaffolds for retinal pigment epithelium (RPE) replacement therapy. *Br. J. Ophthalmol.* **95,** 441–2 (2011).

149. Tezcaner, A., Bugra, K. & Hasirci, V. Retinal pigment epithelium cell culture on surface modified poly(hydroxybutyrate-co-hydroxyvalerate) thin films. *Biomaterials* **24,** 4573–4583 (2003).

150. Thumann, G. *et al.* The in vitro and in vivo behaviour of retinal pigment epithelial cells

cultured on ultrathin collagen membranes. *Biomaterials* **30,** 287–94 (2009).

151. Warnke, P. H. *et al.* Primordium of an artificial Bruch's membrane made of nanofibers for engineering of retinal pigment epithelium cell monolayers. *Acta Biomater.* **9,** 9414–22 (2013).

152. Shadforth, A. M. a, George, K. a, Kwan, A. S., Chirila, T. V & Harkin, D. G. The cultivation of human retinal pigment epithelial cells on Bombyx mori silk fibroin. *Biomaterials* **33,** 4110–7 (2012).

153. Martínez-Osorio, H. *et al.* Genetically engineered elastin-like polymer as a substratum to culture cells from the ocular surface. *Curr. Eye Res.* **34,** 48–56 (2009).

154. Xiang, P. *et al.* A novel Bruch's membrane-mimetic electrospun substrate scaffold for human retinal pigment epithelium cells. *Biomaterials* **35,** 9777–88 (2014).

155. Dunn, K. C., Aotaki-Keen, a E., Putkey, F. R. & Hjelmeland, L. M. ARPE-19, a human retinal pigment epithelial cell line with differentiated properties. *Exp. Eye Res.* **62,** 155–169 (1996).

156. Thieltges, F., Stanzel, B. V, Liu, Z. & Holz, F. G. A nanofibrillar surface promotes superior growth characteristics in cultured human retinal pigment epithelium. *Ophthalmic Res.* **46,** 133–40 (2011).

157. Schindler, M. *et al.* A synthetic nanofibrillar matrix promotes in vivo-like organization and morphogenesis for cells in culture. *Biomaterials* **26,** 5624–5631 (2005).

158. Nisbet, D. R., Forsythe, J. S., Shen, W., Finkelstein, D. I. & Horne, M. K. Review paper: a review of the cellular response on electrospun nanofibers for tissue engineering. *J. Biomater. Appl.* **24,** 7–29 (2009).

159. Hu, J. & Bok, D. The use of cultured human fetal retinal pigment epithelium in studies of the classical retinoid visual cycle and retinoid-based disease processes. *Exp. Eye Res.* **126,** 46–50 (2014).

160. Hamann, S., Kiilgaard, J. F., La Cour, M., Prause, J. U. & Zeuthen, T. Cotransport of H+, lactate, and H2O in porcine retinal pigment epithelial cells. *Exp. Eye Res.* **76,** 493–504 (2003).

161. Philp, N. J., Ochrietor, J. D., Rudoy, C., Muramatsu, T. & Linser, P. J. Loss of MCT1, MCT3, and MCT4 expression in the retinal pigment epithelium and neural retina of the 5A11/basigin-null mouse. *Investig. Ophthalmol. Vis. Sci.* **44,** 1305–1311 (2003).

162. Philp, N. J., Wang, D., Yoon, H. & Hjelmeland, L. M. Polarized expression of monocarboxylate transporters in human retinal pigment epithelium and ARPE-19 cells. *Investig. Ophthalmol. Vis. Sci.* **44,** 1716–1721 (2003).

163. Reichhart, N. & Strauß, O. Ion channels and transporters of the retinal pigment epithelium. *Exp. Eye Res.* **126,** 27–37 (2014).

164. Xiang, P., Li, M., Zhang, C. Y., Chen, D. L. & Zhou, Z. H. Cytocompatibility of electrospun nanofiber tubular scaffolds for small diameter tissue engineering blood vessels. *Int. J. Biol. Macromol.* **49,** 281–288 (2011).

165. Haneef, A. S. & Downes, S. Assessing the Suitability of Electrospun Poly(Ethylene Terephthalate) and Polystyrene as Cell Carrier Substrates for Potential Subsequent Implantation as a Synthetic Bruch's Membrane. *Int. J. Polym. Mater. Polym. Biomater.* **64,** 320–332 (2015).

166. Krishna, Y. *et al.* Expanded polytetrafluoroethylene as a substrate for retinal pigment epithelial cell growth and transplantation in age-related macular degeneration. *Br. J. Ophthalmol.* **95,** 569–73 (2011).

167. Liu, Z., Yu, N., Holz, F. G., Yang, F. & Stanzel, B. V. Enhancement of retinal pigment epithelial culture characteristics and subretinal space tolerance of scaffolds with 200 nm fiber topography. *Biomaterials* **35,** 2837–50 (2014).

168. McHugh, K. J., Tao, S. L. & Saint-Geniez, M. Porous poly(ε-caprolactone) scaffolds for

retinal pigment epithelium transplantation. *Invest. Ophthalmol. Vis. Sci.* **55,** 1754–62 (2014).

169. Tao, S. *et al.* Survival, migration and differentiation of retinal progenitor cells transplanted on micro-machined poly(methyl methacrylate) scaffolds to the subretinal space. *Lab Chip* **7,** 695–701 (2007).

170. Heath, D. E. & Cooper, S. L. Interaction of endothelial cells with methacrylic terpolymer biomaterials. *J. Biomed. Mater. Res.* **92B,** 289–296 (2009).

171. Gentile, F. *et al.* Biomaterials cells preferentially grow on rough substrates. *Biomaterials* **31,** 7205–7212 (2010).

172. Treharne, A. J., Grossel, M. C., Lotery, A. J. & Thomson, H. a. The chemistry of retinal transplantation: the influence of polymer scaffold properties on retinal cell adhesion and control. *Br. J. Ophthalmol.* **95,** 768–73 (2011).

173. Chen, R., Yu, X. & Li, L. Esters Using Low Energy Collision-Induced Dissociation in Electrospray Ionization. *J Am Soc Mass Spectrom* **13,** 888–897 (2002).

174. Sakamoto, H., Anase, T., Osuga, H. & Kimura, K. Complexation and fluorescence behavior of a copolymer bearing azacrown ether and anthracene moieties. *React. Funct. Polym.* **71,** 569–573 (2011).

175. Hussain, A. a, Lee, Y., Zhang, J.-J. & Marshall, J. Disturbed matrix metalloproteinase activity of Bruch's membrane in age-related macular degeneration. *Invest. Ophthalmol. Vis. Sci.* **52,** 4459–66 (2011).

176. Schraermeyer, U. *et al.* Porcine Iris Pigment Epithelial Cells can take up Retinal Outer Segments. *Exp. Eye Res.* **65,** 277–287 (1997).

177. Mao, Y. & Finnemann, S. C. Analysis of Photoreceptor Outer Segment Phagocytosis by RPE cells in culture. *Methods Mol. Biol.* **935,** 285–295 (2013).

178. Krohne, T. U., Holz, F. G. & Kopitz, J. Apical-to-basolateral transcytosis of photoreceptor outer segments induced by lipid peroxidation products in human retinal pigment epithelial cells. *Invest. Ophthalmol. Vis. Sci.* **51,** 553–60 (2010).

179. Barhate, R. S. & Ramakrishna, S. Nanofibrous filtering media: Filtration problems and solutions from tiny materials. *J. Memb. Sci.* **296,** 1–8 (2007).

180. Barhate, R. S., Loong, C. K. & Ramakrishna, S. Preparation and characterization of nanofibrous filtering media. *J. Memb. Sci.* **283,** 209–218 (2006).

181. Zhang, S., Shim, W. S. & Kim, J. Design of ultra-fine nonwovens via electrospinning of Nylon 6: Spinning parameters and filtration efficiency. *Mater. Des.* **30,** 3659–3666 (2009).

182. Dalila, N., Affandi, N. & Bach, Y. A non-destructive method for thickness measurement of thin electrospun membranes using white light profilometry. *J. Mater. Sci. Lett.* **45,** 1411–1418 (2010).

183. Kivioja, A. O., Jääskeläinen, A.-S., Ahtee, V. & Vuorinen, T. Thickness measurement of thin polymer films by total internal reflection Raman and attenuated total reflection infrared spectroscopy. *Vib. Spectrosc.* **61,** 1–9 (2012).

184. Meyer, M. W., Nguyen, V. H. T. & Smith, E. A. Scanning angle Raman spectroscopy measurements of thin polymer films for thickness and composition analyses. *Vib. Spectrosc.* **65,** 94–100 (2013).

185. McCarty, K. F. Raman scattering as a technique of measuring film thickness: interference effects in thin growing films. *Appl Opt* **26,** 4482–6 (1987).

186. Gesang, T., Fanter, D., Hoper, R., Possart, W. & D, H. O. Comparative film thickness determination by atomic force microscopy and ellipsometry for ultrathin polymer films. *Surf. Interface Anal.* **23,** 797–808 (1995).

187. Ton-That, C., Shard, a. G. & Bradley, R. H. Thickness of spin-cast polymer thin films determined by angle-resolved XPS and AFM tip-scratch methods. *Langmuir* **16,** 2281–2284 (2000).

188. Kane, S. R., Ashby, P. D. & Pruitt, L. a. ATR-FTIR as a thickness measurement technique for hydrated polymer-on-polymer coatings. *J. Biomed. Mater. Res. - Part B Appl. Biomater.* **91,** 613–620 (2009).

189. Hong, X., Gan, Y. & Wang, Y. Facile measurement of polymer film thickness ranging from nanometer to micrometer scale using atomic force microscopy. *Surf. Interface Anal.* **43,** 1299–1303 (2011).

190. Healy, N. *et al.* Polycrystalline silicon optical fibres with atomically smooth surfaces. *Opt. Lett.* **36,** 2480–2482 (2011).

191. Freischlad, K. Optical surface profiling: profilometer advances benefit surface analysis, film-thickness measurement. *Laser Focus World* **46,** 7–15 (2010).

192. Bamberg, E. & Rakwal, D. Experimental investigation of wire electrical discharge machining of gallium-doped germanium. *J. Mater. Process. Technol.* **197,** 419–427 (2008).

193. Alirezaei, S., Monirvaghefi, S. M., Saatchi, a., Ürgen, M. & Kazmanlı, K. Novel investigation on tribological properties of Ni–P–Ag–Al2O3 hybrid nanocomposite coatings. *Tribol. Int.* **62,** 110–116 (2013).

194. Karampelas, M. *et al.* Evaluation of retinal pigment epithelium-Bruch's membrane complex thickness in dry age-related macular degeneration using optical coherence tomography. *Br. J. Ophthalmol.* **97,** 1256–61 (2013).

195. Srinivasan, V. J. *et al.* Characterization of outer retinal morphology with high-speed, ultrahigh-resolution optical coherence tomography. *Invest. Ophthalmol. Vis. Sci.* **49,** 1571–1579 (2008).

196. Kim, J. H., Kim, J. R., Kang, S. W., Kim, S. J. & Ha, H. S. Thinner choroid and greater drusen extent in retinal angiomatous proliferation than in typical exudative age-related macular degeneration. *Am. J. Ophthalmol.* **155,** 743–9, 749–2 (2013).

197. Bloom, S. M. & Singal, I. P. *The outer Bruch membrane layer: a previously undescribed spectral-domain optical coherence tomography finding. Retina Philadelphia Pa* **31,** 316–323 (2011).

198. Drexler, W. *et al.* Quantification of photoreceptor layer thickness in different macular pathologies using ultrahigh resolution optical coherence tomography. *Ophthalmic Technol. XIV* **5314,** 132–137 (2004).

199. Iijima, H., Iida, T., Imai, M., Gohdo, T. & Tsukahara, S. Optical coherence tomography of orange-red subretinal lesions in eyes with idiopathic polypoidal choroidal vasculopathy. *Am. J. Ophthalmol.* **129,** 21–6 (2000).

200. Querques, G., Georges, A., Ben Moussa, N., Sterkers, M. & Souied, E. H. Appearance of regressing drusen on optical coherence tomography in age-related macular degeneration. *Ophthalmology* **121,** 173–9 (2014).

201. Sallo, F. *et al.* Bruch's membrane changes in transgenic mice overexpressing the human biglycan and apolipoprotein b-100 genes. *Exp. Eye Res.* **89,** 178–186 (2009).

202. Tsukahara, I. *et al.* Early attachment of uncultured retinal pigment epithelium from aged donors onto Bruch's membrane explants. *Exp. Eye Res.* **74,** 255–66 (2002).

203. Nag, T. C. Bruch's membrane with an elastic lamina in the eye of a teleost. *J. Anat.* **182,** 113–115 (1993).

204. Rina, S. *et al.* Three-Dimensional Spheroidal Culture Visualization of Membranogenesis of Bruch's Membrane and Basolateral Functions of the Retinal Pigment Epithelium. *Invest. Ophthalmol. Vis. Sci.* **54,** 1740–1749 (2013).

205. Bailey, T. A., Alexander, R. A., Dubovy, S. R., Luthert, P. J. & Chong, N. H. Measurement of TIMP-3 expression and Bruch's membrane thickness in human macula. *Exp. Eye Res.* **73,** 851–858 (2001).

206. Okubo, A. *et al.* The relationships of age changes in retinal pigment epithelium and Bruch's membrane. *Exp. Eye Res.* **40,** 443–449 (1999).

207. Ramrattan, R. S. *et al.* Morphometric Analysis of Bruch's Membrane, the Choriocapillaris, and the Choroid in Aging. *Invest. Ophthalmol. Vis. Sci.* **35,** 2857–2864 (1994).

208. Neuhoff, V., Arold, N., Taube, D. & Ehrhardt, W. Improved staining of proteins in polyacrylamide gels including isoelectric focusing gels with clear background at nanogram sensitivity using Coomassie Brilliant Blue G-250 and R-250. *Electrophoresis* **9,** 255–262 (1988).

209. Nivinskas, H. & Cole, K. D. Environmentally Benign Staining Procedure for Electrophoresis Gels Using Coomassie Brilliant Blue. *Biotechniques* **20,** 380–385 (1996).

210. Meyer, T. S. & Lamberts, B. L. Use of Coomassie Brilliant Blue R250 for the electrophoresis of microgram quantities of parotid saliva proteins on acrylamide-gel strips. *Biochim. Biophys. Acta* **107,** 144–145 (1965).

211. Fazekas De St Groth, S., Webster, R. G. & Datyner, A. Two new staining procedures for quantitative estimation of proteins on electrophoretic strips. *Biochim. Biophys. Acta* **71,** 377–391 (1963).

212. Yaji, N., Yamato, M., Yang, J., Okano, T. & Hori, S. Transplantation of tissue-engineered retinal pigment epithelial cell sheets in a rabbit model. *Biomaterials* **30,** 797–803 (2009).

213. Kang, S. J., Schmack, I., Benson, H. E. & Grossniklaus, H. E. Histopathological findings in postmortem eyes after photodynamic therapy for choroidal neovascularisation in age-related macular degeneration: report of two cases. *Br. J. Ophthalmol.* **91,** 1602–6 (2007).

214. Schnurrbusch, U. E., Welt, K., Horn, L. C., Wiedemann, P. & Wolf, S. Histological findings of surgically excised choroidal neovascular membranes after photodynamic therapy. *Br. J. Ophthalmol.* **85,** 1086–91 (2001).

215. Curcio, C. A., Millican, C. L. & Bailey, T. Lipids in human Bruch's membrane: histochemistry and ultrastructure. *Invest. Ophthalmol. Vis. Sci.* **40,** S921–S921 (1999).

216. Haimovici, R., Gantz, D. L., Rumelt, S., Freddo, T. F. & Small, D. M. The lipid composition of drusen, Bruch's membrane, and sclera by hot stage polarizing light microscopy. *Invest. Ophthalmol. Vis. Sci.* **42,** 1592–1599 (2001).

217. A.F Maarten Altelaar,I. Klinked, K. Jalink, Lange, R. P. J. De, Adam, R. a. . & R.M.A Heeren. Gold enhanced biomolecular surface imaging of cells and tissue by SIMS and MALDI Mass Spectrometry. *Anal Chem* **78,** 734–742 (2006).

218. Chong, N. H. V. *et al.* Decreased thickness and integrity of the macular elastic layer of Bruch's membrane correspond to the distribution of lesions associated with age-related macular degeneration. *Am. J. Pathol.* **166,** 241–51 (2005).

219. Lu, J. T., Lee, C. J., Bent, S. F., Fishman, H. a. & Sabelman, E. E. Thin collagen film scaffolds for retinal epithelial cell culture. *Biomaterials* **28,** 1486–1494 (2007).

220. Doshi, J. & Reneker, D. H. Electrospinning process and applications of electrospun fibres. *J. Electrostat.* **35,** 151–160 (1995).

221. Deitzel, J. M., Kleinmayer, J., Harris, D. & Beck Tan, N. C. The effect of processing variables on the morphology of electrospun nanofibres and textiles. *Polymer (Guildf).* **42,** 261–272 (2001).

222. Eda, G. & Shivkumar, S. Bead structure variations during electrospinning of polystyrene. *J. Mater. Sci.* **41,** 5704–5708 (2006).

223. Fridrikh, S. V, Yu, J. H., Brenner, M. P. & Rutledge, G. C. Controlling the fiber diameter during electrospinning. *Phys. Rev. Lett.* **90,** 144502 (2003).

224. Liu, Y., He, J.-H. H., Yu, J.-Y. & Zeng, H.-M. Controlling numbers and sizes of beads in electrospun nanofibers. *Polym. Int.* **57,** 632–636 (2008).

225. Huan, S. *et al.* Effect of Experimental Parameters on Morphological, Mechanical and Hydrophobic Properties of Electrospun Polystyrene Fibers. *Materials (Basel).* **8,** 2718–2734 (2015).

226. Buchko, C. J., Chen, L. C., Shen, Y. & Martina, D. C. Processing and microstructural

characterization of porous biocompatible\rprotein polymer thin films. *Polymer (Guildf).* **40,** 7397–7407 (1999).

227. Megelski, S., S.Stephens, J., Chase, D. B. & F.Rabolt, J. Micro-and Nanostructured Surface Morphology on Electrospum Polymer Fibers. *Macromolecules* **35,** 8456–8466 (2002).

228. Min, B. M. *et al.* Electrospinning of silk fibroin nanofibers and its effect on the adhesion and spreading of normal human keratinocytes and fibroblasts in vitro. *Biomaterials* **25,** 1289–1297 (2004).

229. Goldbaum, M. H. & Madden, K. A new perspective on Bruch's membrane and the retinal pigment epithelium. *Br. J. Ophthalmol.* **66,** 17–25 (1982).

230. Cankova, Z., Huang, J.-D., Kruth, H. S. & Johnson, M. Passage of low-density lipoproteins through Bruch's membrane and choroid. *Exp. Eye Res.* **93,** 947–55 (2011).

231. Thomson, H. a *et al.* Biodegradable poly(α-hydroxy ester) blended microspheres as suitable carriers for retinal pigment epithelium cell transplantation. *J. Biomed. Mater. Res. A* **95,** 1233–43 (2010).

232. Singh, A. K., Srivastava, G. K., Martín, L., Alonso, M. & Pastor, J. C. Bioactive substrates for human retinal pigment epithelial cell growth from elastin-like recombinamers. *J. Biomed. Mater. Res. A* **102,** 639–46 (2014).

233. Alge, C. S., Hauck, S. M., Priglinger, S. G., Kampik, A. & Ueffing, M. Differential protein profiling of primary versus immortalized human RPE cells identifies expression patterns associated with cytoskeletal remodeling and cell survival. *J. Proteome Res.* **5,** 862–878 (2006).

234. Proulx, S., Landreville, S., Guérin, S. L. & Salesse, C. Integrin alpha5 expression by the ARPE-19 cell line: comparison with primary RPE cultures and effect of growth medium on the alpha5 gene promoter strength. *Exp. Eye Res.* **79,** 157–65 (2004).

235. Castillo Jr., B. V, Little, C. W., del Cerro, C. & del Cerro, M. An improved method of isolating fetal human retinal pigment epithelium. *Curr Eye Res* **14,** 677–683 (1995).

236. McKay, B. S. & Burke, J. M. Separation of Phenotypically Distinct Subpopulations of Cultured Human Retinal Pigment Epithelial Cells. *Exp. Cell Res.* **213,** 85–92 (1994).

237. Joseph, B. Y. D. P. & Miller, S. S. Apical and Basal Membrane Ion Transport Mechanisms in Bovine RPE. *J. Physiol.* **435,** 439–463 (1991).

238. Stamer, W. D. Aquaporin-1 Channels in Human Retinal Pigment Epithelium: Role in Transepithelial Water Movement. *Invest. Ophthalmol. Vis. Sci.* **44,** 2803–2808 (2003).

239. Terasaki, H. *et al.* Different Effects of Thrombin on VEGF Secretion, Proliferation, and Permeability in Polarized and Non-polarized Retinal Pigment Epithelial Cells. *Curr. Eye Res.* 1–10 (2014). doi:10.3109/02713683.2014.964417

240. Bonilha, V. L. Retinal pigment epithelium (RPE) cytoskeleton in vivo and in vitro. *Exp. Eye Res.* **126,** 38–45 (2014).

241. Wollmann, G. *et al.* Voltage-dependent ion channels in the mouse RPE: Comparison with Norrie disease mice. *Vision Res.* **46,** 688–698 (2006).

242. Verma, V., Sauer, T. & Zhou, M. Constancy of ERp29 Expression in Cultured Retinal Pigment Epithelial Cells in the Ccl2/Cx3cr1 Deficient Mouse Model of Age- Related Macular Degeneration. *Curr. Eye Res.* **33,** 701–707 (2008).

243. Ratnayaka, J. A., Lynn, S. A., Griffiths, H. & Al, E. An ex-vivo platform for manipulation and study of Retinal Pigment Epithelial (RPE) cells in long-term culture. *Invest. Ophthalmol. Vis. Sci.* **56,** 2332 (2015).

244. Keeler, C. E. The Inheritance of a Retinal Abnormality in White Mice. *Proc. Natl. Acad. Sci. U. S. A.* **10,** 329–333 (1924).

245. Hafezi, F., Grimm, C., Simmen, B. C., Wenzel, A. & Remé, C. E. Molecular ophthalmology : an update on animal models for retinal degenerations and dystrophies. *Br. J. Opthalmology* **84,** 922–927 (2000).

246. Alge, C. S. *et al.* Comparative proteome analysis of native differentiated and cultured dedifferentiated human RPE cells. *Investig. Ophthalmol. Vis. Sci.* **44,** 3629–3641 (2003).

247. Geiger, B. A 130K protein from chicken gizzard: Its localization at the termini of microfilament bundles in cultured chicken cells. *Cell* **18,** 193–205 (1979).

248. Geiger, B., Tokuyasu, K. T., Dutton, a H. & Singer, S. J. Vinculin, an intracellular protein localized at specialized sites where microfilament bundles terminate at cell membranes. *Proc. Natl. Acad. Sci. U. S. A.* **77,** 4127–4131 (1980).

249. Avnur, Z. & Geiger, B. Substrate-attached membranes of cultured cells isolation and characterization of ventral cells membranes and the associated cytoskeleton. *J. Mol. Biol.* **153,** 361–379 (1981).

250. Geiger, B., Schmid, E. & Franke, W. Spatial distribution of proteins specific for desmosomes and adhaerens junctions in epithelial cells demonstrated by double immunofluorescence microscopy. *Differentiation* **23,** 189–205 (1983).

251. Schaller, M. D., Otey, C. A., Hildebrand, J. D. & Parsons, J. T. Focal adhesion kinase and paxillan bind to peptides mimicking beta integrin cytoplasmic domains. *J. Cell Biol.* **130,** 1181–1187 (1995).

252. Moiseyev, G., Chen, Y., Takahashi, Y., Wu, B. X. & Ma, J.-X. RPE65 is the isomerohydrolase in the retinoid visual cycle. *Proc. Natl. Acad. Sci. U. S. A.* **102,** 12413–8 (2005).

253. Gundersen, D., Orlowski, J. & Rodriguez-Boulan, E. Apical Polarity of Na,K-ATPase in Retinal Pigment Epithelium Is Linked to a Reversal of the Ankyrin-Fodrin Submembrane Cytoskeleton. *J. Cell Biol.* **112,** 863–872 (1991).

254. Kannan, R. *et al.* Attainment of polarity promotes growth factor secretion by retinal pigment epithelial cells : Relevance to age-related macular degeneration. *Aging (Albany. NY).* **2,** 28–42 (2010).

255. Quinn, R. H. & Miller, S. S. Ion transport mechanisms in native human retinal pigment epithelium. *Invest. Ophthalmol. Vis. Sci.* **33,** 3513–27 (1992).

256. Itoh, M. *et al.* The 220-kD protein colocalizing with cadherins in non-epithelial cells is identical to ZO-1, a tight junction-associated protein in epithelial cells: cDNA cloning and immunoelectron microscopy. *J. Cell Biol.* **121,** 491–502 (1993).

257. Löffler, T., Flunkert, S., Temmel, M. & Hutter-Paier, B. Decreased plasma Aβ in hyperlipidemic APPSL transgenic mice is associated with BBB dysfunction. *Front. Neurosci.* **10,** 1–8 (2016).

258. Schraermeyer, U. & Heimann, K. Current understanding on the role of retinal pigment epithelium and its pigmentation. *Pigment Cell Res.* **12,** 219–236 (1999).

259. Kim, G. M., Lach, R., Michler, G. H., Pötschke, P. & Albrecht, K. Relationships between phase morphology and deformation mechanisms in polymer nanocomposite nanofibres prepared by an electrospinning process. *Nanotechnology* **17,** 963–972 (2006).

260. Mack, J. J. *et al.* Graphite Nanoplatelet Reinforcement of Electrospun Polyacrylonitrile Nanofibers. *Adv. Mater.* **17,** 77–80 (2005).

261. Wang, X., Zhang, K., Zhu, M., Hsiao, B. S. & Chu, B. Enhanced mechanical performance of self-bundled electrospun fiber yarns via post-treatments. *Macromol. Rapid Commun.* **29,** 826–831 (2008).

262. Sen, R. *et al.* Preparation of single-walled carbon nanotube reinforced polystyrene and polyurethane nanofibers and membranes by electrospinning. *Nano Lett.* **4,** 459–464 (2004).

263. Yoon, K., Hsiao, B. S. & Chu, B. Formation of functional polyethersulfone electrospun membrane for water purification by mixed solvent and oxidation processes. *Polymer (Guildf).* **50,** 2893–2899 (2009).

264. Huang, L., Manickam, S. S. & McCutcheon, J. R. Increasing strength of electrospun nanofiber membranes for water filtration using solvent vapor. *J. Memb. Sci.* **436,** 213–220

(2013).

265. Jenkins, A. D., Kratochvil, P., Stepto, R. F. T. & Suter, U. W. Glossary of basic terms in polymer science. *Pure Appl. Chem.* **68,** 2287–2311 (1996).

266. Chenite, A. *et al.* Novel injectable neutral solutions of chitosan form biodegradable gels in situ. *Biomaterials* **21,** 2155–2161 (2000).

267. Ahmadi, R. & De Bruijn, J. D. Biocompatibility and gelation of chitosan-glycerol phosphate hydrogels. *J. Biomed. Mater. Res. - Part A* **86,** 824–832 (2008).

268. Faneca, H., Lima, M. P., Gil, M. H. & Figueiredo, M. M. In Situ Forming Chitosan Hydrogels Prepared via Ionic / Covalent Co-Cross-Linking. *Biomacromolecules* **12,** 3275–3284 (2011).

269. Nimni, M. E., Cheung, D., Strates, B., Kodama, M. & Sheikh, K. Chemically modified collagen: A natural biomaterial for tissue replacement. *J. Biomed. Mater. Res.* **21,** 741–771 (1987).

270. Olde Damink, L. H. H., Dijkstra, P. J. & Feijen, J. Crosslinking of dermal sheep collagen using hexamethylene diisocyanate. *J. Mater. Sci. Mater. Med.* **6,** 429–434 (1995).

271. McClure, M., Sell, S. & Barnes, C. Cross-linking electrospun polydioxanone-soluble elastin blends: material characterization. *J. Eng. …* 1–10 (2008).

272. Kishan, A. P. *et al.* In situ crosslinking of electrospun gelatin for improved fiber morphology retention and tunable degradation. *J. Mater. Chem. B* **3,** 7930–7938 (2015).

273. Choi, S. S., Hong, J. P., Seo, Y. S., Chung, S. M. & Nah, C. Fabrication and characterization of electrospun polybutadiene fibers crosslinked by UV irradiation. *J. Appl. Polym. Sci.* **101,** 2333–2337 (2006).

274. Canary, S. & Stevens, M. Thermally reversible crosslinking of polystyrene via the furan–maleimide Diels–Alder reaction. *J. Polym. Sci. Part A Polym. Chem.* **30,** 1755–1760 (1992).

275. Xiang, T. *et al.* Ionic-strength-sensitive polyethersulfone membrane with improved anti-fouling property modified by zwitterionic polymer via in situ cross-linked polymerization. *J. Memb. Sci.* **476,** 234–242 (2015).

276. Nimmo, C. M., Owen, S. C. & Shoichet, M. S. Diels-Alder Click cross-linked hyaluronic acid hydrogels for tissue engineering. *Biomacromolecules* **12,** 824–30 (2011).

277. Zhu, J. & Sun, G. Bio-functionalized nanofibrous membranes as a hybrid platform for selective antibody recognition and capturing. *RSC Adv.* **5,** 28115–28123 (2015).

278. Duong, T. T., Mckee, S. P., Chemistry, M., Sharp, M. & Point, D. R. L. W. N,N'-Disuccinimidyl Carbonate: A Useful Reagent for Alkoxycarbonylation of Amines. *Tetrahedron Lett.* **33,** 2781–2784 (1992).

279. Tasdelen, M. A. Diels–Alder 'click' reactions: recent applications in polymer and material science. *Polym. Chem.* **2,** 2133 (2011).

280. Crne, M., Park, J. O. & Srinivasarao, M. Electrospinning Physical Gels: The Case of Stereocomplex PMMA. *Macromolecules* **42,** 4353–4355 (2009).

281. Zhou, C., Wang, Q. & Wu, Q. UV-initiated crosslinking of electrospun poly(ethylene oxide) nanofibers with pentaerythritol triacrylate: Effect of irradiation time and incorporated cellulose nanocrystals. *Carbohydr. Polym.* **87,** 1779–1786 (2012).

282. Sullivan, S. T., Tang, C., Kennedy, A., Talwar, S. & Khan, S. A. Electrospinning and heat treatment of whey protein nanofibers. *Food Hydrocoll.* **35,** 36–50 (2014).

283. Anema, S. G. Effect of milk solids concentration on the gels formed by the acidification of heated pH-adjusted skim milk. *Food Chem.* **108,** 110–118 (2008).

284. Zheng, Y. *et al.* PEG-based hydrogel synthesis via the photodimerization of anthracene groups. *Macromolecules* **35,** 5228–5234 (2002).

285. Bouas-Laurent, H., Desvergne, J.-P., Castellan, A. & Lapouyade, R. Photodimerization of anthracenes in fluid solution: (part 2) mechanistic aspects of the photocycloaddition and of

the photochemical and thermal cleavage. *Chem. Soc. Rev.* **30,** 248–263 (2001).

286. Greene, F. D., Misrock, S. L. & Wolfe Jr, J. R. The Structure of Anthracene Photodimers. *J. Am. Chem. Soc.* **77,** 3852 (1955).

287. Bouas-Laurent, H., Desvergne, J.-P., Castellan, A. & Lapouyade, R. Photodimerization of anthracenes in fluid solution: structural aspects. *Chem. Soc. Rev.* **29,** 43–55 (2000).

288. Wells, L. a., Brook, M. a. & Sheardown, H. Generic, anthracene-based hydrogel crosslinkers for photo-controllable drug delivery. *Macromol. Biosci.* **11,** 988–998 (2011).

289. Lu, B., Zhu, D., Hinton, D., Humayun, M. S. & Tai, Y.-C. Mesh-supported submicron parylene-C membranes for culturing retinal pigment epithelial cells. *Biomed. Microdevices* **14,** 659–67 (2012).

290. Pulido, J., Sanders, D., Winters, J. L. & Klingel, R. Clinical outcomes and mechanism of action for rheopheresis treatment of Age-Related Macular Degeneration (AMD). *J. Clin. Apher.* **20,** 185–194 (2005).

291. Zarbin, M. A. Current Concepts in the Pathogenesis of Age-Related Macular Degeneration. *Arch. Ophthalmol.* **122,** 598–614 (2004).

292. Young, R. W. Pathophysiology of age-related macular degeneration. *Surv. Ophthalmol.* **31,** 291–306 (1987).

293. Drilling, S., Gaumer, J. & Lannutti, J. Fabrication of burst pressure competent vascular grafts via electrospinning: Effects of microstructure. *J. Biomed. Mater. Res. Part A* **88,** 923–934 (2008).

294. Khiste, S. V., Ranganath, V. & Nichani, A. S. Evaluation of tensile strength of surgical synthetic absorbable suture materials: an in vitro study. *J. Periodontal Implant Sci.* **43,** 130–135 (2013).

295. Bonilha, V. L., Finnemann, S. C. & Rodriguez-Boulan, E. Ezrin promotes morphogenesis of apical microvilli and basal infoldings in retinal pigment epithelium. *J. Cell Biol.* **147,** 1533–48 (1999).

296. Bonilha, V. L. Retinal pigment epithelium (RPE) cytoskeleton in vivo and in vitro. *Exp. Eye Res.* (2013). doi:10.1016/j.exer.2013.09.015

297. da Silva, G. R. *et al.* Polyurethanes as supports for human retinal pigment epithelium cell growth. *Int. J. Artif. Organs* **34,** 198–209 (2011).

298. Kearns, V. *et al.* Plasma polymer coatings to aid retinal pigment epithelial growth for transplantation in the treatment of age related macular degeneration. *J. Mater. Sci. Mater. Med.* **23,** 2013–21 (2012).

299. Hersel, U., Dahmen, C. & Kessler, H. RGD modified polymers: biomaterials for stimulated cell adhesion and beyond. *Biomaterials* **24,** 4385–4415 (2003).

300. Kuznetsova, A. V, Kurinov, A. M. & Aleksandrova, M. A. Cell Models to Study Regulation of Cell Transformation in Pathologies of Retinal Pigment Epithelium. *J. Ophthalmol.* **2014,** 1–18 (2014).

301. Campochiaro, P. A. Pathogenic mechanisms in proliferative vitreoretinopathy. *Arch. Ophthalmol.* **115,** 237–41 (1997).

302. Esser, P. *et al.* Apoptosis in proliferative vitreoretinal disorders: possible involvement of TGF-beta-induced RPE cell apoptosis. *Exp. Eye Res.* **65,** 365–78 (1997).

303. Miller, H., Miller, B. & Ryan, S. J. The role of retinal pigment epithelium in the involution of subretinal neovascularization. *Investig. Ophthalmol. Vis. Sci.* **27,** 1644–1652 (1986).

304. Chan, C.-M. *et al.* Effects of (-)-epigallocatechin gallate on RPE cell migration and adhesion. *Mol. Vis.* **16,** 586–95 (2010).

305. Sheridan, C., Hiscott, P. & Grierson, I. in *Essentials in Ophthalmology* 101–119 (2005).

306. Srivastava, G. K. *et al.* Flow cytometry assessment of the purity of human retinal pigment epithelial primary cell cultures. *J. Immunol. Methods* **389,** 61–8 (2013).

307. Srivastava, G. K. *et al.* Elastin-like recombinamers as substrates for retinal pigment epithelial cell growth. *J. Biomed. Mater. Res. - Part A* **97 A,** 243–250 (2011).

308. Akrami, H., Soheili, Z.-S. & Pakravesh, J. Evaluation of RPE65, CRALBP, VEGF, CD68 and Tyrosinase Gene Expression in Human REtinal Pigment Epithelial Cells Cultured on Amniotic Membrane. *Biochem. Genet.* **49,** 313–322 (2011).

309. Saari, J. C. *et al.* Visual cycle impairment in cellular retinaldehyde binding protein (CRALBP) knockout mice results in delayed dark adaptation. *Neuron* **29,** 739–748 (2001).

310. Shiragami, C., Matsuo, T., Shiraga, F. & Matsuo, N. Transplanted and repopulated retinal pigment epithelial cells on damaged Bruch's membrane in rabbits. *Br. J. Ophthalmol.* **82,** 1056–1062 (1998).

311. Toops, K. a, Tan, L. X. & Lakkaraju, A. A detailed three-step protocol for live imaging of intracellular traffic in polarized primary porcine RPE monolayers. *Exp. Eye Res.* **124,** 74–85 (2014).

312. Subrizi, A. *et al.* Generation of hESC-derived retinal pigment epithelium on biopolymer coated polyimide membranes. *Biomaterials* **33,** 8047–54 (2012).

313. Hussain, A. A., Rowe, L. & Marshall, J. Age-related alterations in the diffusional transport of amino acids across the human Bruch's-choroid complex. *J. Opt. Soc. Am. A* **19,** 166–172 (2002).

314. Chaitin, M. H. & Hall, M. O. Defective ingestion of rod outer segments by cultured dystrophic rat pigment epithelial cells. *Investig. Ophthalmol. Vis. Sci.* **24,** 812–820 (1983).

315. Nilsson, S. V. G., Sundelin, S. P., Wihlmark, U. & Brunk, U. T. Aging of cultured retinal pigment epithelial cells: oxidative reaction, lipofuscin formation and blue light damage. *Doc. Ophthalmol.* **106,** 13–16 (2003).

316. Finnemann, S. C., Bonilha, V. L., Marmorstein, A. D. & Rodriguez-Boulan, E. Phagocytosis of rod outer segments by retinal pigment epithelial cells requires avb5 integrin for binding but not for internalization. *Proc. Natl. Acad. Sci. U. S. A.* **94,** 12932–12937 (1997).

317. Mazzoni, F., Safa, H. & Finnemann, S. C. Understanding photoreceptor outer segment phagocytosis: Use and utility of RPE cells in culture. *Exp. Eye Res.* **126,** 51–60 (2014).

318. Finnemann, S. C. & Silverstein, R. L. Differential roles of CD36 and alphavbeta5 integrin in photoreceptor phagocytosis by the retinal pigment epithelium. *J. Exp. Med.* **194,** 1289–1298 (2001).

319. Boulton, M. E. Studying melanin and lipofuscin in RPE cell culture models. *Exp. Eye Res.* **126,** 61–67 (2014).

320. Flood, M. T., Gouras, P. & Kjeldbye, H. Growth characteristics and ultrastructure of human retinal pigment epithelium in vitro. *Invest. Ophthalmol. Vis. Sci.* **19,** 1309–1320 (1980).

321. Mitsuishi, M., Tanuma, T., Matsui, J. & Chen, J. Anthracene Chromophores in Polymer Langmuir - Blodgett Films by an Integrated Optical Waveguide Technique. *Langmuir* **17,** 17–19 (2001).

322. Fox, M. A. & Wooten, M. D. Characterization, Adsorption, and Photochemistry of Self-Assembled Monolayers of 10-Thiodecyl 2-Anthryl Ether on Gold. *Langmuir* **13,** 7099–7105 (1997).

323. Staudinger, H. in *The high molecular weight of organic compounds - rubber and cellulose* 105–123 (1932).

324. Ugarte, M., Hussain, a a & Marshall, J. An experimental study of the elastic properties of the human Bruch's membrane-choroid complex: relevance to ageing. *Br. J. Ophthalmol.* **90,** 621–6 (2006).